



Norwegian University of
Science and Technology

Performance Investigation of a PV/T Component Used as a Part of the Building Envelope

Herman Andersen

Joseph Ekenes

Master of Energy Use and Energy Planning

Submission date: July 2017

Supervisor: Vojislav Novakovic, EPT

Co-supervisor: Yanjun Dai, Shanghai Jiao Tong University

Laurent Georges, EPT

Norwegian University of Science and Technology

Department of Energy and Process Engineering

EPT-M-2017-07

MASTER THESIS

for

Student Herman Andersen

Spring 2017

Performance investigation of a PV/T component used as part of building envelop*Undersøkelse av ytelser for en PV/T komponent som er en del av bygningskroppen***Background and objective**

Super-insulated envelopes of modern buildings put new demands on performances of heating and cooling installations. Solar PV/T component used as part of building envelop is a promising technique that could contribute to enhanced efficiency of energy utilisation in modern buildings.

The goal for this collaborative activity is to analyse and develop design methods regarding natural ventilation effect for the novel solar PV/T component installed as a part of the building envelop at the Green Energy Laboratory (GEL) of the Shanghai Jiao Tong University, China, by use of simulations and laboratory measurements. The necessary background for this work was partly developed through the project assignment accomplished at NTNU. The major part of the work on analysis and development of design methods will be performed during this Master thesis work that will be accomplished at the GEL of the Jiao Tong University in Shanghai.

This collaborative assignment is realised as a part of the Joint Research Centre in Sustainable Energy of NTNU and Shanghai Jiao Tong University.

The following tasks are to be considered:

1. Develop a detailed work plan to analyse natural ventilation effect induced by solar PV/T components in the laboratory plant at GEL, based on simulations and measurements. The analysis should focus on the integration of solar PV/T components. Investigations should possibly consider combination with grid electricity supply, design procedures, as well as the optimal use of ventilation units.
2. Conduct critical analysis of the existing models and simulation tools for natural ventilation effect of solar PV/T components relevant for the GEL installations. Simulation tool TRNSYS should be used for the purpose.
3. Conduct analysis of the natural ventilation effect of the solar PV/T component in the Green Energy Laboratory by use of the most appropriate model(s).
4. Make a draft proposal (6-8 pages) for a scientific paper based on the main results of the work performed in the master thesis.
5. Make proposal for further work on the same topic.

Within 14 days of receiving the written text on the master thesis, the candidate shall submit a research plan for his project to the department.

When the thesis is evaluated, emphasis is put on processing of the results, and that they are presented in tabular and/or graphic form in a clear manner, and that they are analyzed carefully.

The thesis should be formulated as a research report with summary both in English and Norwegian, conclusion, literature references, table of contents etc. During the preparation of the text, the candidate should make an effort to produce a well-structured and easily readable report. In order to ease the evaluation of the thesis, it is important that the cross-references are correct. In the making of the report, strong emphasis should be placed on both a thorough discussion of the results and an orderly presentation.

The candidate is requested to initiate and keep close contact with his/her academic supervisor(s) throughout the working period. The candidate must follow the rules and regulations of NTNU as well as passive directions given by the Department of Energy and Process Engineering.

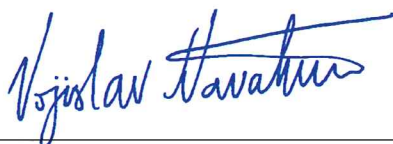
Risk assessment of the candidate's work shall be carried out according to the department's procedures. The risk assessment must be documented and included as part of the final report. Events related to the candidate's work adversely affecting the health, safety or security, must be documented and included as part of the final report. If the documentation on risk assessment represents a large number of pages, the full version is to be submitted electronically to the supervisor and an excerpt is included in the report.

Pursuant to “Regulations concerning the supplementary provisions to the technology study program/Master of Science” at NTNU §20, the Department reserves the permission to utilize all the results and data for teaching and research purposes as well as in future publications.

The final report is to be submitted digitally in DAIM. An executive summary of the thesis including title, student's name, supervisor's name, year, department name, and NTNU's logo and name, shall be submitted to the department as a separate pdf file. Based on an agreement with the supervisor, the final report and other material and documents may be given to the supervisor in digital format.

- Work to be done in lab (Green Energy Laboratory, Shanghai Jiao Tong University, China)
 Field work

Department of Energy and Process Engineering, 16. February 2017



Vojislav Novakovic
Academic Supervisor

Research Advisor:

Prof. Yanjun DAI, Shanghai Jiao Tong University, e-mail: yjdai@sjtu.edu.cn

Ass. Prof. Laurent Georges, NTNU

EPT-M-2017-20

MASTER THESIS

for

Student Joseph Ekenes

Spring 2017

Performance investigation of a PV/T component used as part of building envelop*Undersøkelse av ytelser for en PV/T komponent som er en del av bygningskroppen***Background and objective**

Super-insulated envelopes of modern buildings put new demands on performances of heating and cooling installations. Solar PV/T component used as part of building envelop is a promising technique that could contribute to enhanced efficiency of energy utilisation in modern buildings.

The goal for this collaborative activity is to analyse and develop design methods for the novel solar PV/T component installed as a part of the building envelop at the Green Energy Laboratory (GEL) of the Shanghai Jiao Tong University, China, by use of simulations and laboratory measurements. The necessary background for this work was partly developed through the project assignment accomplished at NTNU. The major part of the work on analysis and development of design methods will be performed during this Master thesis work that will be accomplished at the GEL of the Jiao Tong University in Shanghai.

This collaborative assignment is realised as a part of the Joint Research Centre in Sustainable Energy of NTNU and Shanghai Jiao Tong University.

The following tasks are to be considered:

1. Develop a detailed work plan to analyse solar PV/T components in the laboratory plant at GEL, based on simulations and measurements. The analysis should focus on the integration of solar PV/T components. Investigations should possibly consider combination with grid electricity supply, design procedures, as well as the optimal use of renewable energy sources and electricity storages.
2. Conduct critical analysis of the existing models and simulation tools for solar PV/T components relevant for the GEL installations. Simulation tool TRNSYS should be used for the purpose.
3. Conduct analysis of the solar PV/T component in the Green Energy Laboratory by use of the most appropriate model(s).
4. Make a draft proposal (6-8 pages) for a scientific paper based on the main results of the work performed in the master thesis.
5. Make proposal for further work on the same topic.

Within 14 days of receiving the written text on the master thesis, the candidate shall submit a research plan for his project to the department.

When the thesis is evaluated, emphasis is put on processing of the results, and that they are presented in tabular and/or graphic form in a clear manner, and that they are analyzed carefully.

The thesis should be formulated as a research report with summary both in English and Norwegian, conclusion, literature references, table of contents etc. During the preparation of the text, the candidate should make an effort to produce a well-structured and easily readable report. In order to ease the evaluation of the thesis, it is important that the cross-references are correct. In the making of the report, strong emphasis should be placed on both a thorough discussion of the results and an orderly presentation.

The candidate is requested to initiate and keep close contact with his/her academic supervisor(s) throughout the working period. The candidate must follow the rules and regulations of NTNU as well as passive directions given by the Department of Energy and Process Engineering.

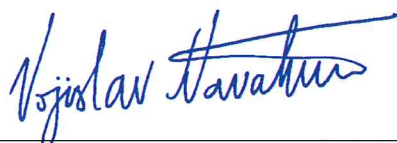
Risk assessment of the candidate's work shall be carried out according to the department's procedures. The risk assessment must be documented and included as part of the final report. Events related to the candidate's work adversely affecting the health, safety or security, must be documented and included as part of the final report. If the documentation on risk assessment represents a large number of pages, the full version is to be submitted electronically to the supervisor and an excerpt is included in the report.

Pursuant to “Regulations concerning the supplementary provisions to the technology study program/Master of Science” at NTNU §20, the Department reserves the permission to utilize all the results and data for teaching and research purposes as well as in future publications.

The final report is to be submitted digitally in DAIM. An executive summary of the thesis including title, student's name, supervisor's name, year, department name, and NTNU's logo and name, shall be submitted to the department as a separate pdf file. Based on an agreement with the supervisor, the final report and other material and documents may be given to the supervisor in digital format.

- Work to be done in lab (Green Energy Laboratory, Shanghai Jiao Tong University, China)
 Field work

Department of Energy and Process Engineering, 16. February 2017



Vojislav Novakovic
Academic Supervisor

Research Advisor:

Prof. Yanjun DAI, Shanghai Jiao Tong University, e-mail: yjdai@sjtu.edu.cn

Ass. Prof. Laurent Georges, NTNU

Preface

This master's thesis was conducted as a part of the study program Energy and Environmental Engineering at the Norwegian University of Science and Technology (NTNU). The thesis is a part of the Joint Research Center in Sustainable Energy of NTNU Shanghai Jiao Tong University (SJTU). The work was carried out during the spring semester of 2017 in Shanghai.

The main objective is to analyse and develop design methods for the novel solar PV/T component installed as a part of the building envelope at the Green Energy Laboratory at SJTU.

The authors would like to thank our supervisor, Professor Vojislav Novakovic for the opportunity to be part of the collaborative research and for consultations throughout the semester. Also, we would like to thank our co-supervisor Professor Yanjun Dai for guidance during our stay at SJTU. Moreover, we would like to thank Professor Laurent Georges for technical support regarding the use of TRNSYS.



Herman Andersen



Joseph Ekenes

Shanghai 2017

Abstract

The goal of this master thesis is to analyse and develop design methods for building integrated photovoltaic/thermal (BIPV/T) technology at the Green Energy Laboratory (GEL) at Shanghai Jiao Tong University (SJTU) in China.

PV/T technology generates electrical and thermal energy in a smaller area, compared to solely PV panels and solar collectors. For a PV panel, the electrical efficiency will decrease when the surface temperature increases, typically during peak solar irradiation. The air or water circulating in the PV/T component cools the PV surface, maintaining higher efficiency and thus higher energy generation.

A water based PV/T component has been calibrated and validated according to measurements conducted in Shanghai, China. Furthermore, the component was used to model a PV/T façade at the south wall of GEL. A façade integrated PV/T system utilising air as heat transfer medium was also modelled, but not validated, as no measurements were available for this component.

The BIPV/T systems were optimised for five parameters; dead band, storage tank size, mass flow rate, tank inlet height from heat source and tank inlet height from mains water supply. Simulations have been conducted to analyse the effect of building integration, both on the building energy demand and the BIPV/T system operation. Simulations were carried out for the same building model with air based BIPV/T system, water based BIPV/T system, air based PV/T system, water based PV/T system and PV façade (BIPV).

The results show that PV/T integrated to the building façade has negligible effect on the total energy demand of the building. The electrical efficiency was highest for the air based BIPV/T system and the water based BIPV/T showed the largest amount of collected thermal useful energy. The BIPV showed the highest electrical solar fraction, as a significant amount of fan energy required for operation of the air based BIPV/T system results in reduced solar fraction for that system.

Sammendrag

Målet med denne masteroppgaven er å analysere og undersøke metoder for design av bygningsintegrert PV/T (BIPV/T) teknologi ved Green Energy Laboratory (GEL) ved Shanghai Jiao Tong University (SJTU) i Kina.

PV/T teknologi kan generere både elektrisk og termisk energi på et mindre areal, sammenlignet med kun PV-paneler eller solfangere. For et PV-panel vil virkningsgraden synke med økende overflate temperatur, som typisk inntreffer under maksimal solinnstråling. Vann eller luft som sirkuleres inne i PV/T-komponenten vil kjøle ned PV-overflaten, og på den måten opprettholde høyere virkningsgrad og høyere energiproduksjon.

En vannbasert PV/T-komponent er kalibrert og validert i henhold til målinger utført i Shanghai, Kina. Videre har komponenten blitt brukt til å modellere en PV/T-fasade på sørveggen av GEL. Et fasadeintegrert PV/T-system med luft som kjølemedium er også modellert, men ikke validert, da måledata for denne komponenten ikke var tilgjengelig.

BIPV/T-systemene er optimalisert for fem parametere; dødbånd, størrelse på varmtvannstank, massestrøm, tankinnløp varmekilde og tankinnløp byvann. Simuleringer er utført for å analysere effekten av bygningsintegrering, både på byggets energibehov og på BIPV/T systemet. Like simuleringer er gjort for samme bygningsmodell med luftbasert BIPV/T-system, vannbasert BIPV/T-system, luftbasert PV/T-system, vannbasert PV/T-system og PV-fasade (BIPV).

Resultatene viser at et fasadeintegrert PV/T-system har neglisjerbar innvirkning på byggets totale energibehov. Elektrisk virkningsgrad var høyest for det luftbaserte BIPV/T-systemet, mens mengden generert termiske energien var høyest for det vannbaserte systemet. PV-fasaden oppnådde høyest andel generert solenergi i forhold til energiforbruk for systemet, ettersom energiforbruket til viften førte til lavere andel i det luftbaserte BIPV/T-systemet.

1 Table of Contents

Abstract.....	vi
Sammendrag.....	vii
List of Figures	xii
List of Tables	xvi
1 Introduction	1
1.1 Objective	1
1.2 Background	1
1.3 Limitations	2
1.4 Outline.....	3
1.5 Research Methods	4
2 Theoretical Background	5
2.1 Photovoltaic.....	5
2.1.1 Manufacturing	6
2.1.2 Photovoltaic Effect.....	7
2.1.3 Monocrystalline.....	8
2.1.4 Multicrystalline	8
2.1.5 Thin Film.....	8
2.1.6 Performance of Photovoltaics	9
2.2 Solar Thermal Collectors	12
2.2.1 Flat Plate Solar Collector	13
2.2.2 Performance of Solar Collectors	14
2.3 Building Integrated PV/T Component	16
2.3.1 Air Based BIPV/T	17
2.3.2 Water Based BIPV/T.....	19
2.3.3 Performance of BIPV/T	19
2.3.4 Sky temperature.....	21
2.3.5 Cover heat loss	21

2.4	Net Zero Energy Buildings	21
2.4.1	Building Design.....	25
2.4.2	Load Matching	25
2.4.3	Smart Grids	27
2.5	BIPV/T System Design	27
2.5.1	BIPV/T Component Tilt Angle	27
2.5.2	BIPV/T Component Area.....	28
2.5.3	Thermal Energy Storage.....	29
2.5.4	Electrical Energy Storage.....	31
2.5.5	Mass Flow Rate.....	32
2.5.6	BIPV/T Components Connected in Parallel and Series	33
2.5.7	DC/AC Converter (Inverter)	35
2.5.8	Heat Pump Coupled BIPV/T Component	35
3	The Green Energy Laboratory	39
3.1	GEL Façade.....	40
3.2	GEL Energy Systems	41
3.2.1	Open-loop Surface Water Source Heat Pump System:	42
3.2.2	Ground-coupled Heat Pump System:	42
3.2.3	CO2 Heat Pump:	43
3.3	GEL Office.....	43
3.4	Measurements.....	44
4	Modelling and Simulation Tools	47
4.1	Mathematical Model of PV/T	49
4.1.1	PV/T Water Model.....	51
4.1.2	PV/T Air Model	57
4.1.3	Radiative Heat Transfer	64
4.1.4	Convective Heat Transfer.....	66
4.1.5	Weather File	68

4.1.6	Pump.....	69
4.1.7	Storage Tank	70
4.2	Validation of the TRNSYS PV/T Component	70
4.3	Calibration of the TRNSYS PV/T Component	72
4.3.1	Baseline Model.....	72
4.3.2	Calibration Measures.....	76
4.3.3	Calibrated Model.....	79
4.4	Performance Evaluation of Calibrated Model.....	87
4.4.1	Thermal Efficiency.....	87
4.4.2	Electrical Efficiency	90
4.4.3	Total Efficiency and Exergy Calculations	90
4.5	GEL Model.....	92
5	Energy Simulations of the GEL Model	94
5.1	GEL Office	96
5.2	Multizone Model (TYPE 56)	98
5.2.1	Building Envelope.....	100
5.2.2	Modelling of the BIPV/T Wall.....	100
5.2.3	Schedule	101
5.2.4	DHW load	101
5.2.5	Internal Gains and Electrical Load.....	101
5.2.6	Ventilation.....	102
5.2.7	Heating and cooling	102
5.2.8	Differential controller (TYPE 2).....	103
5.2.9	Storage Tank (TYPE 60).....	104
5.3	Optimisation of GEL Models.....	105
5.4	Water Based BIPV/T System.....	105
5.4.1	Dead Band.....	107

5.4.2	Size of Storage Tank	109
5.4.3	Specific Flow Rate	111
5.4.4	Inlet from Heat Source	113
5.4.5	Inlet from Cold Side.....	115
5.4.6	Summary	116
5.4.7	Optimised GEL model	119
5.5	Air Based BIPV/T System	119
5.5.1	Dead Band.....	121
5.5.2	Size of Storage Tank	123
5.5.3	Specific Flow Rate	124
5.5.4	Inlet from Heat Source	127
5.5.5	Inlet from Cold Side.....	128
5.5.6	Summary	129
5.5.7	Optimised GEL model	132
6	Performance Analysis of GEL BIPV/T System Models	133
6.1	Thermal Performance of BIPV/T	133
6.2	Summary	136
6.3	Electrical Performance of BIPV/T	136
6.4	Mismatch factors	139
6.5	Summary	142
6.6	Effect of Building Integration	143
6.7	Summary	144
7	Conclusion.....	145
8	Further Work	147
	References	148
	Appendix A: Energy Balances	152
	Appendix B: GEL Office Parameters.....	154

List of Figures

Figure 2-1: Mean annual global irradiance incident on a horizontal surface in W/m^2 [] 5

Figure 2-2: Photovoltaic cell [6] 7

Figure 2-3: Market shares of photovoltaic technologies. Data from [7] 9

Figure 2-4: Highest measured PC cell efficiencies [9]..... 10

Figure 2-5: Covered flat plate collector [13]..... 13

Figure 2-6: Market shares of installed solar collector capacity. Data from [16]..... 14

Figure 2-7: Overview of various BIPV/T technologies [17]..... 17

Figure 2-8: Air based BIPV/T component 18

Figure 2-9: Open loop (a) and closed loop (b) air based BIPV/T systems. Adapted from [13]..... 18

Figure 2-10: Water based BIPV/T component. Flow direction into the page 19

Figure 2-11: Graphical representation of the net-zero energy balance concept. Adapted from [35] 22

Figure 2-12: Exported/delivered and load/generation balances. Adapted from [35] 23

Figure 2-13: General monthly graphs of electric energy load and generation of a building. Adapted from [37] 26

Figure 2-14: Stratified tank with a BIPV/T component side heat exchanger..... 31

Figure 2-15: Electrical configuration of BIPV/T system [5]..... 34

Figure 2-16: Series and parallel connections of BIPV/T [5]..... 35

Figure 2-17: Ground source heat pump operation during cooling and heating season 36

Figure 2-18: Series configuration of a BIPV/T and a ground source heat pump system. Adapted from [54] 37

Figure 2-19: Parallel configuration of a BIPV/T and a ground source heat pump system. Adapted from [54] 38

Figure 3-1: The Green Energy Laboratory [57] 39

Figure 3-2: Atrium showed in picture (left) and on floor plan (right) [57] 40

Figure 3-3: The two layers of the facade (left) and the external facade configuration (right) [56]..... 40

Figure 3-4: GEL façade operation during summer and winter [58] 41

Figure 3-5: Energy technologies installed at the GEL. Adapted from [56]..... 42

Figure 3-6: Floor plan of the 2nd floor in the GEL 43

Figure 3-7: Ambient conditions during the PV/T water measurements 45

Figure 3-8: Solar test rig with one PV/T component connected to a tank..... 46

Figure 4-1: Comparison of real measurements to various simulation tools for PV production [61] 48

Figure 4-2: Modelling process. Adapted from [62]..... 49

Figure 4-3: TRNSYS system sketch of the baseline model 51

Figure 4-4: Water based PV/T component..... 52

Figure 4-5: Cover energy balance of water based PV/T 52

Figure 4-6: Fin effect in the water based PV/T	54
Figure 4-7: Energy balance in the fin area of the absorber	55
Figure 4-8: Energy balance of the fin base of the absorber.....	55
Figure 4-9: System sketch showing the temperature nodes of the air based PV/T	58
Figure 4-10: Cover energy balance of air based PV/T	58
Figure 4-11: Energy balance at the upper surface of the air channel	60
Figure 4-12: Energy balance at the lower surface of the air channel	61
Figure 4-13: Differential balance of the air flow.....	62
Figure 4-14: Sky temperatures calculated by various methods.....	66
Figure 4-15: Instant wind velocity at the GEL.....	67
Figure 4-16: Convective heat transfer coefficients as a function of wind speed by various authors	68
Figure 4-17: Stratified storage tank (TYPE 4)	70
Figure 4-18: Power output of the measured data and the baseline model.....	73
Figure 4-19: PV/T outlet temperatures of the measured data and the baseline model.....	74
Figure 4-20: Calibration signatures of the baseline model.....	75
Figure 4-21: Characteristic signatures of PV/T validation metrics when implementing sky temperature by the method of Berdahl and Martin.....	77
Figure 4-22: Characteristic signature of the PV/T outlet temperatures when implementing h_{wind} by the method of various authors.	78
Figure 4-23: Characteristic signatures of the power output when implementing h_{wind} by the method of various authors.	78
Figure 4-24: Calibration signatures of the validation metrics for the calibrated model.....	80
Figure 4-25: Outlet temperature of the calibrated and baseline models compared to the measured data	81
Figure 4-26: Power output of the calibrated and baseline models compared to the measured data.....	82
Figure 4-27: Residual distribution of the PV/T outlet temperature from the baseline model with a fitted normal distribution curve	84
Figure 4-28: Residual distribution of the PV/T outlet temperature from the calibrated model with a fitted normal distribution curve	85
Figure 4-29: Residual distribution of the PV/T power output from the baseline model with a fitted normal distribution curve	86
Figure 4-30: Residual distribution of the PV/T power output from the calibrated model with a fitted normal distribution curve	87
Figure 4-31: Thermal efficiencies of the calibrated model and the measured data.....	88
Figure 4-32: Thermal efficiencies of the calibrated model, the baseline model and the measured data during the hours of positive efficiency values.....	89

Figure 4-33: Electrical efficiencies of the calibrated model, the baseline model and the measured data	90
Figure 4-34: Total efficiencies of the baseline model, the calibrated model and the measured data	91
Figure 4-35: Total exergy efficiencies for the baseline model, the calibrated model and the measured data	92
Figure 5-1: TRNSYS model of the water based BIPV/T system	94
Figure 5-2: TRNSYS model of the air based BIPV/T system.....	95
Figure 5-3: Solar irradiance for a vertical surface facing south and a horizontal surface	96
Figure 5-4: Ambient temperature and mains water temperature	97
Figure 5-5: Illustration of a real wall and the corresponding black box model.....	99
Figure 5-6: DHW profile (left) and electrical load profile (right) as set in TRNSYS	102
Figure 5-7: Annual heating (negative values) and cooling (positive values) demand	103
Figure 5-8: Controller function	104
Figure 5-9: Monthly values of thermal and electrical efficiencies when varying the dead band.....	108
Figure 5-10: Monthly values of useful energy (column) and operational hours (line) when varying the dead band.....	109
Figure 5-11: Monthly values of thermal and electrical efficiency when varying the storage tank volume	110
Figure 5-12: Monthly values of useful energy (column) and operational hours (line) when varying storage volume	111
Figure 5-13: Monthly values of thermal and electrical efficiency when varying the specific flow rate	112
Figure 5-14: Monthly values of useful energy (column) and operational hours (line) when varying the specific flow rate	113
Figure 5-15: Monthly values of thermal and electrical efficiency when varying the inlet height from the heat source	114
Figure 5-16: Monthly values of useful energy (column) and operational hours (line) when varying the inlet height from the heat source	114
Figure 5-17: Monthly values of thermal and electrical efficiency when varying the inlet height from the cold side.....	115
Figure 5-18: Monthly values of useful energy (column) and operational hours (line) when varying the inlet height from cold side.....	116
Figure 5-19: Monthly values of thermal and electrical efficiency when varying dead bands.....	121
Figure 5-20: Monthly values of useful energy (column) and operational hours (line) when varying the dead band.....	122
Figure 5-21: Monthly values of thermal and electrical efficiency when varying the storage tank volume	123

Figure 5-22: Monthly values of useful energy (column) and operational hours (line) when varying the storage volume	124
Figure 5-23: Monthly values of thermal efficiency when varying the specific flow rate	125
Figure 5-24: Monthly values of electrical efficiency when varying the specific flow rate	126
Figure 5-25: Monthly values of useful energy (column) and operational hours (line) when varying the specific flow rate	127
Figure 5-26: Monthly values of useful energy (column) and operational hours (line) when varying the inlet from the heat source	128
Figure 5-27: Monthly values of useful energy (column) and operational hours (line) when varying the inlet from the cold side	129
Figure 6-1: Thermal efficiency (line) and useful energy (column) of the water and air based BIPV/T systems	133
Figure 6-2: Auxiliary and pump energy consumption and thermal solar fraction of the water based BIPV/T system	134
Figure 6-3: Auxiliary and fan energy consumption and thermal solar fraction of the air based BIPV/T system.....	135
Figure 6-4: Monthly operating hours of the water and air based BIPV/T systems	135
Figure 6-5: Comparison of electrical efficiency and electrical energy production between technologies	137
Figure 6-6: Comparison of PV surface temperatures between technologies in June	138
Figure 6-7: Comparison of electrical efficiency between technologies in June	138
Figure 6-8 Comparison of electrical efficiency between technologies in November	139
Figure 6-9: The electrical production, load covered by production and load for the water based BIPV/T system.....	140
Figure 6-10: The electrical production, load covered by production and load for the BIPV system ..	141
Figure 6-11: The electrical production, load covered by production and load for the air based BIPV/T system.....	142

List of Tables

Table 1: ZEB renewable energy supply option hierarchy [36]	24
Table 2: Mismatch factors and indicators. Adapted from [37].....	26
Table 3: Energy storage systems. Adapted from [5]	32
Table 4: Main parameters of the PV/T test rig	44
Table 5: Parameters used for simulation of the experimental water based PV/T component	50
Table 6: CV(RMSE) and MBE of the two validation metrics for the baseline model.....	75
Table 7: CV(RMSE) and MBE values for wind induced heat transfer and sky temperature calculations	79
Table 8: CV(RMSE) and MBE of the validation metrics for the calibrated and baseline models.	82
Table 9: Thermal, electrical and total efficiencies of the baseline model, the calibrated model and the measured data.....	91
Table 10: Building envelope of the GEL office based on values from NS 3701 and TEK 15 minimum requirements [78]. Adapted from [58]	98
Table 11: Base case values of the water based BIPV/T system	106
Table 12: Optimisation parameters for the water based BIPV/T system	107
Table 13: Solar fractions for various system parameters and test ranges.....	118
Table 14: Chosen values of the final water based BIPV/T system	119
Table 15: Base case values for the air based BIPV/T system	120
Table 16: Optimisation parameters for air based BIPV/T	121
Table 17: Solar fractions for various system parameters and test ranges.....	131
Table 18: Chosen values of the final air based BIPV/T	132
Table 19: Mismatch factors and thermal solar fraction.....	142
Table 20: Energy needs for various solar technologies.....	143
Table 21: Values for the GEL office construction	154
Table 22: Detailed window construction.....	155
Table 23: Internal loads, ventilation rates and system design chosen in accordance with criteria for passive house (NS 3701)	156
Table 24: Components of the GEL office in accordance with minimum demands of passive house requirements [78].	156

Nomenclature

A	Area [m^2]	Nu	Nusselt number [-]
AC	Alternating Current	Q	Energy [J]
B	Energy [J]	\dot{Q}	Rate of heat transfer [W]
C	Cloudiness factor [-]	q	Heat transfer per area [W/m^2]
C_p	Specific heat capacity [J/kgK]	R	Heat transfer resistance [m^2K/W]
C	Speed of light [m/s]	R^2	Determination coefficient [-]
D	Diameter [m] or weighted exported energy [J]	S	Absorbed solar radiation [W/m^2]
DC	Direct Current	T	Temperature [$^{\circ}C$] or [K]
D	Delivered energy [J]	U_L	Collector overall heat transfer coefficient [W/m^2]
E	Energy [J] or weighted exported energy [J]	\hat{y}_i	Simulated data [-]
e	Exported energy [J]	y_i	Measured data [-]
F_R	Heat removal factor [-]	V	Operating voltage [V]
f	Solar fraction [-]	v	Velocity [m/s]
f_{grid}	Grid interaction index [-]	W	Width [m] or work [J]
f_{load}	Load match index [-]	X	Multiplier for PV cell efficiency [-]
f_{par}	Fraction of pump power converted to thermal energy [-]		
G	Irradiance [W/m^2] or weighted energy generation [J]	Greek	
g	Energy generation [J]	α	Absorptance
h	Heat transfer coefficient [W/m^2K] or Planck's constant [m^2kg/s]	γ	Controller function
I	Current [A] or irradiation [Wh/m^2]	ε	Emissivity
IAM	Incident Angle Modifier [-]	λ	Wave length [nm] or thickness [m]
i	Energy carrier	η	Efficiency
k	Thermal conductivity [W/mK]	μ	Cell temperature coefficient [I/K]
L	Length [m]	ζ	Exergy efficiency
l	Energy load [-]	σ	Stefan-Boltzmann constant [W/m^2K^4]
\dot{m}	Mass flow rate [kg/s]	τ	Transmittance
N/n	Number of [-]		
P	Pressure [bar]		

Subscripts

<i>AC</i>	Alternating Current	<i>G</i>	Energy generation
<i>a</i>	Ambient	<i>H</i>	High
<i>abs</i>	Absorber	<i>H</i>	Hydraulic
<i>back</i>	Back surface	<i>hor</i>	Horizontal
<i>C</i>	Cell or condenser	<i>in</i>	Inlet
<i>c</i>	Collector	<i>K</i>	Time step
<i>cond</i>	Conductive	<i>L</i>	Low
<i>conv</i>	Convective	<i>L</i>	Energy load
<i>DC</i>	Direct Current	<i>mp</i>	Maximum power point
<i>d</i>	Diffuse	<i>N</i>	Normal incidence
<i>dp</i>	Dew Point	<i>OC</i>	Open circuit
<i>e</i>	Electrical	<i>out</i>	Outlet
<i>eq</i>	Equivalent	<i>P</i>	Parallel connection
<i>G</i>	Energy generation	<i>ph</i>	Photon
<i>H</i>	High	<i>rad</i>	Radiative
<i>H</i>	Hydraulic	<i>ref</i>	Reference conditions
<i>hor</i>	Horizontal	<i>S</i>	Series connection or surface
<i>in</i>	Inlet	<i>T</i>	On tilted surface
<i>K</i>	Time step	<i>th</i>	Thermal
<i>L</i>	Low	<i>tot</i>	Total
<i>L</i>	Energy load	<i>U</i>	Useful
<i>mp</i>	Maximum power point	<i>S</i>	Series connection or surface
<i>N</i>	Normal incidence	<i>T</i>	On tilted surface
<i>OC</i>	Open circuit	<i>th</i>	Thermal
<i>out</i>	Outlet	<i>tot</i>	Total
<i>P</i>	Parallel connection	<i>U</i>	Useful
<i>ph</i>	Photon		
<i>rad</i>	Radiative		
<i>ref</i>	Reference conditions		

Abbreviations			
<i>AHU</i>	Air Handling Unit	<i>PV</i>	Photovoltaic
<i>AM</i>	Air Mass	<i>PVT</i>	Photovoltaic Thermal
<i>BAS</i>	Building Automation System	<i>RMSE</i>	Root Mean Square Error
<i>BAPV/T</i>	Building Applied Photovoltaic Thermal	<i>SJTU</i>	Shanghai Jiao Tong University
<i>BIPV/T</i>	Building Integrated Photovoltaic Thermal	<i>STC</i>	Standard Test Conditions
<i>CHP</i>	Combined Heat and Power	<i>STD</i>	Standard Deviation
<i>CO₂</i>	Carbon dioxide	<i>TESS</i>	Thermal Energy System Simualtion Inc.
<i>COP</i>	Coefficient of Performance	<i>TRNSYS</i>	Transient System Simulation Tool
<i>CV(RMSE)</i>	Coefficient of Variation of RMSE	<i>ZEB</i>	Zero Energy Building
<i>CZ</i>	Czochralski		
<i>DHW</i>	Domestic Hot Water		
<i>FORTTRAN</i>	Formula Translation		
<i>GEL</i>	Green Energy Laboratory		
<i>GHG</i>	Greenhouse Gas emissions		
<i>HVAC</i>	Heating, Ventilation and Air Conditioning		
<i>IDA ICE</i>	IDA Indoor Climate and Energy		
<i>IDA SE</i>	IDA Simulation Environment		
<i>IWEC</i>	International Weather for Energy Calculations		
<i>LPG</i>	Liquid Petroleum Gas		
<i>MBE</i>	Mean Bias Error		
<i>NMBE</i>	Normalised Mean Bias Error		
<i>NMF</i>	Neutral Model Format		
<i>NOCT</i>	Normal Operating Cell Temperature		
<i>NREL</i>	National Renewable Energy Laboratory		
<i>NTNU</i>	Norwegian University of Science and Technology		
<i>nZEB</i>	Net-zero Energy Building		

1 Introduction

1.1 Objective

The goal of this master thesis is to analyse and develop design methods for building integrated photovoltaic/thermal (BIPV/T) technology at the Green Energy Laboratory (GEL) at Shanghai Jiao Tong University (SJTU) in China. The work will include analysis of both water and air based PV/T technologies and assess the performance of the water and air based BIPV/T systems through simulations with the appropriate simulations tools.

A detailed validation and calibration process will be conducted based on experimental data to ensure realistic results from simulations. Computer models will be developed to assess the effects of PV/T technology integrated in the southern façade of an office space in the GEL. Effects on the building's energy demand as well as the performance of the solar energy technology will be investigated.

This collaborative assignment is realised as a part of the Joint Research Center in Sustainable Energy of the Norwegian University of Science and Technology and Shanghai Jiao Tong University. The main findings will be incorporated in a scientific paper draft proposal included in the end of the report.

1.2 Background

As the consequence of climate changes are getting increasingly more severe, it is important to reduce the energy production from fossil fuels. The sun represents a huge source of clean, renewable energy which must be utilised to ensure a sustainable way of life and preserve the world as we know it today.

Growing populations and expanding cities present the need for alternative technologies for onsite energy generation. The photovoltaic (PV) cell is an established technology for production of electrical energy, with efficiency ranging from 5% – 21% depending on the PV material. However, the efficiency of a PV panel decreases for higher PV surface temperatures introducing the need for additional cooling of the panel. With a colder fluid, i.e. air or water, circulating below the PV panel, the PV temperature is kept lower, maintaining higher efficiency during hours of high solar irradiation.

In the EU, the member states have agreed that all new buildings are going to be nearly zero energy buildings within 2020. Buildings constructed today must follow strict governmental

regulations to maintain low energy consumptions and are thus mostly passive houses and net Zero Energy Buildings (nZEB). As the total building energy demand is reduced in modern buildings, the demand for domestic hot water (DHW) becomes relatively larger. Therefore, renewable solutions for covering the DHW demand are becoming more important.

To reduce the amount of imported electricity from the grid, the energy production should follow the load, i.e. high load matching index should be maintained throughout the year. As solar energy is impossible to regulate, energy storage could be used to minimise grid stress.

BIPV/T is space efficient as it utilises less area for electrical and thermal energy generation compared to traditional solar collectors and PV panels. Façade integrated PV/T systems can make use of an area that has, until now, been found unfitted for energy production. In contrast to PV panels and solar collectors installed on buildings, BIPV/T components offer architectural uniformity as all components are identical.

1.3 Limitations

Measurements of the water based PV/T component were conducted in December, and no measurements from summer operation were available to the authors. Ideally, the water based PV/T model should be calibrated and validated for summer measurements in addition to winter measurements, to ensure that the results of simulations are as realistic as possible for the entire year.

No measurement data was available for the air based PV/T component. Thus, the TRNSYS model for this component is not validated, as the air based was, and the development of the air based BIPV/T model is solely based on simulations.

It was not possible to test the entire desired range of flow rates in TRNSYS for the water and air based BIPV/T system models. The highest tested flow rate was 24 kg/hm² and 63.56 kg/hm² for the water and air based systems, respectively.

As the air and water based BIPV/T technologies operate with different fluids, it is difficult to find a neutral common ground for comparison. The system in this thesis investigates the production of thermal energy for domestic hot water, which introduces the need of a heat exchanger between the BIPV/T component and the tank in the air based BIPV/T. The heat exchanger efficiency limits the amount of heat transferred from the BIPV/T component to the tank, compared to the water based system where the water heated in the BIPV/T component is transferred directly.

1.4 Outline

Chapter 2 presents the relevant theoretical background of the thesis. PV and solar collector technologies are explained in detail, as well as PV/T technology as a combination of the two. Air and water based PV/T are introduced, with a focus on building integration of each one. The concept of nZEBs are explained, with regards to building design, load matching and smart grids. Lastly, relevant considerations for BIPV/T system design are addressed, as well as effects of coupling a BIPV/T component to a heat pump system.

The GEL at SJTU is presented in chapter 3. The apartment on the 2nd floor is modelled as an open office space to simulate the DHW and electrical demand of an office. This model is used for analysing the air and water based BIPV/T in chapter 5. The measurement data received from fellow GEL students and the parameters of the test component is also presented in this chapter.

The modelling process is explained in detail in chapter 4. The mathematical model of the air and water based TRNSYS PV/T models, TYPE 568 and TYPE 563 are presented. In this chapter, a validated and calibrated water based PV/T model is developed for use in further simulations and analysis conducted in chapter 5. The water based PV/T model was validated according to the measurements presented in chapter 3. In the end, the results of the calibrated model are presented.

Chapter 5 includes the modelling approach of the GEL office model, which was described in chapter 3. The office model is connected to an air based and a water based PV/T component presented in the previous chapter. The result is two GEL BIPV/T system models which are used for simulation to analyse the effect of building integration of air and water based PV/T.

Chapter 6 presents the simulations results from the GEL BIPV/T system models developed in chapter 5. The air and water based BIPV/T systems are compared to air and water based PV/T systems as well as a BIPV system, separately connected to the GEL office.

In the conclusion of the thesis in chapter 7, the objectives of the assignment are answered based on the results found in chapter 6.

Chapter 8 presents suggestions for further work. These are possible extensions of the work conducted in this thesis.

1.5 Research Methods

A literature review was conducted to present an overview of the PV/T and BIPV/T technology. This makes up the basis for the theoretical background presented in chapter 2. Also, literature review was used to evaluate various simulation tools and determine which one was most suitable for this assignment.

Data for measurements were used as a basis for validation and calibration of the water based PV/T model. The measurements were not conducted by the authors, but by fellow GEL students. Uncertainties of the measurement components (thermometer, flow meter etc.) have not been addressed as these data were not available.

TRNSYS simulations have been conducted, both for validation and calibration purposes, but also for assessing the long-term performance of the BIPV/T systems.

2 Theoretical Background

The sun is by far the largest source of energy known to man. Within one hour, an amount equal to the entire energy need of the human population is supplied from the sun. Utilising this energy efficiently is more important now than ever as the world needs a shift from fossil fuels to renewable energy sources.

The mean annual global irradiance incident on a surface horizontal to the ground is shown in Figure 2-1. The highest values are present in the Tropics of Cancer and Capricorn. The irradiance at the Equator is slightly lower than that of the Tropic of Cancer due to an increase of cloud cover. Mean annual global irradiance includes both direct normal irradiance and diffuse horizontal irradiance and is determined by the latitude, current season, time of day, inclination of the surface, shading, orientation and the climatic conditions.

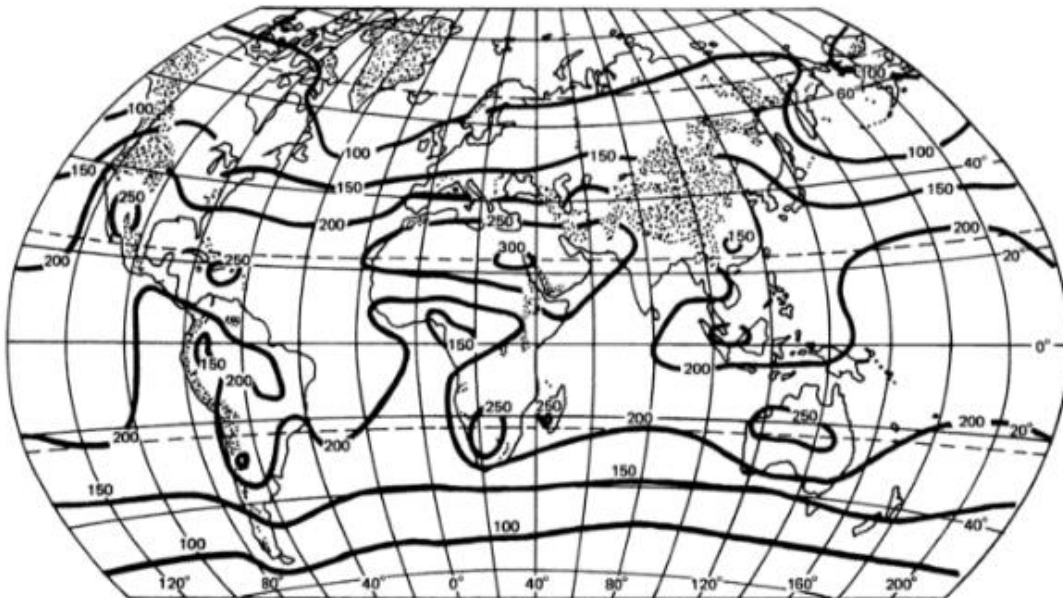


Figure 2-1: Mean annual global irradiance incident on a horizontal surface in W/m^2 [1]

2.1 Photovoltaic

Photovoltaic (PV) technology uses solar cells to generate electricity from solar radiation [1]. Initially, the PV technology was developed for the space industry where space projects were not limited by the cost of materials. However, as production costs of PV have dropped for the last decades, PV is applicable for residential and commercial use.

Photovoltaic technologies can be grouped into three categories: First generation, second generation and third generation. The first and second generations are the most commonly used and will be described in further detail in this thesis.

First generation technology photovoltaic cells include both mono- and multicrystalline silicon cells. The second generation is often referred to as thin films, and includes amorphous silicon, cadmium telluride and copper indium gallium diselenide materials cells. [2]

Recently, there has been a vast development within what is referred to as the third generation of solar cells. It includes organic and polymer based solar cells, introducing new organic-inorganic hybrid materials such as perovskite. They provide easier scalability and aims to reach higher efficiencies at reduced costs compared to the two previous generations. The new generation shows great potential, but is still in the developing stages with few commercially available products and is therefore not given any further consideration in this thesis. [3, 4]

2.1.1 Manufacturing

The PV industry relies mainly on discarded second grade silicon from the semiconductor industry. The solar grade silicon consists of up to ten times as much impurities than that of the semiconductor grade silicon, but still it provides sufficient efficiencies. [5]

The Czochralski (CZ) method is the most commonly used technique to transform silicon discards in to crystallised silicon wafer. In the manufacturing process, the silicon is added a small amount of boron to create a p-type base. Furthermore, the wafer is added an n-type semiconductor to create the p-n junction in-between, as well as additional metal layers to conduct electricity. An illustration of a PV cell is shown in Figure 2-2. [5]

Monocrystalline silicon cell manufacturing is a highly energy consuming process. Thus, the manufacturing of multicrystalline and thin film silicon cells are becoming increasingly more common, as they require less energy for production. [5]

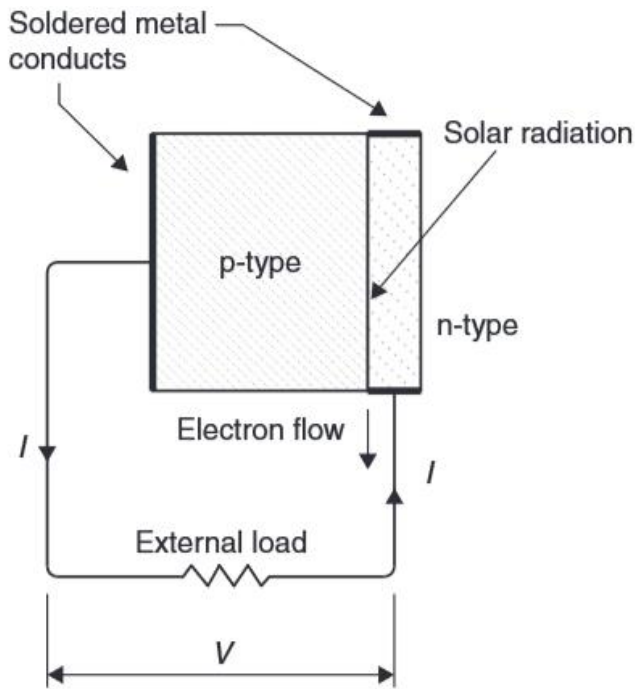


Figure 2-2: Photovoltaic cell [6]

2.1.2 Photovoltaic Effect

When sunlight hits the photovoltaic material, the energy of the photon is absorbed by an electron in the valence band. If the photon energy is larger than the energy of the bandgap, it will cause the electron to be excited from the valence band to the conduction band, where it is now free to move. However, if the energy of the photon is smaller than that of the bandgap, it will be lost as heat. The energy transported by photons are given in eq.(1) where λ is the wavelength, h is Planck constant and c is the speed of light. [6]

$$E_{ph}(\lambda) = \frac{hc}{\lambda} \quad (1)$$

The p-n junction formed in the boundary layer between the two semiconductors creates an electrical field assisting the flow of electrons through the solar cell. The current through the junction depends on an external load being applied to the circuit and the presence of sunlight incident on the photovoltaic material, as illustrated in Figure 2-2. [1]

2.1.3 Monocrystalline

Monocrystalline is the purest grade of silicon, and thus has the highest efficiency of the commercially available products. However, it also requires the largest amount of energy for production, about 100 kWh/kg with the CZ technique. The highest quality of monocrystalline silicon is achieved by using a process called Float Zone. [5, 7]

2.1.4 Multicrystalline

The production costs for monocrystalline silicon cells are large, mainly because of the energy intensive production process. In order to reduce the cost, several crystallisation techniques have been developed, such as the solidification method. The result is a less energy intensive process, but the quality of the crystallised silicon is reduced due to imperfections and impurities in the material. Directional solidification uses about 10 – 15 kWh/kg in the production of multicrystalline silicon. [5]

2.1.5 Thin Film

The thin film technology is promising due to reduced material and energy needs in the production phase. Thin film materials can absorb just as much photon energy as that of crystalline silicon, but with a thinner structure. This makes it more applicable for non-flat surfaces, such as curved façades, car roofs or even integrated in clothing for charging of small devices. [5, 8]

For now, commercial thin film materials are outperformed by thicker and more robust panels, e.g. crystalline silicon, when it comes to efficiency and life time of the material. The four most common thin film materials are amorphous silicon, copper indium diselenide, and cadmium telluride.

In 2015, the production of thin film solar cells was 7 % of the annual production of solar cells, which is dominated by multicrystalline silicon cells, as shown in Figure 2-3. [5, 7]

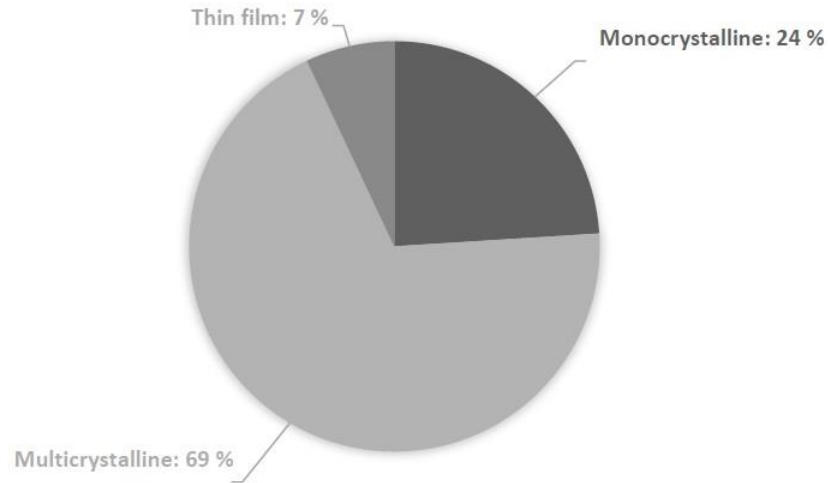


Figure 2-3: Market shares of photovoltaic technologies. Data from [7]

2.1.6 Performance of Photovoltaics

The highest PV efficiencies are reached during laboratory measurements. These efficiencies are usually not valid for the actual commercialised PV panels, which usually report somewhat lower efficiencies. National Renewable Energy Laboratory (NREL) mapped the highest recorded efficiencies, measured under standard test conditions (STC¹), of various PV technologies from 1976 to 2016. The results are shown in Figure 2-4:

¹ STC is an acronym for Standard Test Conditions for solar cells: Irradiance of 1 000 W/m², air mass 1.5 (AM1.5) spectrum and a temperature of 25°C. [5]

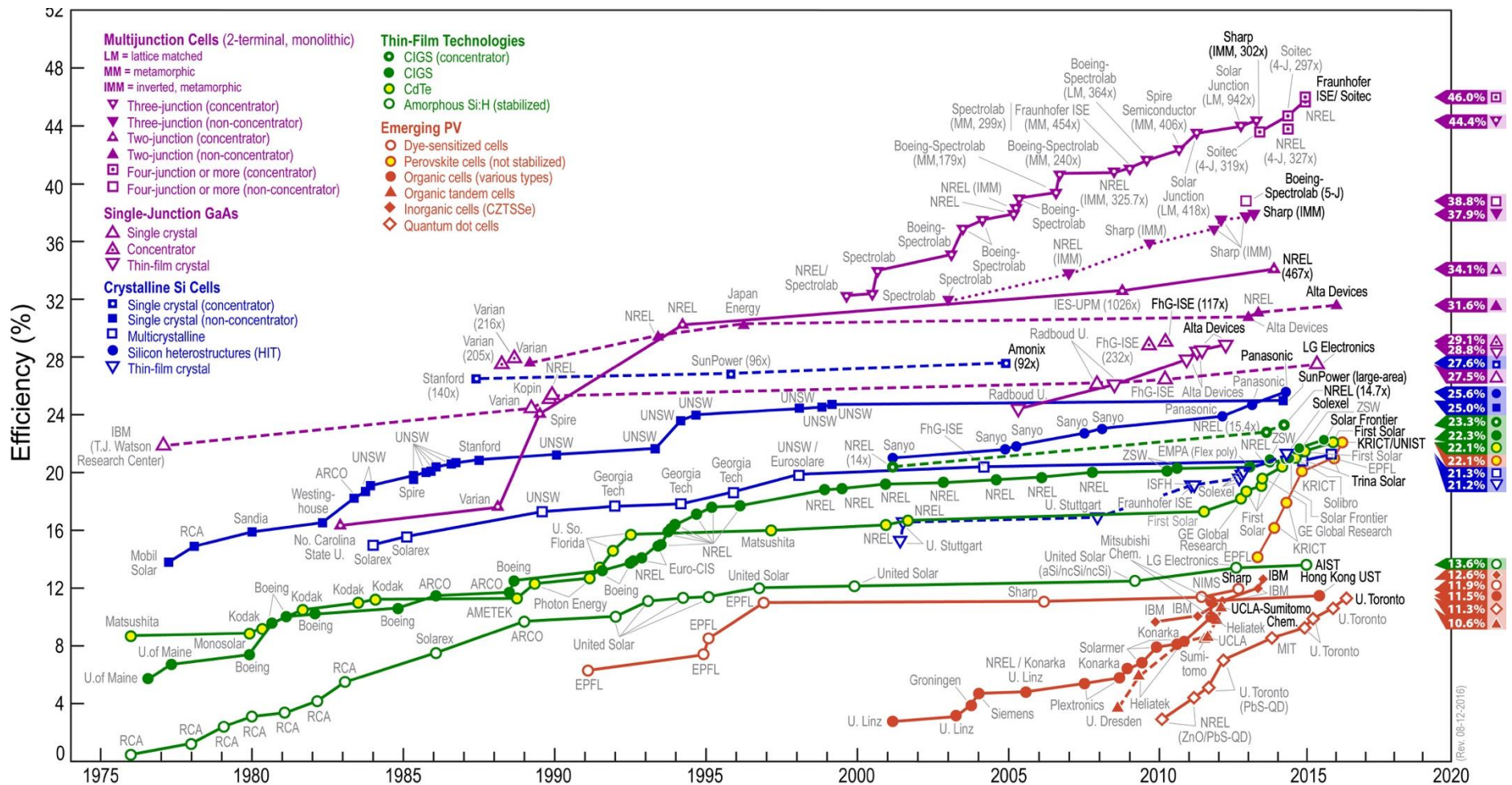


Figure 2-4: Highest measured PV cell efficiencies [9]. This plot is courtesy of the National Renewable Energy Laboratory, Golden, CO

The Shockley-Queisser Efficiency Limit

The *detailed balance limit* of efficiency for PV cells, known as the Shockley-Queisser efficiency limit, is the upper theoretical limit of an ideal p-n junction solar photovoltaic cell [10]. The value was found to be 33.77% for a band gap energy of 1.34 eV. The limit provides a benchmark for the maximum performance of a single junction PV cell. As silicon has a band gap energy of 1.1 eV, the highest achievable theoretical efficiency is, according to the Shockley-Queisser efficiency limit, 32.23%. [11]

Temperature Effect

The solar cell power output is dependent on the temperature of the cell. An increase in cell temperature will reduce the cell voltage with about 2.3 mV per °C for a silicon cell. The relationship between the ambient temperature, T_a , and the operating cell temperature, T_c , is dependent on the normal operating cell temperature, $NOCT^2$, and given as: [5]

$$T_c = \frac{NOCT - 20}{0.8} G + T_a \quad (2)$$

where G is the solar irradiance.

Commercialised PV Efficiency

In laboratories, the aim is to achieve as high efficiency as possible, and the cell is developed based on that one goal in particular. Little concern is given to the economical aspect including the lifetime of the cell and application. For the commercial PV panels, the economical aspect is more important compared to the application in laboratories. Whether a PV panel is economically sound or not may be the deciding factor for commercial manufacturing, and is therefore prioritised at the sacrifice of highest possible efficiency.

The average efficiency of a commercialised monocrystalline panel is 17%, with a maximum of 21%. For the multicrystalline panels, common efficiencies range from 13 to 17%. The efficiencies for the commercial thin film solar cells range from 5 to 11%, with amorphous silicon providing the best efficiency. [5]

² NOCT is an acronym for the Normal Operating Cell Temperature for a solar cell. It is given under the following conditions: Irradiance of 800 W/m², AM1.5 spectrum, ambient temperature of 25°C and wind speed >1 m/s. [5]

The maximum power point efficiency of a PV cell is defined as the maximum power produced by the cell under STC, divided by the solar radiation incident on the cell, shown in eq.(3):

$$\eta_{mp} = \frac{I_{mp} V_{mp}}{A_c G_T} \quad (3)$$

where I_{mp} and V_{mp} are the maximum power point current and voltage, respectively. The solar irradiance incident on the tilted collector area, A_c , is denoted G_T . As the cell efficiency drops at higher cell temperatures and vice versa, Duffie and Beckmann [12] described the temperature dependence of the cell efficiency through eq.(4):

$$\eta_{mp} = \eta_{mp,ref} + \mu_{\eta,mp} (T_C - T_{C,ref}) \quad (4)$$

where $\eta_{mp,ref}$ is the efficiency measured at STC, $\mu_{\eta,mp}$ is the cell efficiency temperature coefficient, η_{mp} is the maximum cell efficiency and T_C and $T_{C,ref}$ are the cell temperature and the cell temperature at STC, respectively.

The cell efficiency temperature coefficient is obtained by solving the equation for the maximum power efficiency over a range of temperatures, as shown in the following equation:

$$\mu_{\eta,mp} = \frac{d\eta_{mp}}{dT} = \left(I_{mp} \frac{dV_{mp}}{dT} + V_{mp} \frac{dI_{mp}}{dT} \right) \frac{1}{A_c G_T} \quad (5)$$

As $\mu_{\eta,mp}$ is small for many PV panels, the value of $\frac{dI_{mp}}{dT}$ is regarded as equal to zero and $\frac{dV_{mp}}{dT}$ considered equal to $\frac{dV_{OC}}{dT}$. As a result of these approximations, the temperature coefficient of the maximum power efficiency can be given as:

$$\mu_{\eta,mp} \approx \frac{I_{mp}}{A_c G_T} \frac{dV_{OC}}{dT} = \eta_{mp,ref} \frac{\mu V_{OC}}{V_{mp}} \quad (6)$$

where V_{OC} is the open circuit voltage, i.e. the voltage at $I = 0 A$.

2.2 Solar Thermal Collectors

The basic principle of solar thermal collectors involves absorption of solar radiation and heat exchange by running a working fluid through a heat exchanger. The thermal energy output is then often used for domestic hot water, hydronic heating or industry related heating. [13]

There is a large variety of solar thermal collectors available, and they are primarily grouped into stationary collectors and collectors that change position by single or dual axis solar tracking. In addition, a distinction is made between collectors that use different heat transfer medium (e.g. water and glycol mixture, air or heat transfer oil), concentrated or non-concentrated collectors, as well as covered or uncovered collectors. [6]

In this thesis, an uncovered, flat plate PV/T component is analysed and thus only the flat plate solar collector will be described in further detail. The other main types of commercial solar collectors are concentrating solar collectors and evacuated tube collectors. Also, it should be mentioned that there is vast ongoing research in the field of solar collectors, but these technologies are not yet commercialised.

2.2.1 Flat Plate Solar Collector

A flat plate collector absorbs shortwave solar radiation, which is then used to heat the working fluid flowing through the pipes in the collector. The insulated frame covers the area of the pipe that is not in contact with the absorber, and thus reduces the conductive heat loss from the pipes. In addition, a transparent cover may be added to allow short wave radiation to pass and reflect longwave radiation emitted by the absorber, consequently reducing the radiative heat loss from the collector (greenhouse effect). [13]

There is also a convective heat loss from the collector, which is dependent on local conditions such as wind speeds and ambient temperatures. The convective heat loss is reduced by using a transparent cover as shown in Figure 2-5, and even more with a double-glazed cover. However, this will also reduce the overall transmittance-absorptance product of the collector. [13, 14]

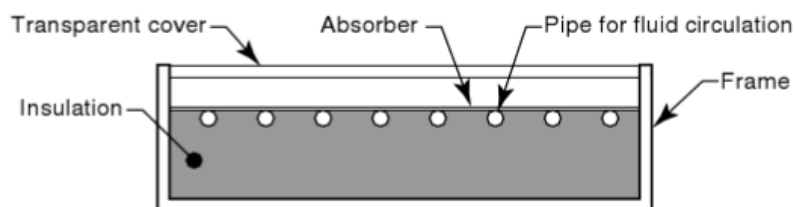


Figure 2-5: Covered flat plate collector [13]

The solar collectors should face towards the equator in order to optimally harvest solar energy. The optimal tilt angle for a flat plate collector is equal to the latitude of the site plus

10° if the system is designed for optimal winter performance or minus 10° for optimal summer performance [6].

Covered flat plate collectors are most common for building integration as they can easily replace conventional building materials and serve as a wind barrier in the construction [15]. Flat plate collectors represent 22% of the global installed solar collector capacity, which is dominated by evacuated tube collectors (numbers from 2014), as show in Figure 2-6:

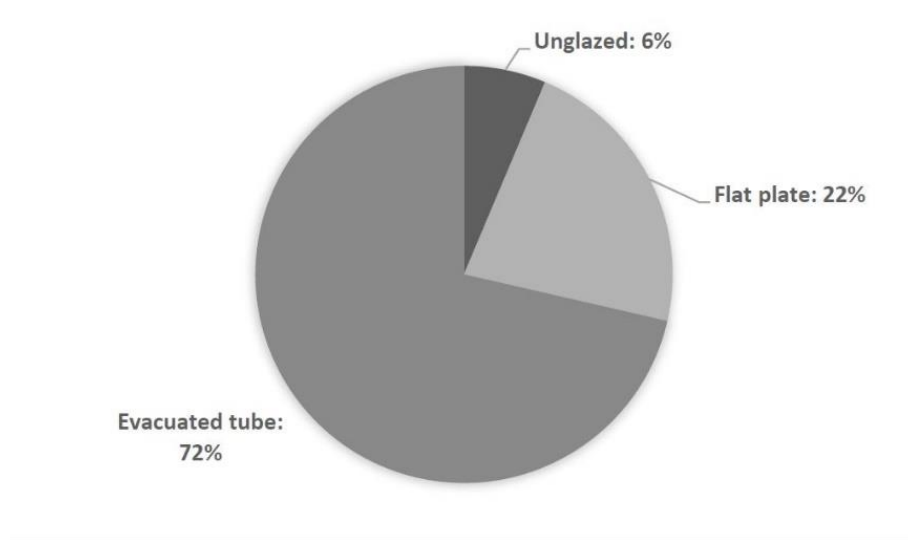


Figure 2-6: Market shares of installed solar collector capacity. Data from [16]

2.2.2 Performance of Solar Collectors

The useful energy gain from a solar collector, \dot{Q}_u , is represented by an energy balance including the incoming solar radiation on an absorber area and the thermal and optical losses from the collector. The thermal and optical losses are combined and shown as U_L multiplied by the difference between the mean absorber plate temperature and the ambient air temperature: [12]

$$\dot{Q}_u = A_c [S - U_L (\bar{T}_{abs} - T_a)] \quad (7)$$

where:

$S = G_T(\tau\alpha)$, absorbed solar radiation, gives \dot{Q}_u [W], as G_T [W/m²] is irradiance and $(\tau\alpha)$ is the transmittance-absorptance product.

- S = $I_T(\tau\alpha)_{avg}$. Meteorological data are mostly given in time steps of one hour, therefore it is often preferred to integrate G_T over an hour, into irradiation, I_T . The transmittance-absorptance product, $(\tau\alpha)_{avg}$, is the average of the same period. [12]
- U_L = Collector heat and optical losses [$\text{W}/\text{m}^2\text{K}$]
- \bar{T}_{abs} = Mean absorber plate temperature [K]
- T_a = Ambient air temperature [K]

The mean absorber plate temperature, T_{abs} , is difficult to quantify as it depends greatly on the overall design and performance of the collector. Therefore, an adaptation of eq.(7) which replaces the mean temperature of the absorber plate with the fluid inlet temperature is often preferred. This is done by introducing a heat removal factor, F_R , as shown in the following equation:

$$\dot{Q}_u = A_c F_R [S - U_L (T_{fluid,in} - T_a)] \quad (8)$$

where $T_{fluid,in}$ is the fluid inlet temperature and F_R represents the ratio between the actual collector output and the hypothetical output if the mean absorber plate temperature was the same as the fluid inlet temperature. F_R is given as:

$$F_R = \frac{\dot{m} C_p (T_{fluid,out} - T_{fluid,in})}{A_c [S - U_L (T_{fluid,in} - T_a)]} \quad (9)$$

where:

- \dot{m} = Mass flow rate in the collector [kg/s]
- C_p = Specific heat capacity [J/kgK]
- $T_{fluid,out}$ = Fluid outlet temperature [K]

The solar collector efficiency measured over a period of time is given as:

$$\eta_{th} = \frac{\int \dot{Q}_u dt}{A_c \int G_T dt} , \quad (10)$$

2.3 Building Integrated PV/T Component

As described in subchapter 2.1.6, the PV panel efficiencies are limited to the range from 5% to 21%, the remaining solar irradiance which is not reflected is converted to heat. This heat will increase the cell temperature in the PV panels, which will lead to a reduction in power output. This has led to the desire to cool down the PV panels, utilising the thermal output from the PV for heating purposes in the process. This process is known as photovoltaic thermal (PV/T) technology. PV/T components that are architecturally and functionally integrated into the building envelope are called building integrated photovoltaic thermal (BIPV/T) components. The BIPV/T differs from the building applied PV/T (BAPV/T) as the BIPV/T components replace structural materials such as roof shingles and wall cladding. The BIPV/T component may serve several purposes as it can be used as a barrier against the weather and noise, in addition to generating electrical and thermal energy. [13]

In urban areas, people live denser than in rural areas and high-rise buildings are common in many cities. This means that the rooftop area is very small compared to the overall energy use of the building. As the BIPV/T technology can be integrated into the façade as well as the roof, a bigger area can be utilised for electricity and heat production. Also, the combination of the two technologies may show that there is no need to compete for the same roof or façade area, as both electrical and thermal output is provided.

There is a vast amount of technologies of BIPV/T as seen in Figure 2-7. In addition, there are combinations which include the different photovoltaic materials described in subchapters 2.1.3 – 2.1.5. The types of BIPV/T systems that will be evaluated in this thesis are the water and air based uncovered flat plate BIPV/T.

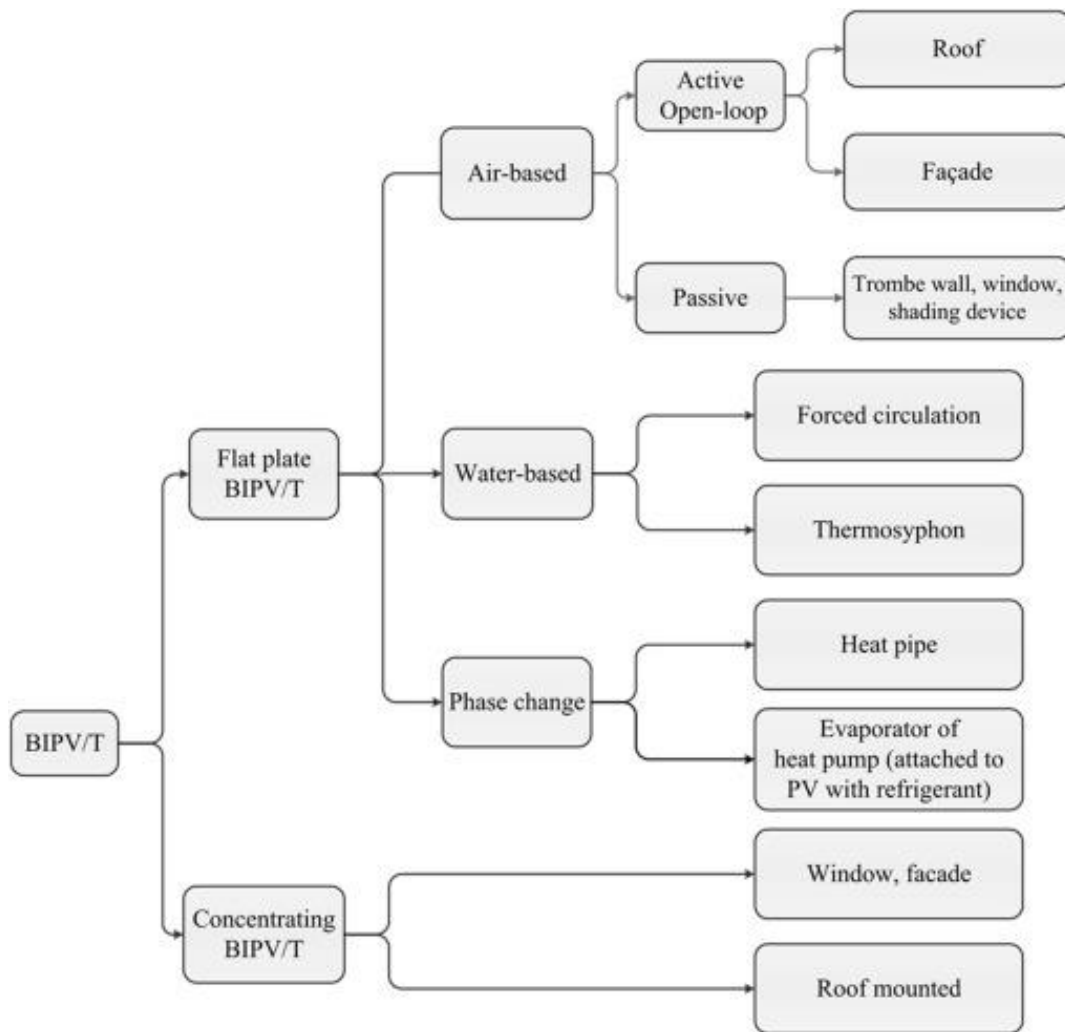


Figure 2-7: Overview of various BIPV/T technologies [17]

2.3.1 Air Based BIPV/T

In the air based BIPV/T component, heat is transferred from the PV panel to cooler air flowing through an air channel beneath the PV panel. A principle sketch of a BIPV/T air component is shown in Figure 2-8:

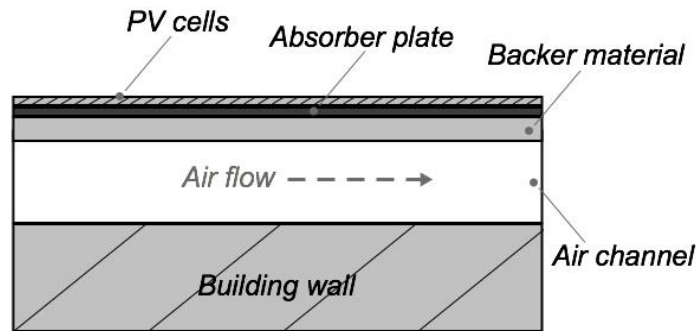


Figure 2-8: Air based BIPV/T component

The air flow is driven by either thermosyphon effects for free circulation or a fan for forced circulation. The heated air from the BIPV/T may be used in an open loop or closed loop system. In the open loop system, the heated air is used directly in the building ventilation system. It is mixed with the ambient air to regulate the temperature of the air entering the building and thus reduces the building energy consumption. In the closed loop system, the air is used indirectly in a heat exchanger connected to e.g. a DHW tank to be used in a high temperature system. Figure 2-9 (a) and (b) show principle system sketches of open and closed loop systems, respectively: [13]

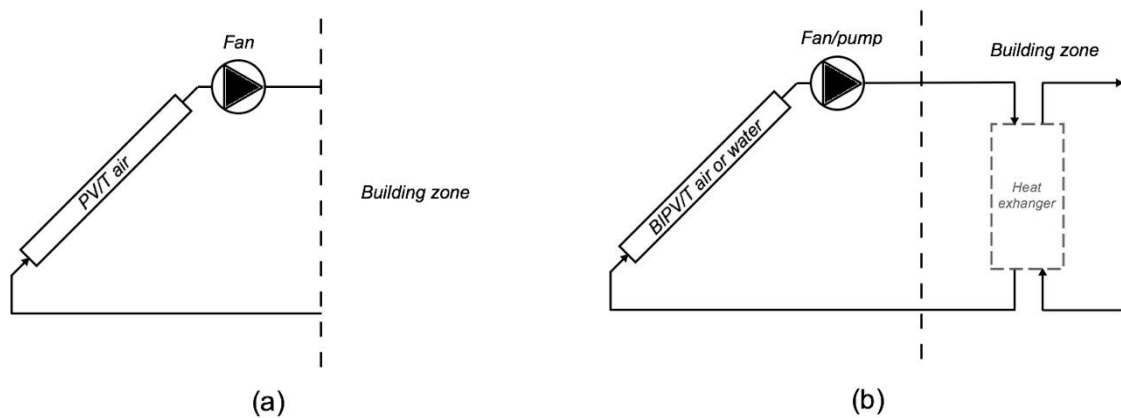


Figure 2-9: Open loop (a) and closed loop (b) air based BIPV/T systems. Adapted from [13]

Generally, the electrical efficiency is higher in open loop systems than in closed loop systems. Although some of the heat is extracted in the heat exchanger in the closed loop system, the returning air entering the BIPV/T is not as cool as for the open loop system and therefore the PV temperature gets higher in the closed loop system. [13]

The energy balance of the air based BIPV/T is described in detail in subchapter 4.1.2.

2.3.2 Water Based BIPV/T

The water based BIPV/T component is similar to the air based, but instead of air flowing in an air channel, water circulates in tubes beneath the PV panel, as seen in Figure 2-10:

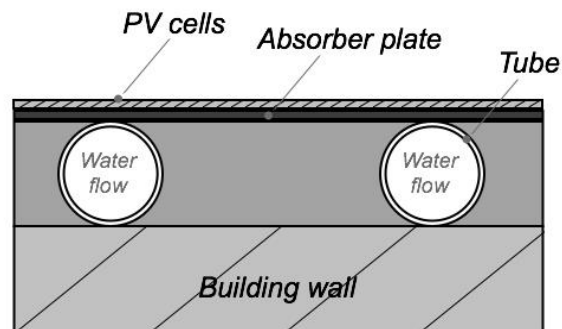


Figure 2-10: Water based BIPV/T component. Flow direction into the page

The principle is the same as for the flat plate solar collector described in subchapter 2.2.1. As for the air based BIPV/T, the fluid flow is free or forced, i.e. driven by thermosyphon effects or by a pump. The water based BIPV/T is used in closed loop systems and integrated into the building envelope so that the back of the component acts a part of e.g. the building wall construction.

The energy balance of the water based BIPV/T is described in detail in subchapter 4.1.1.

2.3.3 Performance of BIPV/T

Typically, air based BIPV/T system have reduced thermal performance due to lower density, thermal conductivity and specific heat capacity of air than water. In the case of thermosyphon fluid circulation, the power consumption of the pump or fan is eliminated. However, the design of the BIPV/T component is of high importance to ensure sufficiently large mass flow rate in the system. Therefore, façade integration may be more beneficial compared to roof integration to make best possible use of the buoyancy effect.

The air based BIPV/T system requires less maintenance than the water based system, and potential leakages will not cause significant damage to the system. However, for the closed loop BIPV/T air system, the increased PV cell temperature will accelerate component deterioration. [13]

BIPV/T Efficiencies

The total efficiency, η_{tot} , is the sum of the thermal and electrical efficiencies:

$$\eta_{tot} = \eta_{th} + \eta_e \quad (11)$$

Previous studies documenting the total efficiency of uncovered BIPV/T water or air components have proven difficult to find. Studies by Kim et al. [18] and Athienitis [19] reported total efficiencies of 47% and 55%, respectively, for corresponding uncovered BIPV/T water and air components. Studies on uncovered PV/T [20-24] report thermal efficiencies ranging between 45% – 60% for water based and 38% – 46% for air based PV/T. Electrical efficiency from 9.5% to 14.5% was reported for water based PV/T and from 10.4% to 13% for air based PV/T.

Studies on other BIPV/T [25-32] report thermal efficiencies between 37.5% – 72% for water based BIPV/T and between 17.2% – 53.7% for air based BIPV/T. Electrical efficiencies in the range 4.9% – 11.6% and 10% – 15.5% were reported for water and air based BIPV/T, respectively. These numbers provide a rough basis of comparison for the magnitude of the expected thermal and electrical performance of the uncovered BIPV/T component analysed in this thesis. However, measurements and simulations should be carried out to determine the performance of the specific component.

Exergy and Anergy

The total efficiency, η_{tot} , accounts for both thermal and electrical energy, but not the quality of the energy. The exergy, often referred to as available energy, is the amount of energy that can be transformed into other forms of energy without losses, and thus addresses the energy quality. The counterpart of exergy is anergy (unavailable energy). Electrical energy consists solely of exergy, whereas thermal energy is part exergy and part anergy. The correlation between energy, exergy and anergy is given in Eq.(12):

$$Energy(Q) = Exergy(E) + Anergy(B) = Constant \quad (12)$$

The exergetic part of the thermal energy, the thermal exergy, is limited by the Carnot efficiency, η_{Carnot} : [33]

$$\eta_{Carnot} = \frac{T_{sink} - T_{source}}{T_{sink}} = 1 - \frac{T_{source}}{T_{sink}} \quad (13)$$

where T_{sink} and T_{source} are the absolute temperatures of the heat sink and source.

Then, the thermal exergy is given as:

$$E_{th} = Q_{th} \cdot \eta_{Carnot} \quad (14)$$

Similarly, the thermal exergy efficiency, ξ_{th} , is given as the product of the thermal and Carnot efficiencies:

$$\xi_{th} = \eta_{th} \eta_{Carnot} \quad (15)$$

2.3.4 Sky temperature

The amount of water vapour in the air is dependent on the relative humidity and the temperature of the air, and is the main contributor to atmospheric radiation between the sky and a surface near the ground. The amount of water vapour decreases as the altitude increases resulting in colder sky temperatures at higher altitudes. Without the water vapour in the sky the sky temperature would approach absolute zero. [34]

The heat exchange between the sky and a body near the ground is given by:

$$\dot{Q}_{sky,net} = \varepsilon \sigma A_c (T_{body}^4 - T_{sky}^4) \quad (16)$$

where ε is the effective emissivity of the sky, σ is the Stefan-Boltzmann constant and T_{body} and T_{sky} are the body temperature and the sky temperature.

2.3.5 Cover heat loss

External winds will affect the convective heat transfer from the top cover of the PV/T component. The convective heat loss to the ambient from the top surface of the component is given in TRNSYS as:

$$\dot{Q}_{loss,top,conv} = h_{outer} A_c (\bar{T}_{PV} - T_a) \quad (17)$$

where h_{outer} is the heat transfer coefficient from the top of the component to the ambient air and T_{PV} is the mean temperature of the PV surface.

2.4 Net Zero Energy Buildings

A net-Zero Energy Building (nZEB) can concisely be defined as a building where the energy consumption is balanced by on-site generation of renewable energy, i.e. a zero energy balance

is reached. The zero energy balance is usually calculated as the net balance over a time period of one year. Thus, the building is not required to be self-sufficient at all times, but should exchange energy with the grid. Figure 2-11, adapted from Sartori et al. [35], illustrates the nZEB balance concept:

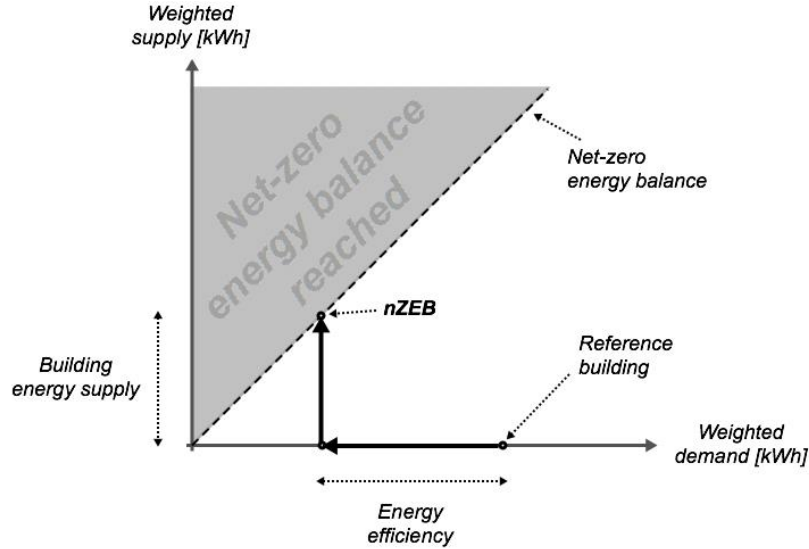


Figure 2-11: Graphical representation of the net-zero energy balance concept. Adapted from [35]

A net-zero energy balance is reached for all points on or above the net-zero balance line in the positive direction on the y-axis. By reducing the weighted demand on the x-axis, less supplied energy is required to reach a net-zero energy balance. The energy efficiency is represented by the distance from the reference building on the x-axis towards the origin.

There are two main approaches when calculating the net energy balance of a nZEB, the delivered/exported balance and the load/generation balance. The net energy balance within a system boundary, can be calculated by assessing the exported and delivered primary energy, as in eq.(18): [35]

$$\sum e_i \cdot w_{e,i} - \sum d_i \cdot w_{d,i} = E - D \geq 0 \quad (18)$$

where:

- e = Exported energy
- d = Delivered energy

- w = Weighting factor
- i = Energy carrier
- E = Weighted exported energy
- D = Weighted delivered energy

When information about exported and delivered energy is unavailable, an energy balance based on generation and load may be applied to calculate the net energy balance: [35]

$$\sum g_i \cdot w_{g,i} - \sum l_i \cdot w_{l,i} = E - D \geq 0 \tag{19}$$

- g = Energy generation
- l = Energy load
- G = Weighted energy generation
- L = Weighted energy load

The two approaches, load/generation balance and delivered/exported balance, are visualised in Figure 2-12:

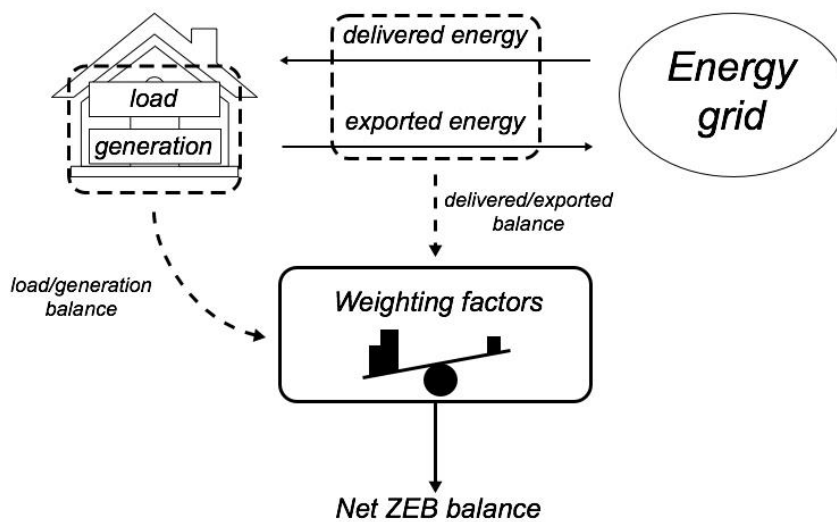


Figure 2-12: Exported/delivered and load/generation balances. Adapted from [35]

The exported/delivered energy balance is considered most accurate since it involves the grid interaction. The weighting factors are used to convert the energy from different energy carriers to a common metric (primary energy). Weighting factors are not necessarily solely

based on scientific or engineering considerations, but may also be determined based on political goals. This should be in mind when comparing performance of energy systems from different locations based on net primary energy need/surplus.

Torcellini et al. [36] point out that a nZEB definition should encourage energy efficiency, i.e. primarily minimise the building’s energy consumption, and then utilise of on-site, renewable energy sources. They proposed a ranking of renewable energy sources in order of preferred application:

Table 1: ZEB renewable energy supply option hierarchy [36]

<i>Option number</i>	<i>ZEB supply-side options</i>	<i>Examples</i>
0	Reduce site energy use through low-energy building technologies.	Daylighting, high-efficiency HVAC equipment, natural ventilation, evaporative cooling.
<i>On-site supply options</i>		
1	Use renewable energy sources within the building’s footprint	PV, solar collector, PV/T and wind located on the building.
2	Use renewable energy sources available at the site.	PV, solar collector, PV/T, low-impact hydro and wind located on-site, but not on the building.
<i>Off-site supply options</i>		
3	Use renewable sources off site to generate energy on site.	Biomass, wood pellets, ethanol or biodiesel that can be imported, or waste streams from on-site processes that can be used to generate electricity and heat.
4	Purchase off-site renewable energy sources.	Utility-based wind, PV, emission credits or other “green” purchase options. Hydroelectric is sometimes considered.

In the literature, ZEB may refer to *Zero Emission Buildings* as well as *Zero Energy Buildings*. The zero emission and energy balances follow the same calculation procedure, the only difference is in the weighting factors. The zero energy balance uses primary energy [kWh] for weighting, whereas the zero emission balance uses greenhouse gas (GHG) emissions [kg

CO_{2eq}]. In this thesis, ZEB is used as an abbreviation for Zero Energy Building, and the zero energy balance is based on primary energy.

2.4.1 Building Design

For a nZEB, factors concerning energy use should be considered significantly earlier in the design process than for a conventional building. Energy saving strategies such as integrating passive solar design (siting, orientation), a high-performance building envelope (insulation thickness, solar shading), load management, daylighting and natural ventilation should be taken into consideration already at the beginning of the early design phase. [13]

The building should be located and oriented with passive solar energy in mind, e.g. accounting for higher solar irradiation on the façades facing the equator. A high-performance envelope is well insulated in order to reduce heat loss during the winter time. However, this also makes super-insulated buildings prone to overheating during the summer time. Thus, adaptive solar shading should be applied to the building envelope to control the amount of solar energy let into the building during summer.

A nZEB should be designed to efficiently provide a comfortable environment to its occupants while simultaneously fulfilling the net zero energy demand. The occupants of a building will adapt themselves and their environment to meet their demands for thermal comfort. Thus, there is a clear link between thermal comfort, occupant behaviour and energy use for heating and cooling. [13]

2.4.2 Load Matching

Load matching refers to how well the energy generation matches the load of the building. A perfect fit would eliminate the need for energy storage and/or exporting energy to the grid. However, for typical on-site systems such as PV/T, energy generation is dependent on solar irradiance which varies throughout the year. Figure 2-13 shows the general energy load compared to the generation per month for a year. This figure shows results for electricity, but is valid for all energy carriers.

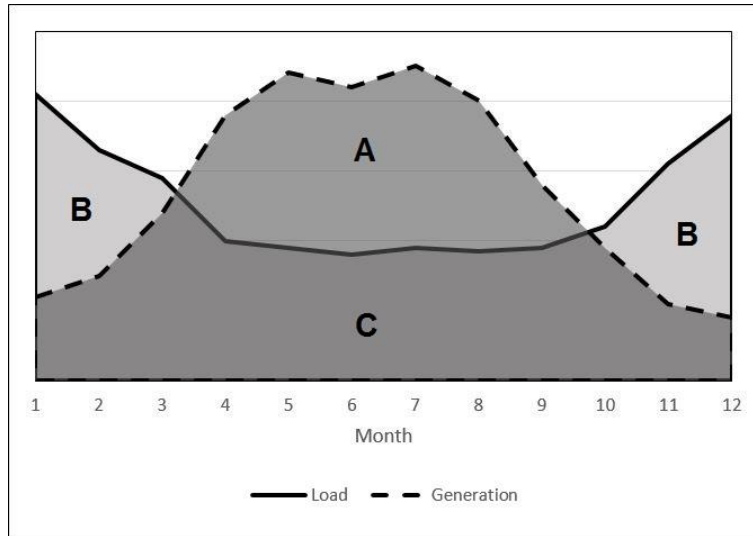


Figure 2-13: General monthly graphs of electric energy load and generation of a building. Adapted from [37]

The areas A, B and C are identified as electricity generation (A+C) and electricity load (B+C). Based on Figure 2-13, Dokka et al. [37] proposed three mismatch factors to be used in the design phase to analyse the energy balance seasonal mismatch of ZEBs, by comparing the results of different energy system solutions. The three mismatch indicators are presented in Table 2:

Table 2: Mismatch factors and indicators. Adapted from [37]

<i>Factor group</i>	<i>Mismatch factor</i>	
Load matching	$\text{load match} = \frac{C}{B+C}$	
	$\text{unmatched generation} = \frac{A}{A+C}$	
Energy carrier compensation	$\text{carrier surplus} = \frac{A-B}{A+C}$	(only if $A > B$)

The *load match* is the match between on-site generation and load and the *unmatched generation* is the amount of annual generation that is not matched by the load and therefore needs to be exported to the grid. The *carrier surplus* is the part of unmatched generation that compensates for other energy carriers and/or embodied energy and/or gives a net surplus.

The load match may also be expressed based on the load/generation energy balance, for N number of data sets, as in Eq.(20). The term in brackets indicates that the maximum value of the load match is 1 (100%).

$$f_{load,i} = \frac{1}{N_{year}} \sum \min \left[1, \frac{g_{i(t)}}{l_{i(t)}} \right] \quad (20)$$

When dealing with solar energy, the load match index is usually referred to as the *solar fraction*. The solar fraction is sensitive to the time interval chosen, and this should be specified when presenting results. [35]

2.4.3 Smart Grids

ZEBs are dependent on renewable energy which may be unpredictable in terms of production, introducing the need for a flexible electricity grid. A *smart grid* communicates with an energy meter at the end user, allowing immediate feedback on the building's energy consumption. A predictive control system considers the aggregated loads and total generation foreseen for a group of buildings as a function of the expected weather.

Smart buildings equipped with a building automation system (BAS) can respond dynamically to changes in electricity price, weather forecast and occupant behaviour to determine an optimal energy management strategy. The BAS will also decide if the power generated on site should be used internally, exported to the grid or stored. This will reduce the peak demand for the grid and the grid stress.

2.5 BIPV/T System Design

2.5.1 BIPV/T Component Tilt Angle

As the trajectory of the sun varies according to the seasons the optimal tilt angle for PV/T performance will also change seasonally. Shanghai is located at a latitude of 31°, hence the optimal tilt angle is 21° and 41° for optimal summer and winter performance respectively. For maximum annual energy production, the optimal angle is equal to the latitude of 31°. As an additional general rule, the BIPV/T component surface should face towards equator, which in the case of Shanghai is south. In contrast to a BAPV/T system, the tilt angle of a BIPV/T façade cannot be adjusted according to the optimal angles of summer and winter performance. A vertical installation of a BIPV/T system will cause a reduction in the performance of the system compared to the optimal tilt angle. However, in high latitudes the vertical BIPV/T façade might be beneficial as it avoids accumulation of snow. [38]

2.5.2 BIPV/T Component Area

Electrical Dimensioning

By utilising uncovered BIPV/T, the electrical energy production is prioritised over the thermal energy production as described in the literature by Chow [39] and Fujisawa and Tani [40].

This implies that the size of the BIPV/T component area should be dimensioned giving priority to the electricity load of the office building, rather than the DHW load.

The cost of the BIPV/T components is a determining factor in the price of the on-site produced electrical power. An oversized system will raise the price of the generated power whereas an undersized system will reduce the reliability of the supplied power. [5]

As the thermal and the electrical systems are combined in the BIPV/T, the electrical energy production is a result of the fluid temperature as well as the BIPV/T component area. The temperature of the fluid flowing in to the BIPV/T component is heavily influenced by the size and geometry of the storage tank and affects the mean temperature of the PV surface, consequently increasing or decreasing the electrical energy production. [41]

The vertical BIPV/T component area required to supply the electrical and thermal load of a building is considered to be larger than that of a stand-alone PV/T system due to the reduced solar irradiance collected throughout a year. However, an area of the building which would otherwise remain unused is utilised for generation of thermal and electrical power.

Solar irradiation data for Shanghai and the load data of the building are important factors when sizing the BIPV/T for electrical production. The average power demand as well as daily and seasonal electrical load profiles has to be taken under consideration when designing a BIPV/T system, as well as economic limitations. [5]

Thermal Dimensioning

The optimal BIPV/T component area for production of thermal energy is dependent on the solar irradiance, the DHW load and the storage tank. Kalogirou [6] describes the f-chart method which is a method developed in order to evaluate the solar energy performance of both air and water based solar collector systems through correlation of a vast number of simulation results developed by Klein et al [42]. The solar fraction, f , represents the percentage of DHW demand that is delivered by the solar system, which is normally in the range of 50% – 70%. In this method, the primary design variable is the collector area and

thermal energy storage, collector type, load, heat exchanger and flow rate are secondary design variables. However, since the thermal and electrical performance of the BIPV/T may not coincide with each other, dimensioning and design of such a system requires new approaches [43]. In order to get more accurate results, modelling and simulation tools are recommended e.g. TRNSYS [6].

Oversizing of the BIPV/T area may lead to frequently high tank temperatures in the summer time. The circulation pump is in addition to the dead band controlled according to a maximum temperature of the tank, which is normally set close to the boiling temperature of the water. If this temperature is reached, the circulation pump is shut off, causing the absorber plate temperature to quickly rise. When this happens, the stagnation temperature of the absorber eventually reaches 220°C – 300°C and the water in the BIPV/T component starts to evaporate. Water is then forced into the expansion vessel and the remaining water in the component evaporates. The evaporated water increases the temperature of the system components and the system pressure. The component dries out and the remaining steam is superheated until the solar irradiance decreases and the component fills up with water through condensation. The dimensioning of the expansion vessel is an important factor in order to maintain safe operation. [44]

2.5.3 Thermal Energy Storage

Thermal storage is needed when the thermal generation does not coincide with the thermal energy demand. There are many ways of storing thermal energy e.g. in phase changing materials, boreholes etc. The use of a water tank as a thermal storage is most common in studies of BIPV/T and what is considered in this thesis.

The performance of a water tank is dependent on parameters such as tank geometry, tank volume and the component area. An auxiliary heating source can be used in order to provide additional heat when the solar system is not able to provide a temperature set by the load. According to Duff [45], the auxiliary heat should be provided in such a way that it does not interfere with the solar system e.g. adding an additional tank designated for solar storage without auxiliary heating. The heat exchanger should have sufficiently large capacitance, also the tank should be insulated and thermal bridges avoided in the upper part of the tank.

Water Tank Volume

Experimental studies have shown that increasing the ratio between the height and the diameter of the tank increases the thermal stratification. Cole and Bellinger [46] suggested that by setting the height to diameter ratio to four, optimal stratification is achieved. In addition, the ratio between the volume of the tank and the area of the BIPV/T component is an important parameter. Duffie and Beckman [38] report that the volume of the water tank per unit area of a solar collector will usually be around $0.05 - 0.1 \text{ m}^3/\text{m}^2$ of collector area. This however, may be different for an uncovered BIPV/T component and should be optimised accordingly.

A study conducted by Comakli [47] concludes that by increasing the tank volume, the thermal efficiency of the solar collector also increases. However, the temperature of the usable water in the tank decreases. Depending on the application of the hot water, the temperature of the produced water may be just as important as the thermal efficiency of the BIPV/T system.

Stratification

The temperature gradient between the top and the bottom of the water tank is called stratification. The cold water accumulates at the bottom of the tank due to increased density with decreasing temperature. The performance of the BIPV/T system is strongly affected by the stratification of the thermal storage tank. More heat is transferred from the component to the tank when the water temperature in the bottom part is lower than the upper part, given that the heat exchanger is placed in the bottom next to the supply of cold water as seen in Figure 2-14:

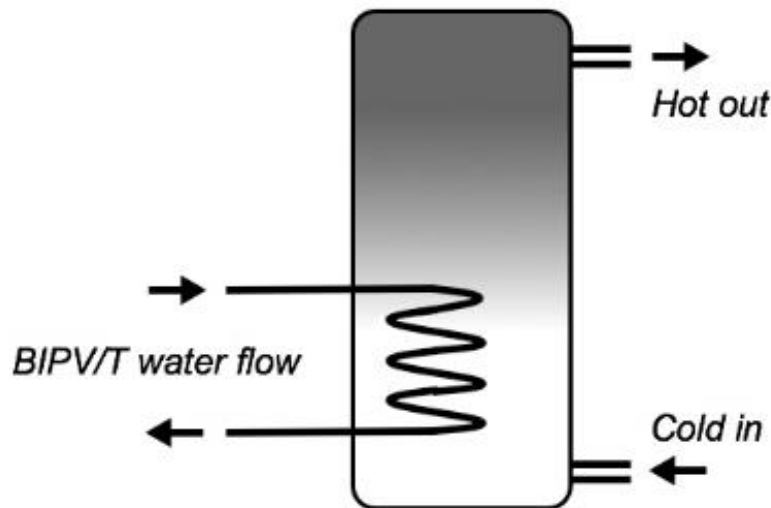


Figure 2-14: Stratified tank with a BIPV/T component side heat exchanger

A greater degree of stratification can be achieved with a low flow rate at the inlet and outlet of the tank from the BIPV/T and to the load, respectively [48].

An issue with stratified tanks is susceptibility to Legionella growth, as a large volume of the tank keeps a temperature below 60°C³. The temperature of the water going out for consumption should be at least 60°C, and in addition the whole tank should be heated to 60°C once a day to avoid Legionella growth [45].

Heat Exchanger

By using a BIPV/T component side heat exchanger, the thermal energy produced by the component is transferred to the tank. If the area of the heat exchanger is too small then the temperature of the BIPV/T component water inlet and outlet will increase. Heat transfer from the component to the tank at a higher temperature will reduce the amount of available energy transferred to the tank, which leads to a larger demand of auxiliary, thus reducing the solar fraction of the system. [45]

2.5.4 Electrical Energy Storage

In many industrialised countries, exporting the electricity production from BIPV/T systems to the grid is becoming a reality. Using the grid for storage of electricity would eliminate the need for an on-site electrical storage unit, which is normally required for stand-alone systems.

³ 60°C is the recommended minimum temperature in order to avoid Legionella growth [49]

This however, requires that the loads vary in proportion to the irradiation, e.g. air-conditioning refrigeration and pumping power. It is also possible to set the operation of some loads to match BIPV/T power production, e.g. washing machines and clothing dryers. [5]

The utility companies do not pay the same amount for the exported BIPV/T electricity as the consumer pays to import electricity from the grid. The import and export prices vary from country to country depending on government regulations. Therefore, on-site electrical storage might be a viable solution as produced BIPV/T electricity can be consumed when there is no on-site production. An economic analysis should therefore be conducted when designing such a system.

The most commonly used method of electrical energy storage for PV production is the utilisation of lead-acid batteries due to the low price and accessibility. Other, less common means of storing PV electrical energy is given in Table 3. [5]

Table 3: Energy storage systems. Adapted from [5]

<i>Energy stored</i>	<i>Technology</i>	<i>Remarks</i>
Mechanical	Pumped water	Commonly used in large scale energy storage.
	Compressed air	Demonstrated in combination with large scale storage.
	Flywheel	Under investigation for small scale systems.
Electromagnetic	Electric current in superconducting ring	New development potential using “high-temperature” super conducting materials.
Chemical	Batteries	Good availability and cost effective.
	Hydrogen production	Established technology.

2.5.5 Mass Flow Rate

High flow rates increase the heat removal factor F_R , thus improving the thermal efficiency. However, research performed by Duff [45] has shown that low flow rate through the component results in a higher solar fraction when combined with a stratified water tank

system. By using a low flow rate the investment cost of the system is reduced as less pump or fan power is needed, a smaller tube diameter is required, as well as a smaller amount of insulation for the tubes. If an auxiliary heater is installed at the top of the tank, a large flow rate might transfer the auxiliary heat to the component inlet, reducing the efficiency of the component.

Duff also recommends that the mass flow rate in a solar thermal collector is in the range between 12 – 24 kg/hm² of collector area. However, this flow rate is not optimised for the behaviour of a PV/T system with regards to electrical production. Recent studies [43] conducted on flow rates in water based PV/T systems show that the optimal flow rate is around 50 kg/hm² of component area and that an increase in flow rate does not increase the energy output substantially .

The optimal mass flow rate should be chosen in the BIPV/T system in order to increase the overall efficiency. With a large mass flow rate inside the air channel, the fluid convection coefficient will increase and the PV surface will be more effectively cooled down, thus improving the efficiency and increasing the electrical power produced.

According to a parametric study performed by Tiwari et al. [50], an air speed of around 2 m/s and an air channel gap between 0.03 – 0.06 m give the best performance for the overall efficiency of the PV/T air system. Air speeds exceeding 2 m/s inside the PV/T air system showed a reduction in the overall efficiency. Another study conducted by Goossens et al. [51] coincides with this research, as they conclude that an air channel gap of 0.055 m gives the best performance. Using this information, the recommended flowrate per component area is 0.1225 kg/sm².

2.5.6 BIPV/T Components Connected in Parallel and Series

Electrical configuration

Most PV panels are designed to work with a 12 V nominal voltage battery. V_{DC} is the operating voltage for the system, and is normally set equal to sum of the nominal battery voltage in a battery sub storage. The number of BIPV/T components put together in series, N_s , is given as:

$$N_s = \frac{V_{DC}}{V_m} \quad (21)$$

where V_m is the operating voltage of one BIPV/T component, which is normally set as 12 V. [5]

The number of BIPV/T components to be connected in parallel strings, N_p , is related to the current required by the load:

$$N_p = (SF) \frac{I_{PV}}{I_{SC}} \quad (22)$$

where (SF) is a sizing factor used to oversize the amount of current produced by the BIPV/T components. I_{PV} is the nominal current which is needed from the BIPV/T system under STC. [5]. An example of an electrical configuration of a BIPV/T system is shown in Figure 2-15:

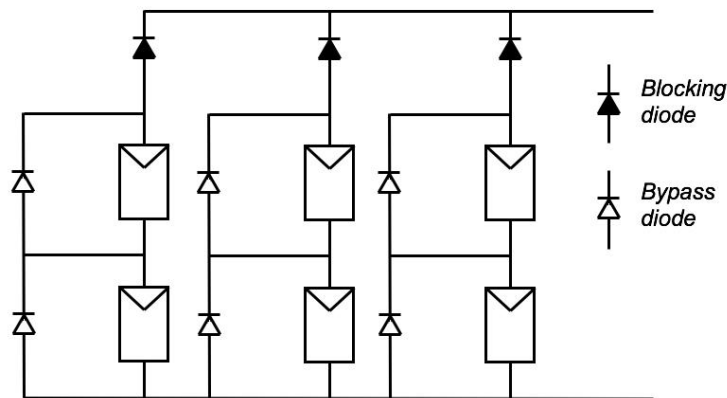


Figure 2-15: Electrical configuration of BIPV/T system [5]

Thermal configuration

It is possible to connect multiple BIPV/T components hydraulically in series and parallel configuration. When the BIPV/T components are hydraulically connected in parallel the supply temperature to the components are all the same, in contrast to a series configuration where the output of one component is the input to the next one, thus producing higher outlet water temperatures. Components connected in series also have the same mass flow rate. Whether one configuration is chosen over another depends on the desired temperature of the hot water produced. Parallel installation of BIPV/T components results in a lower pressure drop and reduces the energy consumption of the circulation fan or pump [43]. The two different configurations can be seen in Figure 2-16: [6]

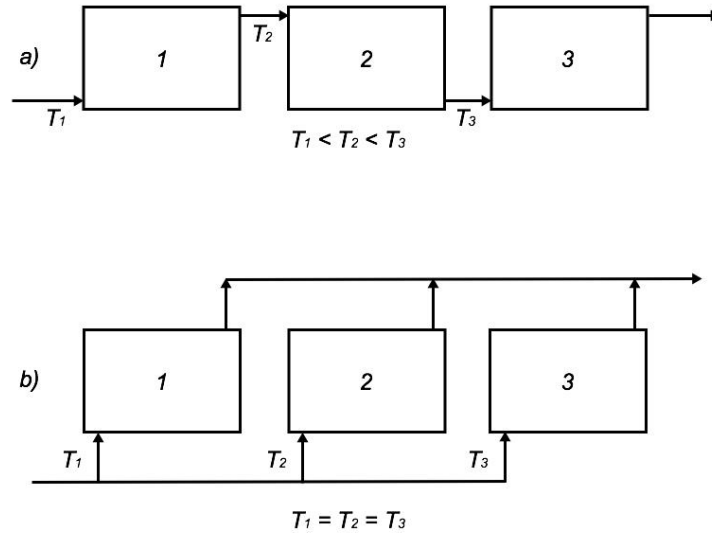


Figure 2-16: Series and parallel connections of BIPV/T [5]

2.5.7 DC/AC Converter (Inverter)

An inverter makes it possible to transform DC power from the BIPV/T or the battery storage to AC power, which can be used by AC appliances or it can be exported directly to the electricity grid. The transformation is performed by using electronic switches to reverse the polarity of the electricity which is supplied by the BIPV/T to the load periodically. The inverter normally operates between 75% – 95% depending on the value of the load current. [5]

2.5.8 Heat Pump Coupled BIPV/T Component

A heat pump collects low temperature heat from the surroundings mainly with help of a working fluid, compressor, evaporator, condenser. It provides heat for a heating system and/or DHW at a higher temperature than that of the heat source. The energy used to extract the heat is less than the amount from a conventional electric heater. The relation is given as:

$$COP = \frac{Q_C}{W} , \quad (23)$$

where Q_C is the heat provided to the heating system from the condenser, W is the work put in to the compressor and COP is the coefficient of performance.

Ground source heat pump

Ground source heat pumps utilise the ground as a heat source for the evaporator during the heating season and as a heat sink during periods with a cooling need as shown in Figure 2-17. Normally, depths between 30 – 200 m are used for boreholes in soil or rock. Temperatures remain relatively constant at depths larger than 15 m and are usually higher than the ambient air during cold periods, and lower during hot periods. Consequently, the COP is higher for ground source heat pumps compared to an air source heat pump. [6, 52]

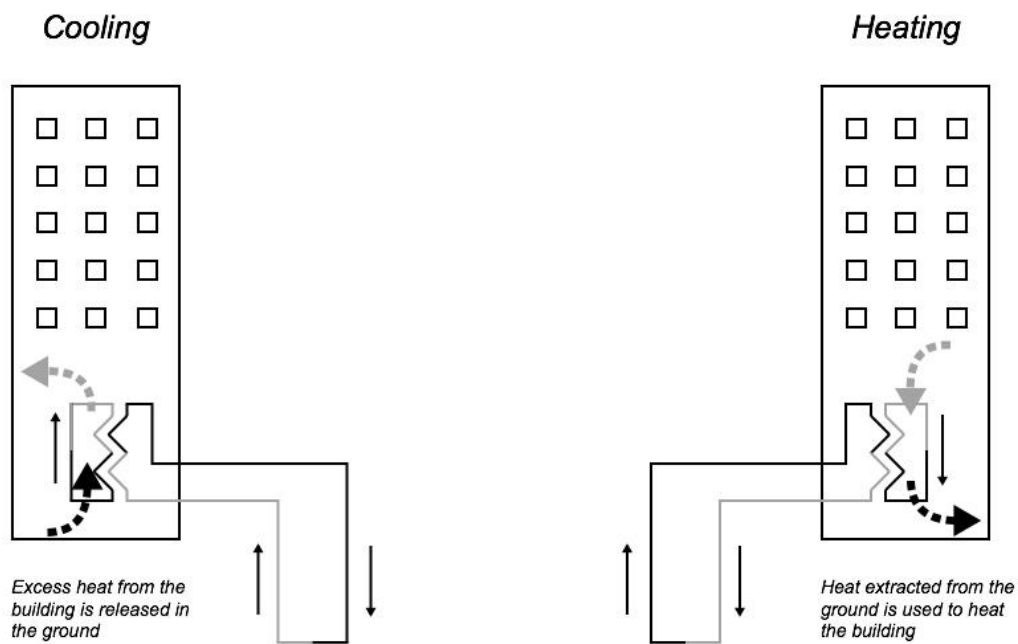


Figure 2-17: Ground source heat pump operation during cooling and heating season

In the boreholes, heat is exchanged between the ground and the heat transfer medium flowing through the heat exchanger. The heat in the borehole is transferred through conduction and the temperature of the borehole will depend on factors such as the thermal conductivity, specific heat, density, water content and the mass flow rate through the ground. Boreholes could be used for seasonal energy storage when there is a period with surplus of solar energy produced and the energy demand of the building is small. When there is a period with increased energy demand the heat pump could use the stored heat in the boreholes as a heat source. [6]

BIPV/T and Ground Source Heat Pump System Design

It is possible to couple a BIPV/T component and a heat pump through series and parallel configurations. In a series configuration, the BIPV/T component acts as a heat source for the heat pump through a borehole heat exchanger as shown in Figure 2-18, heating the brine

circulating in the evaporator. By doing this the BIPV/T is operating with the lowest possible temperature, while at the same time increasing the COP of the heat pump. [53]

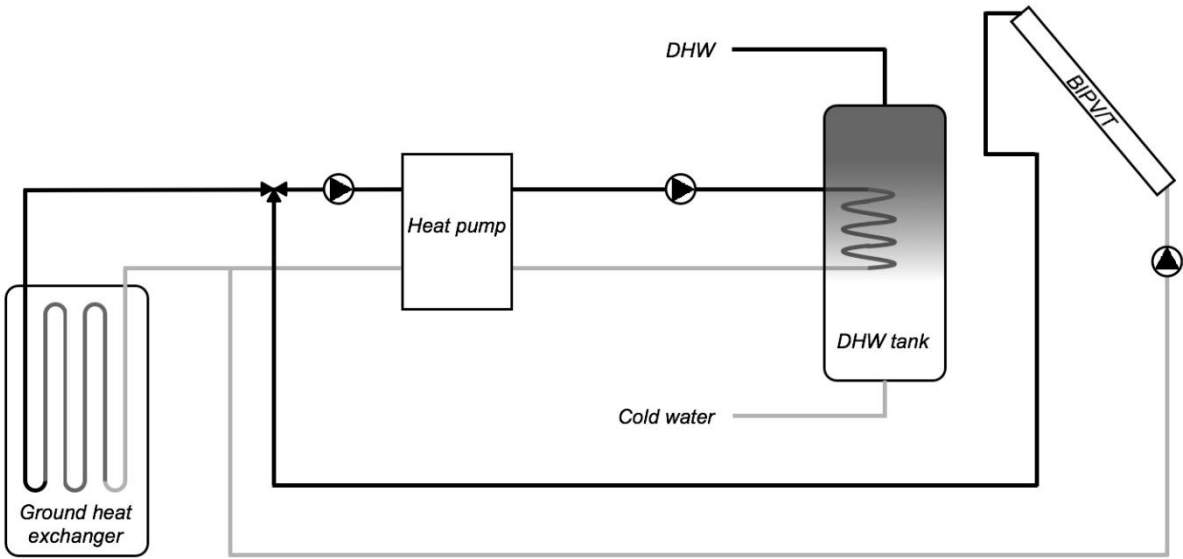
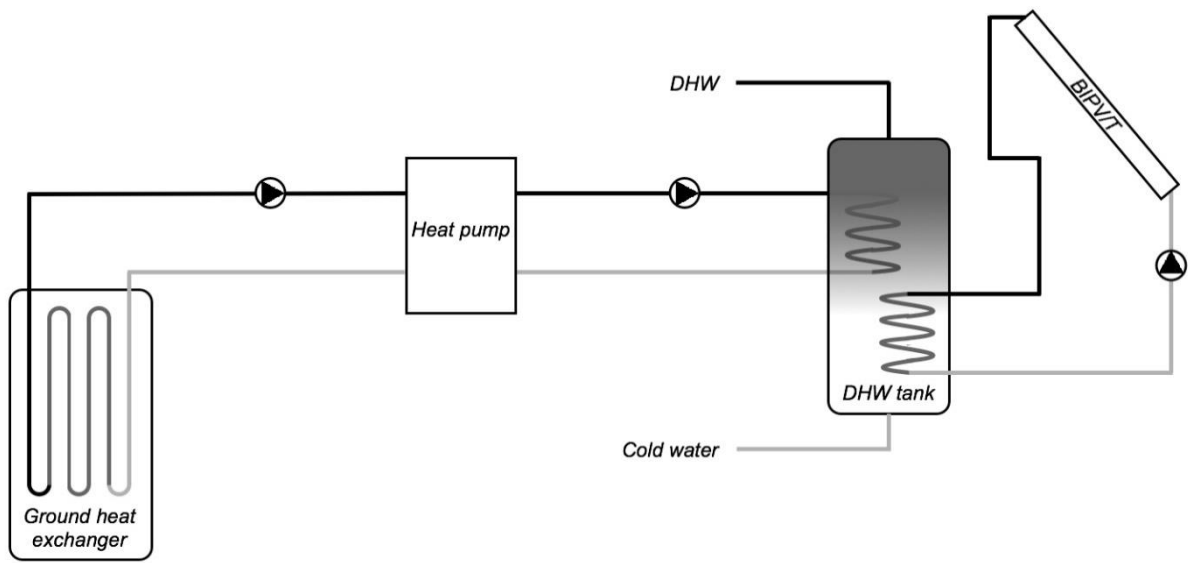


Figure 2-18: Series configuration of a BIPV/T and a ground source heat pump system. Adapted from [54]

In a parallel configuration, the BIPV/T component and the heat pump work independently to supply heat to one or more storages, as shown in Figure 2-19. This is the most common configuration for solar assisted heat pumps according to a study conducted by Fraunhofer Institute for Solar Energy Systems. However, the use of PV/T components in combination with heat pumps are not common, as this technology is rather young. [55]



**Figure 2-19: Parallel configuration of a BIPV/T and a ground source heat pump system.
Adapted from [54]**

3 The Green Energy Laboratory

The Green Energy Laboratory was built in 2012 at Minhang Campus, Shanghai Jiao Tong University (SJTU) as part of a collaboration between the University and the Italian Ministry of Environment, Land and Seas. The Green Energy Laboratory has a footprint area of 816 m² and a total floor area of 1500 m² and serves as a research centre and laboratory. The ground and 1st floors are dedicated to laboratories, meeting rooms and classrooms and two apartments are placed on the 2nd floor. Here, different smart control systems are being tested for control of lighting, ventilation and heat pump systems using Wi-Fi remote controllers.

The HVAC system in the GEL has the possibility of interchanging configurations in order to test different combinations of HVAC technologies. In addition, the roof area is actively being used for various kinds of solar technologies, such as photovoltaic panels and vacuum tube solar collectors as well as concentrating solar collectors. The roof above the apartments is facing south and tilted at angle optimising the efficiency of installed solar collectors and PV panels, as can be seen in Figure 3-1: [56]



Figure 3-1: The Green Energy Laboratory [57]

The centre of the building is an open atrium that extends all the way to a skylight which can be opened, as seen in Figure 3-2. This has two functions: In sunny winter days, the atrium serves as a heat storage by storing heat in the concrete balconies. In the summer, the skylight opening can be adjusted for cooling by natural ventilation.



Figure 3-2: Atrium showed in picture (left) and on floor plan (right) [57]

3.1 GEL Façade

Large efforts have been made in order to maximize the natural ventilation effect, as well as to provide shading for the building. The façade of the GEL consists of two layers for energy shown to the left in Figure 3-3. The internal glazed surface provides waterproofing and insulation whereas the external layers provide shading and ventilation of the building. The external layer of the façade is made up of tiles of Italian cotto stone arranged in frames, as shown to the right in Figure 3-3: [57]



Figure 3-3: The two layers of the facade (left) and the external facade configuration (right) [56]

The tiles are designed to block solar irradiation during summer, when the sun is high in the sky. Thus, the temperature of the air in close vicinity to the building is kept lower than the ambient, preventing overheating during summer. During winter, when the sun is lower, solar irradiation passes through the tiles to benefit from solar heat gain of the building. The principle is shown in Figure 3-4:

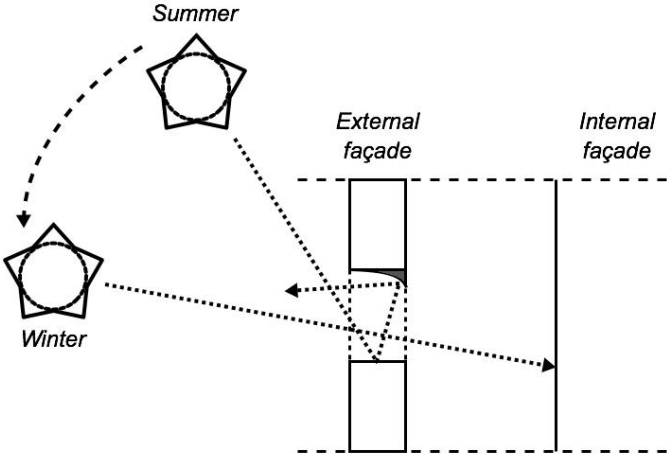


Figure 3-4: GEL façade operation during summer and winter [58]

The double skin façade is applied to all façades of the GEL, except for the south wall of the apartments on the 2nd floor. Today, this area is not used for solar energy generation either.

3.2 GEL Energy Systems

Various chillers and the AHU is installed inside the roof structure of GEL. Water and ground source heat pumps and a combined heat and power (CHP) generator are installed in a separate technical room. The installations are used for heating and cooling of the building, and supplies various laboratories as well as the apartments on the 2nd floor. Figure 3-5 shows an overview of the energy technologies currently installed at the GEL.

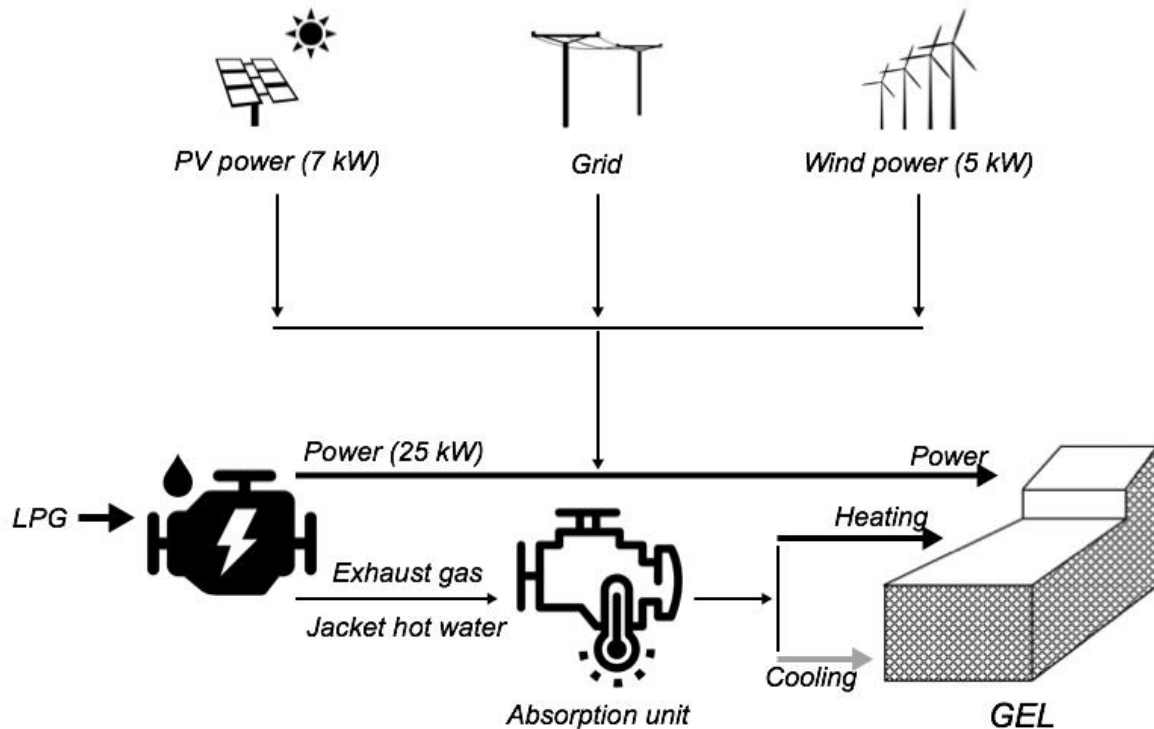


Figure 3-5: Energy technologies installed at the GEL. Adapted from [56]⁴

Electrical power is supplied to GEL using an independent energy system, which includes a 7 kW PV installation and a 5 kW wind power generator. Power can also be supplied by a 25 kW Liquid Petroleum Gas (LPG) generator, where the exhaust gas is used in the absorption unit to provide heating or cooling. [56]

3.2.1 Open-loop Surface Water Source Heat Pump System:

In order to provide heating and cooling, an open loop water to water heat pump is installed. In cooling mode, water from a nearby river cools down the condenser, whereas in heating mode, the river water heats the evaporator. Hot or cold water is then supplied to the rooms.

3.2.2 Ground-coupled Heat Pump System:

The ground coupled heat pump system consists of nine boreholes. The boreholes are divided into groups of three with borehole depths of 50, 60, and 80 meters and are located to the east of the GEL. It is designed in order to optimize the extraction of heat and to maintain a desired temperature range around the boreholes.

⁴ Figures: "solar panel" and "wind farm" by Ron Scott, "wires" by Jules Renvoisé, "engine temperature" by BomSymbols, "engine" by Thengakola and "pattern" by Eliricon from the Noun Project [59].

3.2.3 CO₂ Heat Pump:

The CO₂ heat pump is a novel installation which integrates a solar thermal driven absorption chiller and a heat pump. The unit operates by super cooling the CO₂ gas leaving the gas cooler in cooling mode. The CO₂ heat pump is only assisted by the solar thermal driven absorption chiller in cooling mode when the temperature of the water tank is high enough. In heating mode, the CO₂ heat pump operates unassisted while supplying the space heating and domestic hot water demands. [56]

3.3 GEL Office

As the scope of this thesis is BIPV/T for office buildings, a model has been developed based on the GEL. The eastern apartment on the 2nd floor is assumed to be an 88 m² office area with a ceiling height of 3 metres. The area of the office is outlined in the floor plan of the 2nd floor of the GEL in Figure 2-1. It is assumed that the office is an open landscape and can be modelled as one thermal zone. A more detailed description of the office and the modelling approach is given in chapter 5.



Figure 3-6: Floor plan of the 2nd floor in the GEL

3.4 Measurements

In order to validate the PV/T component in TRNSYS, measurements of an unglazed PV/T water component connected to a tank were carried out by fellow GEL student, Zhang Lu. The main parameters of the PV/T test rig are presented in Table 4:

Table 4: Main parameters of the PV/T test rig

<i>Parameter</i>	<i>Value</i>
Area	1.26 m ²
Electrical efficiency	15%
Inclination	45°
Tank size	100 l
Mass flow rate	100 l/h
Pumping power	46 W

Technical data sheets on the measurement instruments was not available, as the measurements in December were not performed by the authors. Ideally, this information should be available in order to assess the accuracy and uncertainty of the instruments.

The measurements were conducted on the 7th of December 2016 and include inlet, outlet, ambient and tank temperatures as well as voltage, electricity, solar irradiance, power output and electrical and thermal efficiencies of the PV/T component. Figure 3-7 shows the ambient conditions, i.e. ambient temperature and solar irradiance on a tilted surface for the day of the measurements.

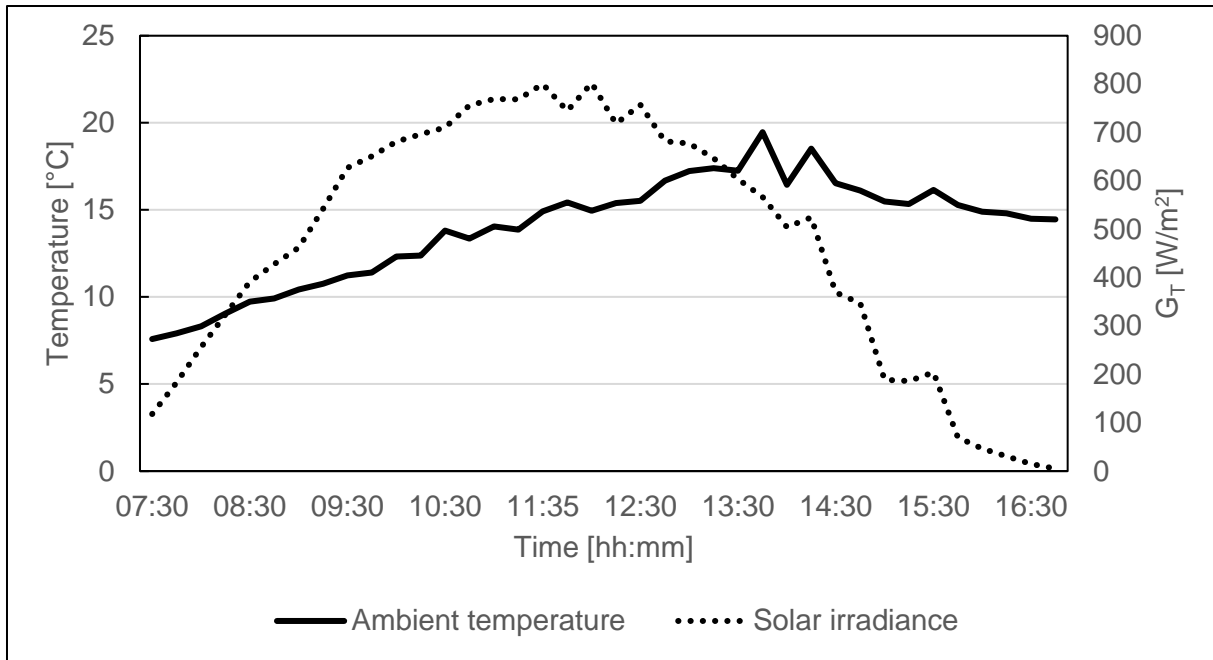


Figure 3-7: Ambient conditions during the PV/T water measurements

The ambient temperature varies from approximately 7.6°C at the start of the measurements to a peak value of 19.8°C at 14:20. The solar irradiance reaches its peak value of 831 W/m² at 11:15.

Summer measurements were planned, but not ready within the deadline for this thesis. Another set of measurements would be beneficial in order to accurately validate the model for both summer and winter conditions. The test rig for the planned PV/T water summer measurements is shown in Figure 3-8: Solar test rig with one PV/T component connected to a tank. The rig is similar to the one used for the winter simulations in December. The rig fits four solar energy components, i.e. PV panels, solar collectors and PV/T components, at the time and two-and-two components can be angled between 0° – 90°.



Figure 3-8: Solar test rig with one PV/T component connected to a tank

4 Modelling and Simulation Tools

Multiple simulation tools, e.g. TRNSYS, IDA ICE and Polysun, were considered before developing the computer model of the BIPV/T component. Polysun has the possibility of PV/T simulation but with limited capability when it comes to the implementation of a building model.

IDA Indoor Climate and Energy (IDA ICE) provides the user with detailed simulations of thermal comfort, indoor air quality and energy consumption in buildings. The developers intend to implement BIPV in the near future, while BIPV/T is not yet planned for implementation. IDA ICE uses an equation-based language called Neutral Model Format (NMF). This makes it possible to replace and upgrade program codes. In order to do so IDA Simulation Environment (IDA SE) or Modelica has to be used to create a model, which then can be used in combination with IDA ICE. After communication with the developers of IDA ICE, the use of these tools in order to create PV/T models for IDA ICE was not deemed appropriate for a master thesis, as it is too time consuming. [60]

In the end, TRNSYS was found to be the best alternative, because it provides the most accurate representation of the BIPV/T components investigated in this thesis. TRNSYS is a software used to simulate the behaviour of transient systems. In TRNSYS, the models are based on ordinary differential equations or algebraic equations. Each component of a system is represented by appropriate mathematical models as a *TYPE*. TRNSYS contains a library of several *TYPE*s grouped by energy domain. *TYPE 563* and *TYPE 567/568* from the Thermal Energy System Specialists (TESS) library are used in this thesis to represent the BIPV/T components. All *TYPE*s can be edited by the user through a compatible FORTRAN compiler. In the model, the *TYPE*s are interconnected through links, representing the ducts or piping in the actual system.

Figure 4-1 shows the monthly electricity output of a PV system estimated by several simulation tools compared to the real measured values. TRNSYS provides the most accurate monthly energy generation with only slight deviations compared to the real measurements.

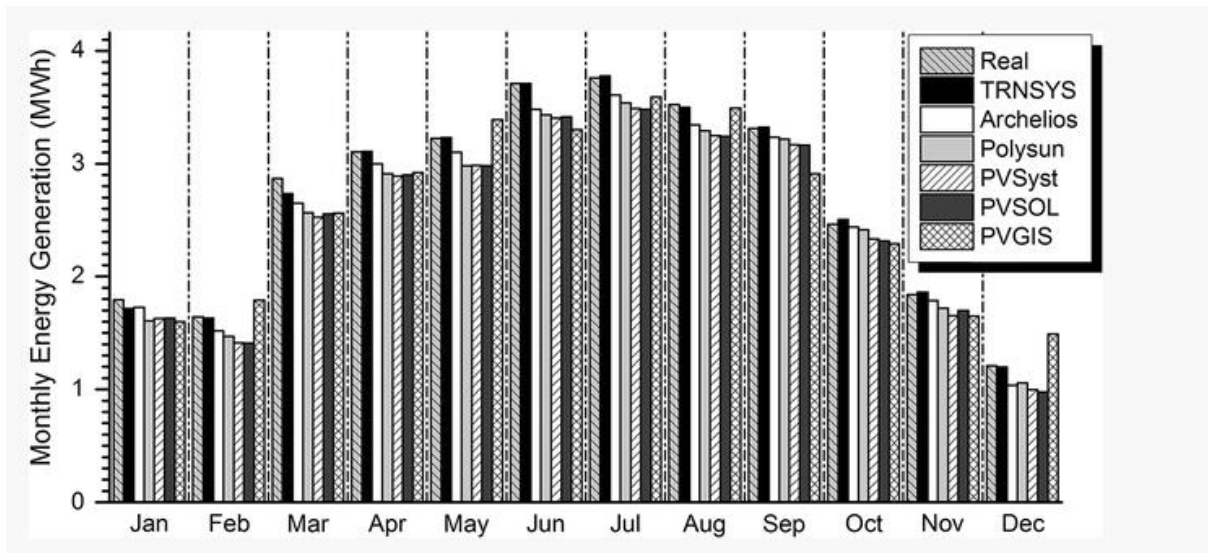


Figure 4-1: Comparison of real measurements to various simulation tools for PV production [61]

TRNSYS was found to be almost exclusively used in the literature related to simulations of BIPV/T with a few exceptions.

When the PV/T component is integrated to the building construction, it is important that the real physics of the building as well as the solar technology are simulated in an accurate manner. The solar irradiance is either reflected or absorbed by the BIPV/T component, which in turn will affect the heat balance of the building [24]. TRNSYS TYPE 563 and TYPE 567/568 allows for building integration as it allows for the coupling of a TYPE 56 Multizone model.

The modelling process combines an experimental and a computational procedure. The experimental part is focused around conducting measurements of the actual BIPV/T components to determine their instant behaviours. The computational part concerns modelling the behaviour of the components and analysing their applicability in a holistic energy system. To develop a sufficiently accurate model, the simulation results of the model must be compared to the results from the measurements. If deviations occur, the model is calibrated to imitate the behaviour of the actual component according to the measured results. This is part of the essential iterative validation process, which is crucial in order to develop an accurate model that is valid for further simulations and long-term investigations. The complete modelling process is visualised in the flow chart in Figure 4-2:

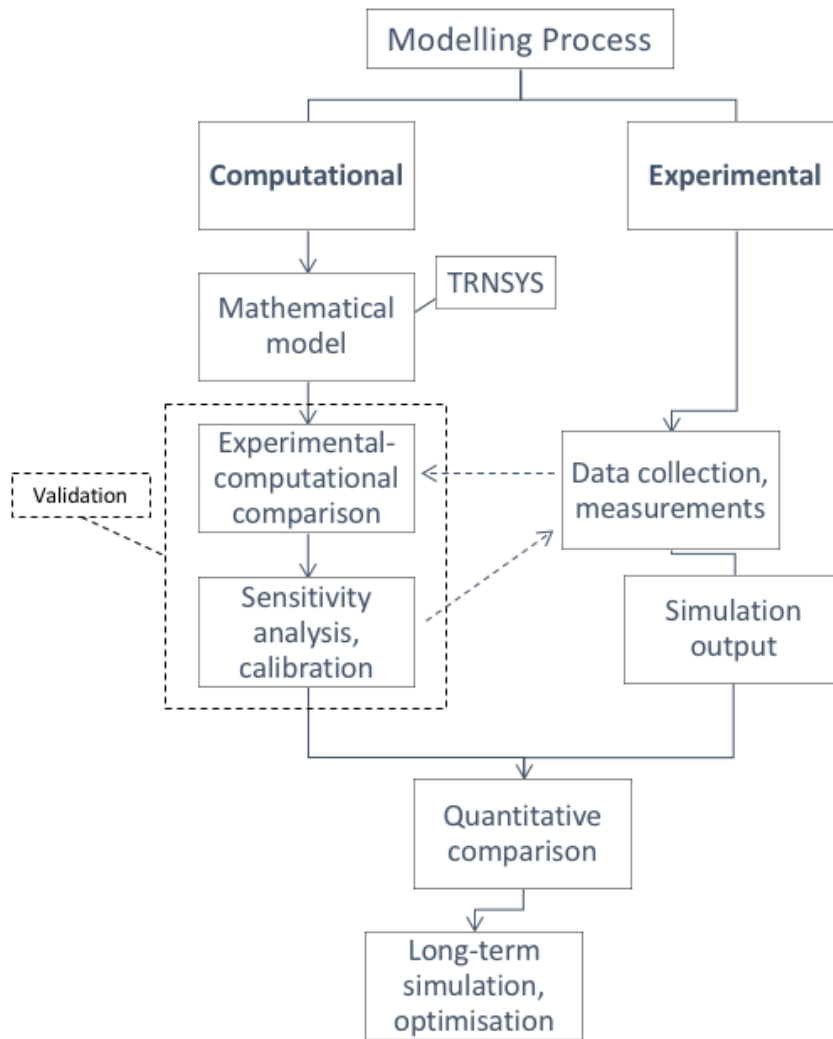


Figure 4-2: Modelling process. Adapted from [62]

4.1 Mathematical Model of PV/T

A baseline model was developed by adding the known parameters from the experimental measurements, listed in Table 5, to the TRNSYS model. No baseline model was developed for the air based PV/T component, as measurements were not available.

Table 5: Parameters used for simulation of the experimental water based PV/T component.
***indicates that the parameter is unknown when conducting the measurements and the value is left as the default value suggested by TRNSYS.**

<i>Parameters</i>	<i>Value</i>
Component area	1.26 m ²
Nominal efficiency of PV panel	0.15 (15%)
Tube spacing*	0.125 m
Tube diameter*	0.01 m
Absorber thickness*	0.0005 m
Glass cover transmittance*	0.9 (90%)
Number of glass cover	0
Temperature coefficient of PV cell efficiency*	-0.005 /°C
Radiation coefficient of PV cell efficiency*	0.000025 hm ² /kJ
Storage tank volume	0.1 m ³

More complex parameters were not changed from the standard value suggested by TRNSYS. This model was used to assess the effect of various measures on the TRNSYS model during the early stages of the modelling process.

The baseline model consists of a pump, a tank, an experimental weather file, a PV/T component, a data reader and a printer. This model was used to ensure proper operation of the PV/T component, with a minimum of variables to easily point out possible sources of error. Other components such as a heat distribution system, building model and renewable energy sources were included in the further development of a model that represents the GEL described in the upcoming chapter 4.5. The flowchart of the baseline model is displayed in Figure 4-3:

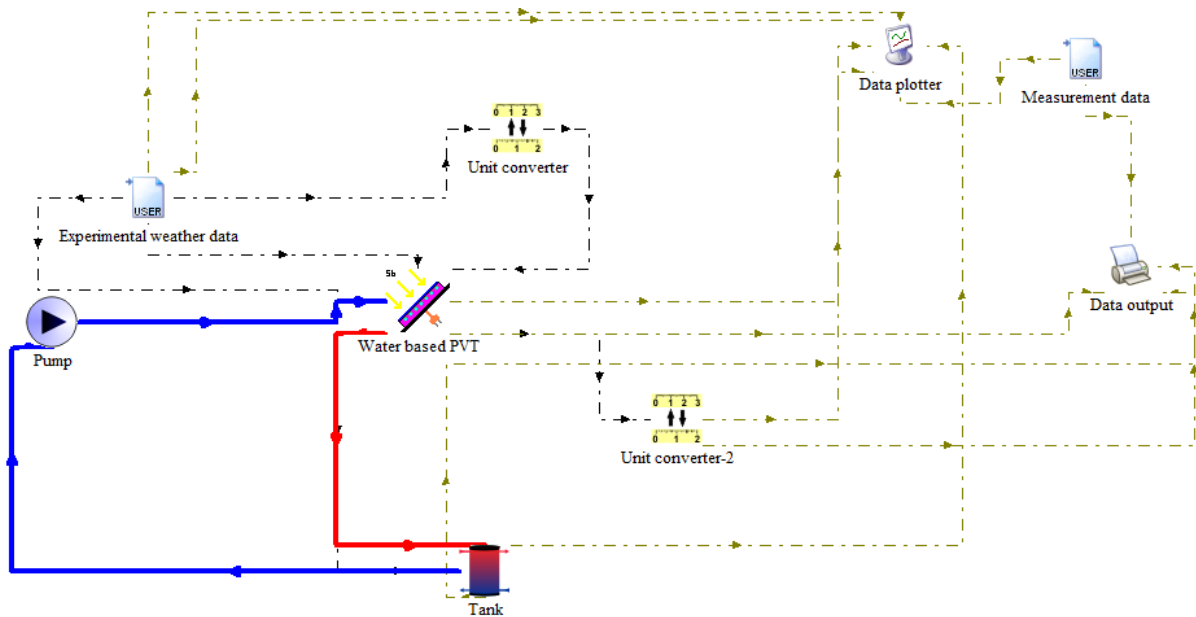


Figure 4-3: TRNSYS system sketch of the baseline model

4.1.1 PV/T Water Model

The PV/T water component is represented by a TYPE 563: Combined Solar PV/T Collector. The mathematical model is adapted from the Thermal Energy System Simulation Inc.(TESS) library and is based on equations from Duffie and Beckman [12]. TYPE 563 models an uncovered solar collector which generates power from embedded PV cells and simultaneously provides heat to a fluid stream flowing through tubes bonded to an absorber plate beneath the PV cells. Linear factors relate the PV cell efficiency and the cell temperature, as well as the incident solar radiation. The cells are assumed to operate under maximum power point conditions. TYPE 563 allows for connection to the TYPE 56 multizone building model. This way, the impact of the PV/T component on the buildings heating and cooling loads can be investigated

Figure 4-4 shows the cross section of the PV/T component with the flow direction in the tubes into to the page:

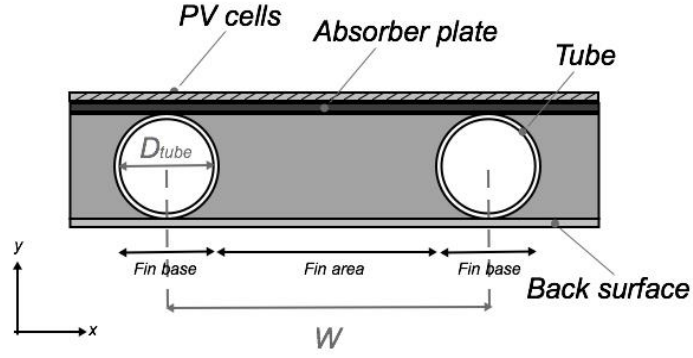


Figure 4-4: Water based PV/T component

PV/T Cover Energy Balance

The energy balance of the PV/T cover surface is expressed by the net rate of thermal energy absorbed by the component, $\dot{Q}_{absorbed, conv}$, the convective and radiative heat losses, $\dot{Q}_{loss, top, conv}$ and $\dot{Q}_{loss, top, rad}$, to the ambient and the sky, respectively, as well as conductive heat transfer, $\dot{Q}_{PV \rightarrow abs, cond}$, from the PV cells to the absorber plate.

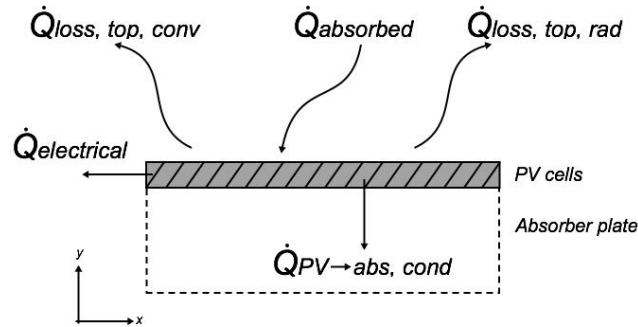


Figure 4-5: Cover energy balance of water based PV/T

The thermal energy balance of the cover is given as:

$$\dot{Q}_{absorbed} = \dot{Q}_{loss, top, conv} + \dot{Q}_{loss, top, rad} + \dot{Q}_{PV \rightarrow abs, cond} \quad (24)$$

where

$$\dot{Q}_{PV \rightarrow abs, cond} = A_c \frac{\bar{T}_{PV} - \bar{T}_{abs}}{R_{PV \rightarrow abs}} \quad (25)$$

where \bar{T}_{abs} and \bar{T}_{PV} is the mean surface temperature of the absorber plate and the PV cells, respectively. $R_{PV \rightarrow abs}$ is the resistance between the PV cells and the absorber plate.

The convective heat transfer from the top of the PV/T component to the ambient, $\dot{Q}_{loss, top, conv}$, is the cover heat loss described in subchapter 2.3.5.

$$\dot{Q}_{loss, top, conv} = h_{PV, conv} A_c (\bar{T}_{PV} - T_a) \quad (26)$$

where $h_{outer} = h_{PV, conv}$.

$\dot{Q}_{loss, top, rad}$ is defined according to subchapter 2.3.4, as the heat exchange between the sky and a body near the ground:

$$\dot{Q}_{loss, top, rad} = h_{PV, rad} A_c \Delta T = \varepsilon \sigma A_c (T_{PV}^4 - T_{sky}^4) \quad (27)$$

where $T_{body} = T_{PV}$ and the radiative heat transfer coefficient, $h_{PV, rad}$, is defined as:

$$h_{PV, rad} = \varepsilon \sigma (T_{PV} + T_{sky}) (T_{PV}^2 + T_{sky}^2) \quad (28)$$

The rate of thermal energy absorbed by the PV/T component is given as:

$$\dot{Q}_{absorbed} = A_c (\tau \alpha)_n IAM \cdot G_t (1 - \eta_{PV}) \quad (29)$$

where

IAM is the Incident Angle Modifier which is introduced to get the transmittance-absorptance at various incidence angles. η_{PV} is the PV cell efficiency defined as:

$$\eta_{PV} = \eta_{ref} \cdot X_{CellTemp} \cdot X_{Radiation} \quad (30)$$

where η_{ref} is the nominal cell efficiency and $X_{CellTemp}$ and $X_{Radiation}$ are the multipliers for the PV cell efficiency as a function of cell temperature and incident radiation, respectively.

The rate of electrical energy generated by the PV cells, $\dot{Q}_{electrical}$, is given by:

$$\dot{Q}_{electrical} = A_c (\tau \alpha)_n IAM \cdot G_T \eta_{PV} \quad (31)$$

Absorber Plate Energy Balance

Heat transfer will occur along both the x-axis and the y-axis of the absorber plate. In the sections between the tubes in the PV/T component, the absorber acts as a fin and heat is transferred straight to the PV/T back surface, not to the tubes. The base of the fin is located at $x = \frac{(W - D_{tube})}{2}$ when $x = 0$ is the midpoint between two adjacent tubes, W is the width between two tubes and D_{tube} is the tube diameter, as illustrated in Figure 4-6:

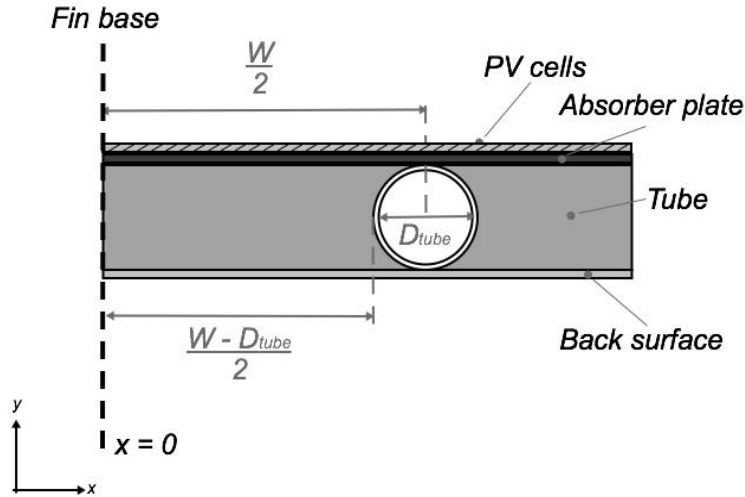


Figure 4-6: Fin effect in the water based PV/T

The energy balance in the fin area of the absorber is given by the conductive heat transfer from the PV cells to the absorber and from the absorber to the back surface along the y-axis. Along the x-axis, the heat is transferred through conduction along the absorber plate. Equation (32) expresses the energy balance in a given point in the fin area of the absorber plate:

$$k\lambda \frac{d^2 T_{abs}}{dx^2} = \frac{T_{abs} - T_{back}}{R_{back}} - \frac{T_{PV} - T_{abs}}{R_{PV \rightarrow abs}} \quad (32)$$

where the left side of eq.(32) is the conduction along the absorber plate, q'_{fin} . The conduction through a cross sectional area (in the yz-plane) of the absorber plate, $A_{cs,yz}$, is denoted as $\dot{Q}_{abs,cond}$. k is the thermal conductivity of the absorber plate material and λ is the plate thickness. T_{back} is the surface temperature at the back of the PV/T component. $R_{PV \rightarrow abs}$ and R_{back} are the thermal resistances from the PV cells to the absorber and from the absorber through the back of the component, respectively.

R_{back} is defined as:

$$R_{back} = R_{abs \rightarrow back} + \frac{1}{h_{inner}} \quad (33)$$

where $R_{abs \rightarrow back}$ is the thermal resistance of the material between the absorber plate and the back surface of the component. h_{inner} is the heat transfer coefficient from the back of the component to the air.

shows the heat transfer in the fin area of the absorber:

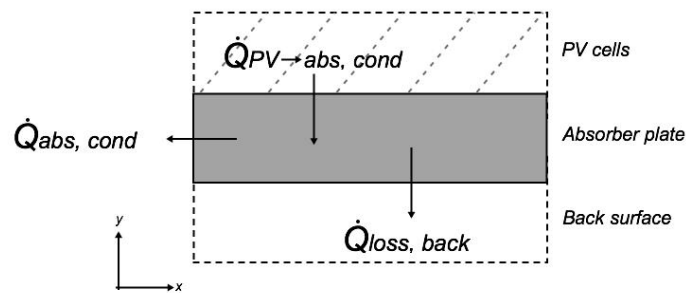


Figure 4-7: Energy balance in the fin area of the absorber

$\dot{Q}_{loss, back}$ is the rate of energy that is transferred to the back of the component, given by:

$$\dot{Q}_{loss, back} = A_c \frac{\bar{T}_{abs} - T_{back}}{R_{back}} \quad (34)$$

In the fin base area of the absorber plate there is an additional heat transfer between the absorber plate and the fluid running through the tube. The heat transfers are shown in :

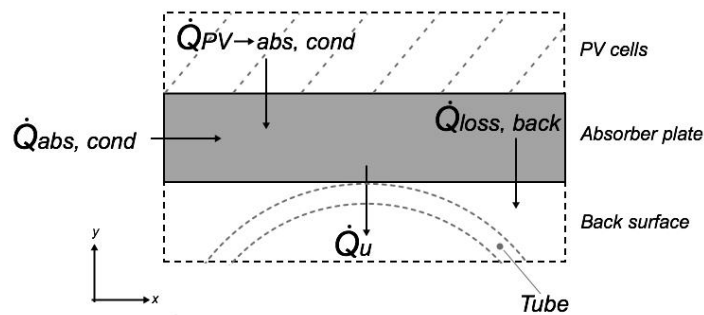


Figure 4-8: Energy balance of the fin base of the absorber

The energy balance for the fin base is given in eq.(35):

$$\dot{q}'_{fluid} = D_{tube} \left(\frac{T_{PV} - T_{base}}{R_{PV \rightarrow abs}} \right) - D_{tube} \left(\frac{T_{base} - T_{back}}{R_{back}} \right) + 2\dot{q}'_{fin} \quad (35)$$

The conductive heat transfer to the fluid, \dot{Q}_u , is the useful heat gain from the PV/T component defined as:

$$\dot{Q}_u = \dot{m}C_p (T_{fluid,out} - T_{fluid,in}) \quad (36)$$

Overall Energy Balance

From eq.(36), $T_{fluid,out}$ is obtained from the following equation for the useful energy gain as a function of the fluid temperature:

$$\dot{q}'_{fluid} = \frac{\kappa}{\theta} T_{fluid} + \frac{\varepsilon}{\theta} \quad (37)$$

The model parameters κ , θ and ε are defined in Appendix A.

An energy balance for a differential section of the fluid moving along the z-direction (into the page) in the tube is expressed as:

$$\dot{m}C_p \frac{dT_{fluid}}{dz} - N_{tubes} \dot{q}'_{fluid} = 0 \quad (38)$$

Equation (37) is inserted into eq.(38) :

$$\frac{dT_{fluid}}{dz} = \frac{N_{tubes}}{\dot{m}C_p} \cdot \frac{\kappa}{\theta} T_{fluid} + \frac{N_{tubes}}{\dot{m}C_p} \cdot \frac{\varepsilon}{\theta} \quad (39)$$

Equation (39) is then integrated from zero to z equal to the length of the tube, L , and solved for the outlet fluid temperature which in turn is used in eq.(36) to determine the useful energy gain from the component, \dot{Q}_u .

Subsequently, the mean fluid temperature can be found through eq.(40):

$$\bar{T}_{fluid} = \frac{1}{L} \int_0^L T_{fluid}(z) dz \quad (40)$$

and the mean fin temperature is found by integrating the fin temperature, T_{fin} , over the width of the fin:

$$\bar{T}_{fin} = \int_0^{\frac{W-D_{tube}}{2}} T_{fin}(x) dx \quad (41)$$

The mean absorber plate temperature is then obtained by area weighting the mean fin base temperature and the mean fin temperature according to eq.(42):

$$\bar{T}_{abs} = \frac{D_{tube}\bar{T}_{base} + (W - D_{tube})\bar{T}_{fin}}{W} \quad (42)$$

Lastly the mean surface temperature of the PV must be found through iteration as $\dot{Q}_{PV \rightarrow abs, cond}$, $\dot{Q}_{loss, top, conv}$ and $\dot{Q}_{loss, top, rad}$ are all dependent on the PV temperature.

The total energy balance around the component is then given as:

$$\dot{Q}_{absorbed} + \dot{Q}_{electrical} = \dot{Q}_{loss, top, conv} + \dot{Q}_{loss, top, rad} + \dot{Q}_u + \dot{Q}_{loss, back} \quad (43)$$

4.1.2 PV/T Air Model

The PV/T air component is represented by a TYPE 568: Un-Glazed Building-Integrated PV System. The mathematical model is adapted from the TESS library and is based on equations from Duffie and Beckman [12]. TYPE 568 models a solar collector which provides cogeneration of power and heat. The power is produced with PV cells and the waste heat from the component is collected with a passing air stream below the PV surface. The model allows for a building zone model to be integrated, which can provide the temperature of the back surface of the component when the mean temperature of the lower air channel surface is given. The temperature nodes of the component can be seen from Figure 4-9.

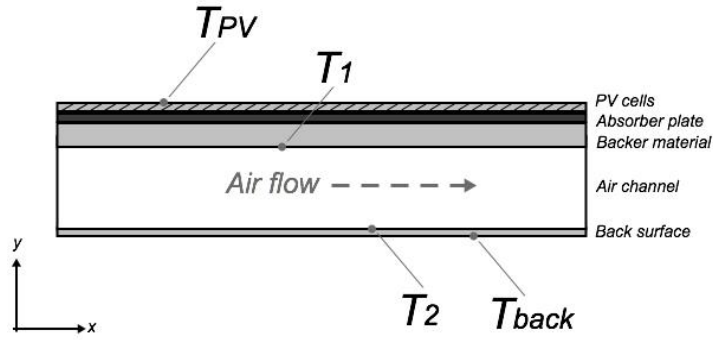


Figure 4-9: System sketch showing the temperature nodes of the air based PV/T

PV/T Cover Energy Balance

The first energy balance describes the PV/T top surface and is expressed by the convective and radiative heat losses to the ambient and the sky, $\dot{Q}_{loss, top, conv}$ and $\dot{Q}_{loss, top, rad}$ respectively, as well as the heat loss due to conduction $\dot{Q}_{PV \rightarrow 1, cond}$ from the PV cells to the upper surface of the air channel as seen in Figure 4-10:

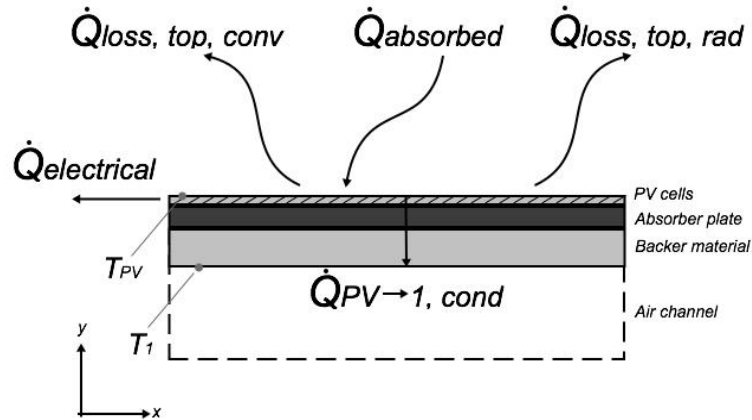


Figure 4-10: Cover energy balance of air based PV/T

The thermal energy balance of the top surface of the component is given as:

$$\dot{Q}_{absorbed} = \dot{Q}_{loss, top, conv} + \dot{Q}_{loss, top, rad} + \dot{Q}_{PV \rightarrow 1, cond} \quad (44)$$

where $\dot{Q}_{PV \rightarrow 1, cond}$ is expressed by:

$$\dot{Q}_{PV \rightarrow 1, cond} = A_c \frac{\bar{T}_{PV} - \bar{T}_1}{R_{PV \rightarrow 1}} \quad (45)$$

where $R_{PV \rightarrow I}$ is the substrate resistance, \bar{T}_{PV} and \bar{T}_I are the mean surface temperatures of the PV cells and the upper surface of the air channel respectively.

$\dot{Q}_{absorbed}$ can also be expressed with the following equation:

$$\dot{Q}_{absorbed} = \alpha_{PV} G_T A_c (1 - \eta_{PV}) \quad (46)$$

where α_{PV} is the absorptance of the PV surface with values ranging between 0 and 1. There are several methods of calculating the PV efficiency η_{PV} . In the first mode, a linear relation modifier is given and the PV efficiency is calculated using a multiplier for the PV cell efficiency $X_{CellTemp}$ which is a function of the cell temperature as seen in eq.(47). The equation also includes a second multiplier $X_{Radiation}$ which is based on the incident radiation on the PV/T component, η_{ref} is the PV efficiency at reference conditions.

$$\eta_{PV} = \eta_{ref} \cdot X_{CellTemp} \cdot X_{Radiation} \quad (47)$$

In the second mode of TYPE 568 it is possible to provide a data file with PV efficiency values based on the cell temperature and the solar radiation. The PV efficiency is provided as an input to the TYPE 568 model in mode 3, giving the possibility of calculating the PV efficiency based on any number of variables.

The power produced by the PV/T air model can be expressed as:

$$\dot{Q}_{electrical} = A_c \alpha_{PV} G_T \eta_{PV} \quad (48)$$

Upper Duct Energy Balance

The second energy balance describes the upper surface of the air channel as illustrated in Figure 4-11:

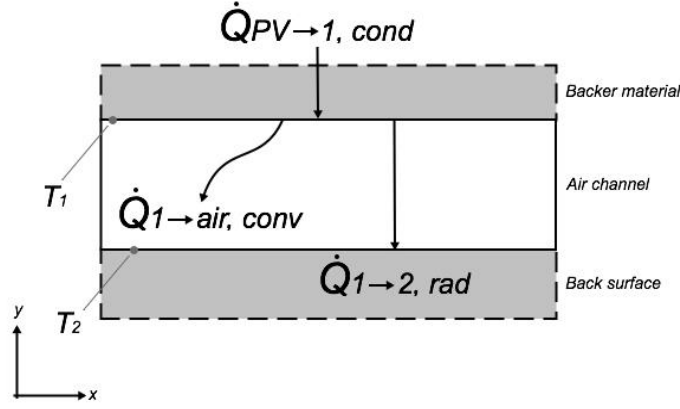


Figure 4-11: Energy balance at the upper surface of the air channel

The energy balance gives the following equation:

$$\dot{Q}_{PV \rightarrow 1, cond} = \dot{Q}_{1 \rightarrow air, conv} - \dot{Q}_{1 \rightarrow 2, rad} \quad (49)$$

where $\dot{Q}_{1 \rightarrow air, conv}$ is the convective heat transfer from the upper surface of the air channel to the air flowing through the component and $\dot{Q}_{1 \rightarrow 2, rad}$ is the radiative heat transfer between the upper and the lower surfaces of the air channel, as seen in eq.(50) and eq.(51) respectively:

$$\dot{Q}_{1 \rightarrow air, conv} = h_{air} A_c (\bar{T}_1 - T_{air}) \quad (50)$$

where $h_{air} = \frac{Nu \cdot k_{air}}{D_h}$ is the heat transfer coefficient from the air flow to the surface of the air channel, Nu is the Nusselt number, k_{air} is the thermal conductivity of the air and D_h is the hydraulic diameter of the air channel. Furthermore, the radiative heat transfer term in the upper surface of the air channel is given by:

$$\dot{Q}_{1 \rightarrow 2, rad} = h_{1 \rightarrow 2, rad} A_c (\bar{T}_1 - \bar{T}_2) \quad (51)$$

Where \bar{T}_2 is the surface temperature of the lower part of the air channel and $h_{1 \rightarrow 2, rad}$ is given in eq.(52) as:

$$h_{1 \rightarrow 2, rad} = \frac{\sigma (T_1^2 + T_2^2) (T_1 + T_2)}{\frac{1}{\varepsilon_1} + \frac{1}{\varepsilon_2} - 1} \quad (52)$$

where ε_1 and ε_2 are the surface emissivities of the upper and lower part of the air channel respectively.

Air Stream Energy Balance

The third energy balance describes the heat exchange between the passing stream of air and the upper and lower air channel surfaces. \dot{Q}_u is the net rate of energy added to the air stream from the component and is given as:

$$\dot{Q}_u = h_{air,conv} A_c (\bar{T}_1 - T_{air}) - h_{air,conv} A_c (T_{air} - \bar{T}_2) \quad (53)$$

Lower Duct Energy Balance

The fourth energy balance describes the heat exchanges from the lower air channel surface to the stream of air by convection, $\dot{Q}_{air \rightarrow 2, conv}$, the radiative heat exchange to the upper air channel surface, $\dot{Q}_{1 \rightarrow 2, rad}$, and the heat exchange through conduction to the back surface of the component, $\dot{Q}_{2 \rightarrow back, cond}$, shown in Figure 4-12:

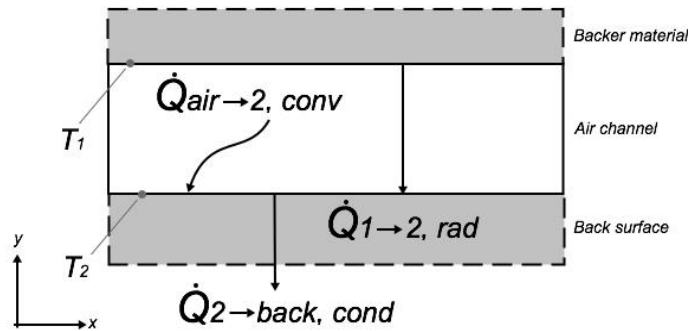


Figure 4-12: Energy balance at the lower surface of the air channel

The energy balance at the lower air channel surface is given as:

$$\dot{Q}_{air \rightarrow 2, conv} + \dot{Q}_{1 \rightarrow 2, rad} = \dot{Q}_{2 \rightarrow back, cond} \quad (54)$$

where $\dot{Q}_{air \rightarrow 2, conv}$ and $\dot{Q}_{2 \rightarrow back, cond}$ are expressed in eq.(55) and eq.(56) respectively:

$$\dot{Q}_{air \rightarrow 2, conv} = h_{air} A_c (T_{air} - \bar{T}_2) \quad (55)$$

$$\dot{Q}_{2 \rightarrow back, cond} = A_c \frac{\bar{T}_2 - T_{back}}{R_{2 \rightarrow back}} \quad (56)$$

where $R_{2 \rightarrow back}$ is the thermal resistance from the lower air channel surface to the back of the component.

Overall Energy Balance

The four energy balances are used in order to express the useful energy gain \dot{q}_u'' across a differential section of the air channel dx , as a function of the air temperature T_{air} illustrated in Figure 4-13 and given in eq.(57):

$$\dot{q}_u'' = aT_{air} + b \quad (57)$$

where the parameters a and b are further described in Appendix A.

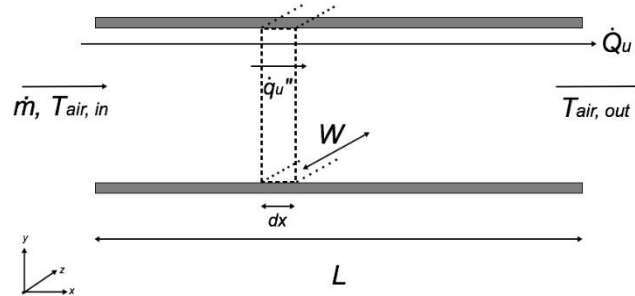


Figure 4-13: Differential balance of the air flow

Using an energy balance for a differential section of the air flowing through the component in the x direction, the following relation is given:

$$\dot{m}C_p \frac{dT_{air}}{dx} - W\dot{q}_u'' = 0 \quad (58)$$

where W is the width of the component.

Inserting eq.(57) into eq.(58) the following relation is given:

$$\frac{dT_{air}}{dx} = \left(\frac{W}{\dot{m}C_p} \right) aT_{air} + \left(\frac{W}{\dot{m}C_p} \right) b \quad (59)$$

The model assumes that a and b are constant in the component along the x direction and therefore an integration of eq.(59) can be performed to find the local air temperature:

$$T_{air}(x) = \left(T_{air,in} + \frac{b}{a} \right) \exp\left(\frac{W}{\dot{m}C_p} a \cdot x \right) - \frac{b}{a} \quad (60)$$

by setting x equal to the length, L , of the component along the flow direction, the outlet air temperature of the PV/T air component can be found as:

$$T_{air,out} = \left(T_{air,in} + \frac{b}{a} \right) \exp\left(-\frac{A_c \cdot a}{\dot{m}C_p} \right) - \frac{b}{a} \quad (61)$$

where the component area $A_c = WL$.

The mean air temperature along the x direction can be found by integrating the fluid temperatures along the flow length of the component and dividing it by the flow length:

$$\bar{T}_{air} = \frac{1}{L} \int_0^L T_{air}(x) dx \quad (62)$$

The PV/T air components' total useful energy gain which is the sum of the differential sections along the x direction can now be expressed by inserting the calculated $T_{air,out}$ from eq.(61) into eq.(63).

$$\dot{Q}_u = \dot{m}C_p (T_{air,out} - T_{air,in}) \quad (63)$$

The four energy balances are then used to find the mean surface temperature of each node inside the component. The equation for the mean upper air channel surface temperature, \bar{T}_1 , is given as:

$$\bar{T}_1 = \frac{S}{m \cdot F'} + \frac{h_{PV,conv} T_a}{m \cdot F'} + \frac{h_{PV,rad} T_{sky}}{m \cdot F'} + \frac{h_{air,conv} \bar{T}_{air}}{m} + \frac{h_{1 \rightarrow 2,rad} h_{air} \bar{T}_{air}}{m \cdot j} + \frac{h_{1 \rightarrow 2,rad} T_{back}}{m \cdot j \cdot R_{2 \rightarrow back}} \quad (64)$$

The same four equations can then be used to find the equation for the mean lower air channel surface temperature, \bar{T}_2 .

$$\bar{T}_2 = \frac{h_{1 \rightarrow 2,rad} \bar{T}_1}{j} + \frac{h_{air,conv} \bar{T}_{air}}{j} + \frac{T_{back}}{j R_{2 \rightarrow back}} \quad (65)$$

Subsequently, the same procedure is used to find the equation for the mean surface temperature of the PV, \bar{T}_{PV} .

$$\bar{T}_{PV} = \frac{R_{PV \rightarrow 1} S}{F'} + \frac{R_{PV \rightarrow 1} h_{PV, conv} T_a}{F'} + \frac{R_{PV \rightarrow 1} h_{PV, rad} T_{sky}}{F'} + \frac{\bar{T}_1}{F'} \quad (66)$$

The solution for these sets of equations are acquired through an iterative process as $\dot{Q}_{absorbed}$, h_{rad} and h_{air} are dependent on the mean temperature of the PV and air channel surfaces. By iteration the relevant heat exchanges can be calculated and the energy balance around the component is given as:

$$Q_{absorbed} + Q_{electrical} = Q_{loss, top, conv} + Q_{loss, top, rad} + Q_u + Q_{loss, back} \quad (67)$$

4.1.3 Radiative Heat Transfer

Sky Temperature

The PV/T component is affected by radiative heat loss to the sky as the upper atmosphere is colder than the surface temperature of the component. Different methods exist in order to include the longwave heat exchange between the PV/T component and the sky. A simplified method, which does not include the dew point temperature is given by Fuentes [63]:

$$T_{sky} = 0.037536T_a^{1.5} + 0.32T_a \quad (68)$$

The methods of Berdahl and Martin [64] in combination with Kasten and Czeplak [65] was implemented for cloudy sky conditions with TYPE 69a.

TYPE 69a is implemented and calculates a variable sky temperature in TRNSYS using input from two TYPE 9 free format readers for dew point temperatures and cloudiness factors. The TRNSYS type calculates the effective emissivity of the sky for clear sky conditions, and takes into account the dew point temperature of the air and gives [64]:

$$\varepsilon_{sky, clear} = 0.711 + 0.56 \left(\frac{T_{dp}}{100} \right) + 0.73 \left(\frac{T_{dp}}{100} \right)^2 + 0.013 \cos \left[2\pi \frac{t}{24} \right] \quad (69)$$

where T_{dp} is the dew point temperature and t is the solar time. The equation has a useful predictability over the range from -20 to 30°C dew point temperature. A correction factor is also commonly used and given as:

$$\Delta\varepsilon = 0.00012(P - 1000) \quad (70)$$

where P is the measured pressure in millibars. The elevation of the GEL is 6 metres based on information from google earth and therefore the pressure difference due to elevation is negligible in this simulation.

In order to calculate T_{sky} the following equation is used:

$$T_{sky} = \varepsilon_{sky,clear}^{\frac{1}{4}} T_a \quad (71)$$

Cloudy sky conditions require a different approach in calculating the sky temperature. ISO 6946 describes a method where the ambient temperature is used as the sky temperature, but this method is only valid for complete cloud coverage [63]. TRNSYS uses another method where a cloudiness factor is described by Kasten and Czeplak as [65]:

$$C_{cover} = \left(1.4286 \frac{G_{d,hor}}{G_{tot,hor}} - 0.3 \right)^{0.5} \quad (72)$$

where $G_{d,hor}$ is the diffuse horizontal irradiance and $G_{tot,hor}$ is the total horizontal irradiance.

The cloudiness factor described by Kasten and Czeplak is valid for places with similar climatic conditions as Hamburg as this method is based on density and occurrence of various cloud types. It is possible that the cloud conditions of Shanghai are different than that of Hamburg and therefore may give a different value than the actual sky temperature and should be taken into consideration when validating the PV/T component.

The cloudiness factor during measurements was set to 0. This value is estimated as the measurements were conducted on a cloudless day. Therefore, the method of Kasten and Czeplak is not applied in this preliminary PV/T component validation but will be implemented in the GEL model as the simulation period will extend over a longer period with varying cloud cover.

In order to calculate the effect of cloud cover, the effective sky emissivity is given as:

$$\varepsilon_{sky} = \varepsilon_{sky,clear} + 0.8 \cdot (1 - \varepsilon_{sky,clear}) \cdot C_{cover} \quad (73)$$

In Figure 4-14 the methods described above and implemented in TYPE 69a are compared with the default value of TRNSYS at 10°C, in addition to a simplified method of calculating T_{sky} by Fuentes.

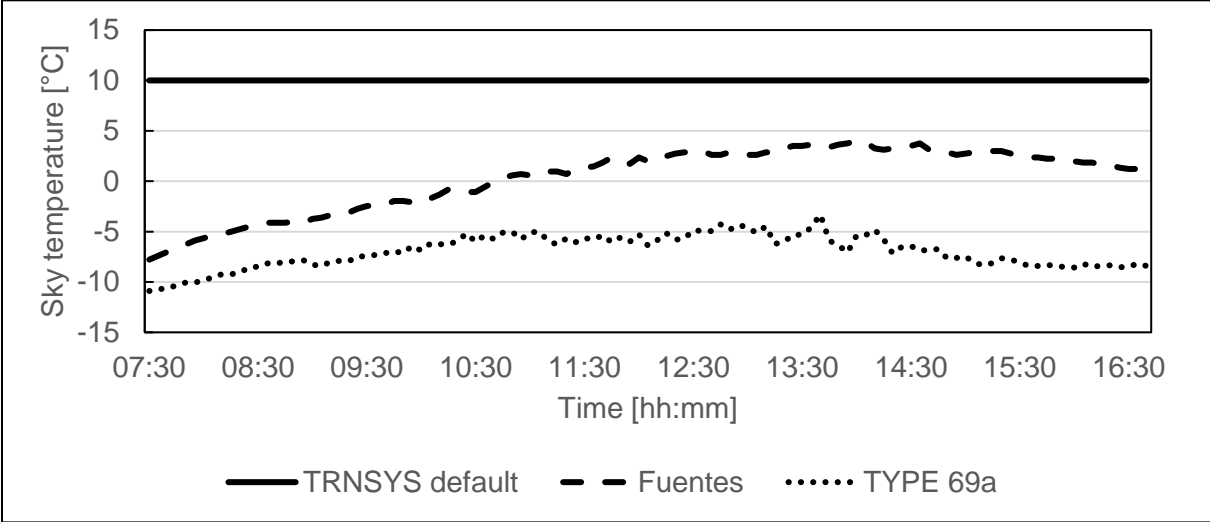


Figure 4-14: Sky temperatures calculated by various methods

The calculations of sky temperatures show from 15 to 20°C difference between the methods described in TYPE 69a compared to the TRNSYS default value. Also, the detailed method in TYPE 69a shows a sky temperature around 5 to 15°C lower than the method developed by Fuentes. Thus, the detailed method of calculating the variable sky temperature using TYPE 69a gives a significantly lower value than both the default value of TRNSYS and Fuentes.

4.1.4 Convective Heat Transfer

Wind Induced Convective Heat Transfer Coefficient

In order to make accurate estimations of the wind induced convective heat transfer coefficient, it is necessary to measure the wind velocity at the location of the PV/T component. Wind data from the test site was collected on December 7th, 2016. The wind velocity was measured on the roof of the GEL building, located approximately 9.9 meters above ground level where the PV/T test rig was installed. The recorded instant wind velocity is shown in Figure 4-15:

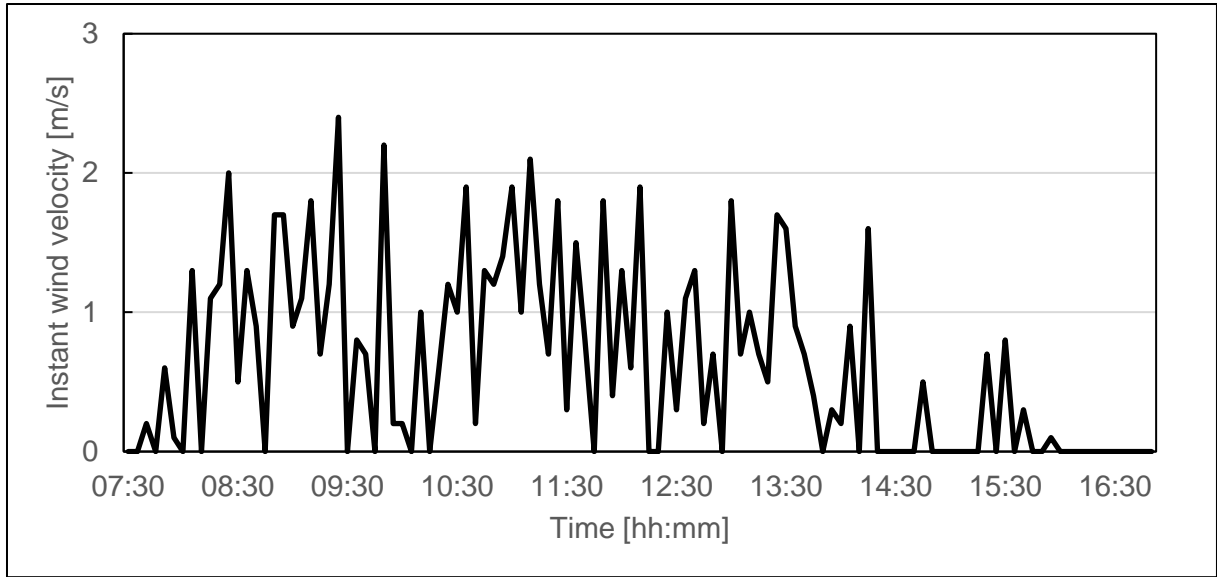


Figure 4-15: Instant wind velocity at the GEL.

The maximum wind velocity occurs around 9:30 with a magnitude of 2.4 m/s.

The convective heat transfer coefficient, h_{wind} , is generally expressed as a linear function of the external wind velocity, v_{wind} :

$$h_{wind} = a \cdot v_{wind} + b \quad (74)$$

where h_{wind} affects the total energy balance of the PV/T component, as an input value of $Q_{loss,top,conv}$:

$$Q_{loss,top,conv} = h_{wind} A_c (T_{pv} - T_a) \quad (75)$$

Watmuff et al. [66] suggests the following relation to account for the external winds' influence on the convective heat transfer coefficient for a solar collector:

$$h_{wind} = 3.0v_{wind} + 2.8 \quad (76)$$

This relation is frequently quoted by other authors investigating wind effects on the convective heat transfer coefficient [30, 67, 68]. Also, Aste et al. used this approach when analysing the wind effects on the convective heat transfer coefficient of an uncovered, flat plate PV/T component, as is the case in this thesis [69].

Watmuff et al. suggests that their relation is more accurate compared to previous quoted works [70, 71], that overestimate the convective heat transfer coefficient by including a radiative term. Thus, the collector is double accounting for radiative heat transfer. [66]

Several approaches for determining the wind effect on the convective heat transfer coefficient have been analysed and plotted in Figure 4-16. All the authors follow the linear structure of eq.(74). The approach of Watmuff et al. is believed to be more detailed than the other methods as it excludes the radiative term from the convective heat transfer coefficient.

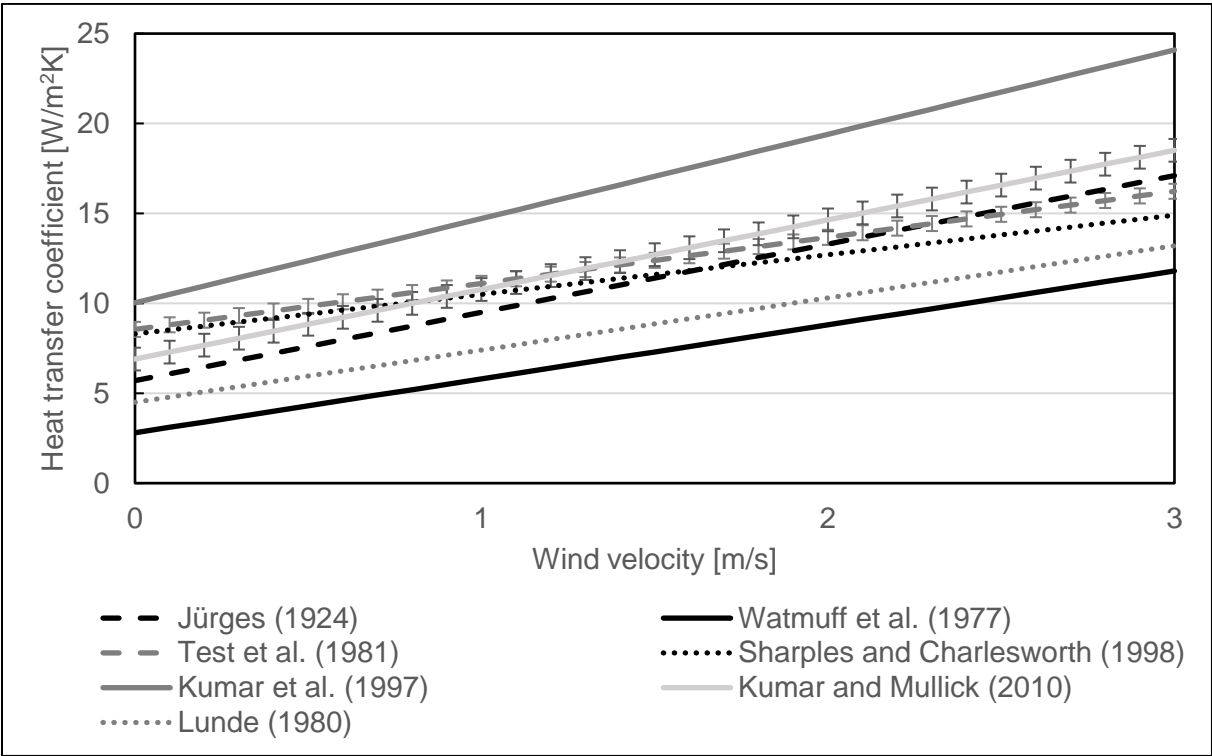


Figure 4-16: Convective heat transfer coefficients as a function of wind speed by various authors

To determine the most realistic approach, three TRNSYS simulations were carried out and compared. The approaches of Kumar et al. [72], Jürges [70] and Watmuff et al. were chosen for further investigation as these represent the entire span of heat transfer coefficient values as shown in Figure 4-16. The result for the simulations are shown in subchapter 4.3.2.

4.1.5 Weather File

When developing a mathematical model for a specific component, like the one at GEL, correct data is crucial for the model verification. As the PV/T experiment was conducted on site at SJTU Minhang Campus, data provided by sensors on the roof of GEL were

implemented in the TRNSYS model to recreate the actual conditions of the on-site experiment. The measured weather data set was implemented to the TRNSYS model using a TYPE 9 free format data reader.

4.1.6 Pump

The measurements of the water based PV/T component were conducted using a TYPE 3 pump with a constant flow rate of 100 l/h. The mass flowrate, \dot{m} , in the pump is given as:

$$\dot{m} = \gamma \dot{m}_{max} \quad (77)$$

where γ is a control function with values of $0 \leq \gamma \leq 1$ and \dot{m}_{max} is the maximum flow rate.

A linear relationship between the flow rate and power consumption is assumed in TYPE 3 by the common control function, γ . Given the known parameters, the power consumption, P , is given by:

$$P = \gamma P_{max} \quad (78)$$

P_{max} is the maximum power consumption.

The pump used in the experiment has the possibility of operating at three different capacities. For this experiment, the pump is considered a constant speed pump operating at 46 W. The control function for a constant speed pump is 1 when the pump is on and 0 when it is off. This means that the outlet flow rate and the power used by the pump is either at zero or at maximum as seen from eq.(77) and eq.(78).

As the pump will lose some heat to the water, the TYPE 3 pump accounts for the temperature increase by introducing f_{par} , the fraction of pump power converted into thermal heat. This value was set to 0.05 by default. The outlet temperature, T_o , of the pump is given as:

$$T_{out} = T_{in} + \frac{P f_{par}}{\dot{m} C_p} \quad (79)$$

where T_{in} is the inlet temperature of the fluid flowing into the pump and P is the power consumption of the pump. Simulations showed that the temperature increase in the pump was negligible.

4.1.7 Storage Tank

The tank used in combination with the PV/T models is a TYPE 4: Stratified fluid storage tank. The amount of stratification in the tank is decided by the number of nodes, N , specified for the tank as seen from Figure 4-17. The value of N ranges between 1 and 15, where N equal to 1 gives a uniform tank temperature. The model includes the possibility of auxiliary power inside the tank controlled by a dead band. Auxiliary power is not utilised until the GEL models are presented, where it is modelled outside of the tank in order to maintain cooler temperatures inside the tank. The mode chosen provides the possibility of changing the heights of the inlets to the tank.

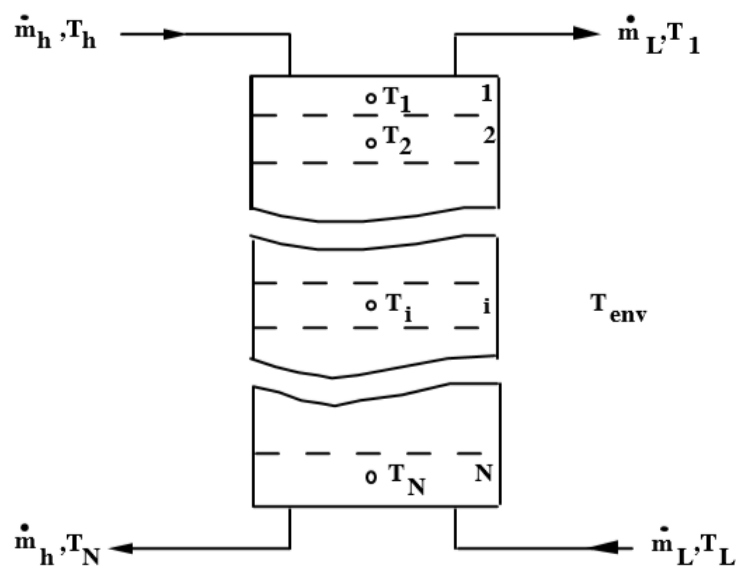


Figure 4-17: Stratified storage tank (TYPE 4)

4.2 Validation of the TRNSYS PV/T Component

In order to perform proper analyses of any simulation results, the simulation data has to closely match the measured data of the system. If the simulation result does not accurately match the data, wrong conclusions may be drawn. The validation metrics chosen to be simulated are:

- Outlet temperature of the PV/T component
- Electrical power output of the PV/T component

Eliminating the number of variables is the key to efficiently analyse the behaviour of the TRNSYS PV/T model. The outlet temperature and power output of the PV/T component were

chosen as the validation metrics to assess both the thermal and electrical performance of the TRNSYS model.

Validation of the TRNSYS model is performed according to several indices such as the Root Mean Square Error (RMSE), the Coefficient of Variation of RMSE (CV(RMSE)), the Mean Bias Error (MBE), the Normalised MBE (NMBE) and the determination coefficient (R^2).

RMSE is defined in eq.(80): [73]

$$RMSE = \sqrt{\frac{\sum_{t=1}^n Residual_t^2}{n-2}} \quad (80)$$

where

$$Residual = \hat{y}_t - y_t \quad (81)$$

Residual is the difference between the simulated data, \hat{y}_t , and the measured data, y_t , and n is the total number of data points. The RMSE is used to calculate the overall magnitude of the errors, but does not provide any information about the bias of the errors, i.e. whether the deviation is a positive or a negative value. It is desired to achieve a small value of RMSE as this indicates a low magnitude of error [73].

The CV(RMSE) can be applied by normalizing the RMSE by the average of the measured data and is given as [74]:

$$CV(RMSE) = \frac{\sqrt{\frac{\sum_{t=1}^n Residual_t^2}{n}}}{\frac{1}{n} \sum_{t=1}^n y_t} \times 100\% \quad (82)$$

To determine the bias of the error, another index is used. The MBE is defined as:

$$MBE = \frac{\sum_{t=1}^n Residual_t}{n} \quad (83)$$

In this index, the positive and negative error cancel each other out, giving an indication of the overall error bias. The calculation of MBE is commonly calculated if the model is used as the baseline for evaluating the performance of the PV/T component after changes in input data are implemented. [73]

The NMBE is the MBE normalized to the average of the measured data and gives a percentage value defined as [74]:

$$NMBE = \frac{\sum_{t=1}^n Residual_t}{\frac{1}{n} \sum_{t=1}^n y_t} \quad (84)$$

R^2 is often used in order to assess the success of a regression equation explaining the variation of the sampled data. If the equation fits the sampled data perfectly, R^2 is equal to 1. R^2 is defined as:

$$R^2 = \frac{\sum_{t=1}^n Residual_t^2}{\sum_{t=1}^n (y_t - \bar{y})^2} \quad (85)$$

In this thesis, if the value of R^2 is considered satisfying the regression equation is used in order to show a trend line of the sampled data. Subsequently the trend line can substitute the sampled data in further analyses. [69, 75]

4.3 Calibration of the TRNSYS PV/T Component

In the calibration process, one parameter of a baseline model is changed at a time in the desired direction in order to fit the measured data in both shape and magnitude. This is an iterative process which is performed until a close match is achieved with an error that is acceptable for the user. The baseline model should be calibrated to achieve a more realistic representation of the actual PV/T component.

4.3.1 Baseline Model

The validation metrics of the baseline model and the measured data are plotted in Figure 4-18 and Figure 4-19:

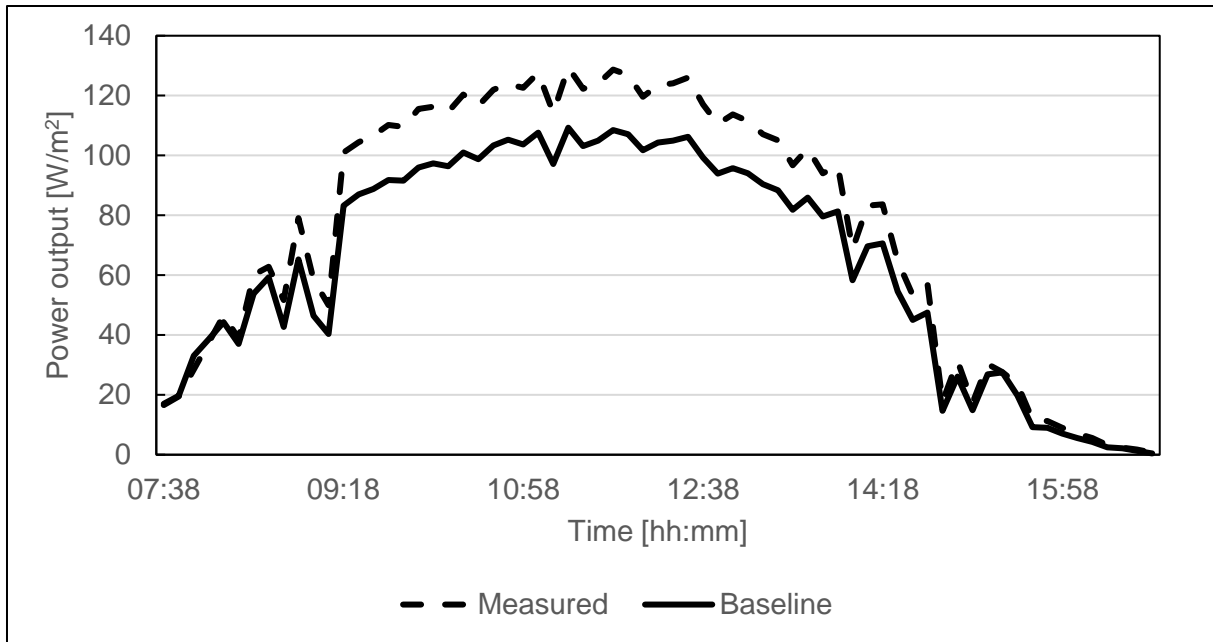


Figure 4-18: Power output of the measured data and the baseline model

The power output of the baseline model is very close to that of the measurements in the start and in the end of the experiments. The measured power output is higher than the model from around 09:00 to 14:30. The maximum peak power output of the measured data and the baseline model are 138 W/m² and 116 W/m² respectively.

The PV/T outlet temperature of the baseline model and the measured data are compared in Figure 4-19. The temperature of the baseline model is higher than the measured from the start of the measurements until around 11:00. Then the lines cross and the measured temperature stays between 2-4°C higher than the temperature simulated in the baseline model until the end of the measuring period. The peak PV/T outlet temperatures of the measured data and the baseline model are 26.1°C and 23.6°C respectively.

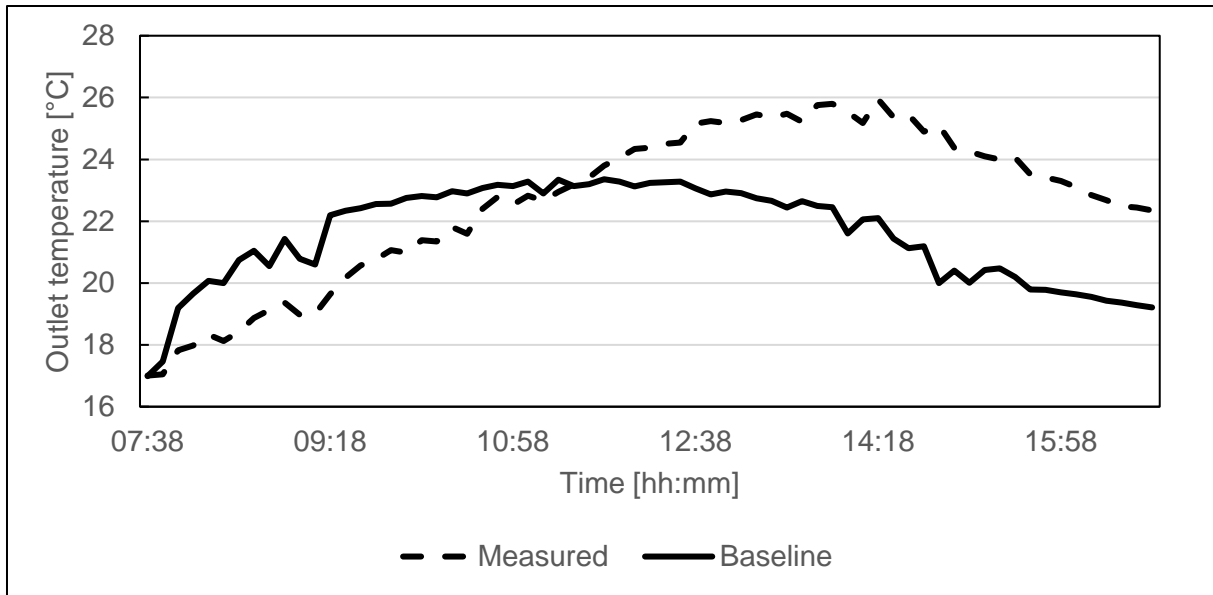


Figure 4-19: PV/T outlet temperatures of the measured data and the baseline model

In order to efficiently calibrate a model, a calibration signature is introduced and given by:

$$Calibration\ signature = \frac{-Residual}{Maximum\ measured\ energy} \times 100\% \quad (86)$$

A calibration signature for the baseline model is displayed in Figure 4-20. It shows the percentage deviation of the baseline model compared to the measured data of the PV/T component. A positive value of the calibration signatures indicates that the validation metrics of the baseline model are lower than that of the measured data.

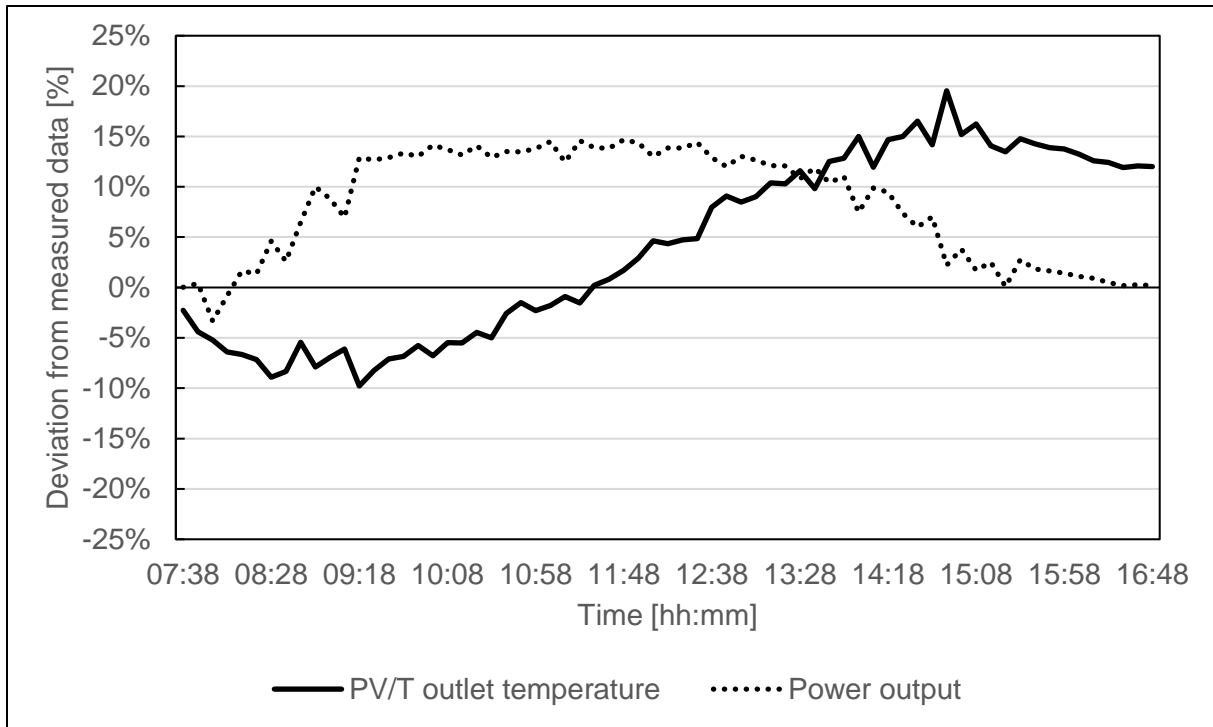


Figure 4-20: Calibration signatures of the baseline model

The maximum deviations from the measured data are approximately 15% and 20% for the power output and the outlet temperature, respectively. Besides from a small dip in the curve in the very beginning, the power output is constantly higher than the measured values, meaning that the baseline model provides lower power output than that of the experiment, which coincides with the trend seen in Figure 4-18.

To address the accuracy of the baseline model and how well it represents the actual PV/T component, the CV(RMSE) and the MBE are calculated and presented in Table 6:

Table 6: CV(RMSE) and MBE of the two validation metrics for the baseline model.

<i>Validation metric</i>	<i>CV(RMSE)</i>	<i>MBE</i>
PV/T outlet temperature	11.34%	-1.03
Power output	18.33%	-11.00

According to *Building Performance Simulation for Design and Operation* [73], a good simulation will minimize the CV(RMSE) and values below 10% are hard to achieve. The CV(RMSE) values for the outlet temperature and power output of 11.34% and 18.33%

indicate that the model is a fairly good representation of the actual component. The negative MBEs of -1.03 and -11.00 indicate that the validation metrics of the baseline model are generally lower than the measured data. The power output of the baseline model is on average 11.00 W lower than the measured values. As seen in Figure 4-19, the PV/T outlet temperature of the baseline model contains both positive and negative deviations and thus the average deviation is 1.03°C.

4.3.2 Calibration Measures

The baseline model described in the previous chapter is a preliminary approximation to the actual PV/T component. Thus, detailed analysis should be conducted to account for more complex physical phenomena, such as the sky temperature and the wind induced convective heat transfer coefficient.

Characteristic signatures are used in order to determine if the change in a simulation input increases or decreases the error compared to a baseline model. They are similar to the calibration signatures except that the measured data are substituted by the data from the baseline model. The characteristic signature is defined as:

$$\text{Characteristic signature} = \frac{\text{Change in energy consumption}}{\text{Maximum energy consumption}} \cdot 100\% \quad (87)$$

The characteristic signature for the sky temperature, T_{sky} , according to the method of Berdahl and Martin was plotted to see its impact on the validation metrics of the PV/T component. The characteristic signatures for PV/T outlet temperature and power output are presented in Figure 4-21:

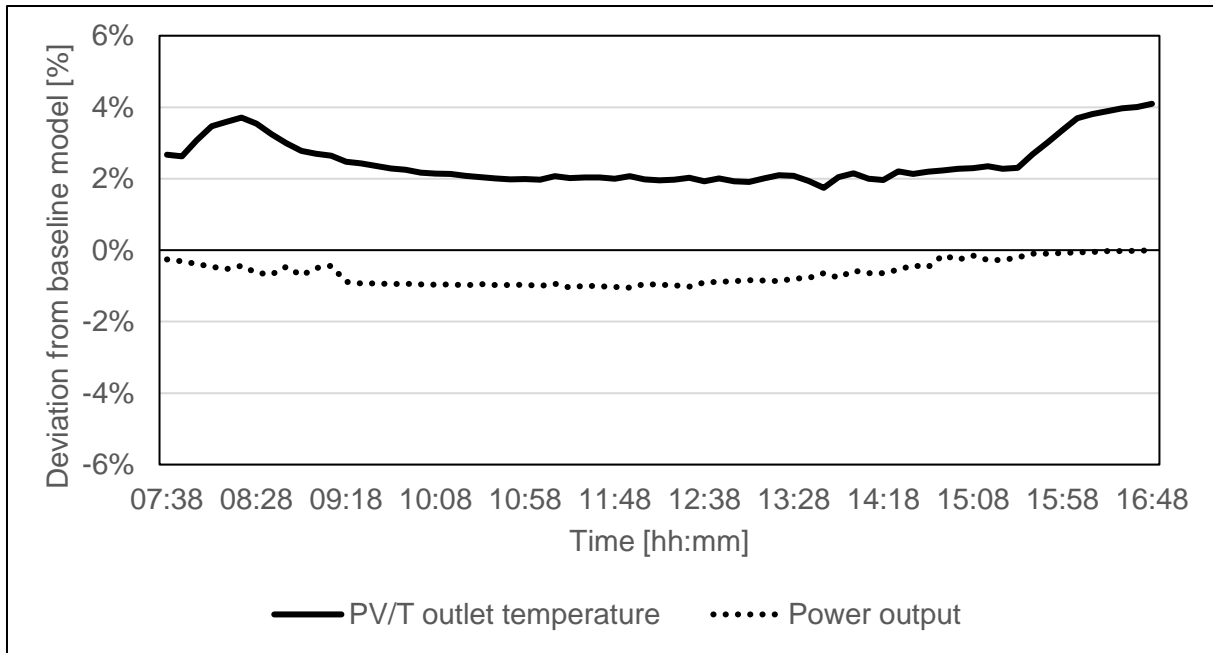


Figure 4-21: Characteristic signatures of PV/T validation metrics when implementing sky temperature by the method of Berdahl and Martin

For the PV/T outlet temperature, the implementation of the sky temperature introduces a deviation compared to the baseline model, where the sky temperature is set constant. For the most part the deviation is 2%, but higher values up to 4% occur in the beginning and in the end of the simulations. The PV/T power output deviates by 1% in the beginning before rising to the baseline level at the end of the simulation period.

Three approaches for calculating the wind induced convective heat transfer coefficients, h_{wind} , were analysed. The characteristic signatures for PV/T outlet temperature and power output are displayed in:Figure 4-22 and Figure 4-23 respectively:

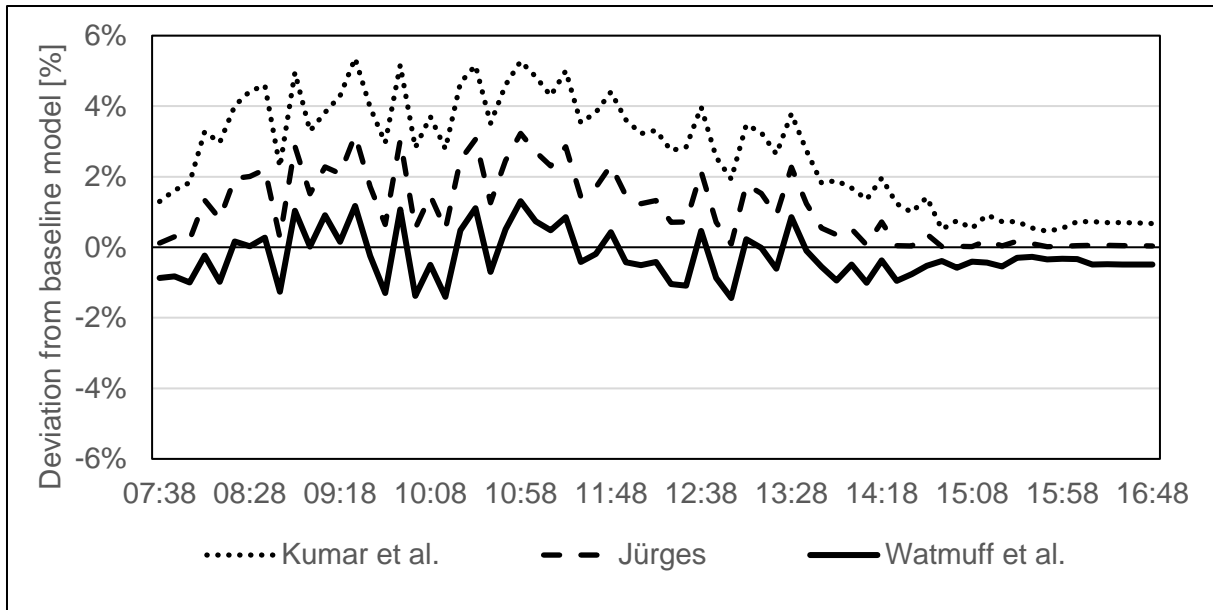


Figure 4-22: Characteristic signature of the PV/T outlet temperatures when implementing h_{wind} by the method of various authors.

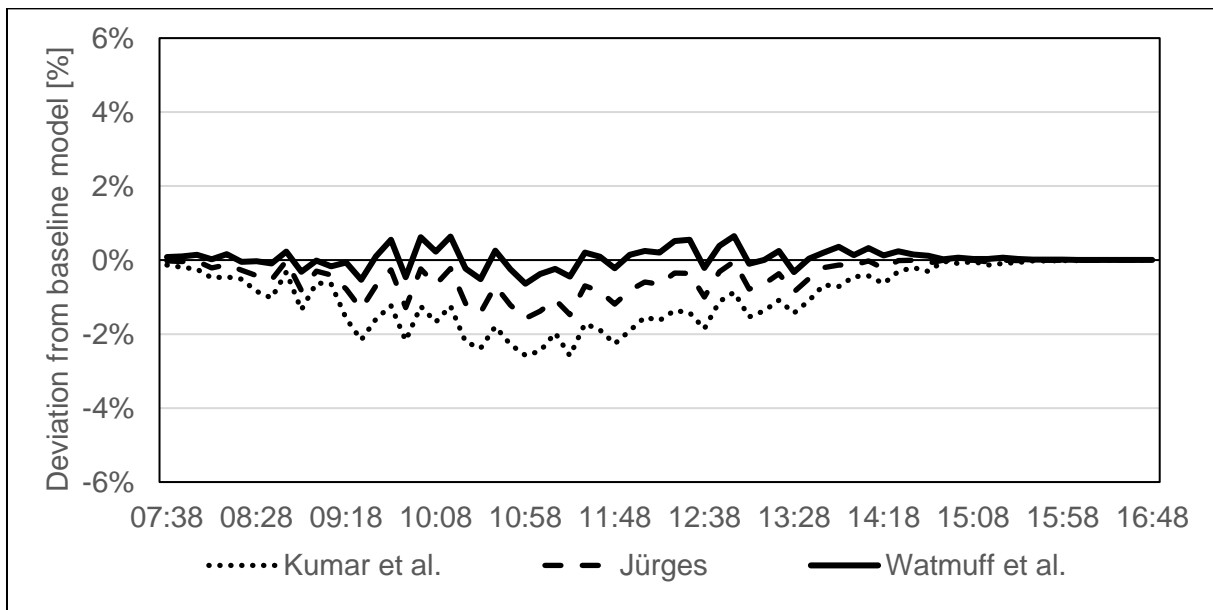


Figure 4-23: Characteristic signatures of the power output when implementing h_{wind} by the method of various authors.

The PV/T outlet temperature and power output are under- and overestimated, respectively, in the cases of Kumar et al. and Jürges. The lowest convective heat transfer coefficient, presented by Watmuff et al., results in smaller deviations from the baseline model for both validation metrics. This implies that the default heat transfer coefficient provided by TRNSYS

coincides with that presented by Watmuff et al., at least for lower winds up to 3 m/s. The maximum deviations for PV/T outlet temperature and power output are around 6% and 2% respectively, for the case of Kumar et al.

Table 7 shows the CV(RMSE) and MBE values for the methods of calculating the wind induced heat transfer coefficient and the sky temperature:

Table 7: CV(RMSE) and MBE values for wind induced heat transfer and sky temperature calculations

		<i>PV/T outlet temperature</i>		<i>Power output</i>	
		<i>CV(RMSE)</i>	<i>MBE</i>	<i>CV(RMSE)</i>	<i>MBE</i>
Wind induced heat transfer coefficients	Kumar et al.	3.46%	-0.65	2.64%	1.17
	Jürges	1.71%	-0.28	1.19%	0.53
	Watmuff et al.	0.81%	0.051	0.52%	-0.036
Sky temperature	Berdahl and Martin	2.78%	-0.58	1.30	0.74

All errors are in general very low, showing a large degree of presented in Table 7 enhances the similarity to the baseline model.

4.3.3 Calibrated Model

In the final, calibrated model, the approaches of Watmuff et al. and Berdahl and Martin are chosen. Thus, the model is a realistic representation of the actual conditions, considering both the sky temperature and the wind induced convective heat transfer coefficient. These two factors were not addressed in the preliminary baseline model.

The calibration signatures of the validation metrics for the calibrated model are presented in Figure 4-25:

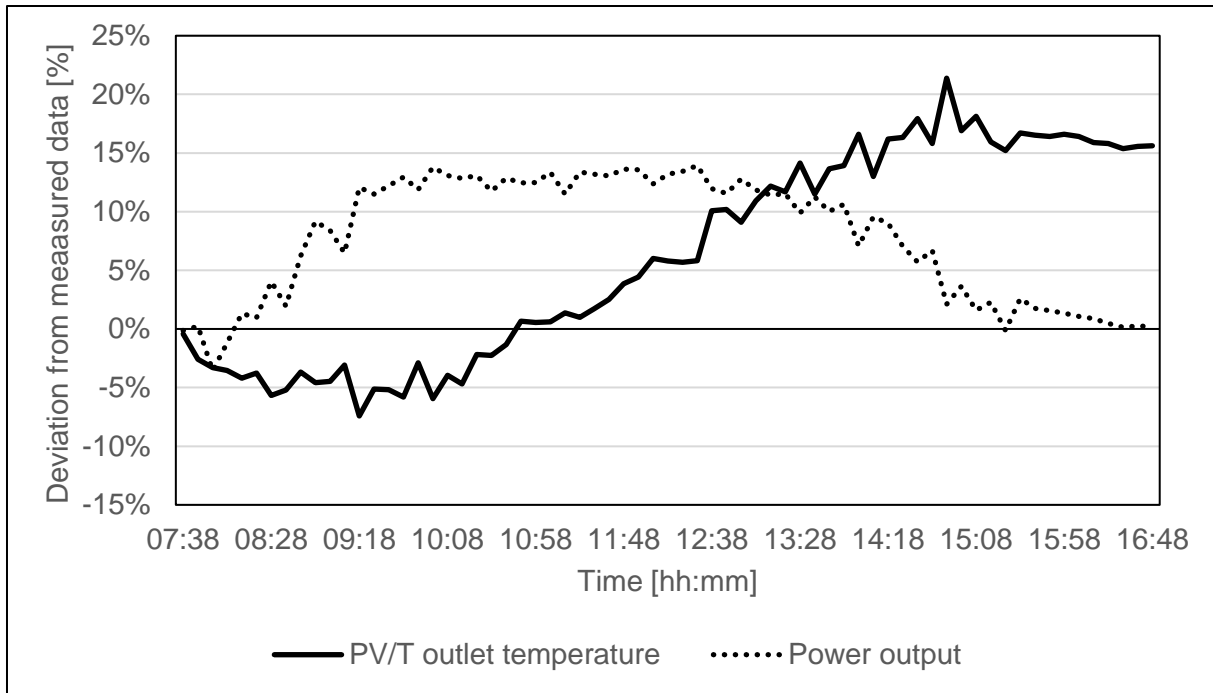


Figure 4-24: Calibration signatures of the validation metrics for the calibrated model.

It bears great resemblance to the calibration signature of the validation metrics for the baseline model, shown in Figure 4-20.

For a more detailed comparison, the validation metrics of the calibrated and baseline models are compared in Figure 4-25 and Figure 4-26:

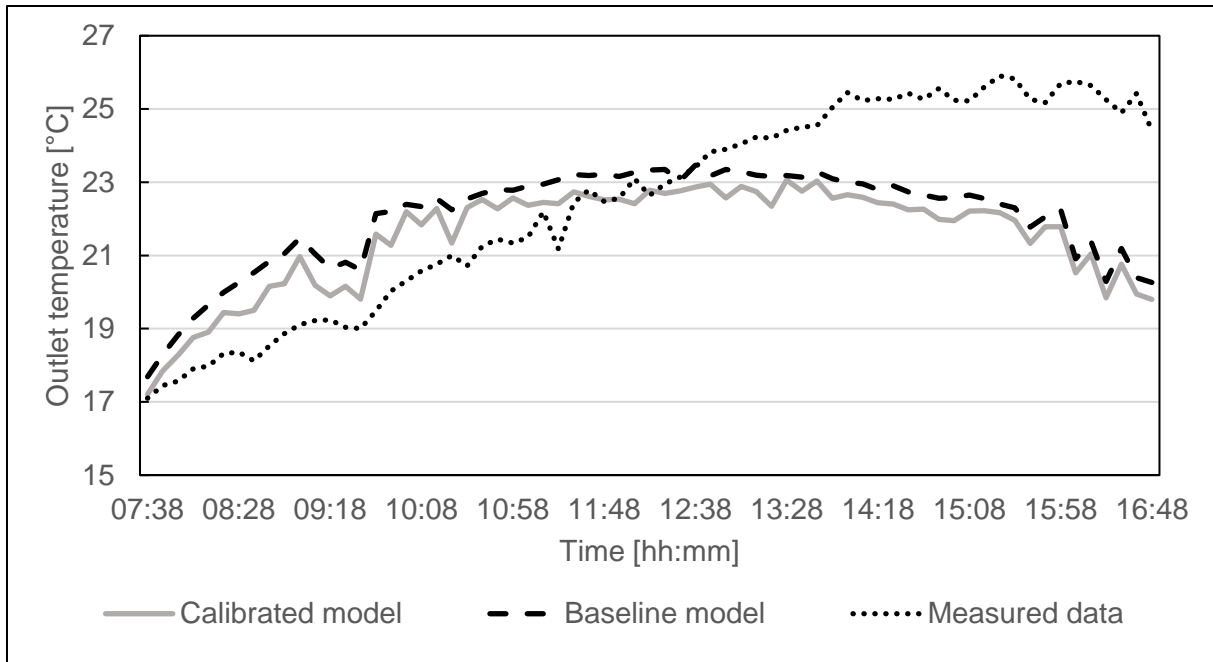


Figure 4-25: Outlet temperature of the calibrated and baseline models compared to the measured data

The outlet temperature from the calibrated model follows the trend of the temperature from the baseline model, but presents slightly lower values. The peak temperature from the calibrated model is 23.4°C and occurs around 12:30. The measured data reaches the peak value at a later time than that of the calibrated model, around 15:30. When compared to the graphs in Figure 3-7, the measured data seems to be more dependent on the ambient temperature whereas the calibrated model is more affected by the solar radiation.

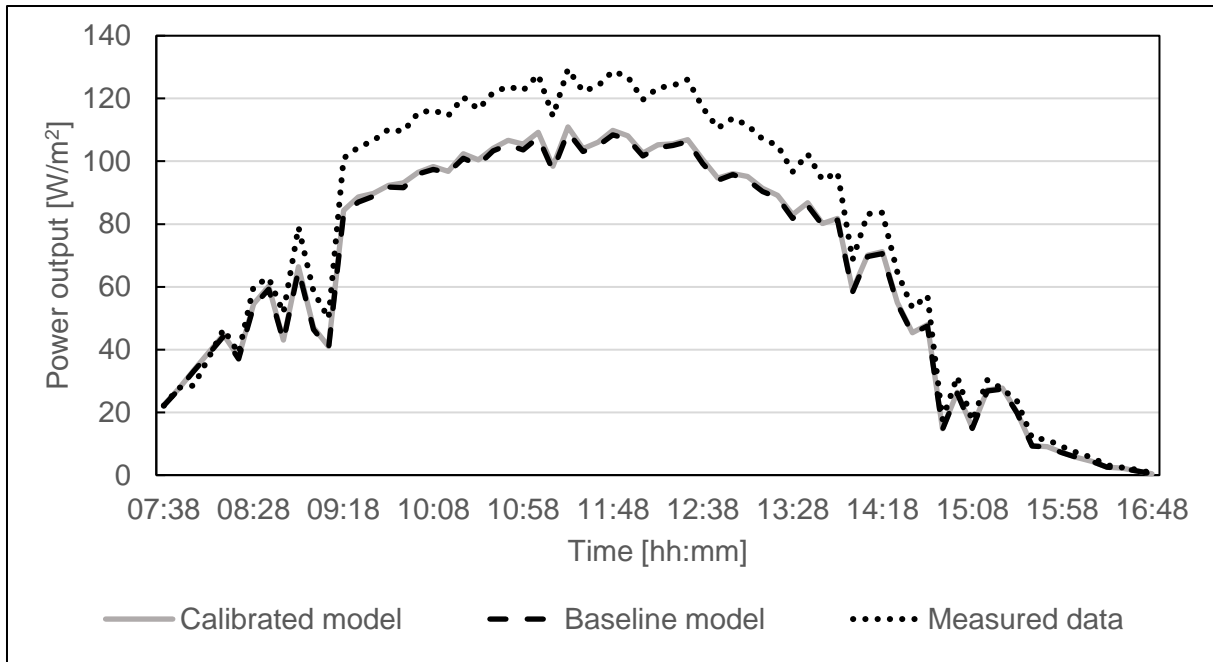


Figure 4-26: Power output of the calibrated and baseline models compared to the measured data

The power output is almost identical for the two models, with larger deviations compared to the measured data from 09:00 to 14:30. As seen from Figure 3-7 this is also when the solar radiation is the highest. This indicates that the computer models are less accurate during the hours with high amounts of solar radiation and that the power output is underestimated during these hours.

In order to measure the difference in power outputs and outlet temperatures, the CV(RMSE) and MBE of the two models are compared in:

Table 8:

Table 8: CV(RMSE) and MBE of the validation metrics for the calibrated and baseline models.

	<i>Outlet temperature</i>		<i>Power output</i>	
	<i>CV(RMSE)</i>	<i>MBE</i>	<i>CV(RMSE)</i>	<i>MBE</i>
Baseline Model	11.34%	-1.03	18.33%	-11.00
Calibrated Model	12.43%	-1.58	17.35%	-10.28

The differences in CV(RMSE) and MBE for the baseline and calibrated models are very small. For the outlet temperature, the baseline model presents slightly smaller errors than the calibrated model. However, the calibrated model shows greater resemblance to the measured data with regards to thermal efficiency, as shown in the following subchapter 4.4, evaluating the performance of the calibrated model.

The power output of the calibrated model is closer to the values of the measured data, which are higher than both computer models. This indicates that the calibrated model is a slightly better match for further analysis, as high power output is usually preferred over thermal output for an uncovered PV/T component.

The calibrated model provides a more realistic representation of the operating conditions of the PV/T component. It considers both the sky temperature and the wind induced convective heat transfer, as described in Chapters 4.1.3 and 4.1.4 respectively.

Gaussian distribution curves have also been fitted to the residuals, which shows the symmetry of the distribution of residuals. This has been done for the two validation metrics. The use of the term standard deviation refers to the range of which the residuals are spread out over giving an indication of how close the residual values is to the mean of residual data.

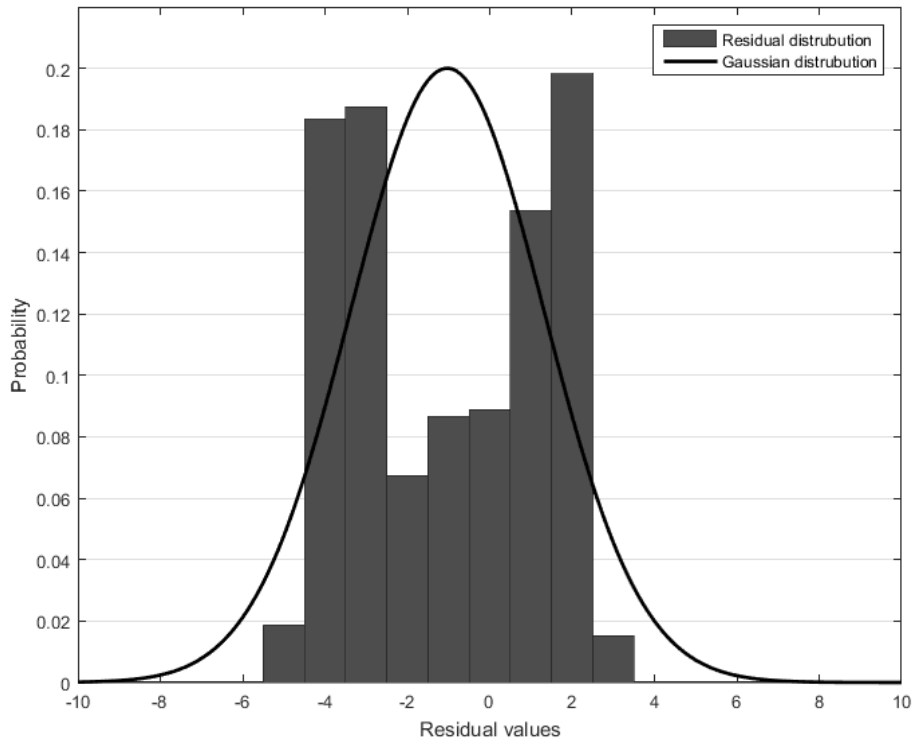


Figure 4-27: Residual distribution of the PV/T outlet temperature from the baseline model with a fitted normal distribution curve

The residual analysis of the residuals with fitted Gaussian distribution curve in Figure 4-27 shows that there is a small negative skewness in the PV/T outlet temperature. There are both negative and positive residuals similar in magnitude, which causes a small negative shift from 0 in the Gaussian distribution curve as there are more frequent distributions of negative residuals. The mean of the residuals is $-1\text{ }^{\circ}\text{C}$ with a standard deviation of $2.3\text{ }^{\circ}\text{C}$.

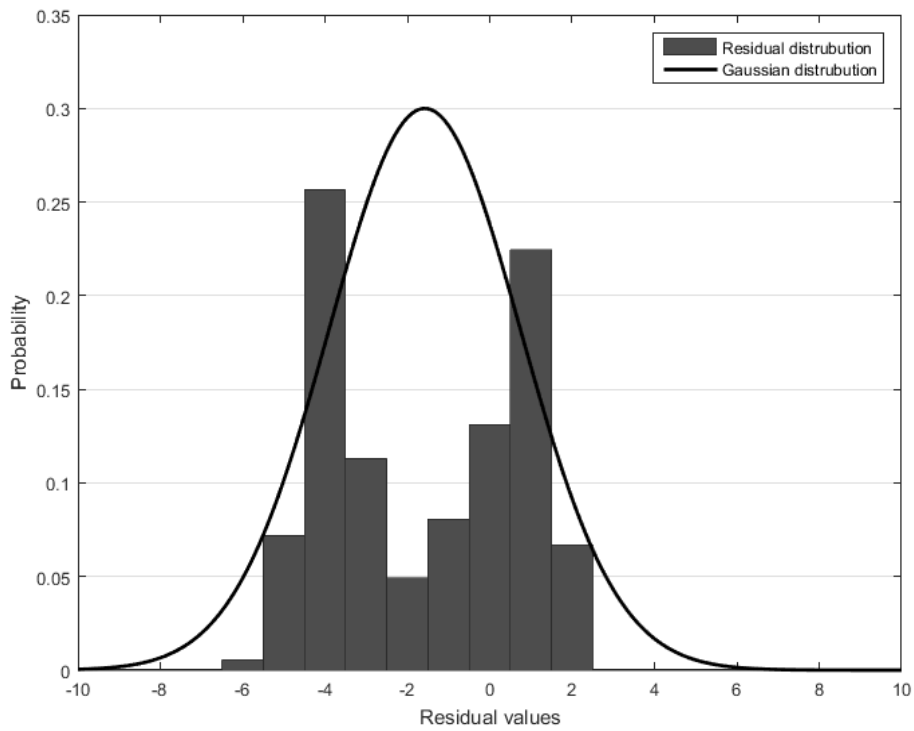


Figure 4-28: Residual distribution of the PV/T outlet temperature from the calibrated model with a fitted normal distribution curve

The distribution of residuals in the calibrated model shown in Figure 4-28 shows the same negative skewness of the outlet temperature residuals with a similar resemblance to the Gaussian distribution. The mean of the residuals is $-1.58\text{ }^{\circ}\text{C}$ with a standard deviation of $2.3\text{ }^{\circ}\text{C}$.

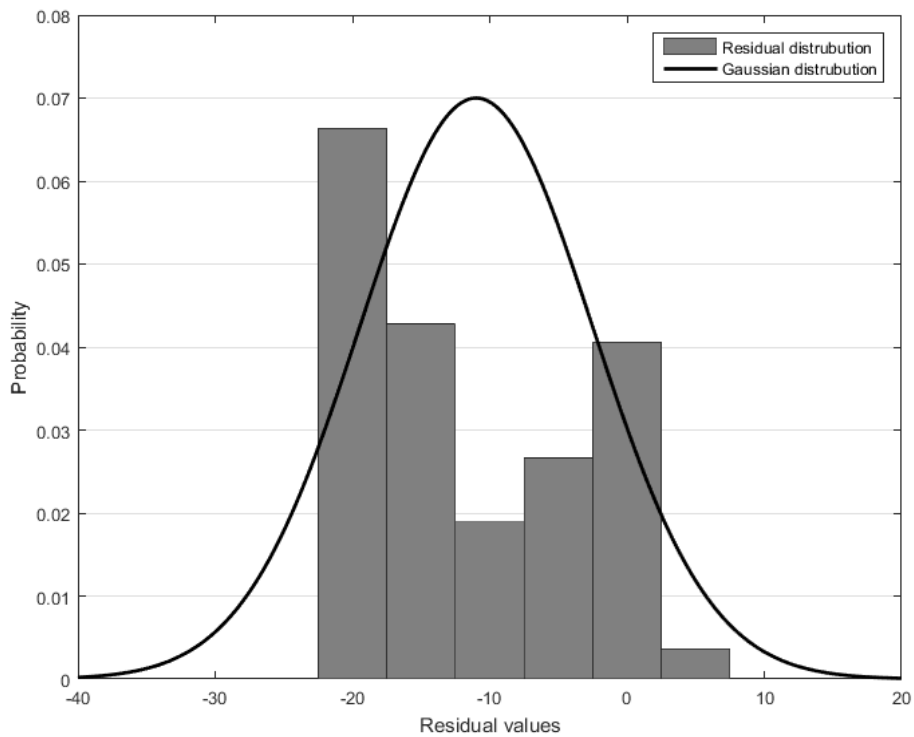


Figure 4-29: Residual distribution of the PV/T power output from the baseline model with a fitted normal distribution curve

The residual distribution of the PV/T power shown in Figure 4-29 has small negative skewness with residual values most frequently observed around -20 W, shifting the centre of the fitted Gaussian distribution curve to the mean at -11 W with a standard deviation of 8.5 W.

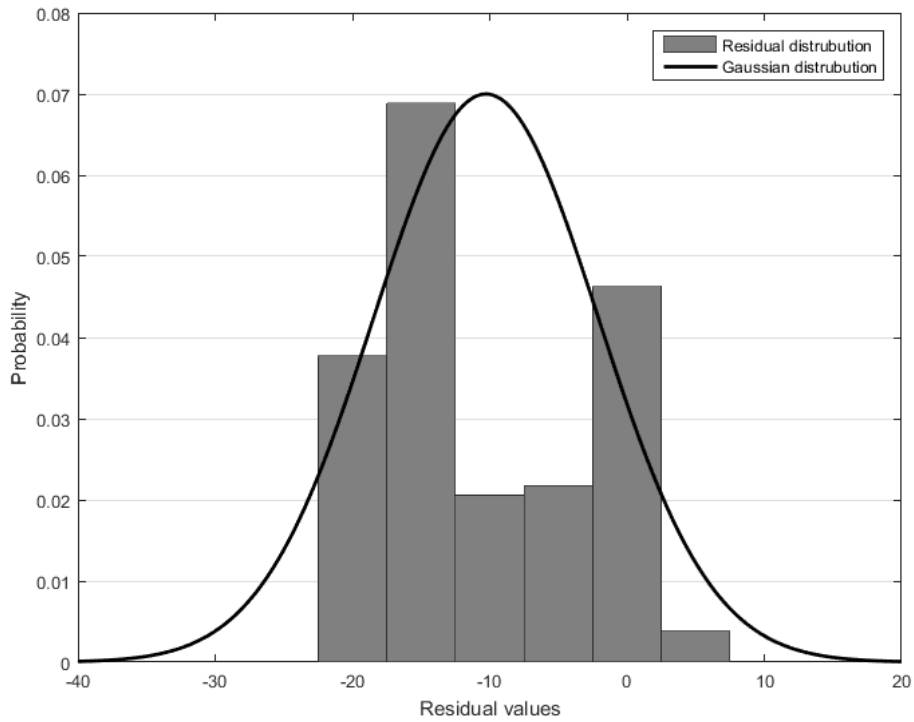


Figure 4-30: Residual distribution of the PV/T power output from the calibrated model with a fitted normal distribution curve

The residual distribution of the calibrated model presented in Figure 4-30 shows a small reduction in the occurrence of residuals around -20 W compared to the baseline model and shows a slightly better resemblance to the measured data. The mean of the residuals is -10 W with a standard deviation of 8.2 W.

4.4 Performance Evaluation of Calibrated Model

To evaluate the performance of the calibrated model, the electrical and thermal efficiencies are calculated and compared to the measured data. In addition, the total exergy efficiency is calculated in order to investigate the energy quality, as addressed in subchapter 2.3.3.

4.4.1 Thermal Efficiency

Figure 4-31 shows the thermal efficiency of the calibrated model and the measured data:

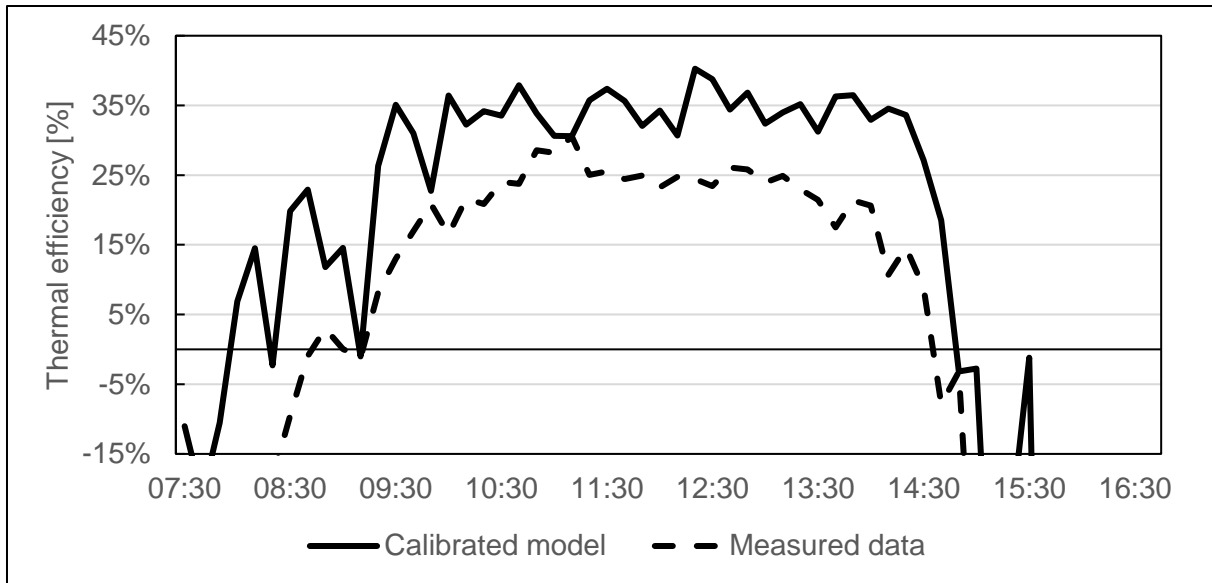


Figure 4-31: Thermal efficiencies of the calibrated model and the measured data

Both the calibrated model and the measured data give negative values of thermal efficiency during the beginning (until 09:10) and the end (from 14:30) of the measurement period, i.e. during the morning and the afternoon. This is caused by the inlet temperature of the PV/T exceeding the outlet temperature due to absence of solar radiation during these hours. The time period from 09:10 to 14:30 has been used as a common ground for further comparison and evaluation of thermal efficiency and performance.

The thermal efficiency graphs of the calibrated model, baseline model and measured data for this time period is shown in Figure 4-32:

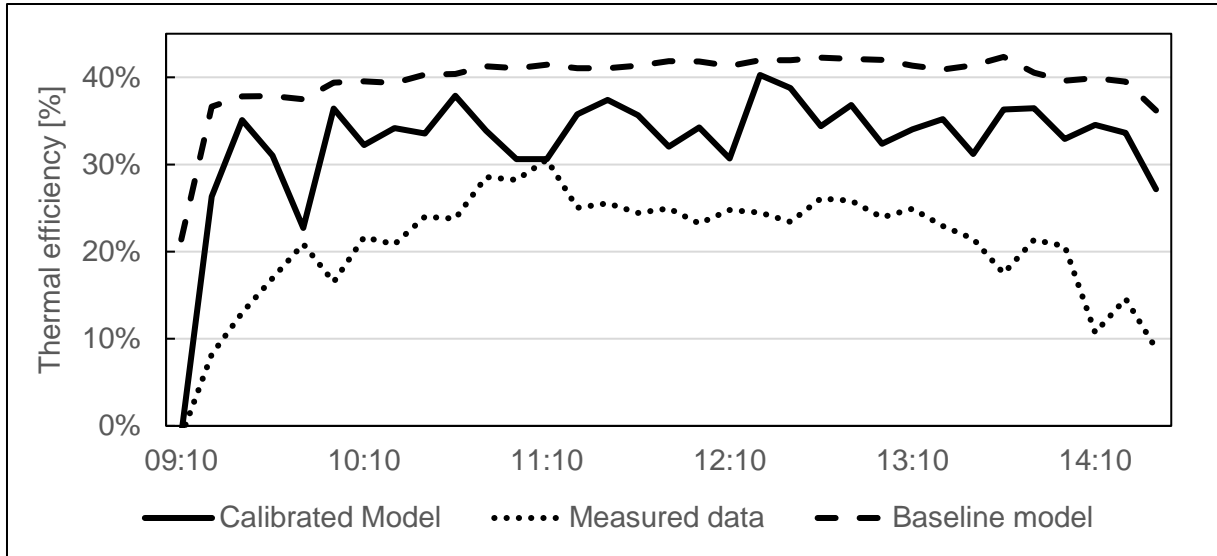


Figure 4-32: Thermal efficiencies of the calibrated model, the baseline model and the measured data during the hours of positive efficiency values

The thermal efficiency of the calibrated model is lower than that of the baseline model, and thus closer to the measured data. This is also seen when calculating the average thermal efficiency for the models and the measured data.

The average thermal efficiency for a given time period is defined according to Eq.(10) in subchapter 2.2.2 as:

$$\eta = \frac{\int \dot{Q}_u dt}{A_c \int G_T dt} \quad (88)$$

where $\int \dot{Q}_u$ is the sum of the useful energy over the time period. \dot{Q}_u is given by the mass flow rate, specific heat capacity and the temperature difference between the inlet and outlet of the PV/T:

$$\dot{Q}_u = \dot{m} C_p (T_{fluid,out} - T_{fluid,in}) \quad (89)$$

The average thermal efficiencies of the baseline model, the calibrated model and the measured data are 40.6%, 33.8% and 22.2% respectively. Although the baseline model showed higher PV/T outlet temperature, the temperature difference between inlet and outlet of the PV/T is lower for the calibrated model. Thus, the thermal efficiency of the calibrated model is closer to that of the measured data, even though the temperature overall is lower.

4.4.2 Electrical Efficiency

The electrical efficiency at STC for the calibrated model was set to $\eta_{ref} = 15\%$, which is equal to that of the component used during measurements. Figure 4-33 shows the calculated electrical efficiencies for the calibrated model, the baseline model and the measured data:

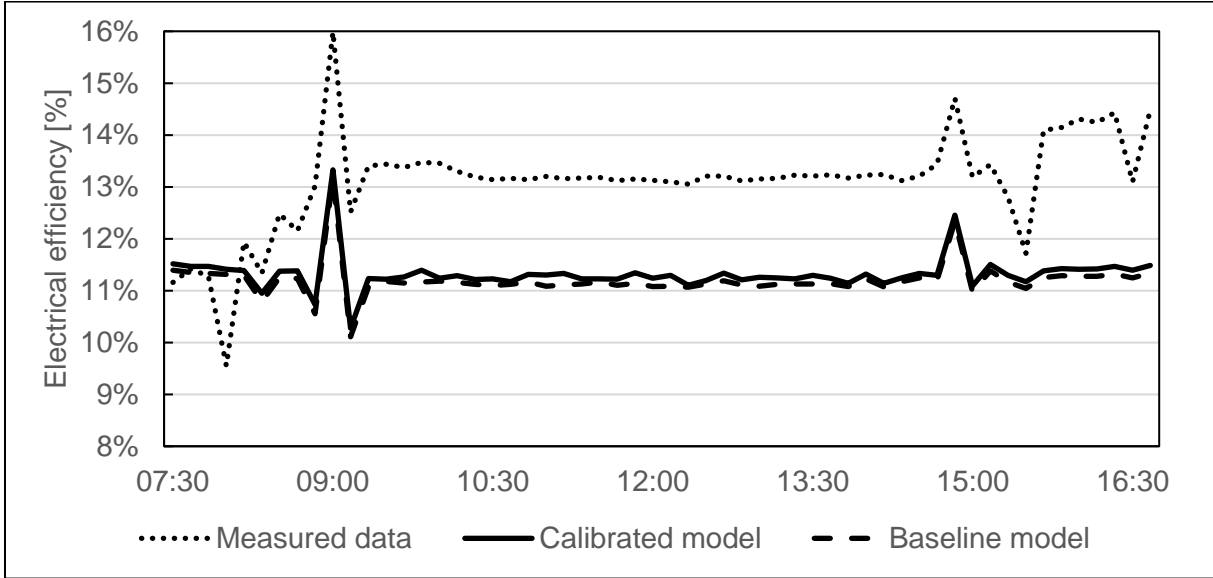


Figure 4-33: Electrical efficiencies of the calibrated model, the baseline model and the measured data

As seen from Figure 4-33, the temperature differences between the calibrated and baseline models does not affect the electrical efficiency to the same extent as the thermal efficiency. The calculated efficiencies are lower than the reference efficiency of 15% as the conditions during measurements do not correspond to STC. The average electrical efficiency for a given time period is based on eq.(3) in subchapter 2.1.6 and given as:

$$\eta_e = \frac{\int \dot{Q}_{electrical} dt}{A_c \int G_T dt} \quad (90)$$

The electrical efficiencies of the baseline model, the calibrated model and the measured data are 11.7%, 11.8% and 13.7%, respectively.

4.4.3 Total Efficiency and Exergy Calculations

The total efficiency of the component, η_{tot} , is the sum of the thermal and electrical efficiencies:

$$\eta_{tot} = \eta_{th} + \eta_e \quad (91)$$

The thermal, electrical and total efficiencies of the baseline model, calibrated model and the measured data are compared in Table 9:

Table 9: Thermal, electrical and total efficiencies of the baseline model, the calibrated model and the measured data

	<i>Baseline model</i>	<i>Calibrated model</i>	<i>Measured data</i>
Thermal efficiency, η_{th}	40.6%	33.8%	22.2%
Electrical efficiency, η_e	11.7%	11.8%	13.7%
Total efficiency, η_{tot}	52.3%	45.6%	35.9%

As the thermal and electrical outputs of a PV/T component are dependent on each other, it is natural that the electrical efficiency is underestimated when the thermal efficiency is overestimated. This is the case for both computer models. The total efficiency of the calibrated model is roughly 10% higher than that of the measured data. The main reason for the deviation is the higher thermal efficiency of the calibrated model. This is showed in Figure 4-34:

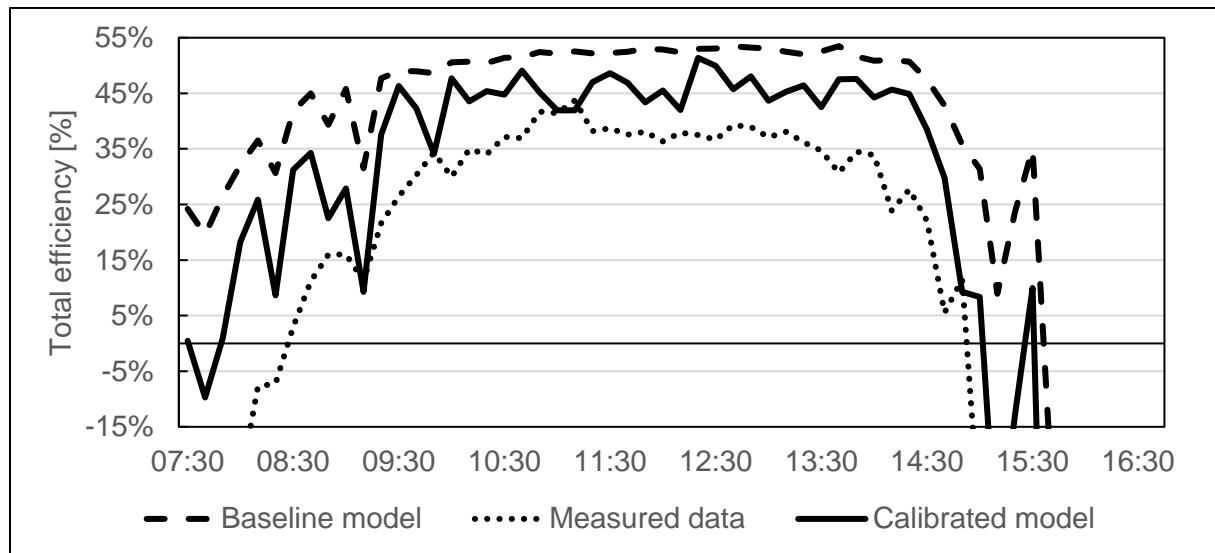


Figure 4-34: Total efficiencies of the baseline model, the calibrated model and the measured data

Following the approach by Fujisawa and Tani, the source temperature in Eq.(13) for calculating the Carnot efficiency is assumed equal to the ambient temperature. The total exergy efficiencies of the calibrated model, the baseline model and the measured data are plotted in Figure 4-35. The values of exergy efficiency are significantly lower than that of the total efficiency, and much closer to the values of electrical efficiency in Figure 4-33. The trend of the curves is more similar to what was seen for the electrical efficiency than for the thermal efficiency. The exergy efficiency is highest for the measured data, around 14% during most of the measuring period. The difference of 1.5% – 2% between the computer models and the measured data reflects the difference seen in Figure 4-33, and the fact that all the electrical energy is exergetic, whereas only a fraction of the thermal energy is.

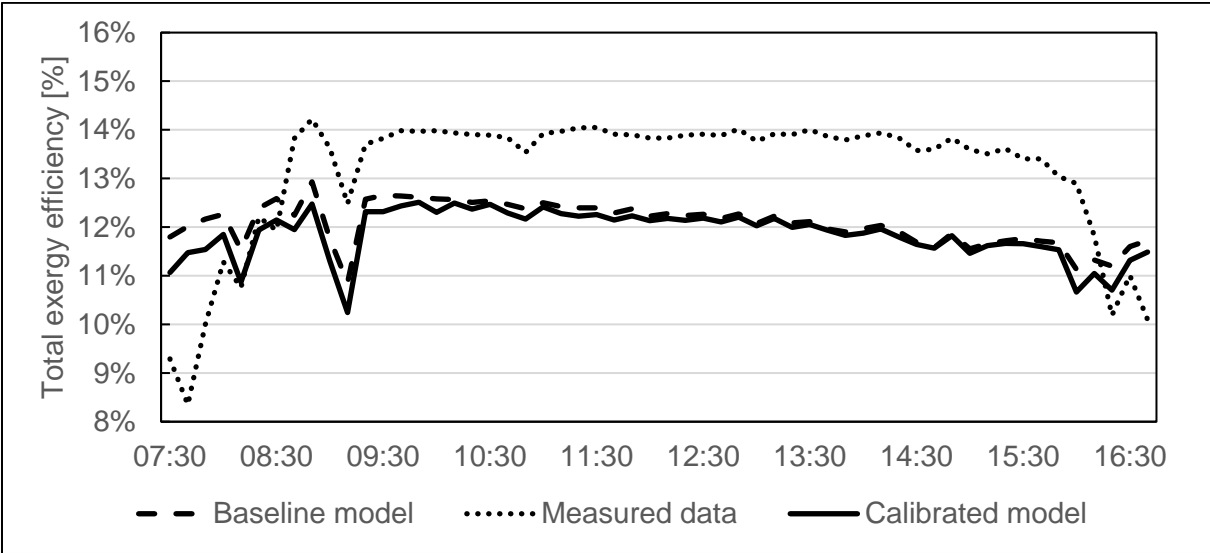


Figure 4-35: Total exergy efficiencies for the baseline model, the calibrated model and the measured data

4.5 GEL Model

For the calibration model, the CV(RMSE) of 12.43% and 17.35% for outlet temperature and power output, respectively, are close to the 10% limit described in the literature [73], and thus the model is regarded as a decent approximation of the real-life conditions. Although the overall efficiency of the calibrated model is higher than that of the measured data, the deviation in electrical efficiency, which is the prioritised output for the unglazed PV/T, is rather small. The results of the validation are in accordance with the validation of TYPE 563 conducted by International Energy Agency (IEA) based on an experimental PV/T test performed by Katic [76, 77].

The calibrated model is the basis for the building model developed in chapter 5, which will be used to conduct simulations for a whole year, to determine the potential of the BIPV/T technology for office buildings. To acquire more accurate results for annual simulations, it would be beneficial to validate the model compared to summer measurements as well as winter measurements, but such measurement data was not available. The wind induced heat transfer coefficients showed minimal influence on the performance of the BIPV/T and are thus neglected.

5 Energy Simulations of the GEL Model

Based on the theory presented in subchapter 2.5 regarding BIPV/T system design, a base case model for annual simulation is created in TRNSYS for both the water and air based BIPV/T systems. System sketches of the models can be seen in Figure 5-1 and Figure 5-2:

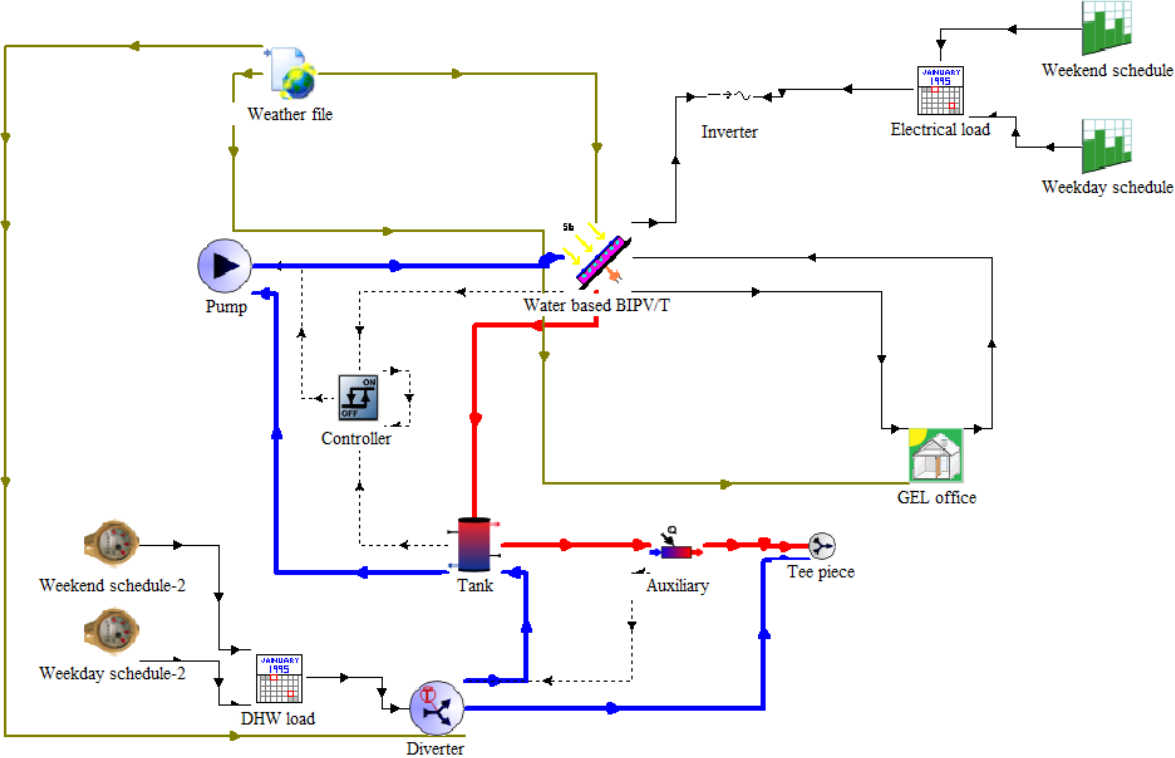


Figure 5-1: TRNSYS model of the water based BIPV/T system

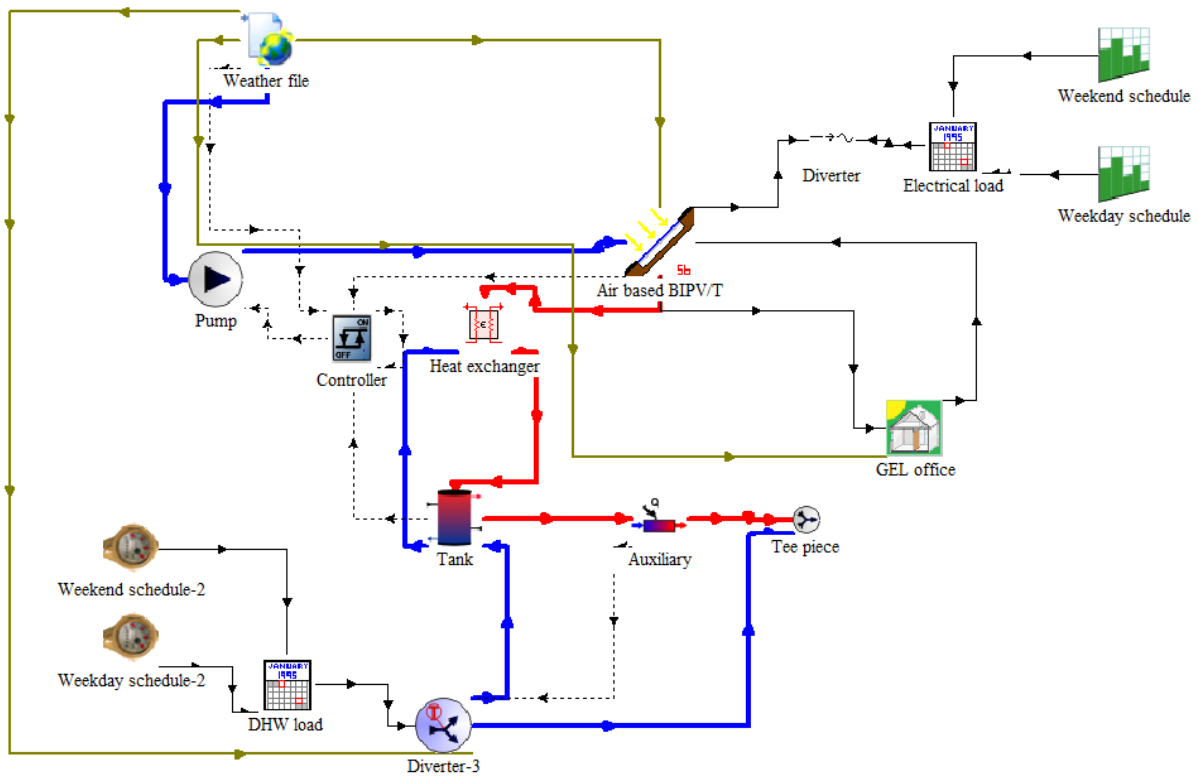


Figure 5-2: TRNSYS model of the air based BIPV/T system

The building model and the DHW and electrical load schedules are the same for both BIPV/T systems. The differences within the system models using water and air based BIPV/T are in the different BIPVT components (TYPE 563 and TYPE 568), the heat exchanger (TYPE 91) and the fan or pump (TYPE 3a or 3b). The heat exchanger is only used in the air based BIPV/T system in order to transfer heat between the BIPV/T outlet air and the water stored in the tank. Also, the air based BIPV/T uses a fan instead of the circulation pump used in the water based BIPV/T. For common parameters, the values of the air based BIPV/T component were set equal to that of the water based in order to evaluate and compare the performance of the two technologies under similar conditions.

Finally, the base case systems are optimised by varying a number of system parameters. Each system parameter is tested within a range while the other parameters remain constant. The value of the system parameter that shows the best performance will be implemented in order to evaluate two optimised BIPV/T systems.

5.1 GEL Office

In the annual simulation, data from a typical meteorological year is implemented by using the data file: “CHN_Shanghai.Shanghai.583670_IWEC.epw”. This is an “International Weather for Energy Calculations (IWEC)” data set developed by ASHRAE that consists of hourly weather data from up to 18 years back and also includes modelled solar radiation [73]

Figure 5-3 shows the hourly solar irradiance for Shanghai on a horizontal surface and a south facing vertical surface (i.e. the façade orientation of the BIPV/T wall). The horizontal irradiance peaks during summer months and reaches maximum values of around 1000 W/m². The BIPV/T wall receives less irradiance during summer months, but peaks during winter months with values of around 800 W/m². This shows that the potential for solar energy is present for vertical BIPV/T facades facing south.

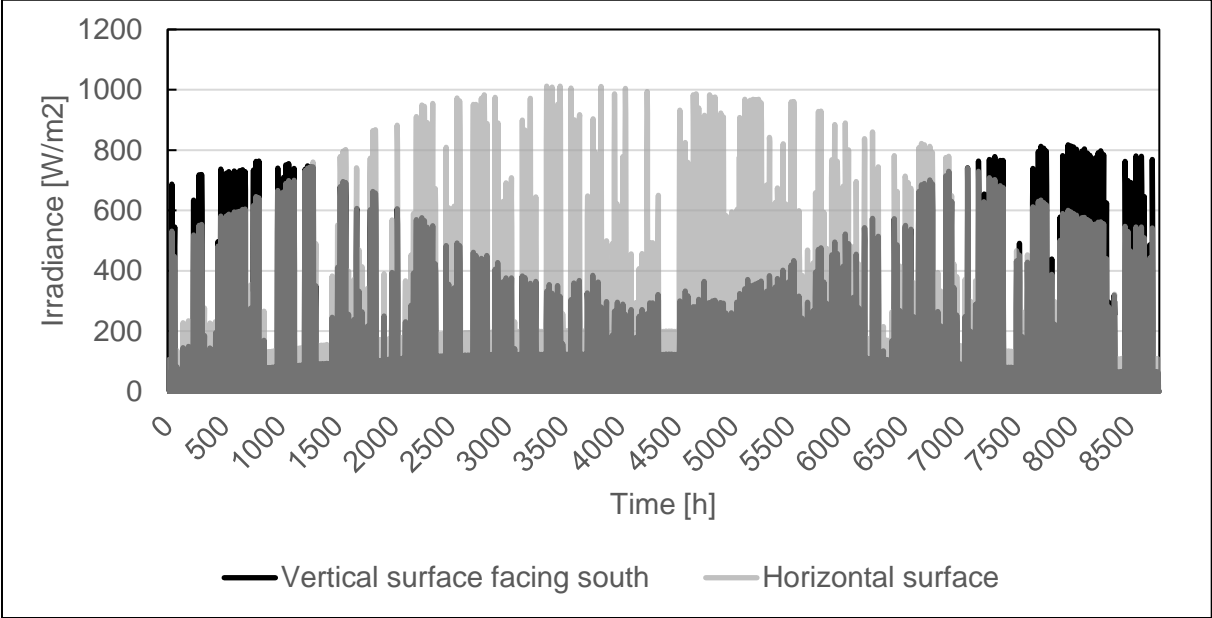


Figure 5-3: Solar irradiance for a vertical surface facing south and a horizontal surface

Both the ambient and the mains water temperatures, shown in Figure 5-4, are important parameters as they indicate the cooling potential of the BIPV/T components. Low temperatures may improve the performance of the air and water based BIPV/T components.

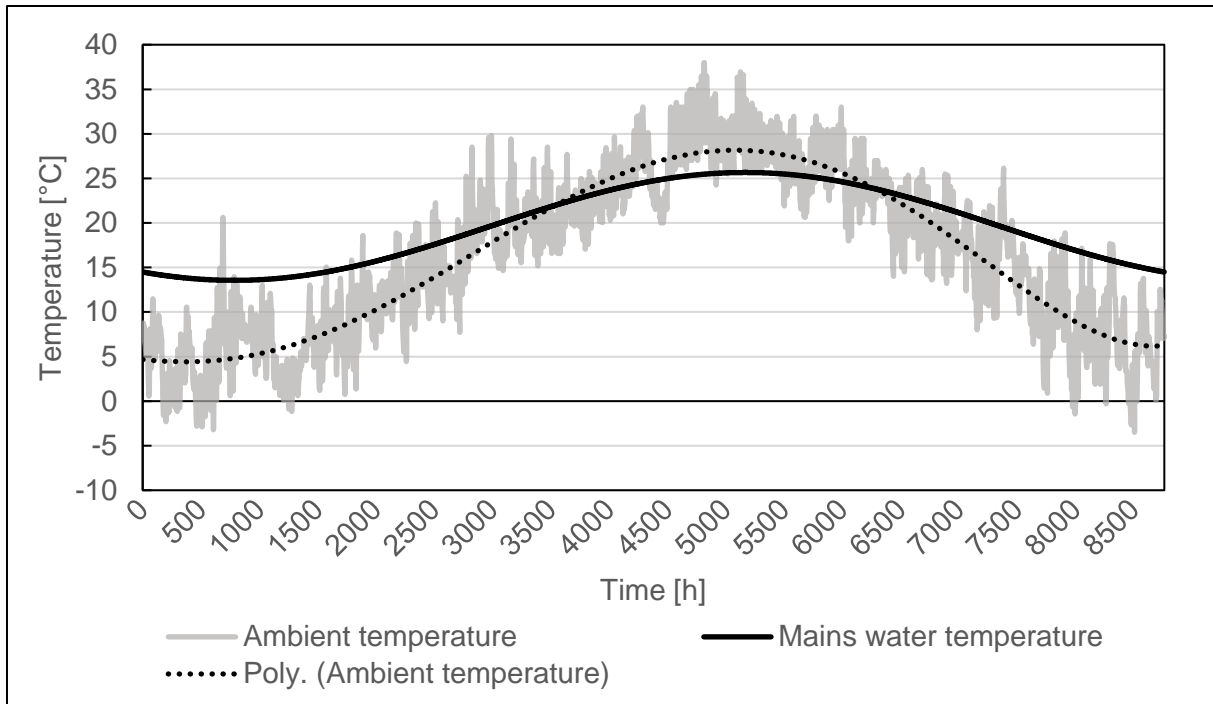


Figure 5-4: Ambient temperature and mains water temperature

The weather in Shanghai is defined as hot summers and cold winters [58] and therefore thermal insulation and airtight construction is important in order to reduce the heating demand during winter months. In order to reduce the cooling demand during summer months solar shading should be utilised. The BIPV/T façade investigated could possibly fulfil these functions and reduce the heating and/or cooling demand.

The Norwegian Standard for passive house and low energy buildings (NS 3701) [78] is used in order to set the criteria for the GEL office building, which also fulfils the minimum requirements for office buildings according to Norwegian TEK 15. An overview of the building constructions with corresponding requirements can be seen from Table 10. Available data from previous research conducted at SJTU [58, 79] are used in order to set values for the geometry and external facades' properties of the building.

Table 10: Building envelope of the GEL office based on values from NS 3701 and TEK 15 minimum requirements [78]. Adapted from [58]

<i>GEL office</i>	<i>Area [m²]</i>	<i>U value [W/m²K]</i>	<i>TEK 15 requirements [W/m²K]</i>
Floor	88	1.9	-
Façade S	45.9	0.1	≤ 0.22
Façade N	45.9	“	“
Façade E	32.6	“	“
Façade W	32.6	“	“
Roof	88	0.085	≤ 0.18
Window N	10.32	0.68	≤ 1.2
Window E	6.96	“	“
Window W	-	-	-
Window S	-	-	-
Other features	Double skin façade		

5.2 Multizone Model (TYPE 56)

In order to connect the PV/T models to a building model, a TYPE 56 is used. The parameters of the building model are not set directly in TYPE 56 because of the complexity of such a model. Therefore, TRNBuild is utilised, which is a separate program used to generate two input files to TYPE 56. TRNBuild creates a building file (*.BUI) based on the input data of each thermal zone set by the user, as well as the output data desired for the simulation. In TYPE 56 both the short-wave and long-wave heat exchange is accounted for using the ASHRAE transfer function. [80]

TYPE 56 is used in this thesis to investigate the heat transfer effect between both the water and air based PV/T, respectively, and a building model. In TRNBuild the walls are modelled based on a transfer function relationship of Mitatalas and Arseneault [80], which describes the thermal history of the wall and is defined from the outer surface of the wall to the inner surface. In TRNBuild a wall is considered a black box model and is shown in Figure 5-5. The following relation is given for the heat conduction through the wall:

$$\dot{q}_{s,i} = \sum_{k=0}^{n_{b_s}} b_s^k T_{s,o}^k - \sum_{k=0}^{n_{c_s}} c_s^k T_{s,i}^k - \sum_{k=1}^{n_{d_s}} d_s^k \dot{q}_{s,i}^k \quad (92)$$

$$\dot{q}_{s,o} = \sum_{k=0}^{n_{a_s}} a_s^k T_{s,o}^k - \sum_{k=0}^{n_{b_s}} b_s^k T_{s,i}^k - \sum_{k=1}^{n_{d_s}} d_s^k \dot{q}_{s,o}^k \quad (93)$$

where k represents the time step related to the time base which is set by the user. If a high value of k is chosen then the wall is set as a heavy wall with a large thermal mass. a, b, c and d are time coefficients of the time series given by TRNBuild. $T_{s,o}$ and $T_{s,i}$ (equal to back surface PV/T temperature, T_{back} , described in subchapter 4.1) is the outside and the inside surface temperature of the wall, respectively. $\dot{q}_{s,o}$ and $\dot{q}_{s,i}$ are defined as the conduction heat flux from the outside to the wall and the conduction heat flux from the wall to the inside surface, respectively.

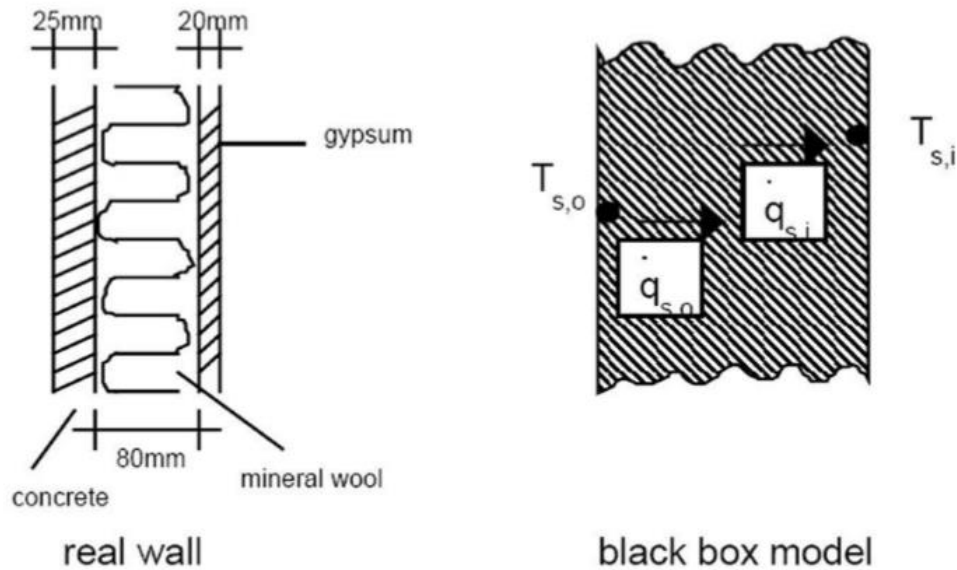


Figure 5-5: Illustration of a real wall and the corresponding black box model

When TYPE 56 is coupled with a TYPE 563 or TYPE 568, the building model will use the temperatures of the absorber plate or the lower air channel surface (T_{abs} and T_2 seen in subchapter 4.1), respectively, as the outside surface temperature of the building model wall. By using the transfer function relationship of Mitatalas and Arseneault, the inside surface temperature of the wall is calculated. The calculated $T_{s,i}$ is then used as the back surface temperature of the PV/T and a new temperature for the absorber plate or the lower air channel surface is calculated for the TYPE 563 and TYPE 568, respectively. These calculations will repeat themselves until convergence is reached. [80]

5.2.1 Building Envelope

The office building is modelled as one thermal zone as the goal is to assess the overall energy need of the office building. As the office building is in the 2nd floor, the floor is set with boundary conditions towards a heated zone with a constant value of 22 °C. There is also a heated zone adjacent to the west wall and the boundary temperature is set to 22 °C which would not cause big influences in heating or cooling demand.

The north and east walls, as well as the roof, are set as external constructions with heat exchanges to the ambient. For all the external facades except the southern façade, the external window shading is set to 50 % in order to model the double skin façade of the GEL building. The total height of the zones is set to 3 meters giving a total volume of 263 m³.

The time base of the transfer function was changed from 1 hour to 2 hours during simulations in TRNBuild because of the high thermal mass of the building envelope.

The window construction Win ID: 4001 with area and U value as given in Table 10 is used for the north and east façades. A low U value is chosen to fulfil the demand in NS 3701. The detailed window construction and the NS 3701 demands are shown in Table 2 and Table 3 in Appendix B. For the south wall, the boundary conditions are set to the back of the BIPV/T. As it is not possible to add windows to a façade with boundary conditions, the windows on the south façade are neglected.

Irradiation for five surfaces (three exterior walls, the roof and the BIPV/T panel) is calculated in TYPE 15-3 and set in TRNSYS related to the orientation and slope of each surface.

5.2.2 Modelling of the BIPV/T Wall

The solar heat gain through the south façade is given as conductive heat through the back surface of the BIPV/T wall. The south wall is created in TRNBuild with a boundary temperature which can be set as an input by the user.

For TYPE 563, additional resistance of the component must be added as there is insulation between the absorber plate and the back surface of the collector. Consequently, the U value of the south wall is set lower in TYPE 563 than in TYPE 568. This way, the U value of the south wall is constant regardless of which BIPV/T technology is simulated. The layer properties of the building construction and the calculation of the south wall can be seen in Appendix B.

5.2.3 Schedule

A schedule for operating hours is set according to the Norwegian Standard for calculation of energy performance of buildings (NS 3031) [81] and is used as a schedule for heating, cooling, lighting and internal gains. Operating hours are set between 07:00 AM and 19:00 PM on weekdays and no operation during the weekends.

5.2.4 DHW load

The hot water consumption is set to 22 l/day person with a peak of 9 l/h [82]. Based on a user profile behaviour of office buildings reported by SINTEF [83] and the occupant density from NS 3701, a DHW profile is made and seen from Figure 5-6 (left). The peak load is 158 l/h in the first office hour from 7 am to 8 am. For the remaining office hours, an average value of 23.8 l/h is used, which totals to a hot water load of 387 l/ day.

5.2.5 Internal Gains and Electrical Load

The internal heat gains from occupants, office equipment and lighting and the power load consumption are set according to NS 3701, and can be found in Table 23 in Appendix B. 100% of the average power load for equipment and lighting is assumed converted to heat. Electrical consumption from equipment and lighting results in an average load of 3484.8 kJ/hr. The NS 3701 schedule is used to set the operating hours as seen in Figure 5-6 (right).

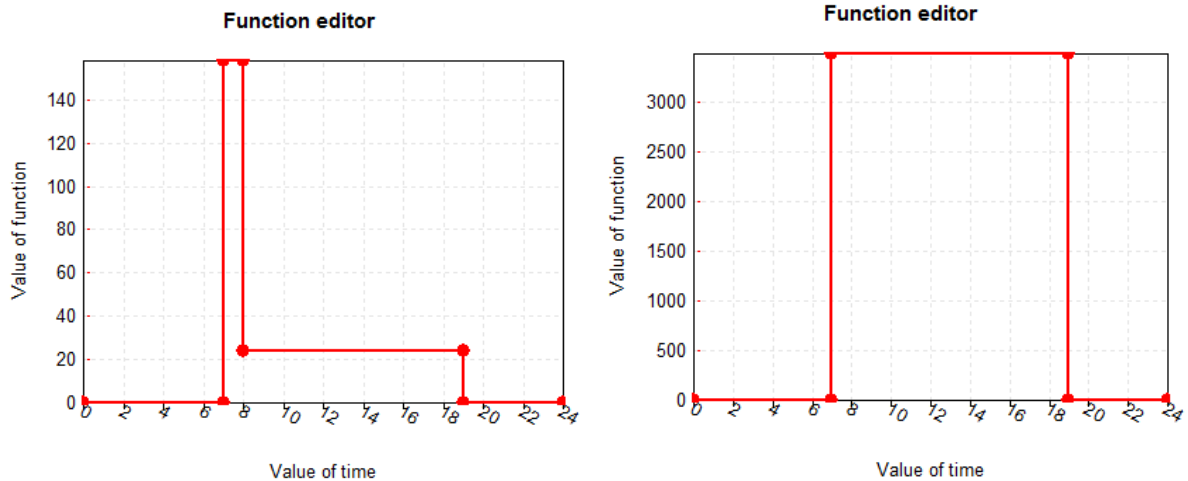


Figure 5-6: DHW profile (left) and electrical load profile (right) as set in TRNSYS

5.2.6 Ventilation

The air exchange is set using the occupant density in NS 3701, resulting in two air changes per hour ($ACH = 2 \text{ h}^{-1}$). The ventilation supplies the building with air from the outside at ambient temperature. This was chosen in order to calculate the power needed to heat or cool the ventilation air to the set point temperature. In addition, the infiltration rate is set to the minimum demand of 0.6 h^{-1} in NS 3701.

5.2.7 Heating and cooling

The set points for heating and cooling are set to 21°C and 26°C during operating hours, respectively. The capacity of the heating and cooling systems are set to unlimited in order to assess the annual heating and cooling demand for the building, which can be seen in Figure 5-7 together with the indoor temperature. It should be noted that the temperature drop and rise below and over heating and cooling set points, respectively, occur outside of operating hours. Based on this simulation, the maximum heating and cooling power is found to be 4.9 kW and 4.4 kW, respectively. The total annual energy demand for heating and cooling of the office building is 63.7 kWh/m^2 .

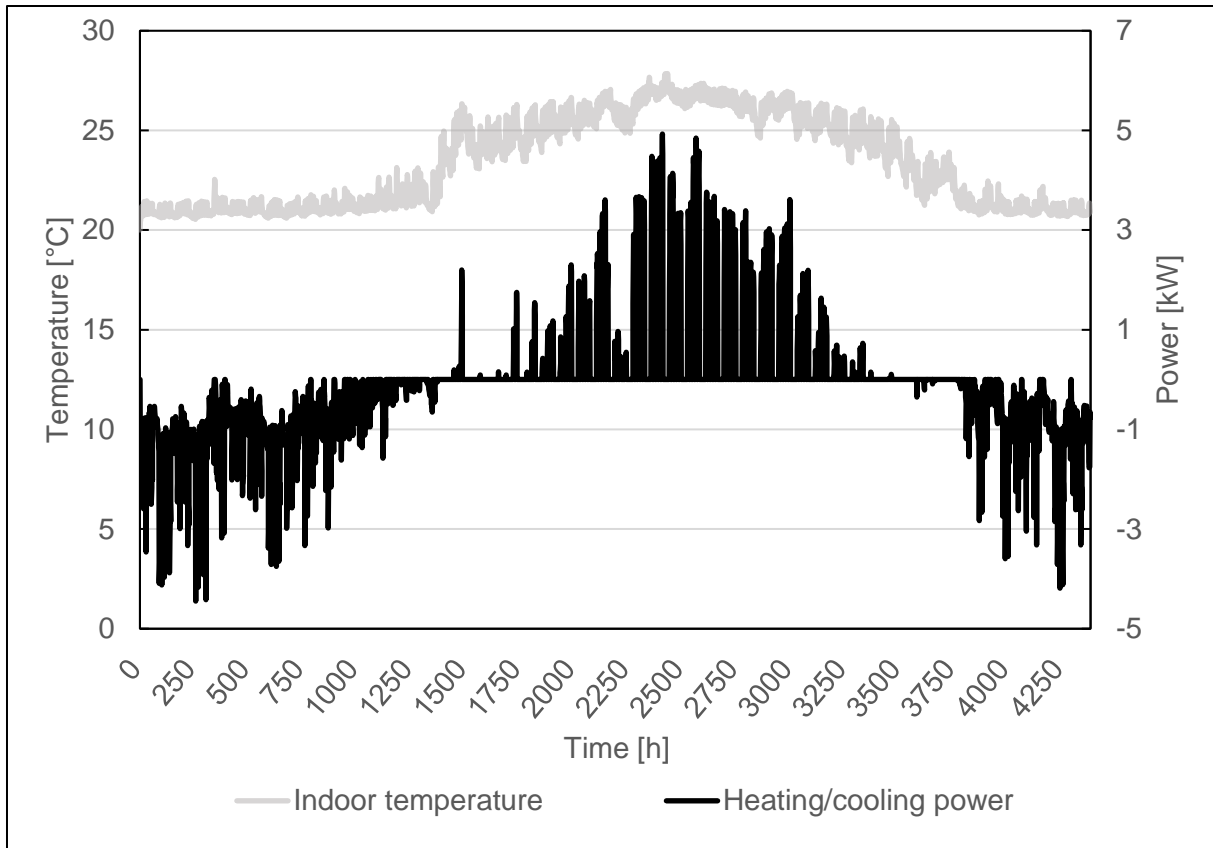


Figure 5-7: Annual heating (negative values) and cooling (positive values) demand

5.2.8 Differential controller (TYPE 2)

TYPE 2 is a differential temperature controller that will adjust the water flow rate in the PV/T component according to the temperature difference between the bottom of the tank, T_L , and the outlet of the PV/T, T_H . The output control function, γ_0 , is set according to the temperature difference of the outlet and inlet water temperatures of the PV/T compared to the corresponding upper and lower dead band, defined as ΔT_H and ΔT_L , respectively. The upper and lower dead band are set as inputs to TYPE 2. For the BIPV/T air component, the ambient air temperature and the PV/T outlet temperature are used as T_L and T_H ; respectively. The control strategy can be seen from Figure 5-8:

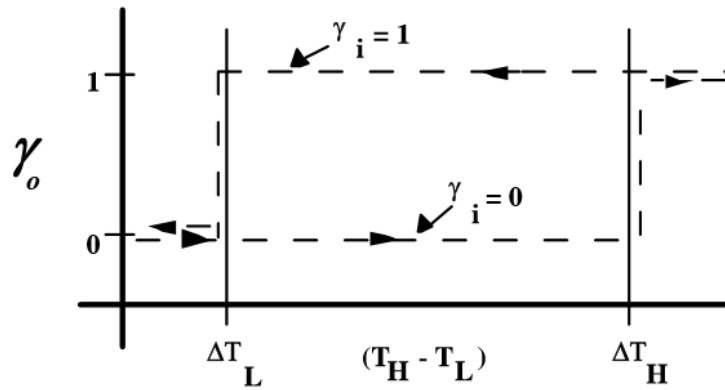


Figure 5-8: Controller function

If the controller previously was on then the controller function is given as:

$$\text{If } \gamma_1 = 1 \text{ and } \Delta T_L \leq (T_H - T_L), \gamma_o = 1 \quad (94)$$

$$\text{If } \gamma_1 \text{ and } \Delta T_L > (T_H - T_L), \gamma_o = 0 \quad (95)$$

If the controller previously was off then the controller function is given as:

$$\text{If } \gamma_1 = 0 \text{ and } \Delta T_H \leq (T_H - T_L), \gamma_o = 1 \quad (96)$$

$$\text{If } \gamma_1 = 0 \text{ and } \Delta T_H > (T_H - T_L), \gamma_o = 0 \quad (97)$$

In the GEL model, the differential controller is used in order to control the main circulation pump. In addition, the controller monitors the tank temperature and sends a control signal of 0 to stop circulation if the water temperature reaches 100 °C, which is the boiling temperature.

5.2.9 Storage Tank (TYPE 60)

The tank used in combination with the PV/T models is a TYPE 60: Stratified fluid storage tank and is the most detailed tank in the TRNSYS standard library. The amount of stratification in the tank is decided by the number of nodes, N, specified for the tank. The value of N ranges between 1 and 100, where N equal to 1 gives a uniform tank temperature. The component uses an internal time step so that the accuracy and speed of the tank simulation are independent on the simulation time step set in TRNSYS. A small time step will increase the accuracy or speed of the tank simulations.

5.3 Optimisation of GEL Models

Based on the theory presented in subchapter 2.5 regarding BIPV/T system design, a base case model is made for both BIPV/T air and water. The base case models are then optimised by varying a number of system parameters. Each system parameter is tested within a range while the other system parameters remain constant. The value of the system parameter that shows the best performance will be implemented in order to evaluate two optimised GEL models utilizing air and water based BIPV/T, respectively.

5.4 Water Based BIPV/T System

The size of the storage tank is set to 600 l. The height of the inlet from the mains water is set to the bottom of the tank and the inlet from the heat source (i.e. the BIPV/T) is set to the top for initial simulations. The outlet height from the tank to the heat source and from the tank to the load is fixed at the bottom and top, respectively. An auxiliary heater is set with a high capacity (10 kW) in order to effectively heat the water going out from the tank when the BIPV/T is not able to provide water at set point temperature. The maximum pump power is set to 46 W when optimising the water based BIPV/T, which is the maximum pump power used in the initial measurements of the water based PV/T. The base case values of the water based BIPV/T system can be seen in Table 11.

Table 11: Base case values of the water based BIPV/T system

<i>Base case parameters</i>	<i>Values</i>
BIPV/T component area [m ²]	45.9
Inclination [°]	90
Inverter efficiency [%]	78
Size of storage tank [l]	600
Tank height to diameter ratio [-]	2
Tank height [m]	1.45
Mass flow rate [kg/hm ²]	2.2
Auxiliary set point [°C]	60
DHW set point [°C]	45
Dead band on/off [°C]	10/2
DHW demand [l]	387
Tank inlet from heat source [m]	1.45
Tank inlet from cold side [m]	0.145

It is chosen to evaluate five system parameters based on four simulations per parameter. The chosen parameters and the test range is seen in Table 12. The base case values are denoted as “bc” in all figures presented regarding the optimisation of the water based BIPV/T system.

Table 12: Optimisation parameters for the water based BIPV/T system

<i>Optimisation parameters</i>	<i>Values</i>			
Dead band [on/off]	8/2	8/4	10/2	10/4
Size of storage tank [l]	300	600	1000	2000
Specific flow rate [kg/hm ²]	2.2	10	16	24
Inlet from heat source [m]	0.58	0.87	1.16	1.45
Inlet from cold side [m]	0.145	0.435	0.725	1.015

When analysing and optimising the performance of the water based BIPV/T system, the thermal efficiency, electrical efficiency, useful energy and operational hours are presented. The thermal efficiency presented is calculated based on the useful energy collected by the BIPV/T component. The useful energy presented together with operational hours is the useful energy collected by the tank given by kWh/m² of office building area. There is no difference between the two forms of useful energy for the water based BIPV/T system as there is no heat exchanger implemented in this model.

The electrical efficiency is not affected by the variation of the parameters and is therefore only represented by one data series in the plots. Peak values of 11% is seen in the winter months of December and January with a following decrease until the lowest point for electrical efficiency is reached in June at 6.35%. The electrical efficiency of the BIPV/T bears great resemblance to the solar irradiance incident on the BIPV/T façade shown in Figure 5-3 in subchapter 5.1, and the lowest electrical efficiency occurs at the same time as the peak for thermal efficiency. This is also the case for most of the parameters of the air based BIPV/T system analysed in subchapter 5.5.

5.4.1 Dead Band

Various values for the upper and lower dead band are simulated to provide a range which ensures that the thermal part of the BIPV/T system is operational when it is possible to collect heat. The effects of varying the dead band can be seen from Figure 5-9 and Figure 5-10:

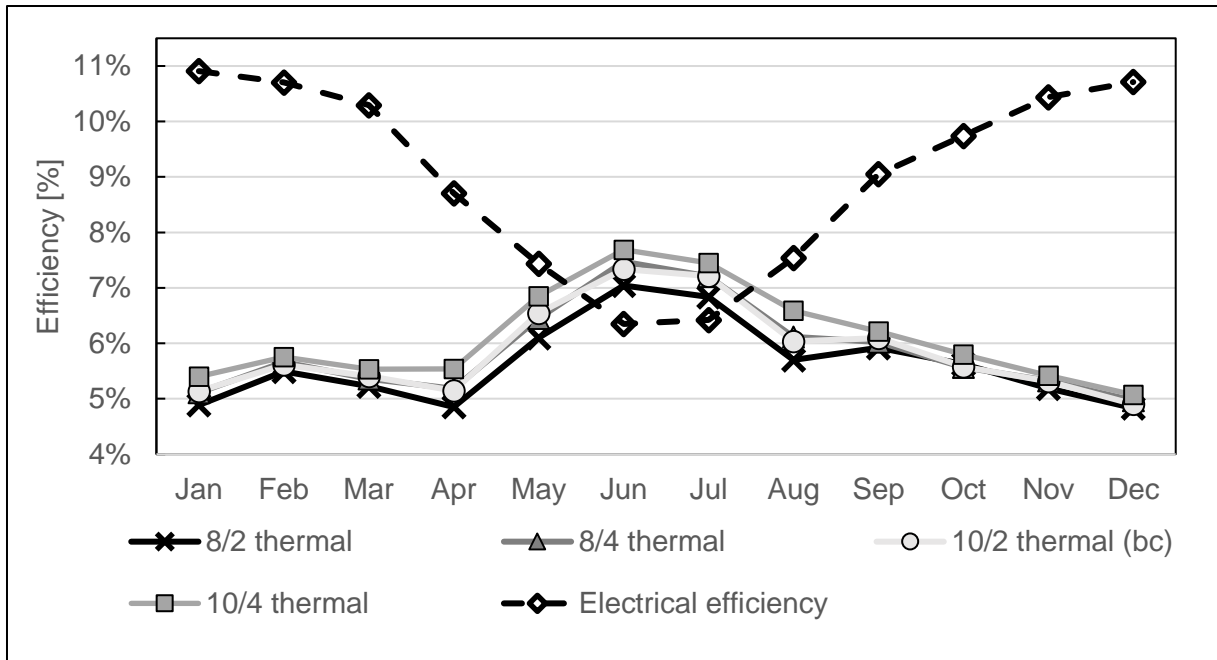


Figure 5-9: Monthly values of thermal and electrical efficiencies when varying the dead band

From Figure 5-9 it can be seen that the thermal efficiency peaks during summer months between April and August. There is some variation in thermal efficiency when adjusting the dead band, and the highest value is reached for the 10/4 dead band. Larger deviations between the dead band strategies can be seen during summer months compared to the closer resemblance seen between September and March. During the peak of thermal efficiency of 7.69% in June, the 10/4 dead band shows an increase of only 0.35% compared to the base case.

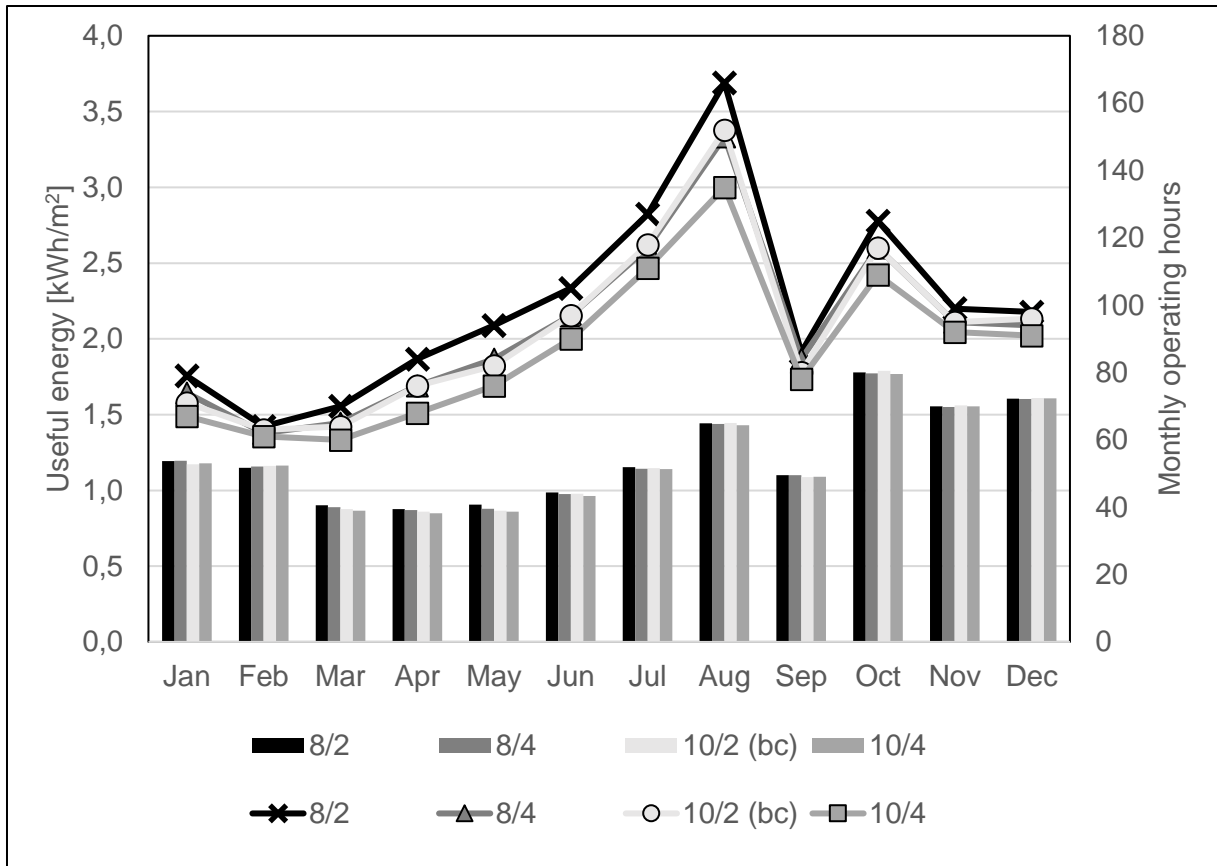


Figure 5-10: Monthly values of useful energy (column) and operational hours (line) when varying the dead band

Figure 5-10 shows the correlation between the monthly useful energy gain collected and the monthly operational time of the BIPV/T system. The 8/2 dead band shows larger monthly values of both the collected useful energy and operational hours. Figure 5-9 shows that the 8/2 dead band has the lowest value of thermal efficiency. This means that the strategy with the lowest value of monthly thermal efficiency is not necessarily the one with lowest value of monthly useful energy gain, as the operational time of the system is increased.

5.4.2 Size of Storage Tank

In order to find the optimal size of the water storage tank, a range from 300 l to 2 000 l has been analysed through annual simulations. The tank height is limited by the ceiling height, and thus the height to diameter ratio of the hot water tank is set to 2 for all simulations. The initial water temperature of the tank is set to 20°C with a total of 10 temperature nodes. The effects of varying the volume of the water storage tank can be seen from Figure 5-11 and Figure 5-12.

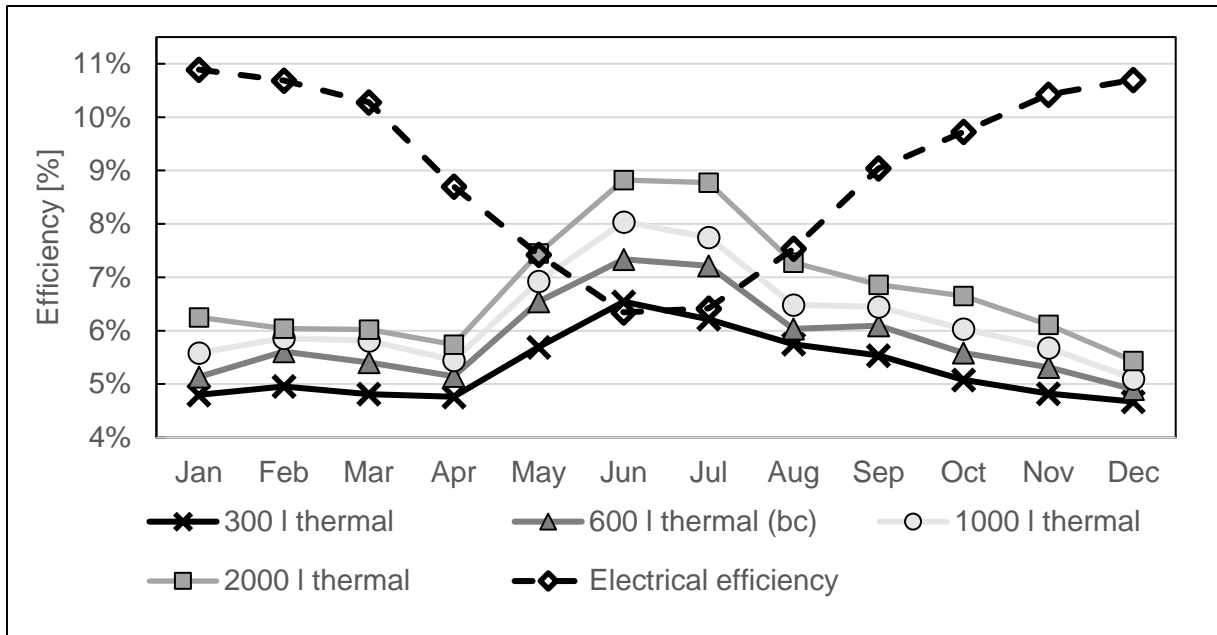


Figure 5-11: Monthly values of thermal and electrical efficiency when varying the storage tank volume

Figure 5-11 shows increased thermal efficiency when increasing the size of the storage tank up to 2 000 l, especially for the summer months. The peak thermal efficiency 8.82% is reached in June. The difference in monthly thermal efficiency between the 2 000 l tank and the base case tank is 1.48 % in June. The difference in thermal efficiency is higher during summer months but is still visible in the period from August to April.

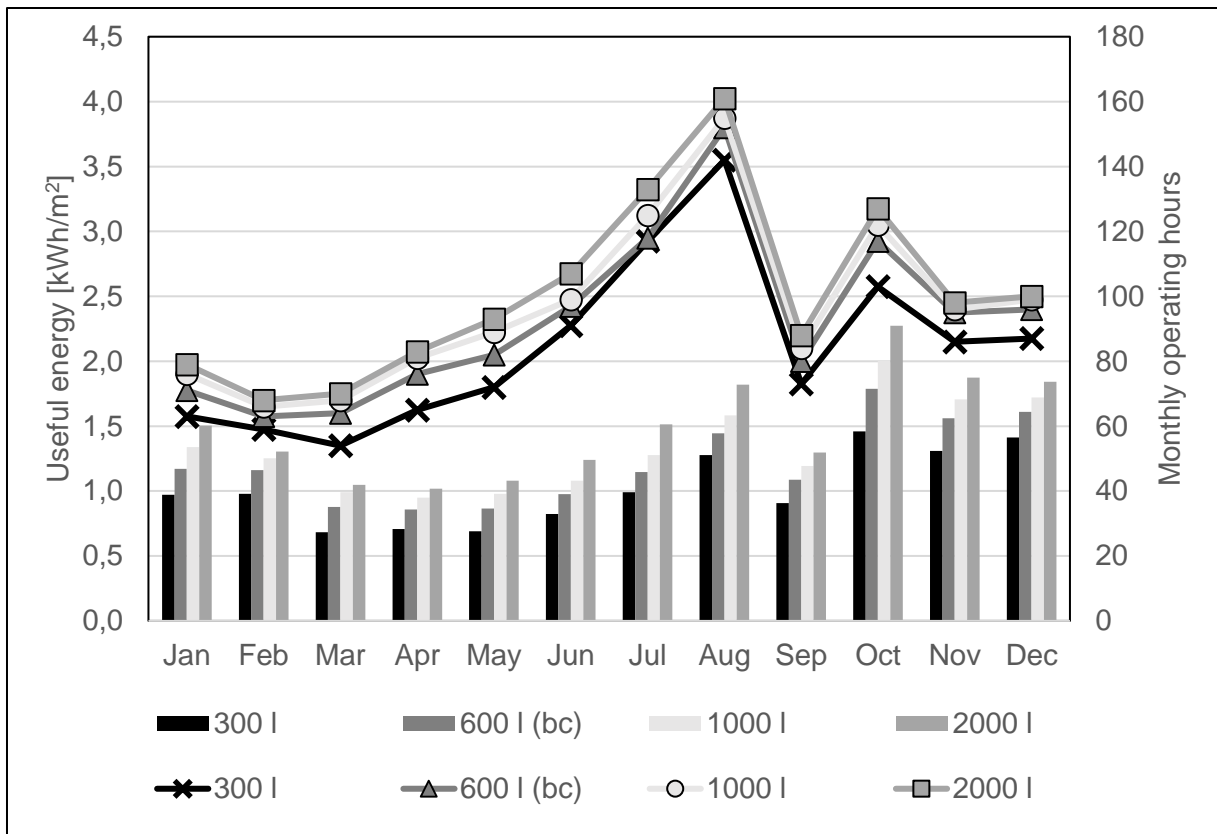


Figure 5-12: Monthly values of useful energy (column) and operational hours (line) when varying storage volume

Figure 5-12 shows great resemblance between the monthly values of operating hours and the useful energy collected by the BIPV/T system. The variation of collected useful energy by varying the storage tank is prominent in all months of the annual simulation. The figure shows that both the monthly collected useful energy and the number of monthly operating hours increases with the increase of storage volume. However, reduced effect is seen after the storage volume is increased from 300 l to 600 l. The increase of storage volume improves the stratification, i.e. increases the temperature difference between the inlet and the outlet of the BIPV/T component. As a result, the BIPV/T system will operate more frequently as values will be more in agreement with the upper and lower dead band set in the controller.

5.4.3 Specific Flow Rate

The specific flow rates that have been used in the test range is shown in

Table 12. Due to limitations in the TRNSYS model, it was not possible to test for a higher flow rates than the maximum value of the testing range. Optimally, a test range with higher flow rates like the values described in subchapter 2.5.5 should be simulated. However, a wide

range of mass flow rates have been tested and the effects on the system performance are shown in Figure 5-13 and Figure 5-14.

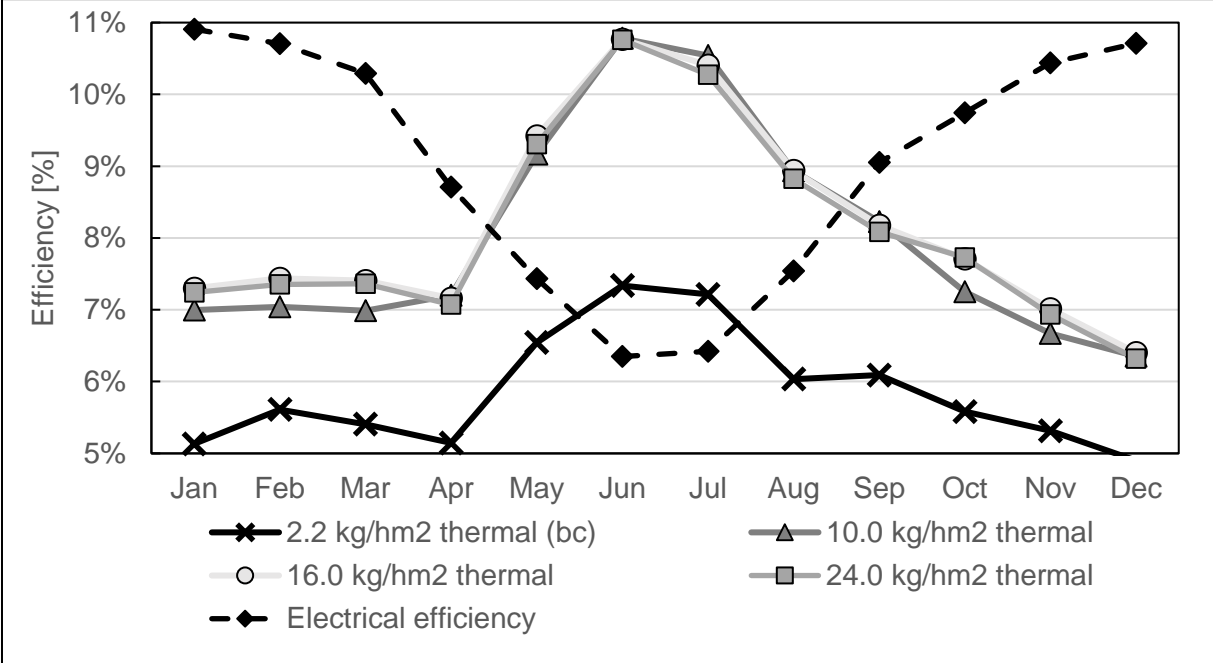


Figure 5-13: Monthly values of thermal and electrical efficiency when varying the specific flow rate

A significant rise in thermal efficiency can be seen when increasing the specific flow rate from the base case value to 10 kg/hm². Further increase shows limited effect on the thermal efficiency, as the same peak value is reached for all flow rates over 2.2 kg/hm². However, small differences are noticed between January and April and between September and December when increasing the specific flow rate from 10 kg/hm² to 24 kg/hm². The peak value of the three higher flow rates is 10.77%, which is significantly higher than the 7.34% reached with the base case flow rate. The period between April and August shows the largest increase in thermal efficiency for all values within the test range.

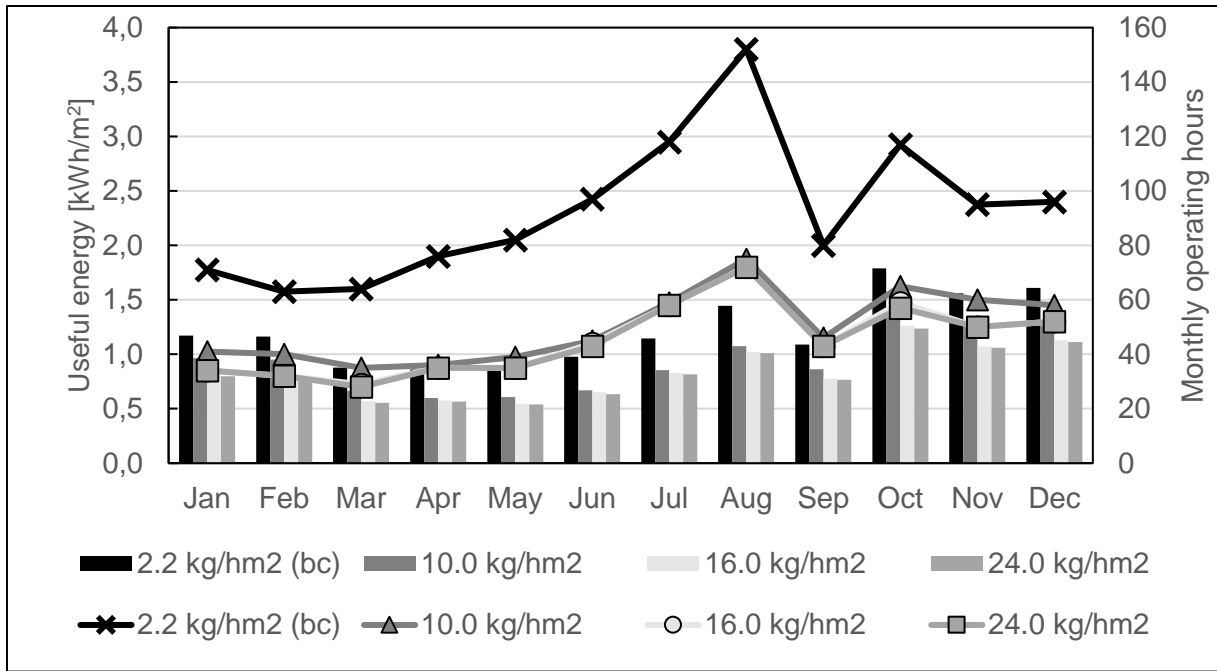


Figure 5-14: Monthly values of useful energy (column) and operational hours (line) when varying the specific flow rate

While the thermal efficiency of the lower flow rate showed in Figure 5-13 was significantly lower than for the other flow rates, the opposite is the case for the number of monthly operating hours. The system with 2.2 kg/hm² flow rate operates twice as many hours (152 compared to 72) as the systems with the other flow rates during August, i.e. when the peak value of monthly operating hours occurs. More operating hours naturally lead to a larger amount of collected useful energy, as seen from the columns in Figure 5-14. Minor changes in monthly operating hours occur at the same time as the minor changes in thermal efficiency from Figure 5-13 when increasing the flow rate from 10 kg/hm² to 16 kg/hm². No changes in monthly operating hours, and very small changes in collected useful energy, are seen when further increasing the flow rate from 16 kg/hm² to 24 kg/hm².

5.4.4 Inlet from Heat Source

The inlet water flowing from the BIPV/T to the water tank is simulated within a test range presented in

Table 12, where the heights specified are given as the distance from the bottom of the tank. The top of the tank is the base case inlet height of 1.45 m. A large range of inlet heights are simulated and the results are presented in Figure 5-15 and Figure 5-16.

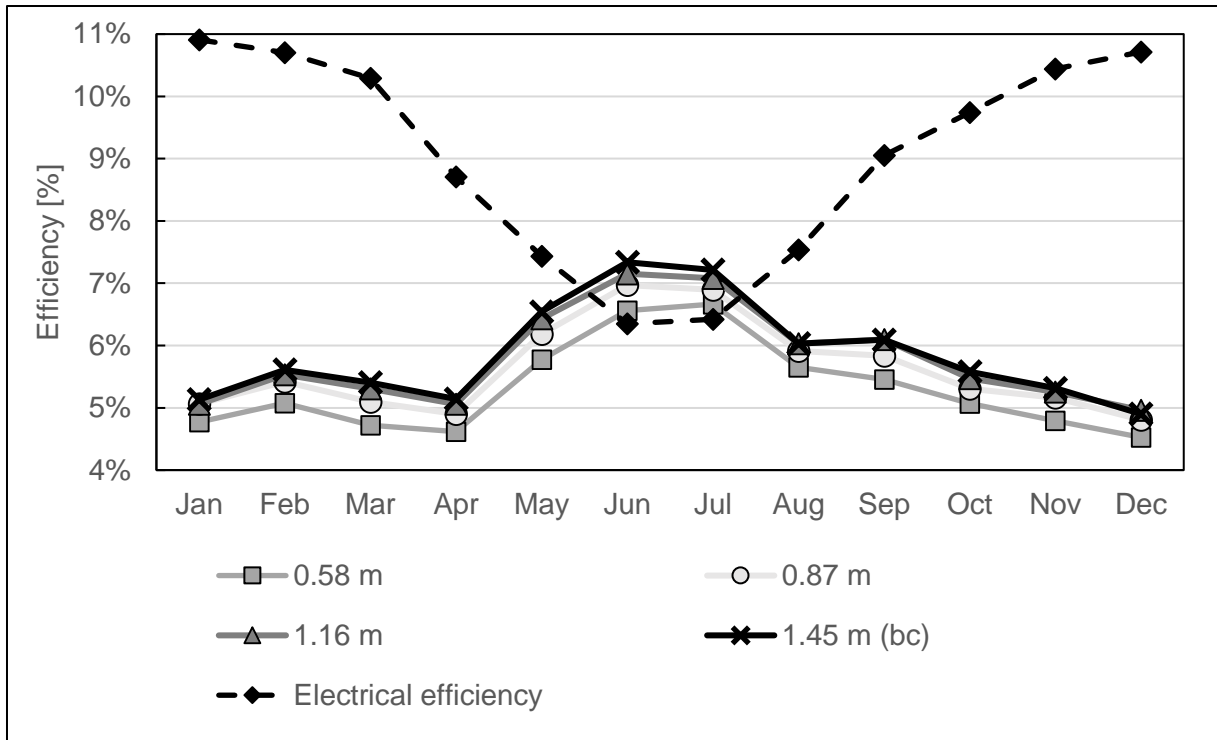


Figure 5-15: Monthly values of thermal and electrical efficiency when varying the inlet height from the heat source

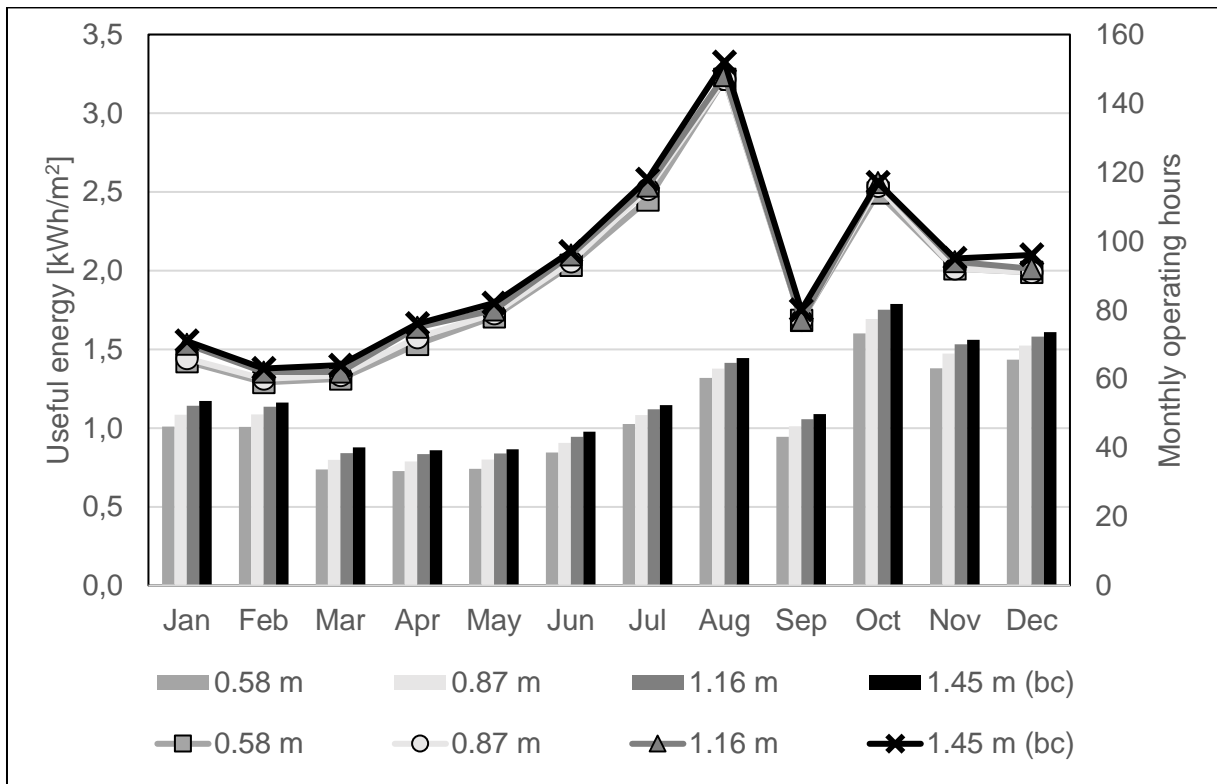


Figure 5-16: Monthly values of useful energy (column) and operational hours (line) when varying the inlet height from the heat source

From Figure 5-15 and Figure 5-16 it is noticed that a higher inlet from the heat source slightly increases the monthly thermal efficiency and the useful energy collected. Minor decrease in the number of monthly operating hours are seen in Figure 5-16 for decreasing inlet heights. All in all, none of the simulated inlet heights improve the system performance compared to the base case.

5.4.5 Inlet from Cold Side

The mains water that enters the tank of the BIPV/T is varied according to the test range given in Table 12. The heights specified are given as the height above the bottom of the tank. The effect of varying the inlet height is given in Figure 5-17 and Figure 5-18.

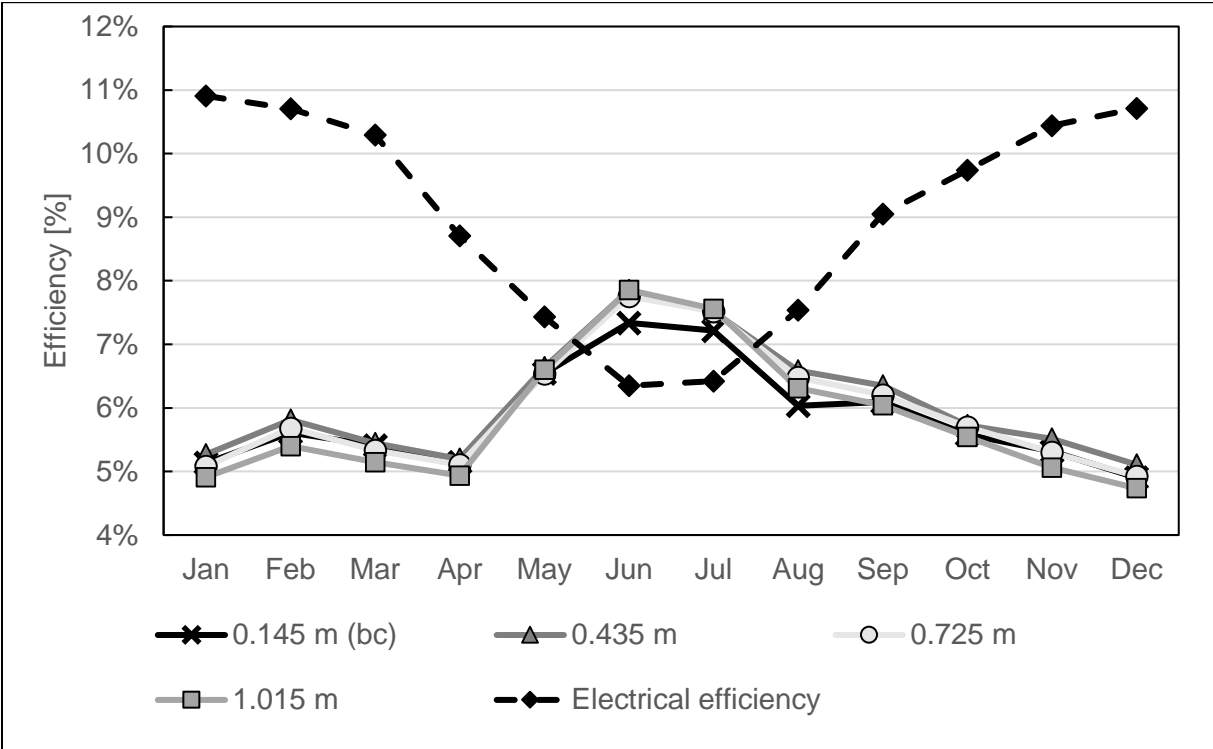


Figure 5-17: Monthly values of thermal and electrical efficiency when varying the inlet height from the cold side

A slight change in thermal efficiency is noticed when increasing the height of the cold side inlet. The highest value can be seen for the inlet position of 1.015 m with a peak of 7.85%, whereas the lowest value can be seen for the base case showing a peak of 7.34%. When increasing the inlet height further, minimal improvement in thermal efficiency is seen.

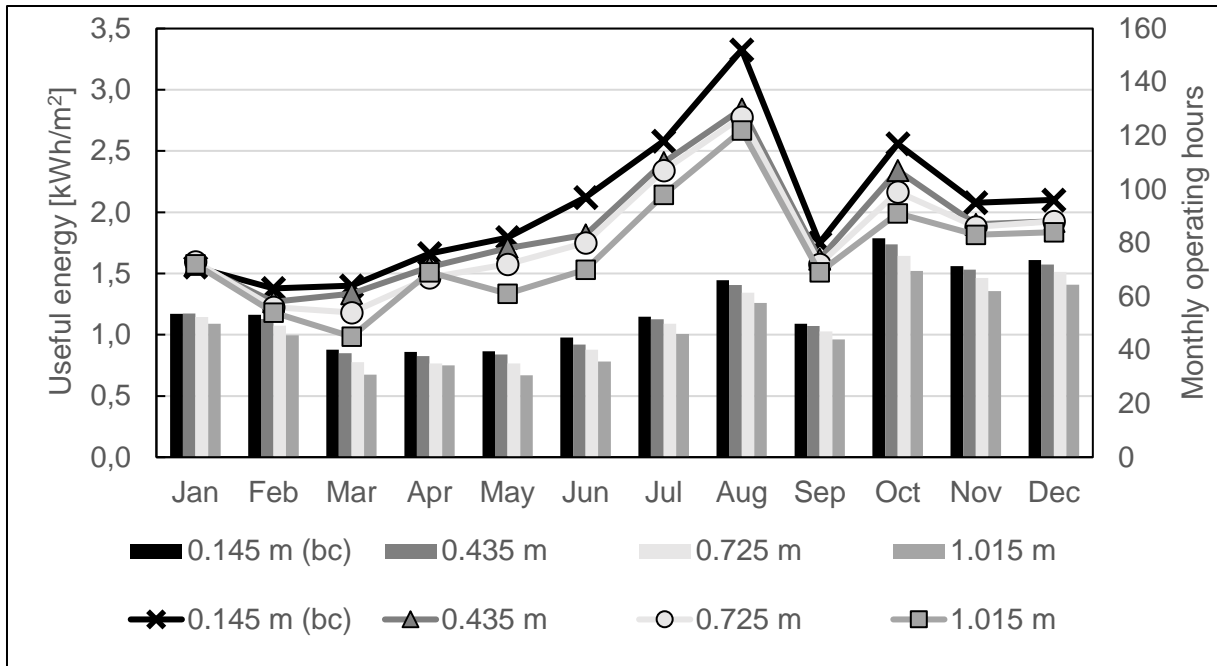


Figure 5-18: Monthly values of useful energy (column) and operational hours (line) when varying the inlet height from cold side

Figure 5-18 shows that the useful energy collected increases along with the number of operating hours. The largest value is seen for the base case and the lowest value for the inlet height of 1.015 m. The results show contrasts between the thermal efficiency shown in Figure 5-17, where the opposite order was shown. This may be because the controller operates based on the temperature in the bottom of the tank, where cooler water is supplied. This causes more frequent operation, resulting in higher monthly values of useful energy. The operation may start during periods with low amounts of solar radiation which again will reduce the thermal efficiency observed in the system.

5.4.6 Summary

- The variation in dead band showed some effect on collected useful energy and monthly operating hours, where the base case showed the highest number of operating hours but the smallest value of thermal efficiency.
- When increasing the storage tank volume, it was observed that the thermal efficiency increased as well as the useful energy gain. The largest tank (2 000 l) showed the best results.
- The increase in specific flow rate showed an increase in thermal efficiency but the collected useful energy as well as the operational time was reduced. The base case,

with the smallest value of specific flow rate, showed significantly higher amounts of useful energy collected and increased operational time compared to the other tested flow rates.

- The variation of the heat source inlet showed that the base case value gave the highest amount of thermal efficiency and collected useful energy. When changing the inlet height from the cold side, the base case showed the highest amount of useful energy collected but the thermal efficiency was somewhat reduced.

There was no noticeable change in electrical efficiency within the tested range. As mentioned earlier, the program with the given model would not allow for larger values of specific flow rate to be tested. This is a clear limitation in the optimisation, however the testing range simulated still showed variation in the thermal efficiency and collected useful energy.

The solar fraction accounts for the power needed to run the pump and the auxiliary power needed to increase the temperature of the DHW that is not being sufficiently heated by the BIPV/T system, and thus provides a good indication of the overall performance of the BIPV/T system. Based on the solar fractions the most favourable system parameter is chosen. The solar fractions for the various system parameters with corresponding testing ranges can be seen in Table 13.

Table 13: Solar fractions for various system parameters and test ranges

<i>System parameter</i>	<i>Test range</i>	<i>Annual solar fraction</i>	
		<i>Thermal</i>	<i>Electrical</i>
Dead band [on/off]	8/2	0.368	0.461
	8/4	0.367	0.461
	10/2 (bc)	0.366	0.461
	10/4	0.365	0.461
Storage tank [l]	300	0.316	0.461
	600 (bc)	0.366	0.461
	1000	0.393	0.461
	2000	0.416	0.461
Specific flow rate [kg/hm ²]	2.2 (bc)	0.366	0.461
	10	0.290	0.463
	16	0.258	0.463
	24	0.254	0.463
Inlet from heat source [m]	0.58	0.323	0.461
	0.87	0.343	0.461
	1.16	0.357	0.461
	1.45 (bc)	0.366	0.461
Inlet from cold side [m]	0.145 (bc)	0.366	0.461
	0.435	0.283	0.461
	0.725	0.341	0.461
	1.015	0.32	0.46

5.4.7 Optimised GEL model

The final water based BIPV/T model is chosen based on the solar fractions given in Table 13. The electrical solar fractions showed no or small changes in the optimisation process. As a consequence, only the thermal solar fractions were considered when choosing the new value of each system parameter. It should be noted that many of the system parameters are dependent on each other. When several system parameters are varied from the base case, the change collectively may not be as significant as the sum of the change in solar fractions shown individually in Table 13, where the remainder of the system parameters are kept constant. However, this simplified method is chosen and is considered reasonable in order to improve the model. The final values of system parameters can be seen in Table 14.

Table 14: Chosen values of the final water based BIPV/T system

<i>System parameter</i>	<i>Value</i>
Dead band [on/off]	8/2
Size of storage tank [l]	2000
Specific flow rate [kg/hm ²]	2.2
Inlet from heat source [m]	1.45
Inlet from cold side [m]	0.145

5.5 Air Based BIPV/T System

The heat exchanger used in the air based BIPV/T model is TYPE 91, which provides a constant efficiency. The efficiency is set as a parameter to a default value of 0.6. This is a simplification of the heat transfer that occurs between the hot side and the cold side, i.e. the outlet air temperature of the BIPV/T component and outlet water. Optimally, a heat exchanger component with a validated performance should be used in order to represent the heat exchanger more realistically. In the air based BIPV/T system, the inlet temperature from the heat source refers to the heat transfer from the heat exchanger in contrast to the water based system where heat is transferred directly between the BIPV/T component and the water storage tank.

The fan power is set to the TRNSYS default value of 277.8 W and is used for all simulations involving the air based BIPV/T. The remainder of the BIPV/T system is the same as in the

previously mentioned GEL model using water based BIPV/T. The values are presented in Table 15:

Table 15: Base case values for the air based BIPV/T system

<i>Base case parameters</i>	<i>Values</i>
BIPV/T collector area [m ²]	45.9
Inclination angle [°]	90°
Inverter efficiency [%]	78
Size of storage tank [l]	600
Tank height to diameter ratio	2
Tank height [m]	1.45
Mass flow rate [kg/hm ²]	10.89
Auxiliary set point [°C]	60
DHW set point [°C]	45
Dead band on/off [°C]	10/2
DHW demand [l]	387
Tank inlet from heat source [m]	1.45
Tank inlet from cold side [m]	0.145

As for the water based system, it is chosen to evaluate five system parameters based on four simulations per parameter. The chosen parameters and the test range is seen Table 16. The base case values are denoted as “bc” in all figures presented regarding the optimisation of the air based BIPV/T system.

When presenting the results of the air based BIPV/T, the thermal efficiency, electrical efficiency, useful energy and operational hours are presented. The thermal efficiency presented is calculated by using the useful energy collected by the BIPV/T component, while the useful energy presented is the useful energy collected by the tank and is given in kWh/m² of office building area. Because the air based BIPV/T delivers heat to the tank through a heat

exchanger, the useful energy collected by the BIPV/T component is larger than the useful energy collected by the tank.

Table 16: Optimisation parameters for air based BIPV/T

<i>Optimisation parameters</i>	<i>Values</i>			
Dead band [on/off]	8/2	8/4	10/2	10/4
Size of storage tank [l]	300	600	1000	2000
Specific flow rate [kg/hm ²]	10.89	21.79	43.57	65.36
Inlet from heat source [m]	0.58	0.87	1.16	1.45
Inlet from cold side [m]	0.145	0.435	0.725	1.015

5.5.1 Dead Band

The dead band is varied according to the values provided in Table 16 and within the same range as for the water based BIPV/T. The effects of adjustments can be seen in Figure 5-19 and Figure 5-20:

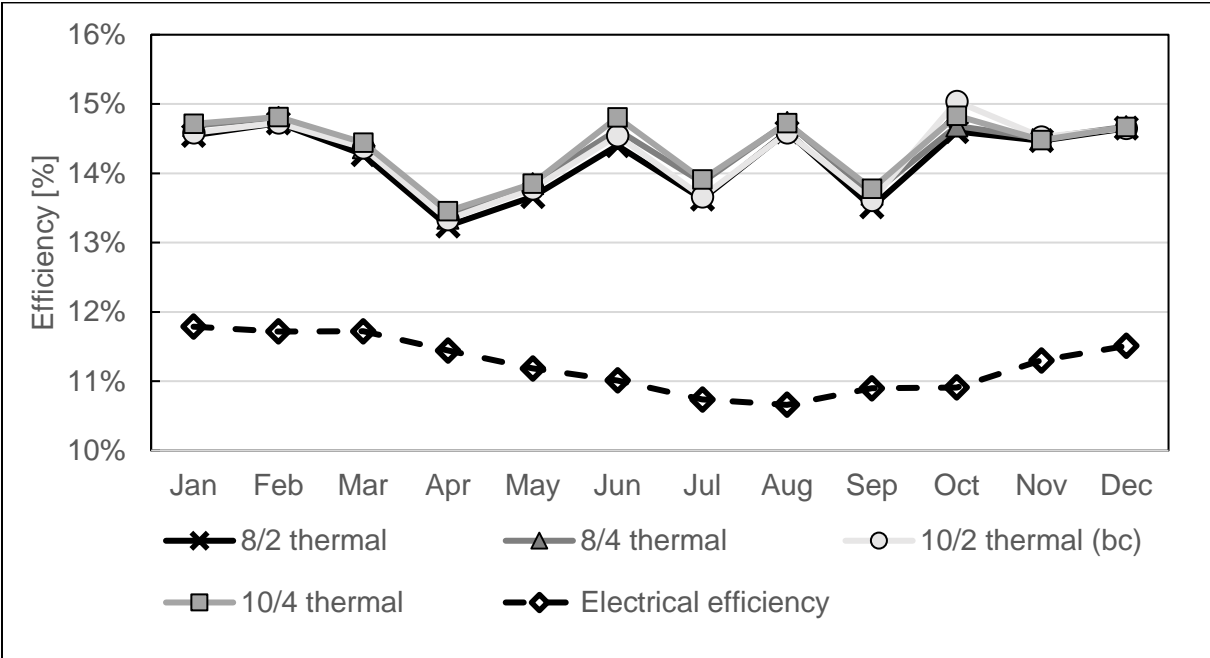


Figure 5-19: Monthly values of thermal and electrical efficiency when varying dead bands

The thermal efficiency of the air based BIPV/T changes with respect to time and shows several high and low points during the annual simulation. The variation of the dead band shows a minimal effect on the thermal efficiency with slightly higher values observed throughout the year when using a dead band of 10/4 compared to the base case value. The peaks show values close to 15% for February, June, August and October, while the lowest point can be observed at roughly 13% for the base case dead band.

The electrical efficiency does not show noticeable change during the annual simulations when varying the dead band, as relatively constant values are seen throughout the year with a small reduction during the period from April to November. The maximum value of 11.79% and the minimum value of 10.66% can be seen in January and August, respectively.

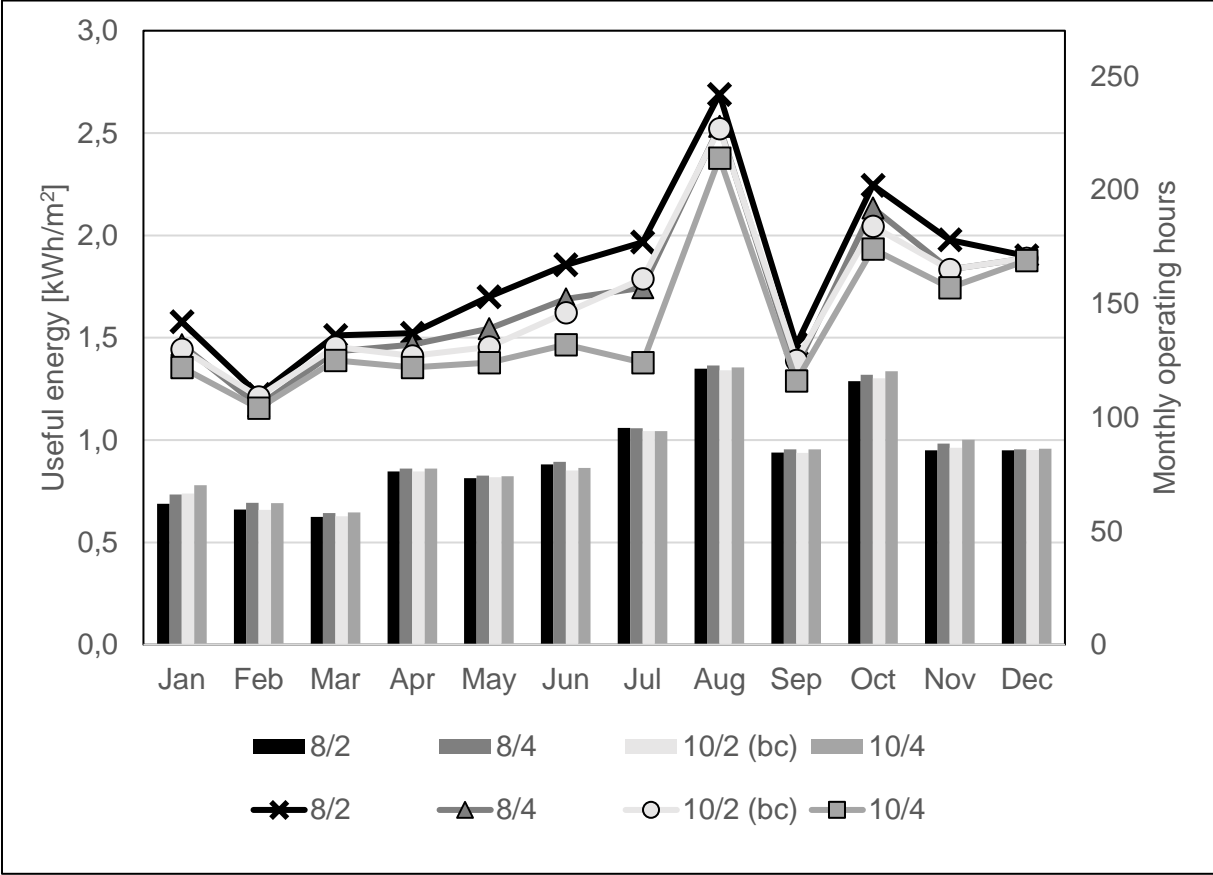


Figure 5-20: Monthly values of useful energy (column) and operational hours (line) when varying the dead band

Figure 5-20 shows that the useful energy collected by the BIPV/T system increases from January to August for all values within the testing range. Two dips in the collected useful energy occur after August and October. Similar values are shown for all the tested dead

bands. A more noticeable change can be seen in the operating hours, where the 8/2 dead band peaks at 242 hours of operation while the base case peaks at 227 hours.

5.5.2 Size of Storage Tank

The same testing range for storage volume and height to diameter ratio is used for the air and water based BIPV/T as the size of the water storage tank is dimensioned based on the DHW load, which is common for the two models. The test range is seen in Table 16 and the effects of varying the water storage tank can be seen from Figure 5-21 and Figure 5-22.

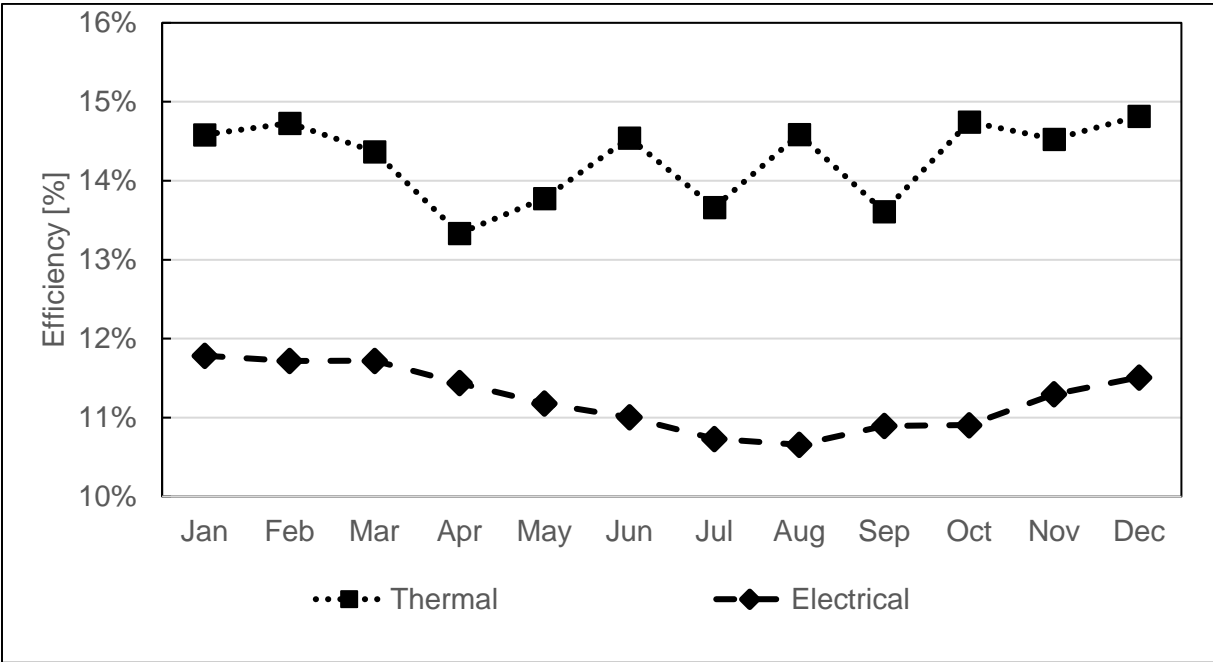


Figure 5-21: Monthly values of thermal and electrical efficiency when varying the storage tank volume

The monthly electrical and thermal efficiencies are the same for all variations of storage tank volume and is presented in the two graphs presented in Figure 5-21. The change in storage tank does not affect the performance of the air based BIPV/T system. The thermal and electrical efficiency is the same as the base case values presented in previous optimisation of system parameters. The peak of electrical and thermal efficiency reaches 10.89% and 14.82%, respectively and the lowest points are observed at 6.42% and 13.33% respectively.

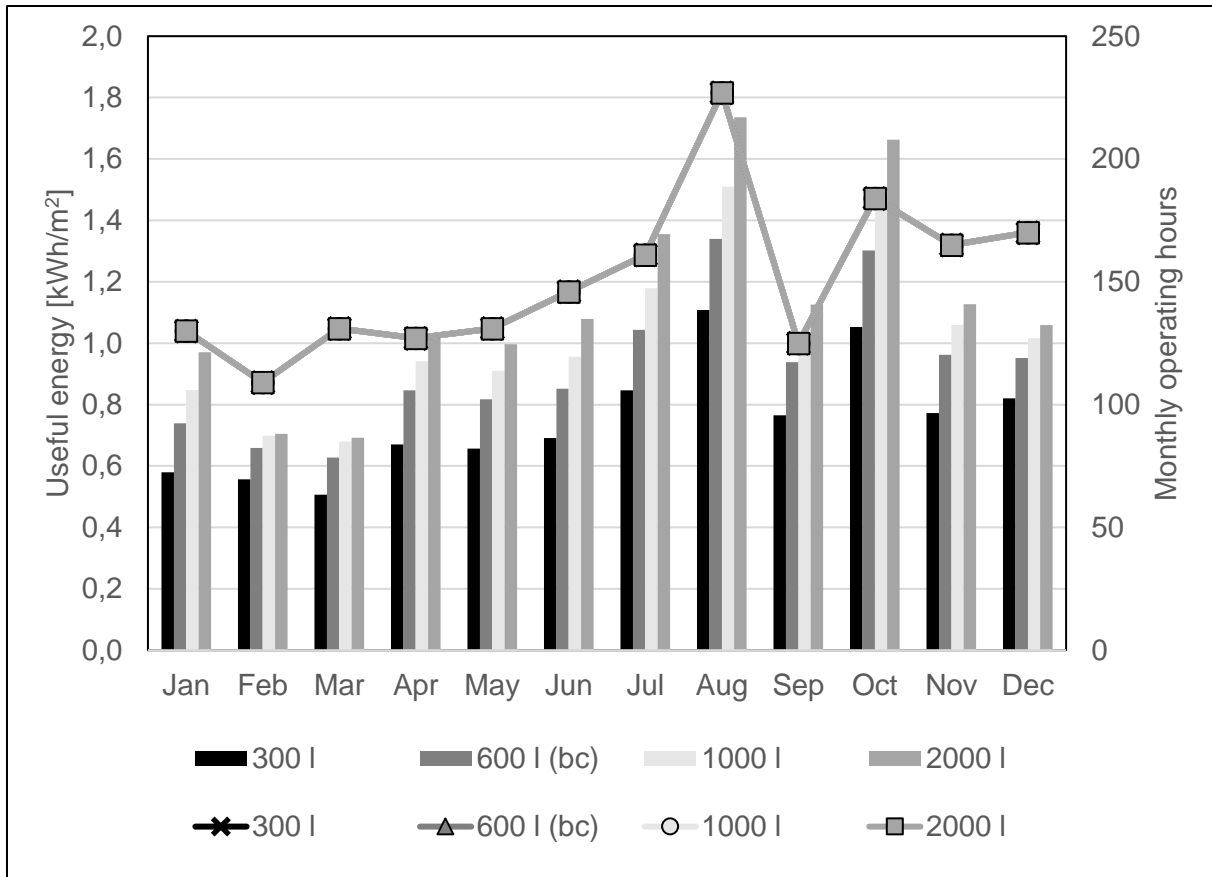


Figure 5-22: Monthly values of useful energy (column) and operational hours (line) when varying the storage volume

The monthly useful energy collected by the BIPV/T system increases with larger storage tank volumes. The highest peak value of useful energy in August can be seen in the storage tank of 2 000 l. The operational hours are independent of the increase in storage tank volume and are the same for all variations within the test range. This is because the dead band is set according to the temperature difference between the ambient air and the outlet air of the air based BIPV/T component, in contrast to the water based BIPV/T model, which uses the bottom tank temperature as the lower temperature input to the controller. As a consequence, any configuration performed on the tank will not have an effect on the operating hours of the air based BIPV/T system.

5.5.3 Specific Flow Rate

It was possible to test a greater range of specific flow rate values for the BIPV/T air but still it was not possible to test for flow rates higher than the upper limit of the testing range given in Table 16. Flow rates closer to the ones described in 2.5.5 was tested for the air based BIPV/T

compared to that of the water based. The results of varying the specific flow rate within the test range can be seen in Figure 5-23, Figure 5-24 and Figure 5-25.

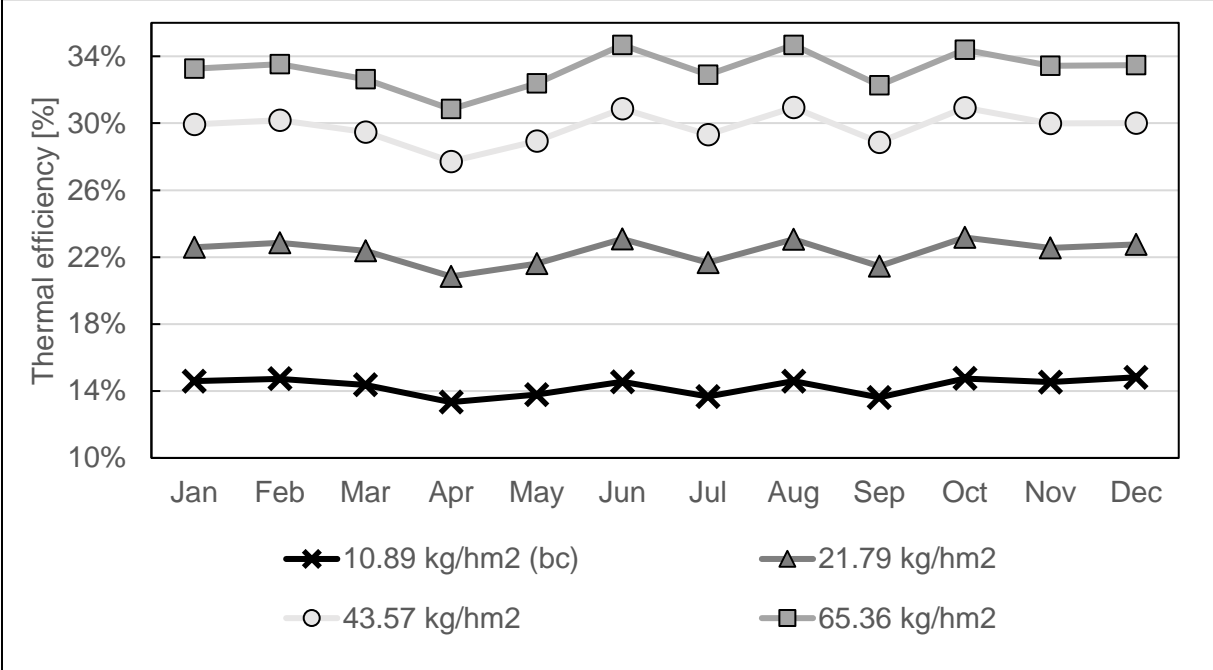


Figure 5-23: Monthly values of thermal efficiency when varying the specific flow rate

As seen from Figure 5-23, the monthly thermal efficiencies for the tested range of specific flow rates show relatively constant values, with large differences in thermal efficiency for the test range. The thermal efficiency increases with the specific flow rate and the highest value can be seen for the specific flow rate of 65.36 kg/hm² with peak values of 34.7% for June, August and October.

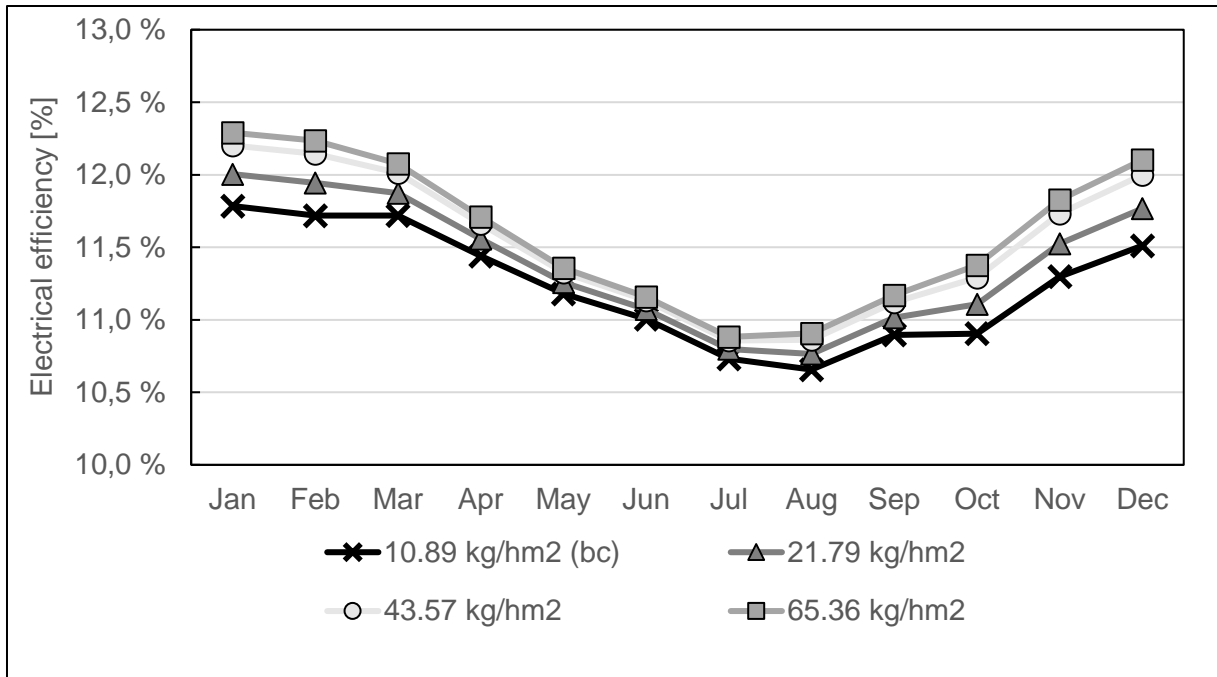


Figure 5-24: Monthly values of electrical efficiency when varying the specific flow rate

The electrical efficiency peaks in January for all the tested values and decreases with time to the lowest point in August, as shown in Figure 5-24. The tested range of specific flow rate shows small but noticeable changes in electrical efficiency, with a peak and low point values of 12.29% and 10.88%, respectively when using a specific flow rate of 65.36 kg/hm² compared to the corresponding base case values of 11.78% and 10.66%.

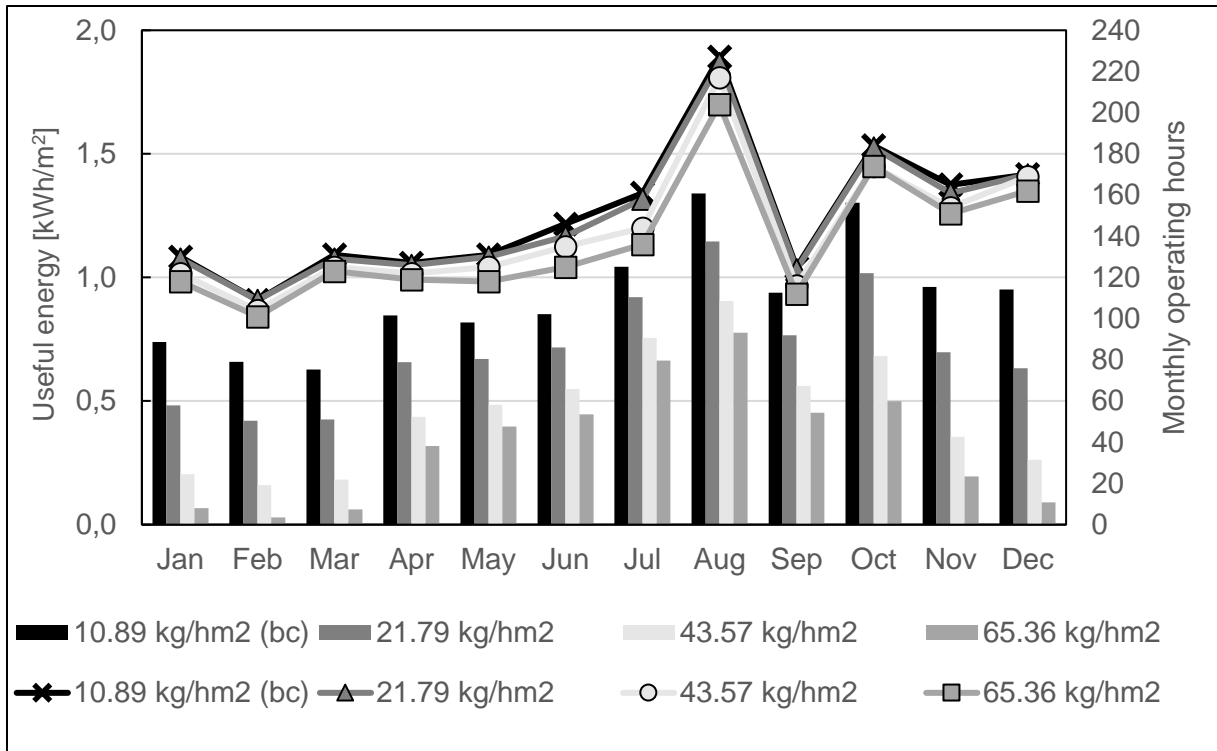


Figure 5-25: Monthly values of useful energy (column) and operational hours (line) when varying the specific flow rate

From Figure 5-25 it can be seen that the useful energy collected increases with the operational hours of the BIPV/T system. The highest value of useful energy can be seen from the base case value, which showed the smallest value of thermal and electrical efficiency shown in Figure 5-23 and Figure 5-24, respectively.

5.5.4 Inlet from Heat Source

In the air based BIPV/T system, the inlet heat source is defined as the temperature of the water going out of the heat exchanger and into the storage tank. It is the heat transferred from the BIPV/T with a loss in efficiency due to the heat exchange between two different heat transfer mediums. The tested inlet heights from the heat exchanger are seen from Table 16, where the heights specified are given as the height above the bottom of the tank. The effect of varying this parameter can be seen in Figure 5-26.

The electrical and thermal efficiencies do not change when varying the inlet from the heat source. The respective values are the same as the ones presented earlier in Figure 5-21.

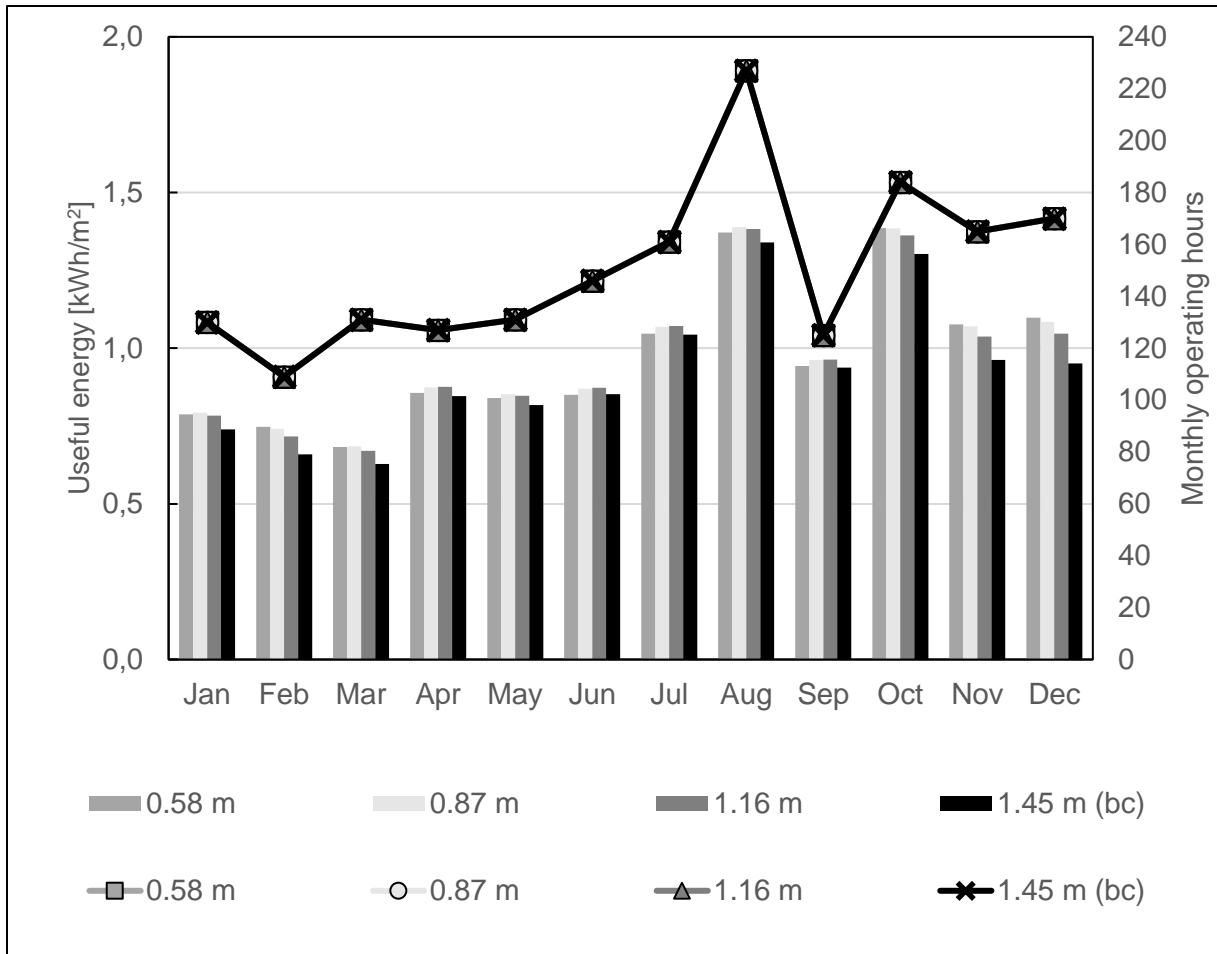


Figure 5-26: Monthly values of useful energy (column) and operational hours (line) when varying the inlet from the heat source

The inlet height at 0.87 m is shown to provide the largest value of useful energy collected over the year. The useful energy is similar in value for the remaining test range, where the base case showed the lowest value of collected useful energy. The number of operating hours are constant for all values of inlet heights in the testing range, because of the control strategy of the air based BIPV/T system as described in subchapter 5.5.2.

5.5.5 Inlet from Cold Side

The mains water that enters the tank of the BIPV/T is varied according to the test range given in . The heights specified are given as the height above the bottom of the tank. The effect of varying the inlet height is given in Figure 5-27.

The electrical and thermal efficiencies do not change when varying the inlet from the cold side. The respective values are the same as the ones presented earlier in Figure 5-21.

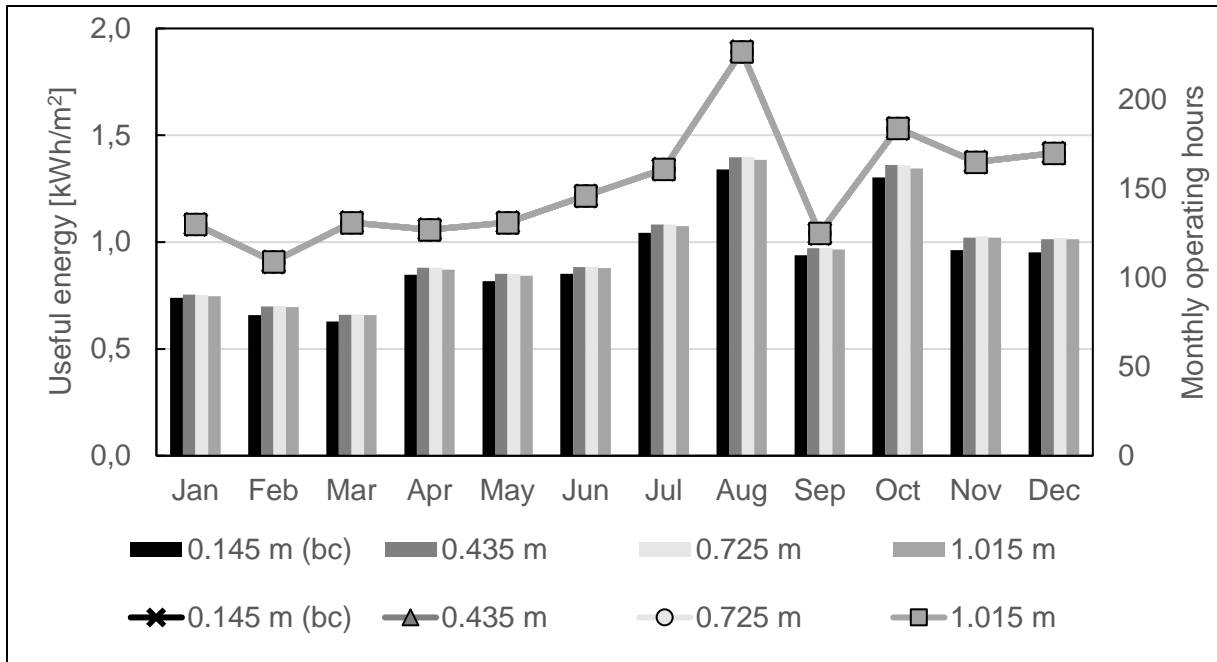


Figure 5-27: Monthly values of useful energy (column) and operational hours (line) when varying the inlet from the cold side

The useful energy collected by the BIPV/T system shows similar values for the tested range, where the base case demonstrates a slightly smaller value compared to the other inlet heights as shown in Figure 5-27. There is no variation in operating hours because of the regulatory strategy implemented in the air based BIPV/T system as described in subchapter 5.5.2.

5.5.6 Summary

- The variation of dead band values showed minimal differences in the collected useful energy with slightly higher values with the 10/4 dead band.
- The change in storage tank showed no effect on the thermal efficiency of the BIPV/T component because of the control strategy used in the BIPV/T system. However, a change in storage tank volume had great impact on the useful energy collected by the tank from the heat exchanger, with the greatest amount collected with the storage tank of 2 000 l.
- The increase of specific flow rate had a great positive impact on the thermal efficiency of the BIPV/T system, and showed a doubling in thermal efficiency between the base case and the flow rate of 65.36 kg/hm². However, the collected useful energy and the operational hours showed larger values for the base case.

- The change in inlet height from the heat exchanger showed no impact on the thermal efficiency and the operational hours of the BIPV/T system. A slightly larger amount of useful energy was collected with a tank inlet height of 0.87 m.
- Variations in the cold side inlet height also showed no impact on the thermal efficiency and the operational hours. Minimal difference was shown within the test range with regards to the useful energy, where the base case showed a slightly lower value.

The electrical efficiency was only improved when varying the specific flow rate, where an increase in efficiency was seen for increased flow rates. The tested range of specific flow rates was also limited in the air based BIPV/T model, but a wide range was still simulated and analysed.

The solar fraction is also used when assessing the air based BIPV/T system to assess the overall efficiency and serves as a basis for choosing the values of the system parameters. The solar fractions obtained by simulations can be seen in Table 17:

Table 17: Solar fractions for various system parameters and test ranges

<i>System parameter</i>	<i>Test range</i>	<i>Yearly solar fraction</i>	
		<i>Thermal</i>	<i>Electrical</i>
Dead band [on/off]	8/2	0.266	0.720
	8/4	0.272	0.724
	10/2 (bc)	0.268	0.724
	10/4	0.274	0.728
Storage tank [l]	300	0.226	0.724
	600 (bc)	0.268	0.724
	1000	0.288	0.724
	2000	0.303	0.724
Specific flow rate [kg/hm ²]	10.89 (bc)	0.268	0.724
	21.79	0.210	0.736
	43.57	0.138	0.747
	65.36	0.101	0.753
Inlet from heat source [m]	0.58	0.277	0.724
	0.87	0.279	0.724
	1.16	0.275	0.724
	1.45 (bc)	0.268	0.724
Inlet from cold side [m]	0.145 (bc)	0.268	0.724
	0.435	0.274	0.724
	0.725	0.274	0.724
	1.015	0.271	0.724

5.5.7 Optimised GEL model

The variation of values within the system parameters shows greater impact on the thermal solar fraction compared to the electrical, as seen in Table 17. Some changes can be seen in the electrical solar fraction but it is considered to be of less importance to the overall performance of the system, thus it is not prioritised when choosing the final values of the system parameters. The final values for the system parameters are shown in Table 18.

Table 18: Chosen values of the final air based BIPV/T

<i>System parameter</i>	<i>Value</i>
Dead band [on/off]	10/4
Size of storage tank [l]	2000
Specific flow rate [kg/hm ²]	10.89
Inlet from heat source [m]	0.87
Inlet from cold side [m]	0.435

6 Performance Analysis of GEL BIPV/T System Models

The final GEL BIPV/T system models, with system parameters from the optimisation process in the previous chapter, have been simulated and the results analysed in the following chapter. The BIPV/T air and water systems at the GEL are analysed and compared by assessing the thermal and electrical performance of each system. Results of annual simulations are presented to investigate the long-term performance and daily simulations have been conducted to further assess distinct differences between the systems. Simulation results from a PV façade (BIPV) are introduced as a reference to assess the electrical production of the air and water based BIPV/T systems and the effect of building integration on the building’s energy demand.

6.1 Thermal Performance of BIPV/T

Figure 6-1 shows the difference in thermal efficiency and useful energy collected by the BIPV/T systems. The air based BIPV/T system shows a steady thermal efficiency between 13% – 15%. The efficiency of the water based BIPV/T system peaks in June at 8.41% and is higher from April to August, compared to the rest of the year where the efficiency is steady, around 6%. However, the water based BIPV/T system collects more useful energy than the air based due to losses in the heat exchanger in the air based system. The only exception in April where the collected energy in the air based system exceeds that of the water based.

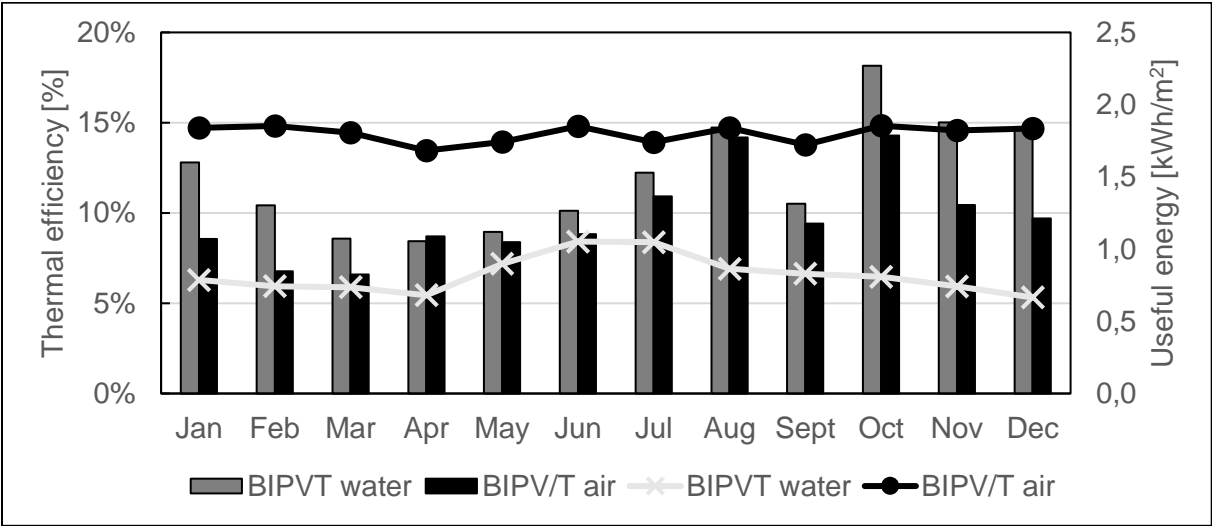


Figure 6-1: Thermal efficiency (line) and useful energy (column) of the water and air based BIPV/T systems

The correlation between the thermal solar fraction and the required auxiliary and pump energies of the water based BIPV/T system can be seen in Figure 6-2. The thermal solar

fraction is higher in the months of lower auxiliary energy demand, which is in correspondence with the increased amount of collected useful energy during the same months, seen in Figure 6-1. The dip in solar fraction in September is a direct result of the smaller amount of useful energy collected during that month.

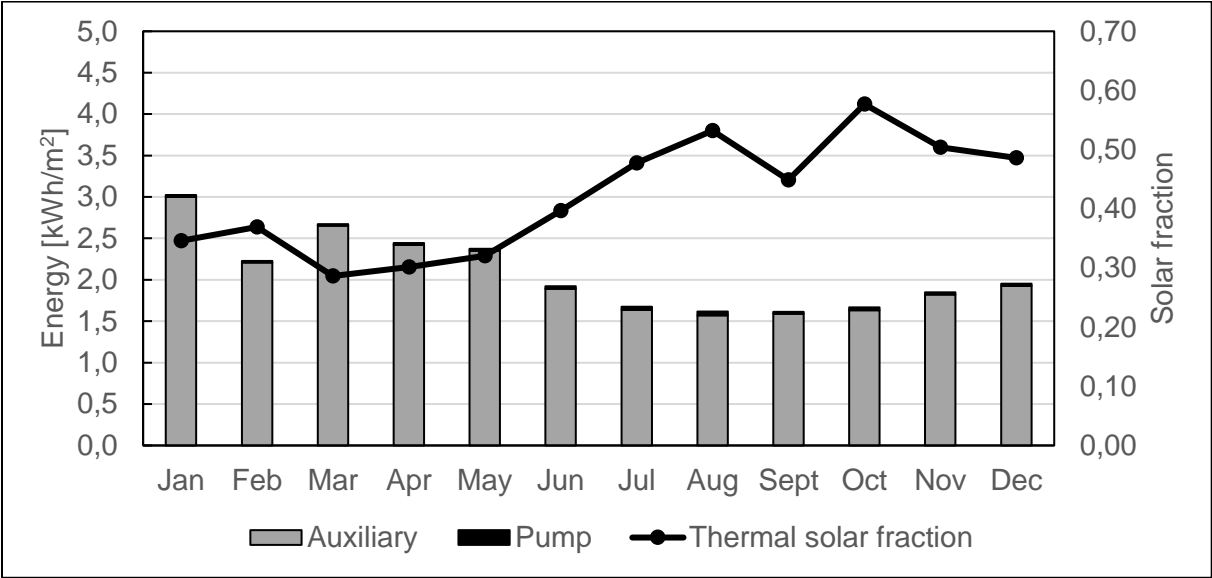


Figure 6-2: Auxiliary and pump energy consumption and thermal solar fraction of the water based BIPV/T system

The same data as in Figure 6-2 are presented for the air based BIPV/T system in Figure 6-3. In addition to lower amounts of collected useful energy, Figure 6-3 shows that the auxiliary energy demand is also higher for the air based BIPV/T system. As a result, the thermal solar fraction is lower for the air based BIPV/T system. As for the water based system, the trend of the thermal solar fraction for the air based system follows that of the useful energy presented in Figure 6-1.

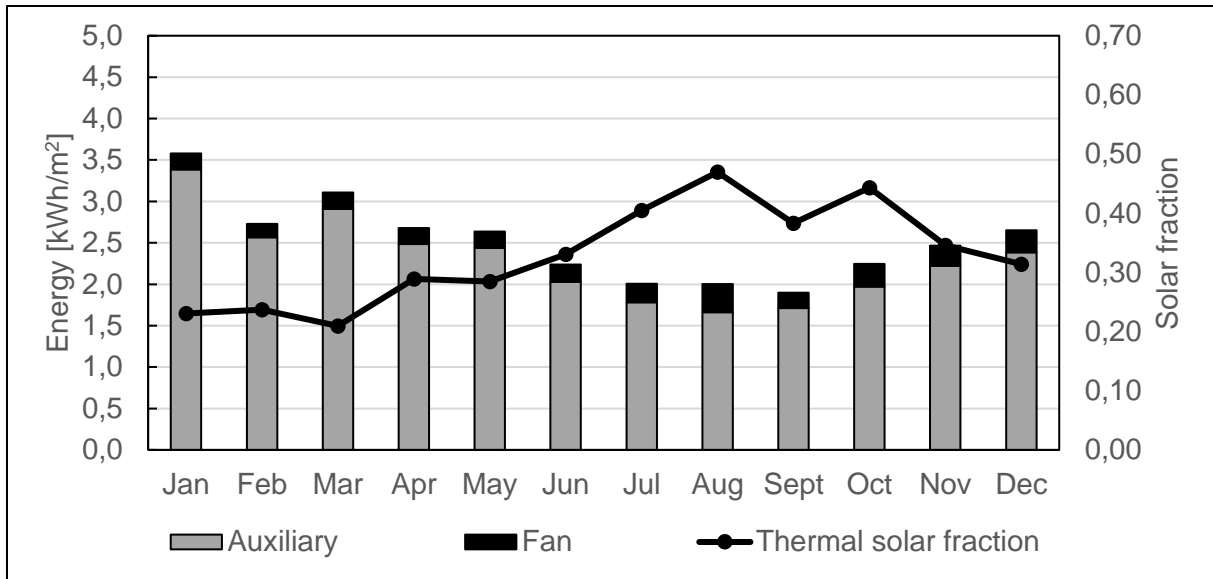


Figure 6-3: Auxiliary and fan energy consumption and thermal solar fraction of the air based BIPV/T system

The air based BIPV/T system presents higher thermal efficiency, as well as more operating hours per month which can be seen in Figure 6-4:

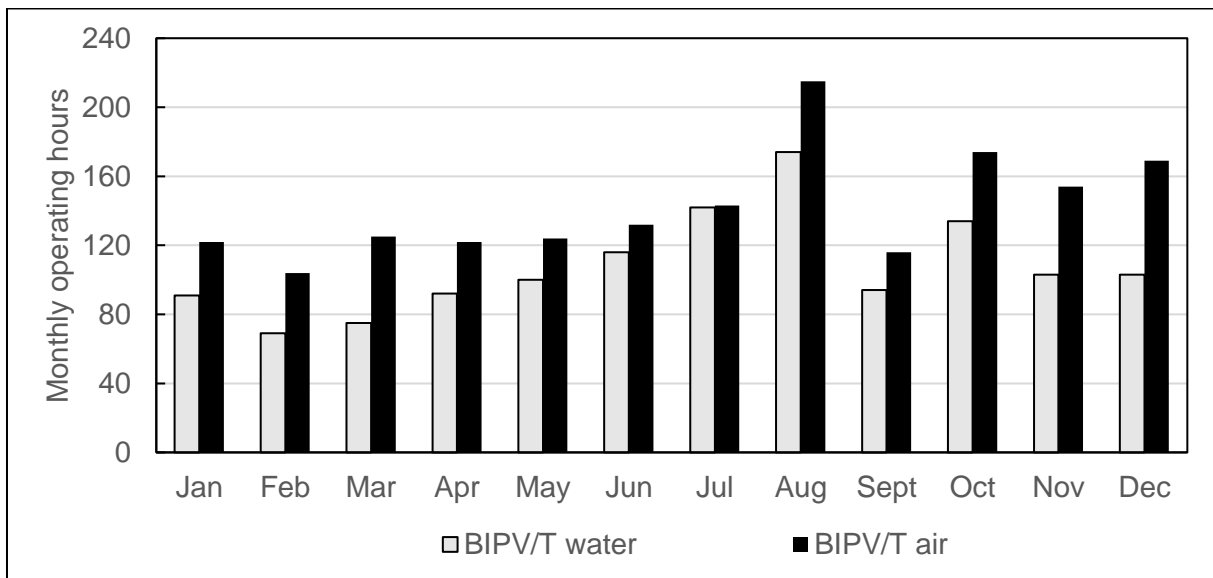


Figure 6-4: Monthly operating hours of the water and air based BIPV/T systems

Thus, it is evident that the 60% efficiency of the heat exchanger in the air based BIPV/T system has a negative impact on the overall system performance, compared to the water based system where water is sent directly into the tank from the BIPV/T outlet without losses.

6.2 Summary

The useful thermal energy output of the air based BIPV/T system is smaller than that of the water based, although the thermal efficiency and the number of monthly operating hours are greater. The reduced useful energy output is caused by the heat exchanger in the system, with an efficiency of 60%, which is the default value suggested by TRNSYS. This highlights the challenge of efficiently transferring heat from the air to the water in the tank. An optimal system design would utilise the heat which is not extracted in the heat exchanger for further use e.g. in an open loop ventilation system. Such a system could possibly reduce the building's heating demand. However, this has not been further investigated in this thesis as a DHW system was chosen to compare the long-term performance of the water and air based BIPV/T technologies.

As seen from the thermal solar fraction, only a small share of the DHW demand can be covered by the BIPV/T. Therefore, the BIPV/T technology may be more suitable as a supplement for thermal energy to e.g. a borehole heat pump system, which is installed at the GEL. By coupling the BIPV/T to the circuit between the boreholes and evaporator inlet, the BIPV/T can increase the inlet fluid temperature of the evaporator and consequently the COP of the heat pump. This may also provide more stable operation for the BIPV/T as the water supplied from the boreholes maintains a low temperature throughout the year.

Furthermore, the façade integrated PV/T receives more solar radiation during the winter months, compared to a roof integrated component. Thus, the façade integrated PV/T will collect more heat during the winter months, when the heating demand is at a maximum.

6.3 Electrical Performance of BIPV/T

The electrical efficiency of the air based BIPV/T system shows efficiencies greater than 11% in the period between November and June. A small dip can be seen between June and September with values slightly below 11%, thus the efficiency can be seen as more or less constant throughout the year as seen from Figure 6-5.

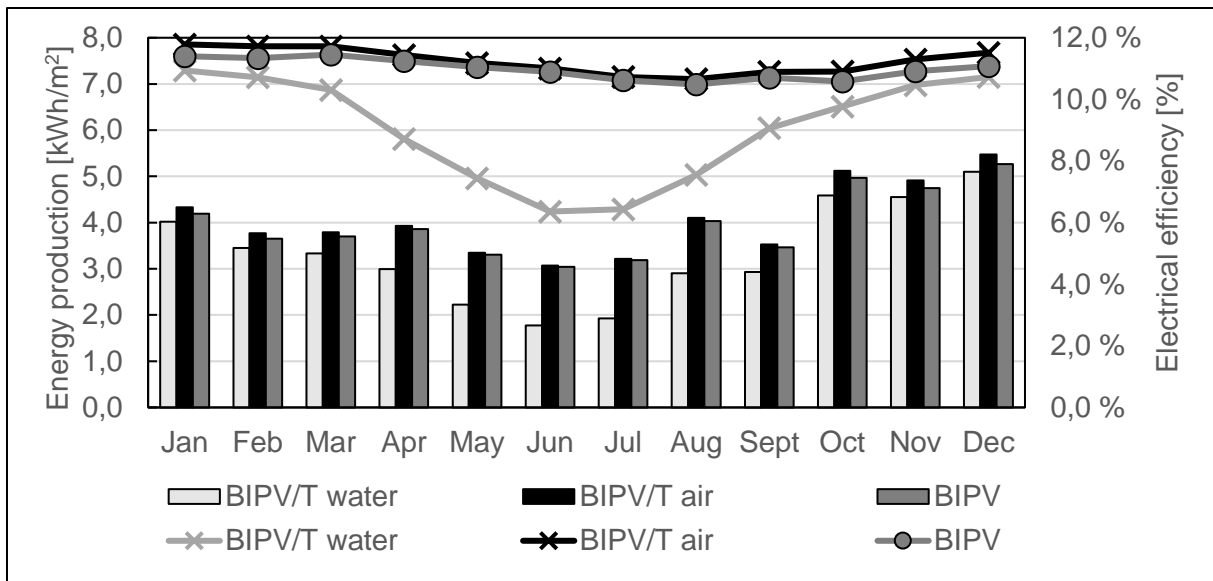


Figure 6-5: Comparison of electrical efficiency and electrical energy production between technologies

The air based BIPV/T shows larger values of electrical efficiency compared to that of the water based and the BIPV reference. The electrical energy production of the air based BIPV/T shows the same trend as the electrical efficiency but the peak in electrical energy production is shifted compared to the peak of efficiency, and can be seen from October to December. This occurs because of the increased numbers of hours where solar irradiance is incident on the BIPV/T façade.

The electrical efficiency of the water based BIPV/T is observed with a peak value in January at 10.94% with a following dip that shows a minimum value of 6.36%. The electrical energy production follows the overall trend of the electrical efficiency but because of the difference in sun hours the peak in electrical energy production can be seen between October and November outside of the electrical efficiency peak.

A large reduction in efficiency and electrical energy production can be seen from May to September for the water based BIPV/T. The difference in electrical efficiency between the air based BIPV/T and the water based BIPV/T is 4.64% in June, where the efficiency of the air based BIPV/T is slightly higher than the BIPV reference. This difference is investigated further in Figure 6-6 by looking at the PV surface temperature of the BIPV/T technologies compared to a BIPV reference.

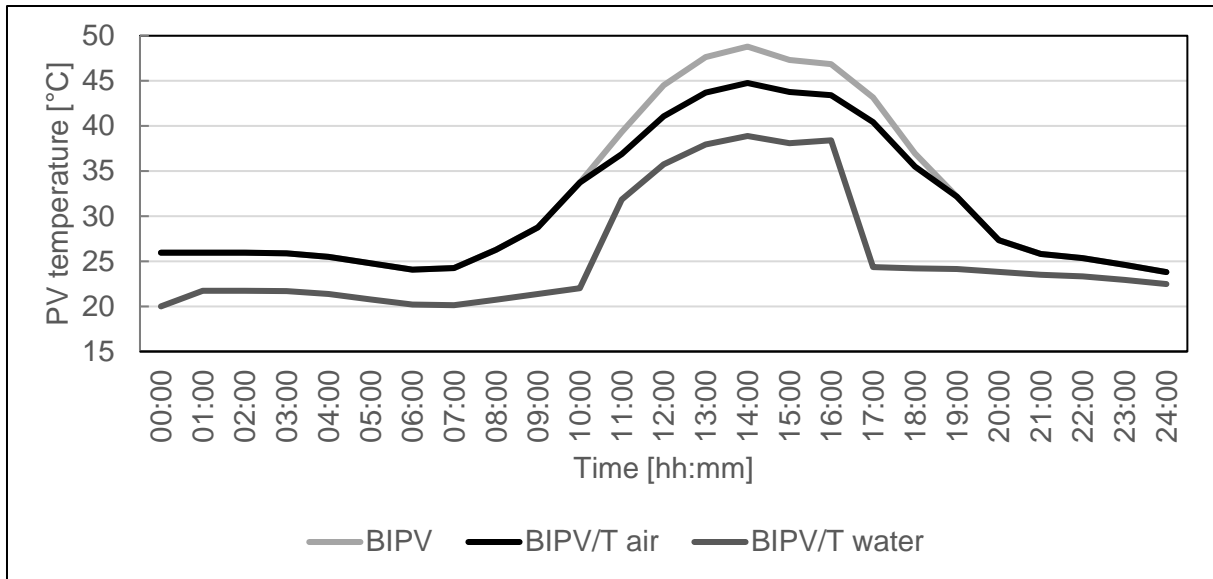


Figure 6-6: Comparison of PV surface temperatures between technologies in June

For the selected day in June, the highest PV surface temperature can be seen for the BIPV reference, followed by the air and water based BIPV/T with values of 49°C, 45°C and 39°C, respectively at 14:00. This shows that the water based BIPV/T has the largest cooling effect on the PV surface.

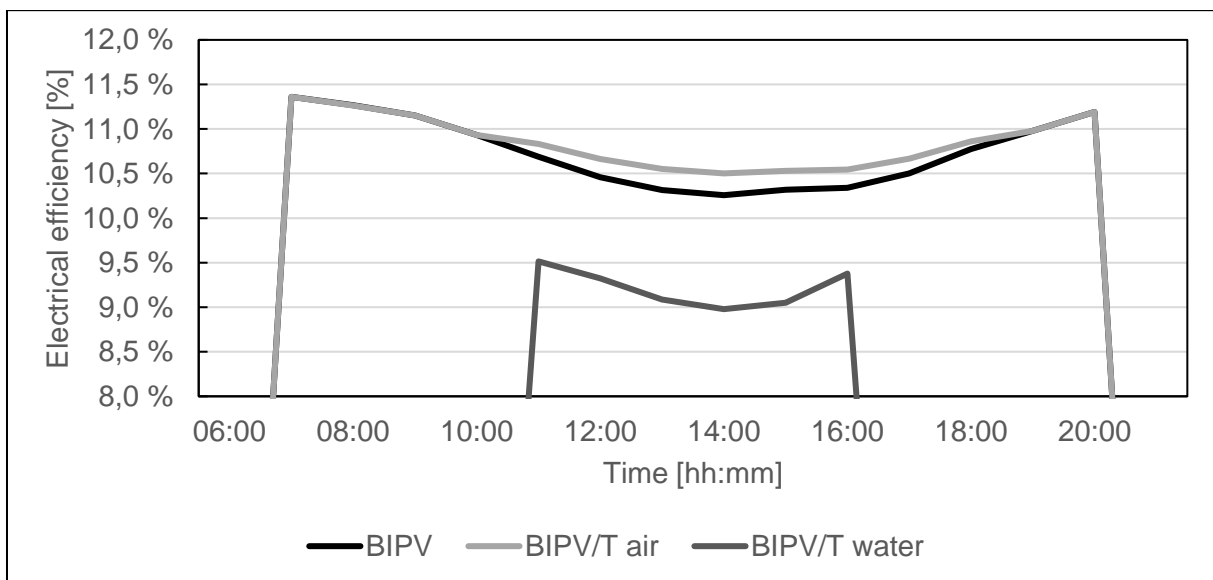


Figure 6-7: Comparison of electrical efficiency between technologies in June

As the electrical efficiency is calculated based on the PV temperature of the component surface one would expect the water based BIPV/T to produce the highest electrical efficiency.

However, as shown in Figure 6-7, this is not the case. The electrical efficiency of the BIPV, air and water based BIPV/T is observed at 10.26%, 10.50% and 8.98%, respectively, at 14:00. The time period in which the water based BIPV/T produces power is also significantly less than that of the BIPV and air based BIPV/T. The number of hours of power production coincides more during periods of larger amounts of solar radiation as shown in Figure 6-8, where power generation starts at 08:00 and ends at 19:00 for all technologies.

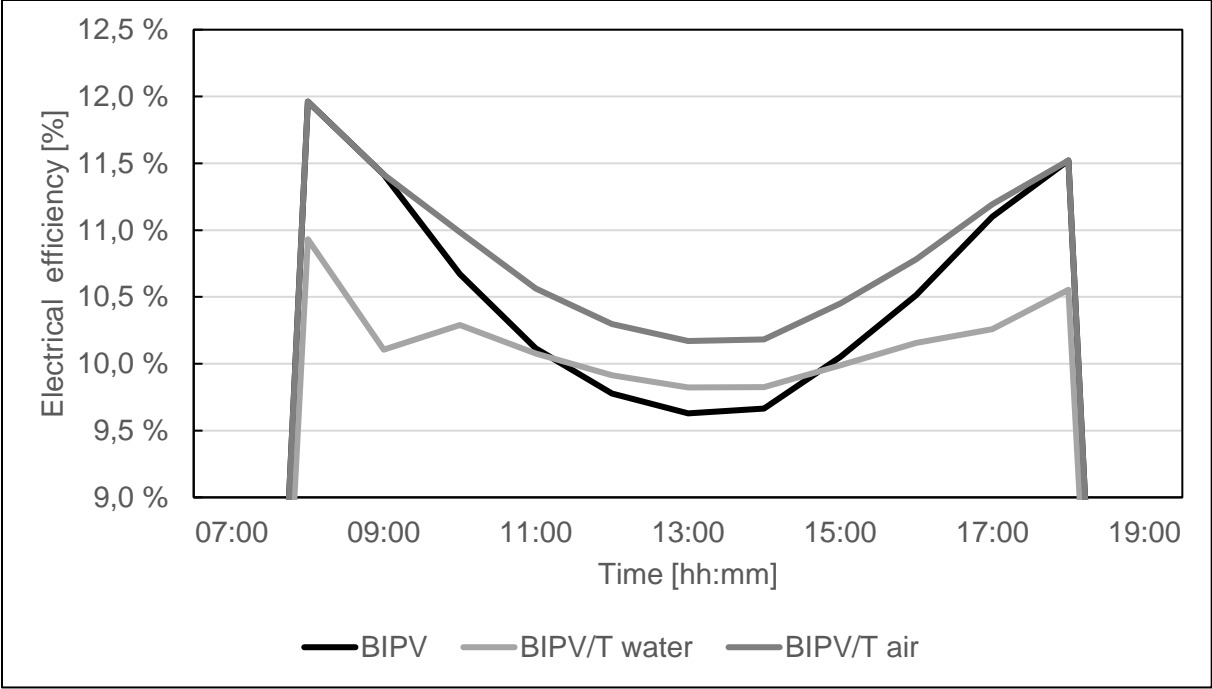


Figure 6-8 Comparison of electrical efficiency between technologies in November

6.4 Mismatch factors

The electrical energy that is produced by the water based BIPV/T system is higher than the electrical load of the office from August to April. Between May and August, the production of electrical energy is not high enough to supply the load. The actual electrical energy that is produced by the water based BIPV/T and consumed by the electrical load is less than the production itself. This is because the electrical power need does not match the electrical production at all times. The electrical load that is covered by the electrical production and the load itself can be seen in Figure 6-9. The yearly unmatched generation, energy carrier surplus and electrical solar fraction are 0.6, 0.13 and 0.46, respectively.

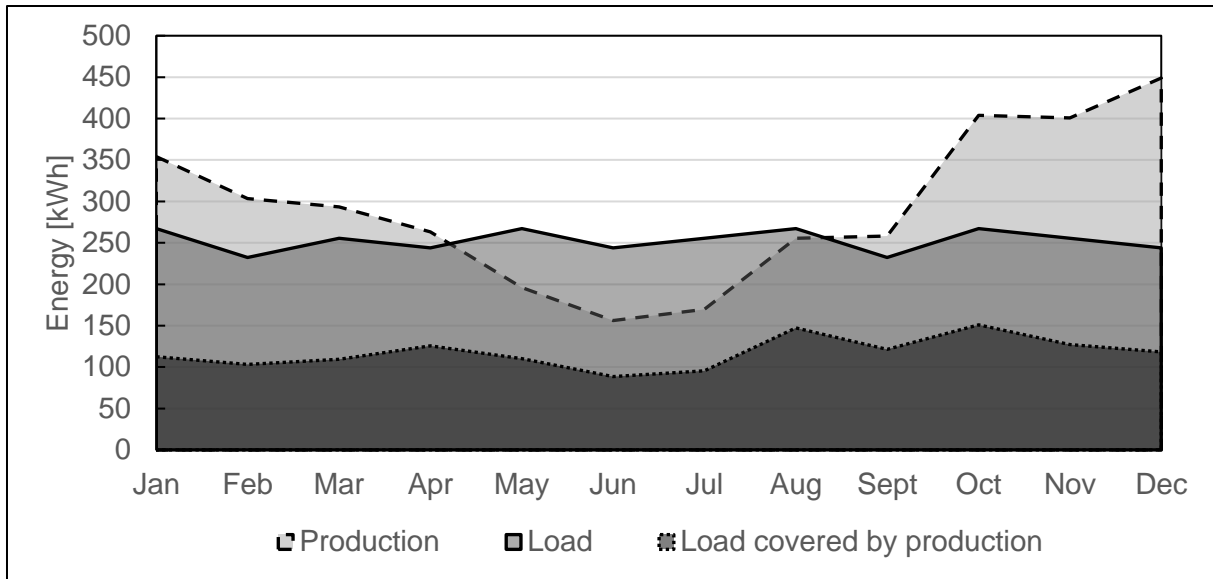


Figure 6-9: The electrical production, load covered by production and load for the water based BIPV/T system

The electrical energy production of the air based BIPV/T experiences small peaks and dips throughout the year and is larger than the electrical energy consumption for all months. The produced electrical energy shows resemblance in both shape and magnitude, especially between October and December as seen in Figure 6-10. The produced electrical power that is used by the load is also larger for the air based BIPV/T. The unmatched generation, carrier surplus and the electrical solar fraction are 0.44, 0.29 and 0.73, respectively. The calculated mismatch factors show less dependency of the grid as more power is produced when power is needed.

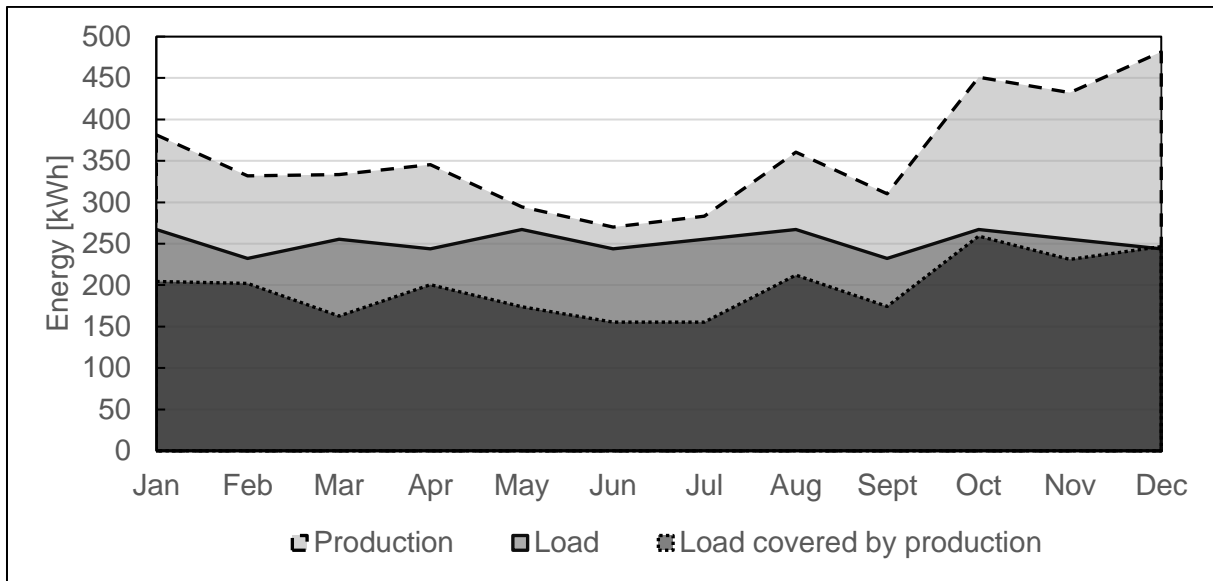


Figure 6-10: The electrical production, load covered by production and load for the BIPV system

The electrical energy produced by the BIPV reference shows great resemblance to that of the air based BIPV/T. The produced electrical energy is slightly less through the whole year, larger change is seen from October to December. This naturally gives similar mismatch factors between the two, giving unmatched generation, carrier surplus and electrical solar fraction as 0.44, 0.27 and 0.77, respectively. The mismatch factors of the technologies are summarised in Table 19.

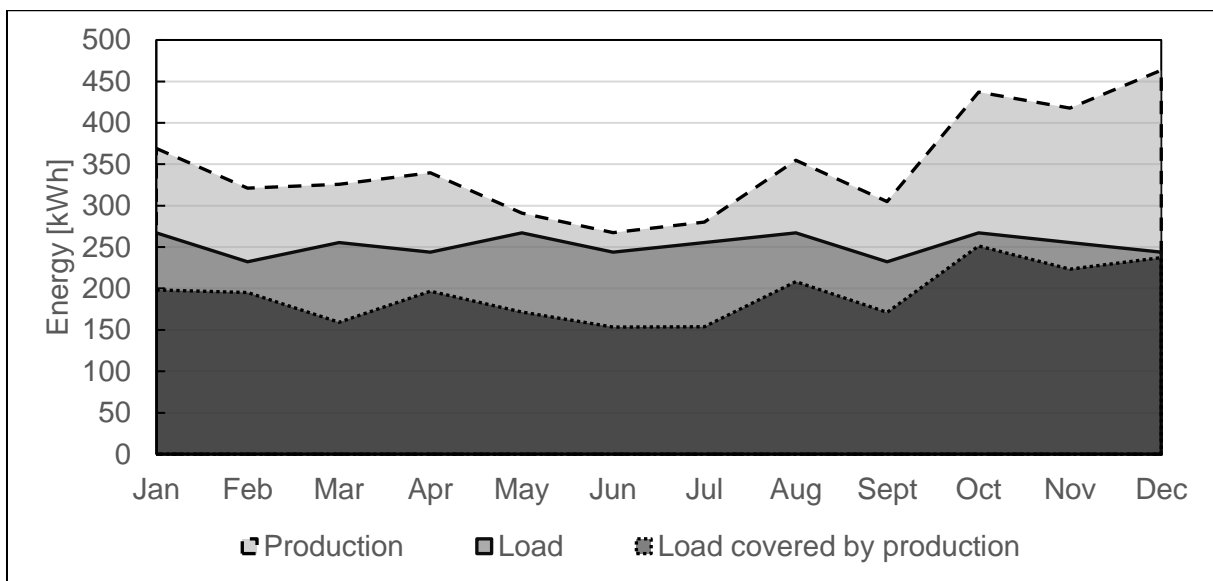


Figure 6-11: The electrical production, load covered by production and load for the air based BIPV/T system

Table 19: Mismatch factors and thermal solar fraction

<i>Technology</i>	<i>Unmatched generation</i>	<i>Carrier surplus</i>	$SF_{electrical}$	$SF_{thermal}$
BIPV	0.44	0.27	0.77	-
BIPV/T _{air}	0.44	0.29	0.73	0.33
BIPV/T _{water}	0.60	0.13	0.46	0.42

6.5 Summary

When analysing the electrical efficiencies of the different BIPV/T technologies and the BIPV reference, the highest efficiency and electrical energy production was observed for the air based BIPV/T. A large dip in electrical performance was seen for the water based BIPV/T. Further analyses of data showed that the dip was not caused by higher PV surface temperatures as the water based BIPV/T component showed the lowest value PV surface temperature. Further, the analysis showed that the water based BIPV/T did not produce electrical power in periods of low solar radiation in contrast to the air based BIPV/T and the BIPV components. This may be caused by differences in the TRNSYS components which may be independent on user input as the same values of performance parameters was used for all technologies. Because of this discrepancy it is challenging to compare the electrical performance of the air and water based BIPV/T. However, a comparison can be made between the electrical performances of the air based BIPV/T and the BIPV reference. The air based BIPV/T system showed cooler PV surface temperature and higher electrical energy production showing the benefit of the technology.

If all the excess power production from the water based BIPV/T was stored it would be possible to be grid independent. The difference in power production and the electrical load is large between April and August. In this period, there are many days without significant power generation. As a consequence, the capacity of the battery would have to be very large in order to supply the electrical load of the office building when the production is scarce. Further analysis could be done by looking at the daily power production and electrical load in order to

size the battery storage. Whether or not the battery storage should be implemented is an economical consideration, where the price electricity import and export should be considered, as well as investment costs of the battery storage.

The electrical power production of the air based BIPV/T shows a greater resemblance to the electrical load of the office building with a surplus of power generation for all months, and showed a slight increase in power production compared to the BIPV reference. The analysis shows that the office building is dependent on importing/storing energy but the load matching and surplus of electrical energy production is larger for the air based BIPV/T. This means that the required battery capacity is reduced, which lowers the cost of being grid independent. However, storing the excess power in the grid and importing power when needed may be a more viable solution as many countries invest in the smart grids enabling export of electricity from smaller energy producers, e.g. BIPV/T electrical energy production from office buildings. Thus, the decision of electricity storage is highly dependent on economic considerations.

6.6 Effect of Building Integration

The yearly building energy need for heating and cooling, as well as yearly auxiliary and pump/fan energy demands for five different solar technologies applied to the same building, are presented in Table 20. This table is used to analyse the effect of PV/T building integration, both on the building and on the PV/T technology.

Table 20: Energy needs for various solar technologies. All units in kWh/m².

<i>Energy need</i>		<i>BIPV/T</i>	<i>PV/T</i>	<i>BIPV/T</i>	<i>PV/T air</i>	<i>BIPV</i>
		<i>water</i>	<i>water</i>	<i>air</i>		
Building	Heating	40.07	40.05	40.13	40.05	39.88
	Cooling	23.52	23.66	23.64	23.66	23.73
	Total	63.59	63.71	63.77	63.71	63.61
DHW	Auxiliary	24.70	24.73	27.56	27.56	-
	Pump/fan	0.34	0.34	2.68	2.67	-

The air and water based PV/T technologies are included to show any variations in auxiliary and fan or pump energy need. The building energy need for air and water based PV/T are the

same as these technologies are not building integrated and therefore do not affect the building's energy demand.

The BIPV/T technologies show slight lower heating due to cooling from the fluid flow inside the components. This effect is also present during the heating season, which increases the heating need compared to a building without building integrated solar technology. For the air based BIPV/T system, the increase in heating demand exceeds the decrease in cooling demand, resulting in higher total building energy need.

The water based BIPV/T system shows slightly lower total building energy demand compared to the BIPV system, which provides an isolating effect during the heating season. However, the cooling effect of the water BIPV/T system is greater, and thus the total energy need is lower.

Less effect is seen in auxiliary and pump/fan energy need. Slightly less auxiliary energy is needed for the water based BIPV/T compared to the water based PV/T system. For the air based BIPV/T system, there is no difference in auxiliary energy demand and the difference in fan power is negligible.

6.7 Summary

Small reductions in the building cooling demands for air and water based BIPV/T systems suggest that the fluid flow has a cooling effect on the building body. This effect was also present during the heating season, leading to a larger heating demand compared to the building without building integrated solar technology. Effects on auxiliary and pump or fan energy needs were negligible as these quantities are less influenced by external parameters.

The effect of building integration proved to be little for the investigated façade. However, a larger effect of building integration may be seen for BIPV/T systems on larger building facades.

7 Conclusion

Analysis and development of design methods have been carried out for the building integration of air and water based PV/T using TRNSYS. The water based BIPV/T model was validated using winter measurements of an actual component in order to assess its performance, both with regards to production of energy and its effect on the energy need of an office building.

The analysis conducted in this thesis reveals a potential for vertically mounted BIPV/T facades in Shanghai. Initial investigation shows that the solar irradiance incident on a façade is present during the whole year with larger amounts of solar irradiance in the winter months.

The analysis of the air and water based optimisation process, revealed that a change of mass flow rate had the greatest impact on the BIPV/T systems, where increased solar fractions were observed when reducing the mass flow rate for both technologies. When increasing the mass flow rate, the electrical performance of the air based BIPV/T increased noticeably, but because of limitations in the TRNSYS model/program higher values of flow rates for the air and water based BIPV/T were not tested. The increase of storage volume had a great positive effect on the amount of useful energy collected to the storage tank for both the air and water based BIPV/T systems.

A comparison between the air and water based BIPV/T showed that the collected useful energy and the solar fraction were greater for the water based system than that of the air based. This indicates that the water based BIPV/T is more applicable for DHW production, but the potential of utilising excess heat for heating of ventilation is present for the air based BIPV/T. Additionally, the air based BIPV/T showed larger electrical efficiencies throughout the annual simulation with substantially larger electrical solar fraction. The air based BIPV/T also showed improved electrical efficiency compared to a BIPV system reference but because of the pump power required to circulate the air, the electrical solar fraction was slightly less than that of the BIPV reference. The benefit of the air based BIPV/T compared to the BIPV is that it provides almost the same electrical solar fraction but in addition it produces heat for DHW.

Some differences were seen in the behaviour of the two BIPV/T systems, where the water based BIPV/T did not produce power during certain periods of low solar irradiance. In order

to reliably compare the electrical performance between the air and water based BIPV/T, a validation based on experimental data from summer months should be carried out.

The analysis shows that the air based BIPV/T is more grid independent as the power production matches the electrical load of the building to a larger extent than for the water based BIPV/T. By looking at monthly values of mismatch factors it can be concluded that the air and water based BIPV/T systems could be independent of the grid but the capacity needed for batteries may be too high as there are longer periods of little or no power production in the summer months. Therefore, import/export of excess power from/to the grid may be a viable solution.

Based on the thermal solar fraction it is concluded that the BIPV/T technology may serve better as a supplement to a borehole heat pump system, which is already installed at GEL. The coupling could also lead to higher performance of the BIPV/T.

The effect of building integration is considered negligible when analysing the change in heating and cooling demand of the GEL office building, as simulation results for PV/T and BIPV/T systems were compared.

8 Further Work

The performance of air and water based BIPV/T systems have been analysed in this thesis, but with a limited scope considering vertical façade integration in an office building with connection to a DHW system. Further analysis could be performed assessing the performance of a BIPV/T system connected to a larger energy system, including design of heating and cooling systems of the building. In that way, the use of air based BIPV/T for heating of ventilation air could be assessed, as a substantial amount of energy is lost in a system where it is only used for heating of DHW.

The study on air based BIPV/T is solely based on simulations. Measurements data would be of great interest in order to validate the simulation results. The water based BIPV/T model is validated based on experimental data from a PV/T component with an angle of 45° during a winter day. Further validation should be done using experimental data from summer months.

Daily loads should be evaluated further and economic analyses should be conducted in order to evaluate the application of battery storage, as just a brief analysis was conducted in this thesis. In addition, the auxiliary power used in order to heat the DHW could be added to the electrical load of the building in order to assess a more detailed electrical load consumption.

Further investigation could be carried out looking at the benefit of connecting a heat pump to the DHW system coupled in series or parallel to the BIPV/T system.

References

1. Agrawal B, Tiwari GN. Building Integrated Photovoltaic Thermal Systems - For Sustainable Developments. Royal Society of Chemistry; 2012.
2. Boreland M, Bagnall D. Current and future photovoltaics. Report for the Office of Science and Innovation (now the Department for Innovation, Universities and Skills), UK. 2006.
3. Celik I, Song Z, Cimaroli AJ, Yan Y, Heben MJ, Apul D. Life cycle assessment (LCA) of perovskite pv cells projected from lab to fab. *Solar Energy Materials and Solar Cells*. 2016;156:157-69.
4. National Energy Research Laboratory. Organic Photovoltaic Solar Cells [Web]. 2017 [cited 2017 10.04.2017]. Available from: <https://www.nrel.gov/pv/organic-photovoltaic-solar-cells.html>.
5. Markvart T. *Solar Electricity*: John Wiley & Sons, Ltd; 2009.
6. Kalogirou SA. *Solar Energy Engineering : Processes and Systems*. Amsterdam: Academic Press; 2014.
7. Dr. Simon Philipps, Warmuth W. *Photovoltaics Report*. Freiburg, Germany: Fraunhofer Institute for Solar Energy, 2016.
8. Burgess D. Thin-film solar cell. *Britannica Academic*. 2015.
9. Laboratory NRE. Best Research-Cell Efficiencies. In: [efficiency-chart.png](https://www.nrel.gov/best-research-cell-efficiencies), editor. www.nrel.gov: National Research Energy Laboratory; 2016.
10. Shockley W, Queisser HJ. Detailed balance limit of efficiency of p-n junction solar cells. *Journal of applied physics*. 1961;32(3):510-9.
11. Rühle S. Tabulated values of the shockley–queisser limit for single junction solar cells. *Solar Energy*. 2016;130:139-47.
12. Duffie JA, Beckman WA. *Solar Engineering of Thermal Processes (4)*. Somerset, US: Wiley; 2013.
13. Athienitis A, O'Brien W. *Solar Heating and Cooling : Modeling, Design, and Optimization of Net-Zero Energy Buildings (1)*. Somerset, DE: Ernst & Sohn; 2015.
14. Giovannetti F, Föste S, Ehrmann N, Rockendorf G. High transmittance, low emissivity glass covers for flat plate collectors: Applications and performance. *Solar Energy*. 2014;104:52-9.
15. Simonsen I, Time B, Andresen I. *Erfaringer med bygningsintegrerte solfangere i Norge ; Experiences with solar thermal collectors in Norway*. SINTEF Academic Press; 2011.
16. Mauthner F, Weiss W, Spörk-Dür M. *Solar Heat Worldwide: Markets and Contribution to the Energy Supply 2014*. International Energy Agency - Solar Heating and Cooling Programme. 2016.
17. Yang T, Athienitis AK. A review of research and developments of building-integrated photovoltaic/thermal (BIPV/T) systems. *Renewable and Sustainable Energy Reviews*. 2016;66:886-912.
18. Kim J-H, Park S-H, Kang J-G, Kim J-T. Experimental performance of heating system with building-integrated PVT (BIPVT) collector. *Energy Procedia*. 2014;48:1374-84.
19. Athienitis AK. *Smart Net-Zero Energy Buildings Strategic Research Network*. NSERC: 2014.
20. Dubey S, Sandhu GS, Tiwari GN. Analytical expression for electrical efficiency of PV/T hybrid air collector. *Applied Energy*. 2009;86(5):697-705.
21. Tripanagnostopoulos Y, Nousia TH, Souliotis M, Yianoulis P. Hybrid photovoltaic/thermal solar systems. *Solar energy*. 2002;72(3):217-34.

22. Zhang X, Zhao X, Smith S, Xu J, Yu X. Review of R&D progress and practical application of the solar photovoltaic/thermal (PV/T) technologies. *Renewable and Sustainable Energy Reviews*. 2012;16(1):599-617.
23. Mishra RK, Tiwari GN. Energy matrices analyses of hybrid photovoltaic thermal (HPVT) water collector with different PV technology. *Solar Energy*. 2013;91:161-73.
24. Chow TT. A review on photovoltaic/thermal hybrid solar technology. *Applied Energy*. 2010;87(2):365-79.
25. Chow TT, Chan ALS, Fong KF, Lin Z, He W, Ji J. Annual performance of building-integrated photovoltaic/water-heating system for warm climate application. *Applied Energy*. 2009;86(5):689-96.
26. Ibrahim A, Fudholi A, Sopian K, Othman MY, Ruslan MH. Efficiencies and improvement potential of building integrated photovoltaic thermal (BIPVT) system. *Energy Conversion and Management*. 2014;77:527-34.
27. Daghigh R, Ruslan MH, Sopian K. Advances in liquid based photovoltaic/thermal (PV/T) collectors. *Renewable and Sustainable Energy Reviews*. 2011;15(8):4156-70.
28. Agrawal B, Tiwari GN. Optimizing the energy and exergy of building integrated photovoltaic thermal (BIPVT) systems under cold climatic conditions. *Applied Energy*. 2010;87(2):417-26.
29. Bambrook SM, Sproul AB. Maximising the energy output of a PVT air system. *Solar Energy*. 2012;86(6):1857-71.
30. Sarhaddi F, Farahat S, Ajam H, Behzadmehr A. Exergetic performance assessment of a solar photovoltaic thermal (PV/T) air collector. *Energy and Buildings*. 2010;42(11):2184-99.
31. Tripanagnostopoulos Y, Nousia T, Souliotis M, editors. Low cost improvements to building integrated air cooled hybrid PV-Thermal systems. *Proceedings of 16th European PV solar energy conference*; 2000.
32. Chen Y, Athienitis AK, Galal K. Modeling, design and thermal performance of a BIPV/T system thermally coupled with a ventilated concrete slab in a low energy solar house: Part 1, BIPV/T system and house energy concept. *Solar Energy*. 2010;84(11):1892-907.
33. Bergman TL, Incropera FP. *Fundamentals of heat and mass transfer*: John Wiley & Sons; 2011.
34. Bliss RW. Atmospheric radiation near the surface of the ground: a summary for engineers. *Solar Energy*. 1961;5(3):103-20.
35. Sartori I, Napolitano A, Voss K. Net zero energy buildings: A consistent definition framework. *Energy and Buildings*. 2012;48:220-32.
36. Torcellini P, Pless S, Deru M, Crawley D. *Zero energy buildings: a critical look at the definition*. National Renewable Energy Laboratory and Department of Energy, US. 2006.
37. Dokka T, Sartori I, Thyholt M, Lien K, Lindberg KB. *A Norwegian zero emission building definition*. Passivhus Norden. 2013.
38. Duffie JA, Beckman WA. *Solar Engineering of Thermal Processes*. 4th ed: Wiley New York; 2013.
39. T. T.Chow, G. N. Tiwari, Menezes C. *Hybrid Solar: A Review on Photovoltaic and Thermal Power Integration*. *International Journal of Photonenergy*, 2012.
40. Fujisawa T, Tani T. Annual exergy evaluation on photovoltaic-thermal hybrid collector. *Solar Energy Materials and Solar Cells*. 1997;47(1):135-48.
41. Krishna Priya GS, Thakare MS, Ghosh PC, Bandyopadhyay S. Sizing of standalone photovoltaic thermal (PVT) systems using design space approach. *Solar Energy*. 2013;97:48-57.
42. Klein SA, Beckman WA, Duffie JA. A design procedure for solar heating systems. *Solar Energy*. 1976;18(2):113-27.

43. Aste N, Del Pero C, Leonforte F. Optimization of Solar Thermal Fraction in PVT Systems. *Energy Procedia*. 2012;30:8-18.
44. Hausner R, Fink C. Stagnation behaviour of solar thermal systems. *Solar Heating & Cooling Programme: International Energy Agency*, 2002.
45. Duff W. *Advanced Solar Domestic Hot Water Systems*. Solar Heating & Cooling Programme: International Energy Agency, 1996.
46. Cole RL, Bellinger FO, editors. *THERMALLY STRATIFIED TANKS*. ASHRAE Transactions; 1982.
47. Çomaklı K, Çakır U, Kaya M, Bakirci K. The relation of collector and storage tank size in solar heating systems. *Energy Conversion and Management*. 2012;63:112-7.
48. Hollands KGT, Lightstone MF. A review of low-flow, stratified-tank solar water heating systems. *Solar Energy*. 1989;43(2):97-105.
49. Andresen I. Planlegging av solvarmeanlegg for lavenergiboliger og passivhus. En introduksjon. SINTEF Byggforsk, 2008.
50. Tiwari A, Sodha MS, Chandra A, Joshi JC. Performance evaluation of photovoltaic thermal solar air collector for composite climate of India. *Solar Energy Materials and Solar Cells*. 2006;90(2):175-89.
51. Goossens D, Goverde H, Catthoor F. Effect of wind on temperature patterns, electrical characteristics, and performance of building-integrated and building-applied inclined photovoltaic modules. Elsevier Editorial System for *Solar Energy*: 2017.
52. Pavlov GK, Olesen BW. *Seasonal Ground Solar Thermal Energy Storage-Review of Systems and Applications*. Technical University of Denmark, 2011.
53. Bertram E, Glembin J, Rockendorf G. Unglazed PVT collectors as additional heat source in heat pump systems with borehole heat exchanger. *Energy Procedia*. 2012;30:414-23.
54. Good C. *Photovoltaic-thermal systems for zero emission residential buildings*. Trondheim: Norwegian University of Science and Technology; 2016.
55. Ruschenburg J, Herkel S. A comparative analysis of market available solar thermal heat pump systems. Fraunhofer Institute for Solar Energy Systems ISE, 2012.
56. Favero & Milan Ingegneria. GEL - Green Energy Laboratory. 2012.
57. Archea Associati. Green Energy Laboratory 2012. Available from: <http://www.archea.it/gel-green-energy-laboratory/>.
58. Shuai D, Wang R, Dai Y. Case Study of Net Zero Energy Apartment in Shanghai. Purdue University Libraries: 2012.
59. The Noun Project. Icons for everything 2017 [16.06.2017]. Available from: www.thenounproject.com.
60. Sahlin P, Grozman P. IDA Simulation Environment-a tool for Modelica based end-user application deployment. Equa Simulation AB, Sweden, 2003.
61. Axaopoulos PJ, Fylladitakis ED, Gkarakis K. Accuracy analysis of software for the estimation and planning of photovoltaic installations. *International Journal of Energy and Environmental Engineering*. 2014;5(1):71.
62. McDowell A. *Thermal Modelling and Optimisation of Building-Integrated Photovoltaic Thermal Systems [MSc thesis]*: University of Canterbury; 2015.
63. Eicker U, Dalibard A. Photovoltaic-thermal collectors for night radiative cooling of buildings. *Solar Energy*. 2011;85(7):1322-35.
64. Berdahl P, Martin M. Emissivity of clear skies. *Solar Energy*. 1984;32(5):663-4.
65. Kasten F, Czeplak G. Solar and terrestrial radiation dependent on the amount and type of cloud. *Solar Energy*. 1980;24(2):177-89.
66. Watmuff J, Charters W, Proctor D. Solar and wind induced external coefficients-solar collectors. *Cooperation Mediterranee pour l'Energie Solaire*. 1977;1:56.

67. El-Sebaili A. Effect of wind speed on active and passive solar stills. *Energy Conversion and Management*. 2004;45(7):1187-204.
68. Anderson TN, Duke M, Morrison G, Carson JK. Performance of a building integrated photovoltaic/thermal (BIPVT) solar collector. *Solar Energy*. 2009;83(4):445-55.
69. Aste N, Del Pero C, Leonforte F, Manfren M. Performance monitoring and modeling of an uncovered photovoltaic-thermal (PVT) water collector. *Solar Energy*. 2016;135:551-68.
70. Jürges W. *Der Wärmeübergang an einer ebenen Wand*: Druck und Verlag von R. Oldenbourg; 1924.
71. McAdams WH. *Heat Transmission*,(1954). McGraw Hills. 1985.
72. Kumar S, Mullick S. Wind heat transfer coefficient in solar collectors in outdoor conditions. *Solar Energy*. 2010;84(6):956-63.
73. Hensen JL, Lamberts R. *Building performance simulation for design and operation*: Routledge; 2012.
74. Yu D, Gudmundsdottir R, Catteau R, Kamel R, Fung A, Mohammadi F, et al. *Validating a Simplified PV Model Against TRNSYS Model*. 2016.
75. Draper NR, Smith H. *Wiley Series in Probability and Statistics : Applied Regression Analysis (3rd Edition)*. Somerset: Somerset, NJ, USA: Wiley; 2014.
76. Katic I. *Measurement Report-Test of PV/T-module "PVtwin"*. Solar Heating & Cooling Programme: International Energy Agency, 2006 Contract No.: Report DC4-1.
77. Darcovich K, Entchev E, Tzscheutschler P. *Integration of Micro-Generation and Related Energy Technologies in Buildings*. IEA EBC Annex 54: Energy in Buildings and Communities Programme, 2014.
78. Norsk Standard. NS 3701. *Criteria for passive houses and low energy buildings - non-residential buildings*2012.
79. Nielsen L. *Analysis of the radiant heating and cooling system in the Green Energy Laboratory [MSc]*: Norwegian University of Science and Technology; 2015.
80. TRNSYS. *Multizone Building modeling with Type56 and TRNBuild*. 2007.
81. Norsk Standard. NS 3031. *Calculation of energy performance of buildings - method and data*2014.
82. The Engineering ToolBox. *Consumption of hot water per person or occupant* [cited 2017 16.05]. Available from: http://www.engineeringtoolbox.com/hot-water-consumption-person-d_91.html.
83. Ulseth R, Alonso Justo M, Haugerud Pedersen L. *Measured load profiles for domestic hot water in buildings with heat supply from district heating*. SINTEF Energy Research, Norway: 2014.

Appendix A: Energy Balances

Overall Energy Balance of Water Based PV/T

In order to calculate the useful energy gain to the fluid q'_{fluid} , several coefficients used in subchapter 4.1.1 are further described:

$$\kappa = -D_{tube} F' \left(h_{PV,rad} + h_{PV,conv} + \frac{1}{R_{back} F'} \right) - 2k\lambda m \tanh \left(m \left(\frac{W - D_{tube}}{2} \right) \right)$$

$$h_{PV,rad} = \varepsilon\sigma(T_{PV} + T_{sky})(T_{PV}^2 + T_{sky}^2)$$

$$\theta = 1 + D_{tube} F' \left(\frac{1}{h_{fluid}\pi D_{tube}} + \frac{1}{C_B} \right) \left(h_{PV,rad} + h_{PV,conv} \frac{1}{R_{back} F'} \right) + 2k\lambda m \tanh \left(m \left(\frac{W - D_{tube}}{2} \right) \right) \left(\frac{1}{h_{fluid}\pi D_{tube}} + \frac{1}{C_B} \right)$$

where C_B is the conductance between the absorber plate and the tubes that are connected to it, h_{fluid} is the fluid heat transfer coefficient.

$$\varepsilon = D_{tube} F' \left(S + h_{PV,rad} T_{sky} + h_{PV,conv} T_a + \frac{T_{back}}{R_{back} F'} \right) + 2k\lambda m \tanh \left(m \left(\frac{W - D_{tube}}{2} \right) \right) \left(\frac{S + h_{PV,rad} T_{sky} + h_{PV,conv} T_a + \frac{T_{back}}{R_{back} F'}}{\frac{1}{R_{PV \rightarrow abs} F'} + \frac{1}{R_{back} F'} - \frac{1}{R_{PV \rightarrow abs}}} \right)$$

$$F' = \frac{1}{h_{PV,rad} R_{PV \rightarrow abs} + h_{PV,conv} R_{PV \rightarrow abs} + 1}$$

$$m = \sqrt{\frac{F' \left(\frac{1}{R_{PV \rightarrow abs} F'} + \frac{1}{R_{back} F'} - \frac{1}{R_{PV \rightarrow abs}} \right)}{k\lambda}}$$

Overall Energy Balance of Air Based PV/T

In order to calculate the useful energy gain q_u , several coefficients used in subchapter 4.1.2 are further described:

$$a = \frac{h_{air}^2}{m} + \frac{2h_{air}^2 \cdot h_{1 \rightarrow 2,rad}}{m \cdot j} - 2h_{air} + \frac{h_{air}^2}{j} + \frac{h_{air}^2 \cdot h_{1 \rightarrow 2,rad}}{m \cdot j^2}$$

$$b = \frac{h_{air,conv} S}{F' m} + \frac{h_{air,conv} h_{PV,conv} T_a}{F' m} + \frac{h_{air,conv} h_{PV,rad} T_{sky}}{F' m} + \frac{h_{air,conv} h_{1 \rightarrow 2,rad} T_{back}}{R_{2 \rightarrow back} j \cdot m} + \frac{h_{air,conv} h_{1 \rightarrow 2,rad} S}{F' j \cdot m} + \frac{h_{air,conv} h_{1 \rightarrow 2,rad} h_{PV,conv} T_a}{F' j \cdot m}$$

$$+ \frac{h_{air,conv} h_{1 \rightarrow 2,rad} h_{PV,rad} T_{sky}}{F' j \cdot m} + \frac{h_{air,conv} h_{1 \rightarrow 2,rad}^2 T_{back}}{R_{2 \rightarrow back} j^2 m}$$

$$F' = h_{PV,rad} R_{PV \rightarrow 1} + h_{PV,conv} R_{PV \rightarrow 1} + 1$$

$$j = h_{air,conv} + h_{1 \rightarrow 2,rad} + \frac{1}{R_{2 \rightarrow back}}$$

$$m = \frac{1}{R_{PV \rightarrow 1}} - \frac{1}{R_{PV \rightarrow 1} F'} + h_{air,conv} + h_{1 \rightarrow 2,rad} - \frac{h_{1 \rightarrow 2,rad}^2}{j}$$

Appendix B: GEL Office Parameters

Building Model

The default resistance of the insulating material of the BIPV/T back surface is given as 3 $\text{hm}^2\text{K/kJ}$ and is later changed to 0.5 $\text{hm}^2\text{K/kJ}$.

Calculation of the south wall with the BIPV/T collector integrated is done by:

$$U_{BIPV/T \text{ wall}} = \frac{1}{R_{inner} + R_{wall} + R_{BIPV/T \text{ component}} + R_{outer}}$$

$$= \frac{1}{R_{inner} + \frac{d_{\text{mineral wool}}}{\lambda_{\text{mineral wool}}} + R_{\text{remaining wall layers}} + R_{BIPV/T \text{ component}} + R_{outer}}$$

Given the U value of the original wall construction the insulation thickness of the mineral wool was reduced in TRNBuild in order to maintain the original U value of 0.1 $\text{W/m}^2\text{K}$ resulting in a mineral wool thickness of 0.23 m.

Table 21: Values for the GEL office construction

<i>Wall</i>	<i>Layer</i>	<i>Thickness</i> [m]	<i>Conductivity</i> [kJ/hmk]	<i>Thermal Capacity</i> [kj/kgK]	<i>Density</i> [kg/m ³]	<i>Thermal resistance</i> [hm ² K/kJ]
	Aerated concrete	0.1	0.72	0.84	700	0.14
<i>External wall</i>	Air gap	-	-	-	-	0.49
	Mineral wool	0.3/0.23*	0.144	0.84	80	2.1/1.6
	Aluminium	0.002	730	0.88	2700	2.4·10 ⁻⁶
<i>Floor</i>	Concrete slab	0.12	4.068	1	1400	0.03
	Light concrete	0.045	2.016	1	1000	0.02
	Cement mortar	0.07	5	1	2000	0.01
	Spruce pine	0.012	0.36	2	600	0.03

	Concrete slab	0.12	4.068	1	1400	0.03
	Light concrete	0.045	2.016	1	1000	0.02
<i>Roof</i>	Cement mortar	0.07	5	1	2000	0.01
	Mineral wool	0.450	0.144	0.84	80	3.13
	Spruce pine	0.012	0.36	2	600	0.03

Table 22: Detailed window construction

<i>Window ID</i>	<i>Description</i>	<i>U-value</i> <i>[W/m²K]</i>	<i>g-value [-]</i>	<i>Construction</i> <i>[mm]</i>
4001	Krypton	0.68	0.407	4/8/4/8/4

The power load consumption is set according to Table 23 using values from the electrical consumption for equipment and lighting resulting in an average load of 3484.8 kJ/hr. The NS 3701 schedule is used in order to set the operating hours as seen from Figure 5-6 in subchapter 5.2.5.

For the air based BIPV/T wall, the U value for the entire wall is used in order to calculate the back resistance of the BIPV/T component, calculated to 2.71 hm²K/kJ.

System components

Table 23: Internal loads, ventilation rates and system design chosen in accordance with criteria for passive house (NS 3701)

<i>Building category</i>	<i>Power and Heat load equip. [W/m²]</i>	<i>Power and heat load lights. [W/m²]</i>	<i>Heat load per person [W/m²]</i>	<i>Airflow in operation [m³/(m²h)]</i>	<i>Airflow outside of operation [m³/(m²h)]</i>	<i>Presence [m²/person]</i>
Office	6	5	4	6	1	5

Table 24: Components of the GEL office in accordance with minimum demands of passive house requirements [78].

<i>Components</i>	<i>Passive house requirement</i>	<i>Office building</i>
U value windows and doors	$\leq 0.8 \text{ W}/(\text{m}^2 \text{ K})$	0.68 W/(m ² K)
Normalised thermal bridge	$\leq 0.03 \text{ W}/(\text{m}^2 \text{ K})$	-
Yearly average efficiency for heat exchanger	$\geq 80 \%$	-
SFP	$\leq 1.5 \text{ kW}/(\text{m}^3/\text{s})$	-
Infiltration	$\leq 0.6 \text{ h}^{-1}$	0.6
Dynamic daylight and constant light control	$\geq 60 \%$ of installed effect has to be connected to a control system	-

Performance Investigation of a PV/T Component Used as Part of Building Envelope

Herman Andersen and Joseph Ekenes

KEYWORDS: Air based BIPV/T, Water based BIPV/T, Electricity storage, Performance analysis

ABSTRACT: A water based PV/T component has been calibrated and validated according to measurements conducted in Shanghai, China. Furthermore, the component was used to model a PV/T façade at the south wall of GEL. A façade integrated PV/T system utilising air as heat transfer medium was also modelled, but not validated, as no measurements were available for this component.

The BIPV/T systems were optimised for five parameters; dead band, storage tank size, mass flow rate, tank inlet height from heat source and tank inlet height from mains water supply. Simulations have been conducted to analyse the effect of building integration, both on the building energy demand and the BIPV/T system operation. Simulations were carried out for the same building model with air based BIPV/T system, water based BIPV/T system, air based PV/T system, water based PV/T system and PV façade (BIPV).

The results show that PV/T integrated to the building façade has negligible effect on the total energy demand of the building. The electrical efficiency was highest for the air based BIPV/T system and the water based BIPV/T showed the largest amount of collected thermal useful energy. The BIPV showed the highest electrical solar fraction, as a significant amount of fan energy required for operation of the air based BIPV/T system results in reduced solar fraction for that system.

Introduction

Growing populations and expanding cities present the need for alternative technologies for onsite energy generation. The photovoltaic (PV) cell is an established technology for production of electrical energy, with efficiency ranging from 5% – 21% depending on the PV material. However, the efficiency of a PV panel decreases for higher PV surface temperatures introducing the need for additional cooling of the panel. With a colder fluid, i.e. air or water, circulating below the PV panel, the PV temperature is kept lower, maintaining higher efficiency during hours of high solar irradiation.

In the EU, the member states have agreed that all new buildings are going to be nearly zero energy buildings within 2020.

Buildings constructed today must follow strict governmental regulations to maintain low energy consumptions and are thus mostly passive houses and net Zero Energy Buildings (nZEB). As the total building energy demand is reduced in modern buildings, the demand for domestic hot water (DHW) becomes relatively larger. Therefore, renewable solutions for covering the DHW demand are becoming more important.

To reduce the amount of imported electricity from the grid, the energy production should follow the load, i.e. high load matching index should be maintained throughout the year. As solar energy is impossible to regulate, energy storage could be used to minimise grid stress.

BIPV/T is space efficient as it utilises less area for electrical and thermal energy generation compared to traditional solar collectors and PV panels. Façade integrated PV/T systems can make use of an area that has, until now, been found unfitted for energy production. In contrast to PV panels and solar collectors installed on buildings, BIPV/T components offer architectural uniformity as all components are identical.

PV/T models

The air and water based PV/T components are represented by TYPE 568 and TYPE 563 in TRNSYS. The TRNSYS components from the Thermal Energy System Simulation Inc.(TESS) library is based on equations from Duffie and Beckman [12]. TYPE 568 and TYPE 563 models an uncovered solar collector which generates power from embedded PV cells and simultaneously provides heat to a fluid stream flowing through an air channel and through tubes, respectively. Linear factors relate the PV cell efficiency and the cell temperature, as well as the incident solar radiation. The cells are assumed to operate under maximum power point conditions. Both TYPE 568 and TYPE 563 allows for connection to the TYPE 56 multizone building model. This way, the impact of the PV/T component on the buildings heating and cooling loads can be investigated. Principle sketches of the two technologies can be seen in Figure 1 and Figure 2.

The differences in the two components is mainly related to different heat transfer mediums and the way they collect heat expressed by the useful energy gain seen from eq.(1).

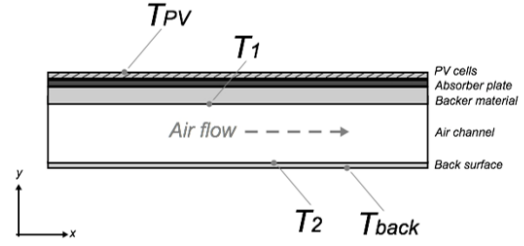


Figure 1: Air based PV/T component

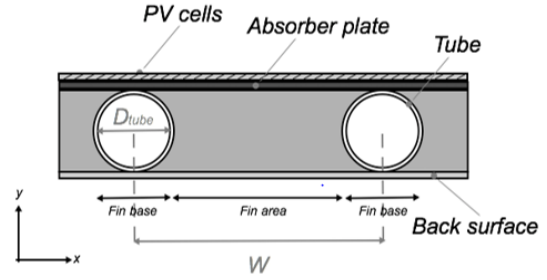


Figure 2: Water based PV/T component

$$\dot{Q}_u = \dot{m}C_p (T_{fluid,out} - T_{fluid,in}) \quad (1)$$

where T_{fluid} is the temperature of air or water passing through the PV/T collectors.

The overall energy balance for the two PV/T components are given as:

$$Q_{absorbed} + Q_{el} = Q_{loss,top} + Q_u + Q_{loss,back} \quad (2)$$

Where $Q_{loss,top}$ are convective and radiative losses.

BIPVT efficiency

The total efficiency, η_{tot} , is the sum of the thermal and electrical efficiencies given as:

$$\eta_e = \frac{IV}{A_c G_T} \quad (3)$$

$$\eta_{th} = \frac{\int \dot{Q}_u dt}{A_c \int G_T dt} \quad (4)$$

$$\eta_{tot} = \eta_{th} + \eta_e \quad (5)$$

Previous studies documenting the total efficiency of uncovered BIPV/T water or

air components have proven difficult to find. Studies by Kim et al. (1) and Athienitis (2) reported total efficiencies of 47% and 55%, respectively, for corresponding uncovered BIPV/T water and air components. Studies on uncovered PV/T (3-7) report thermal efficiencies ranging between 45% – 60% for water based and 38% – 46% for air based PV/T. Electrical efficiency from 9.5% to 14.5% was reported for water based PV/T and from 10.4% to 13% for air based PV/T.

Studies on other BIPV/T (8-15) report thermal efficiencies between 37.5% – 72% for water based BIPV/T and between 17.2% – 53.7% for air based BIPV/T. Electrical efficiencies in the range 4.9% – 11.6% and 10% – 15.5% were reported for water and air based BIPV/T, respectively. These numbers provide a rough basis of comparison for the magnitude of the expected thermal and electrical performance of the uncovered BIPV/T component analysed in this thesis. However, measurements and simulations should be carried out to determine the performance of the specific component.

Performance indicators

Table 1 in combination with Figure 3 shows the performance indicators used in the thesis to evaluate the performance of the BIPV/T technologies.

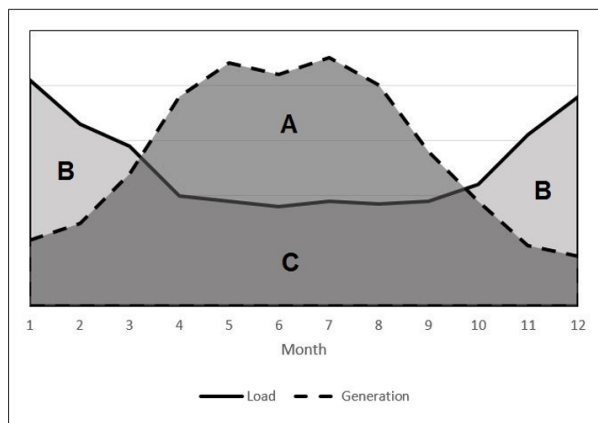


Figure 3: General monthly graphs of electric energy load and generation of a building. Adapted from [37]

Table 1: Mismatch factors and indicators. Adapted from [37]

Factor group	Mismatch factor
Load matching	load match = $\frac{C}{B+C}$
	unmatched generation = $\frac{A}{A+C}$
Energy carrier compensation	carrier surplus = $\frac{A-B}{A+C}$ (only if A>B)

PV/T validation

In order to validate the water based PV/T component in TRNSYS, measurements of an unglazed PV/T water component connected to a tank were carried out by a fellow GEL student. The main parameters of the PV/T test rig are presented in Table 2.

Table 2: Main parameters of the PV/T test rig

Parameter	Value
Area	1.26 m ²
Electrical efficiency	15%
Inclination	45°
Tank size	100 l
Mass flow rate	100 l/h
Pumping power	46 W

The water based PV/T component was validated using the PV/T outlet temperature and the power output as validation metrics. The deviation from the measured data can be seen in Figure 4.

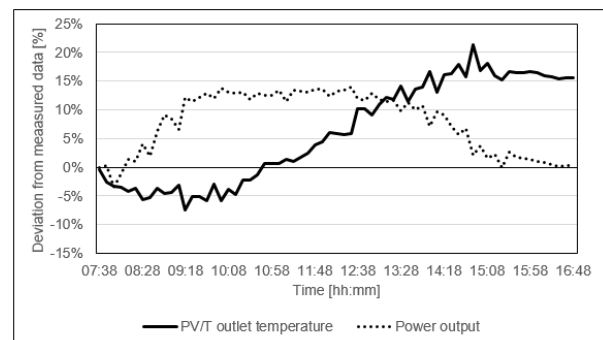


Figure 4: Calibration signatures of the validation metrics for the calibrated model

For the calibration model, the CV(RMSE) of 12.43% and 17.35% for outlet temperature and power output, respectively, are close to the 10% limit described in the literature (16), and thus the model is regarded as a decent approximation of the real-life conditions. Although the overall efficiency of the calibrated model is higher than that of the measured data, the deviation in electrical efficiency, which is the prioritised output for the unglazed PV/T, is rather small. The results of the validation are in accordance with the validation of TYPE 563 conducted by International Energy Agency (IEA) based on an experimental PV/T test performed by Katic (17, 18).

GEL office

The Norwegian Standard for passive house and low energy buildings (NS 3701) (19) is used in order to set the criteria for the GEL office building, which also fulfils the minimum requirements for office buildings according to Norwegian TEK 15.

Based on this simulation, the maximum heating and cooling power is found to be 4.9 kW and 4.4 kW, respectively as seen in Figure 5. The total annual energy demand for heating and cooling of the office building is 63.7 kWh/m².

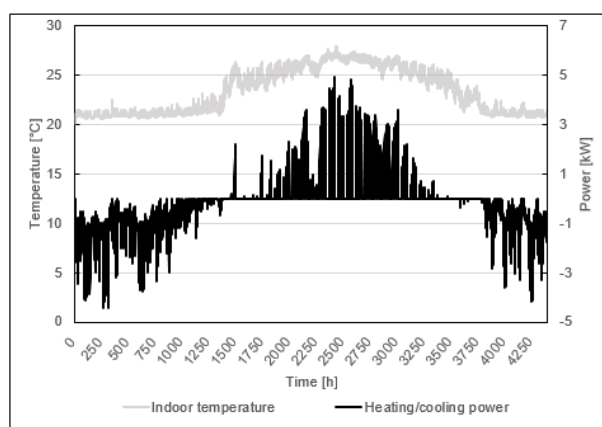


Figure 5: Annual heating (negative values) and cooling (positive values) demand

Optimised GEL models

The air and water based BIPV/T systems are optimised with the use of TRNSYS simulations. The final values of both the air and water based BIPV/T systems can be seen in Table 3 and Table 4.

Table 3: Final values of the water based BIPV/T system

<i>System parameter</i>	<i>Value</i>
Dead band [on/off]	8/2
Size of storage tank [l]	2000
Specific flow rate [kg/hm ²]	2.2
Inlet from heat source [m]	1.45
Inlet from cold side [m]	0.145

Table 4: Final values of the final air based BIPV/T

<i>System parameter</i>	<i>Value</i>
Dead band [on/off]	10/4
Size of storage tank [l]	2000
Specific flow rate [kg/hm ²]	10.89
Inlet from heat source [m]	0.87
Inlet from cold side [m]	0.435

Thermal Performance

Figure 6 shows the thermal efficiency and the useful energy collected. The useful thermal energy output of the air based BIPV/T system is smaller than that of the water based, although the thermal efficiency and the number of monthly operating hours are greater. The reduced useful energy output is caused by the heat exchanger in the system, with an efficiency of 60%, which is the default value suggested by TRNSYS. This highlights the challenge of efficiently transferring heat from the air to the water in the tank. An optimal system design would utilise the heat which is not extracted in the heat exchanger for further use e.g. in an open loop ventilation system. Such a system could possibly reduce the building's heating demand. However, this has not been further investigated in this thesis as a

DHW system was chosen to compare the long-term performance of the water and air based BIPV/T technologies.

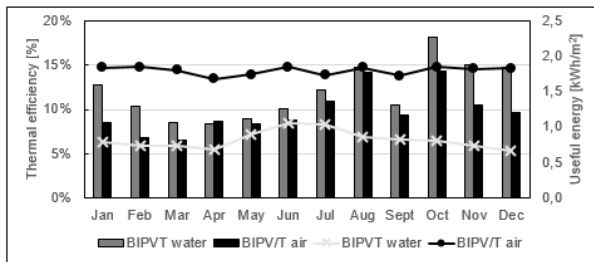


Figure 6: Thermal efficiency (line) and useful energy (column) of the water and air based BIPV/T systems

Electrical Performance

When analysing the electrical efficiencies of the different BIPV/T technologies and the BIPV reference, the highest efficiency and electrical energy production was observed for the air based BIPV/T as seen in Figure 7. A large dip in electrical performance was seen for the water based BIPV/T. Further analyses of data showed that the dip was not caused by higher PV surface temperatures as the water based BIPV/T component showed the lowest value PV surface temperature as seen in Figure 8. Further, the analysis showed that the water based BIPV/T did not produce electrical power in periods of low solar radiation in contrast to the air based BIPV/T and the BIPV components. This may be caused by differences in the TRNSYS components which may be independent on user input as the same values of performance parameters was used for all technologies.

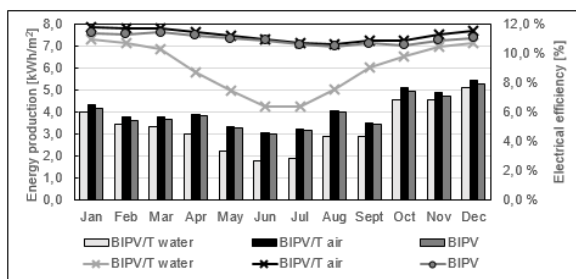


Figure 7: Comparison of electrical efficiency and electrical energy production between technologies

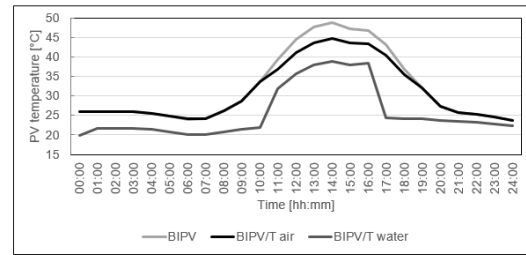


Figure 8: Comparison of PV surface temperatures between technologies in June.

Mismatch factors

The electrical power production of the air based BIPV/T shows a greater resemblance to the electrical load of the office building with a surplus of power generation for all months, and showed a slight increase in power production compared to the BIPV reference. The load matching of the air based BIPV/T system can be seen in Figure 9.

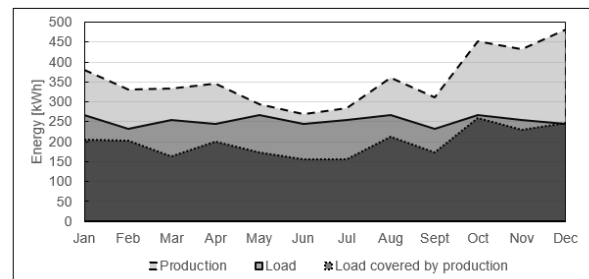


Figure 9: The electrical production, load covered by production and load

The analysis shows that the office building is dependent on importing/storing energy but the load matching and surplus of electrical energy production is larger for the air based BIPV/T. This means that the required battery capacity is reduced, which lowers the cost of being grid independent. However, storing the excess power in the grid and importing power when needed may be a more viable solution as many countries invest in smart grids enabling export of electricity from smaller energy producers, e.g. BIPV/T electrical energy production from office buildings. Thus, the

decision of electricity storage is highly dependent on economic considerations. The overview of mismatch factors and the thermal solar fraction can be seen in Table 5.

Table 5: Mismatch factors and thermal solar fraction

Technology	Unmatched generation	Carrier surplus	$SF_{electrical}$	$SF_{thermal}$
BIPV	0.44	0.27	0.77	-
BIPV/T _{air}	0.44	0.29	0.73	0.33
BIPV/T _{water}	0.60	0.13	0.46	0.42

Effect of Building Integration

The effect of building integration proved to be small for the investigated façade as seen from Table 6. Small reductions in the building cooling demands for air and water based BIPV/T suggests that the fluid flow has a cooling effect on the building body. This effect was also present during the heating season, leading to a larger heating demand compared to the building without building integrated solar technology. Effects on auxiliary and pump or fan energy needs were negligible as these quantities are less influenced by external parameters.

However, a larger effect of building integration may be seen for BIPV/T systems on larger building facades.

Table 6: Building energy need when implementing various solar technologies. All units in kWh/m²

Energy need	BIPV/T water	PV/T water	BIPV/T air	PV/T air	BIPV
Building	Heating	40.07	40.05	40.13	40.05
	Cooling	23.52	23.66	23.64	23.66
	Total	63.59	63.71	63.77	63.71
DHW	Auxiliary	24.70	24.73	27.56	27.56
	Pump/fan	0.34	0.34	2.68	2.67

Conclusion

Analysis and development of design methods have been carried out for the building integration of air and water based PV/T using TRNSYS. The water based

BIPV/T model was validated using winter measurements of an actual component in order to assess its' performance both in regards to production of energy and its' effect on the energy need of an office building.

The analysis conducted in this thesis reveals a potential for vertically mounted BIPV/T facades in Shanghai. Initial investigation shows that the solar irradiance incident on a vertically mounted façade is present during the whole year with larger amounts of solar irradiance in the winter months.

The analysis of the air and water based optimisation process, revealed that an increase of mass flow rate had the greatest impact on the BIPV/T systems, where increased solar fractions were observed when reducing the mass flow rate for both technologies. When increasing the mass flow rate the electrical performance of the air based BIPV/T increased noticeably, but because of limitations in the TRNSYS model/program higher values of flow rate for the air and water based BIPV/T were not tested. The increase of storage volume had a large positive effect on the amount useful energy collected to the storage tank for both the air and water based BIPV/T systems.

A comparison between the air and water based BIPV/T showed that the collected useful energy and the solar fraction was greater for the water based system than that of the air based. This indicates that the water based BIPV/T is more applicable for DHW production, but the potential of utilising excess heat for heating of ventilation is present for the air based BIPV/T. Additionally, the air based BIPV/T showed larger electrical efficiencies throughout the annual simulation with substantially larger electrical solar fraction. The air based BIPV/T also showed improved electrical efficiency compared to a BIPV system reference but because of the pump power

required to circulate the air, the electrical solar fraction was slightly less than that of the BIPV reference. The benefit of the air based BIPV/T compared to the BIPV is that it provides almost the same electrical solar fraction but in addition it produces heat for DHW.

Some differences were seen in the behaviour of the two BIPV/T systems, where the water based BIPV/T did not produce power during certain periods of low solar irradiance. In order to reliably compare the electrical performance between the air and water based BIPV/T, a validation based on experimental data from summer months should be carried out.

The analysis shows that the air based BIPV/T is more grid independent and that the power production matches the electrical load of the building to a larger extent than that of the water based BIPV/T. By looking at monthly values of mismatch factors it can be concluded that the air and water based BIPV/T systems could be independent of the grid but the capacity needed for batteries may be too high as there are longer periods of little or no power production in the summer months. Therefore, storing excess power in the grid may be a viable solution.

Based on the thermal solar fraction it is concluded that the BIPV/T technology may serve better as a supplement to a borehole heat pump system, which is already installed at GEL. The coupling could also lead to higher performance of the BIPV/T.

The effect of building integration is considered negligible when analysing the change in heating and cooling demand of the GEL office building, as simulation results for PV/T and BIPV/T systems were compared.

References

1. Kim J-H, Park S-H, Kang J-G, Kim J-T. Experimental performance of heating system with building-integrated PVT (BIPVT) collector. *Energy Procedia*. 2014;48:1374-84.
2. Athienitis AK. Smart Net-Zero Energy Buildings Strategic Research Network. NSERC; 2014.
3. Dubey S, Sandhu GS, Tiwari GN. Analytical expression for electrical efficiency of PV/T hybrid air collector. *Applied Energy*. 2009;86(5):697-705.
4. Tripanagnostopoulos Y, Nousia TH, Souliotis M, Yianoulis P. Hybrid photovoltaic/thermal solar systems. *Solar energy*. 2002;72(3):217-34.
5. Zhang X, Zhao X, Smith S, Xu J, Yu X. Review of R&D progress and practical application of the solar photovoltaic/thermal (PV/T) technologies. *Renewable and Sustainable Energy Reviews*. 2012;16(1):599-617.
6. Mishra RK, Tiwari GN. Energy matrices analyses of hybrid photovoltaic thermal (HPVT) water collector with different PV technology. *Solar Energy*. 2013;91:161-73.
7. Chow TT. A review on photovoltaic/thermal hybrid solar technology. *Applied Energy*. 2010;87(2):365-79.
8. Chow TT, Chan ALS, Fong KF, Lin Z, He W, Ji J. Annual performance of building-integrated photovoltaic/water-heating system for warm climate application. *Applied Energy*. 2009;86(5):689-96.
9. Ibrahim A, Fudholi A, Sopian K, Othman MY, Ruslan MH. Efficiencies and improvement potential of building integrated photovoltaic thermal (BIPVT) system. *Energy Conversion and Management*. 2014;77:527-34.
10. Daghigh R, Ruslan MH, Sopian K. Advances in liquid based photovoltaic/thermal (PV/T) collectors. *Renewable and Sustainable Energy Reviews*. 2011;15(8):4156-70.
11. Agrawal B, Tiwari GN. Optimizing the energy and exergy of building integrated photovoltaic thermal (BIPVT) systems under cold climatic conditions. *Applied Energy*. 2010;87(2):417-26.

12. Bambrook SM, Sproul AB. Maximising the energy output of a PVT air system. *Solar Energy*. 2012;86(6):1857-71.
13. Sarhaddi F, Farahat S, Ajam H, Behzadmehr A. Exergetic performance assessment of a solar photovoltaic thermal (PV/T) air collector. *Energy and Buildings*. 2010;42(11):2184-99.
14. Tripanagnostopoulos Y, Nousia T, Souliotis M, editors. Low cost improvements to building integrated air cooled hybrid PV-Thermal systems. *Proceedings of 16th European PV solar energy conference*; 2000.
15. Chen Y, Athienitis AK, Galal K. Modeling, design and thermal performance of a BIPV/T system thermally coupled with a ventilated concrete slab in a low energy solar house: Part 1, BIPV/T system and house energy concept. *Solar Energy*. 2010;84(11):1892-907.
16. Hensen JL, Lamberts R. *Building performance simulation for design and operation*: Routledge; 2012.
17. Katic I. *Measurement Report-Test of PV/T-module "PVtwin"*. Solar Heating & Cooling Programme: International Energy Agency; 2006. Contract No.: Report DC4-1.
18. Darcovich K, Entchev E, Tzscheutschler P. *Integration of Micro-Generation and Related Energy Technologies in Buildings*. IEA EBC Annex 54: Energy in Buildings and Communities Programme; 2014.
19. Norsk Standard. NS 3701. *Criteria for passive houses and low energy buildings - non-residential buildings*2012.